NOVEL BIOFUEL FORMULATIONS FOR ENHANCED VEHICLE PERFORMANCE AWARD DE-FC26-07NT43278

FINAL SCIENTIFIC/TECHNICAL REPORT

Dennis J. Miller (PI), Ramani Narayan, Kris A. Berglund, Carl T. Lira
Department of Chemical Engineering and Materials Science
Harold J. Schock, Farhad Jaberi, Tonghun Lee
Department of Mechanical Engineering
Michigan State University
East Lansing, Michigan 48824

In partnership with

Ford Motor Company
Research and Innovation Center, Dearborn, Michigan 48121

James Anderson, Timothy Wallington
Systems Analytics and Environmental Sciences
Eric Kurtz, Will Ruona
Powertrain Systems and Application Engineering
Heinz Hass, Environmental Science
Research and Advanced Engineering Center, Aachen, Germany

August 30, 2013

Executive Summary

This interdisciplinary research program at Michigan State University, in collaboration with Ford Motor Company, has explored the application of tailored or designed biofuels for enhanced vehicle performance and reduced emissions. The project has included a broad range of experimental research, from chemical and biological formation of advanced biofuel components to multicylinder engine testing of blended biofuels to determine engine performance parameters. In addition, the project included computation modeling of biofuel physical and combustion properties, and simulation of advanced combustion modes in model engines and in single cylinder engines.

Formation of advanced biofuel components included the fermentation of five-carbon and six-carbon sugars to n-butanol and to butyric acid, two four-carbon building blocks. Chemical transformations include the esterification of the butyric acid produced to make butyrate esters, and the esterification of succinic acid with n-butanol to make dibutyl succinate (DBS) as attractive biofuel components. The conversion of standard biodiesel, made from canola or soy oil, from the methyl ester to the butyl ester (which has better fuel properties), and the ozonolysis of biodiesel and the raw oil to produce nonanoate fuel components were also examined in detail.

Physical and combustion properties of these advanced biofuel components were determined during the project. Physical properties such as vapor pressure, heat of evaporation, density, and surface tension, and low temperature properties of cloud point and cold filter plugging point were examined for pure components and for blends of components with biodiesel and standard petroleum diesel. Combustion properties, particularly emission delay that is the key parameter in compression ignition engines, was measured in the MSU Rapid Compression Machine (RCM), an apparatus that was designed and constructed during the project simulating the compression stroke of an internal combustion engine under highly instrumented conditions.

Simulation of and experimentation on combustion in single and multicylinder engines was carried out in detail throughout the project. The combustion behavior of biofuel blends neat and in petroleum were characterized in the MSU optical engine, in part to validate results obtained in the RCM and to provide data for comparison with simulations. Simulation of in-cylinder, low-temperature combustion included development of an extensive fuel injection model that included fuel spray breakup, evaporation, and ignition, along with prediction of cylinder temperature, pressure, and work produced.

Single cylinder and multicylinder engine tests under advanced low-temperature combustion conditions conducted at Ford Motor Company validated experimental and simulation results obtained in the MSU engine and in MSU simulations. Single cylinder engine tests of an advanced biofuel containing biodiesel and dibutyl succinate, carried out under low-temperature combustion conditions, showed similar power generation and gas-phase emissions (CO, HC, NOx), but a reduction in particulates of as much as 60% relative to neat biodiesel and 95% relative to petroleum diesel at the same operating conditions. This remarkable finding suggests that biofuels may be able to play a role in eliminating the need for particulate removal systems in diesel vehicles. The multicylinder engine tests at Ford, carried out using butyl nonanoate as an advanced biofuel, also gave promising results, showing a strong decline in particulate emissions and simultaneously a modest decrease in NOx emissions relative to standard petroleum diesel at the same conditions.

In summary, this project has shown that advanced biofuels and their blends are capable of maintaining performance while reducing emissions, particularly particulates (soot), in

compression ignition engines. The interdisciplinary nature of biofuel production and testing has identified fuel properties that are capable of producing such performance, thus providing direction for the implementation of renewable fuels for U.S. transportation. The testing and simulation studies have deepened our understanding of combustion 1) by advancing the rigor with which simulations can be carried out and 2) by illustrating that differences in biofuel and petroleum fuel properties can be used to predict differences in combustion behavior in engines. The future viability of biofuels for compression ignition (diesel) engines is now subject to economic (cost) uncertainty more so than to technical barriers, as the advanced biofuel blends developed here can improve cold-weather fuel properties, provide similar engine performance, and reduce emissions.

4. Comparison of accomplishments with goals and objectives of project

The formal objectives for this project are shown in italics below, and a short narrative describing the extent to which the objective has been met is given below each.

1. *Formulation of biofuel components: Biofuel components will be synthesized through a variety of experimental routes. This will enable a broad selection of biofuels that can be blended to provide optimal physical and combustion characteristics, and have a technical pathway to commercial production. The objective is to identify and evaluate catalysts and reaction conditions that give good yields of the desired components from their starting biomass materials.*

   Objective met. A broad range of biofuel components were produced by various means on the project, ranging from biological fermentation of biomass sugars to ozonolysis of plant oils. In many cases, the efficiency of production of these fuel components improved significantly as a result of the work conducted during the project.

2. *Blending and characterization of biofuel components Biofuel components will be blended and characterized to provide biofuels with optimal physical and combustion properties. Conventional diesel fuel may also be blended with the components to obtain fuels with acceptable physical and combustion properties while maintaining technical and economic feasibility. This will provide a database of biofuel properties that can be used in conjunction with experimental and computational engine studies to optimize the blends for compression ignition (CI) and spark ignition (SI) engines.*

   Objective met. Physical properties such as vapor pressure, heat of vaporization, density, and surface tension, and combustion properties such as heat of combustion and ignition delay were measured for the biofuel components made. The biofuel components produced were blended with each other, with biodiesel, and with standard petroleum diesel. Properties of these blends were also extensively characterized.

3. *Advanced engine concepts for low temperature combustion: Advanced fuel delivery systems for CI low temperature combustion (LTC) regimes will be developed with application to biofuel utilization. LTC and other high efficiency combustion regimes can substantially increase efficiency while meeting mandated emissions requirements, and*

this research will provide data needed to utilize biofuels in a high efficiency engine. Since the biofuels will be blended, this also provides the ability to tailor the fuel to an optimal mix for a given engine and combustion regime.

Objective met. Extensive single cylinder engine tests were carried out in the MSU optical engine and in single cylinder engine tests at Ford to characterize biofuel performance. These results were used to validate combustion simulations performed during the project. Improved combustion performance and reduced emissions were observed for advanced biofuel blends.

4. *Multicylinder/vehicle evaluation: Multi-cylinder CI engine testing of the biofuel blends will be conducted to validate the performance in a production engine. This will allow performance comparison of the biofuel blends relative to conventional diesel fuels. Incorporation of the biodiesel/LTC research will also allow investigation of biofuel performance in advanced engine operation modes.*

Objective met. Multicylinder engine tests conducted with collaborators at Ford Motor Company showed good engine performance and significant reduction in emissions under advanced operating conditions.

5. Summary of Project Activities

A complete report of technical activities on the project is attached as an appendix to this report. The appendix is titled "Technical Report of Project Activities."

6. Products Developed Under Award

A. Archival Journal Publications

A. Banaeizadeh, A. Afshari, H.S. Schock, F.A. Jaberi, "Large-Eddy Simulations of Turbulent Flows in Internal Combustion Engines," Int. J. of Heat and Mass Transfer, Vol. 60, pp. 781-796, 2013.

A. Banaeizadeh, Z. Li, and F. A. Jaberi, "Compressible Scalar FMDF Model for Large-Eddy Simulations of High speed Turbulent Flows," AIAA Journal, 49(10):2130–2143, 2011.

C. Allen, E. Toulson, D. Tepe, H. Schock, D. Miller, T. Lee, "An Investigation of the Influence of Fatty Ester Composition on Biodiesel Combustion," Fuel, accepted and in press (2013).

C. Allen, E. Toulson, D. Hung, H. Schock, D. Miller, T. Lee, "Ignition Characteristics of Diesel and Canola Biodiesel Sprays in the Low Temperature Combustion Regime," Energy & Fuels, 25 (7), 2895-2908 (2011).

E. Toulson, C. Allen, J. McFarlane, D. Miller, H. Schock, T. Lee, "Modeling the Auto-Ignition of Fuel Blends with a Multi-Step Model," Energy and Fuels, 25 (2), 632-639 (2011).

E. Toulson, C. Allen, D. Miller, T. Lee, "Optimization of a Multi-step Model for the Autoignition of Dimethyl Ether in a Rapid Compression Machine," Energy and Fuels, 24 (6), 3510-3516 (2010).

E. Toulson, C. Allen, D. Miller, T. Lee, "Modeling the Auto-Ignition of Oxygenated Fuels using a Multi-Step Model," Energy and Fuels, 24 (2), 888-896 (2010).

Hassan, A.M.; Miller, D.J.; Lira, C.T. "The StePPE Method for Vapor Pressure and Liquid Density Predictions of Hydrocarbons", in preparation to J. Chem. Phys. B. (2013).

Hassan, A.M; Vu, D.T.; Bernard-Brunel, D.; Elliott, J.R.; Miller, D.J; Lira, C.T, "Application of SPEAD to bioderived esters and acetals" Ind. Eng. Chem. Res. 51(8), 3209-3214, (2012).

Murkute, A.; Jackson, J.E.; and Miller, D.J., "A Supported $MnCeO_x$ Catalyst for Ketonization of Carboxylic Acids," *J. Catal*. **278**, 189-199 (2011).

Pappu, Venkat KS., Yanez-McKay, A.J., Peereboom, L., Muller, E.; Lira, C.T. and Miller, D.J., "A Kinetic Model for the Amberlyst 15-Catalyzed Transesterification of Methyl Stearate with n-Butanol," *Bioresource Technology,* **102**, 4270-4272 (2011).

Pappu, V.K.S.; Kanyi, V.; Muller, E.; Peereboom, L.; Lira, C.T.; Miller, D.J. "Butyric acid esterification over solid acid catalysts: The effect of alcohol carbon chain length and a kinetic model for the Amberlyst 70 catalyzed esterification with 2-ethylhexanol," *Bioresource Technology,* **130**, 793-797 (2013).

Santhanakrishnan, A.; Shannon, A.; Peereboom, L; Lira, C.T.; Miller, D.J. "Kinetics of mixed alcohol esterification of butyric acid," *Ind. & Eng. Chem. Res.*, **52**, 1845-1853 (2013).

Hong, Xi; Lira, C.T.; Miller, D.J. "Kinetics of glycerol acetal formation from glycerol and 1,1-diethoxyethane," *Chemical Engineering Journal,* **222**, 374-381 (2013).

Graiver, D.; Patil, M.; Narayan, R; "Recent advances in ozonation of vegetable oils," Recent Patents on Materials Science **3**(3), 203- 218.

B. Conference Papers

H. Abdulrahman, F.A. Jaberi, V. Arghode, A. Gupta, "Numerical and Experimental Study of Turbulent Mixing and Reaction in Colorless Distributed Combustion Systems ". *48th Joint Propulsion Meeting.* AIAA. August 2012.

Li , Z., Banaeizadeh, A., Rezaeiravesh, S. and Jaberi, F.A., "Advanced Modeling of High Speed Turbulent Reacting," AIAA-2012-0116, 50th AIAA Aerospace Sciences Meeting Including the New Horizons Forum and Aerospace Exposition, Nashville, TN, January 9-12, 2012.

A. Banaeizadeh, Z. Li and F.A. Jaberi, Large Eddy Simulation of Turbulent Combustion via Filtered Mass Density Function, 47th AIAA/ASME/SAE/ASEE Joint Propulsion Conference, San Diego, August 2011.

A. Banaeizadeh, H. Schock, and F.A. Jaberi, "LES/FMDF of Spray Combustion in Internal Combustion Engines." National Combustion Meeting, The Combustion Institute, Ann Arbor, Michigan, May 2009.

Murkute, A.; Jackson, J.E.; Miller, D.J. "Novel Solid Base Catalyst for Condensation of Carboxylic Acids," Proc. 2009 Annual Meeting of the American Institute of Chemical Engineers, Nashville, TN, November 9-13, 2009.

Pappu, V.K.S., V.M. Kanyi, D.J. Miller, "Branced-Chain Alcohol Esters as Low-Temperature Biofuel Constituents," Proc. 2010 Annual Meeting of the American Institute of Chemical Engineers, Salt Lake City, UT, November 7-12, 2010.

Pappu, V.K.S.; Kolah, A.K.; Lira, C.T.; Miller, D.J. "Methyl Stearate Transesterification with n-Butanol: Process Intensification Using Distillation with External Side Reactors," Proc. Annual Meeting of the AIChE, October 16-21, Minneapolis, MN, (2011).

Lown, A.; Peereboom, L.; Miller, D.J.; Lira, C.T., "Surrogate Development for Cloud Point and Distillation Curve Modeling of Bio-Derived Fuel Blends," Proc. Annual Meeting of the AIChE, Pittsburgh, PA, October 29 – November 2, 2012.

Santhanakrishnan, A.; Shannon, A.; Peereboom, L.; Lira, C.T.; Miller, D.J., "Kinetics of Mixed Alcohol Ethanol/Butanol Esterification of Butyric Acid," Proc. Annual Meeting of the AIChE, Pittsburgh, PA, October 29 – November 2, 2012.

C. Presentations

"Large Eddy Simulations of Turbulent Spray Combustion in Internal Combustion Engines," FORD-MSU Powertrain Meeting. Energy and Automotive Research Lab, East Lansing, MI. January 2012.

Large Eddy Simulations of Turbulent Spray Combustion in Internal Combustion Engines, Joint Chrysler-MSU Meeting. Energy and Automotive Research Lab, East Lansing, MI. *June 2012.*

"Large Eddy Simulation of Turbulent Combustion via Filtered Mass Density Function," 47th AIAA/ASME/SAE/ASEE Joint Propulsion Conference and 9th Annual International Energy Conversion Engineering Conference, July 2011.
"CFD of MultiPhase Flows," 1st FRIB and Mechanical Engineering Symposium, East Lansing, MI, April 2011.

"Large Eddy Simulations of Two-Phase Turbulent Reacting Flows," Department of Mechanical Engineering, University of Virginia, Charlottesville, VA, February 2011.

"Large Eddy Simulations of Multi-Phase Turbulent Reacting Flows," ICER, MSU, October 2010.

Hassan, A. M.; Zalokar, J; Miller, D.J.; Lira, C.T. "VLE of potential biofuel compounds using SPEAD simulations" 2010 Midwest Thermodynamics and Statistical Mechanics Conference, June 2-3, University of Notre Dame, South Bend, IN, (2010).

Vu, D.T.; Bernard-Brunel, D.; Hassan, A.M.; Elliott, J.R.; Miller D.J.; Lira C.T. "Vapor Pressures of Oxygenated Compounds using a Step Potential Perturbation Method", presented at the Seventeenth Symposium on Thermophysical Properties, June 21-26, Boulder, CO, (2009).

Hassan, A.M.; Vu, D.T.; Bernard-Brunel, D.; Elliott, J.R.; Miller, D.J.; Lira, C.T. "Vapor pressures of oxygenated compounds: SPEAD Parameters and applications", presented at the 2009 Midwest Thermodynamics and Statistical Mechanics Conference, May 19-20, Detroit, MI, (2009).

Santhanakrishnan, A.; Peereboom, L.; Miller, D.J. "Kinetics of Mixed Alcohol Ethanol/Butanol Esterification of Butyric Acid with Amberlyst 70,"Proc. Corn Utilization and Technology Conference, Indianapolis, Indiana, June 4-6, 2012.

7. Computer Simulations

The programming code for the two major computer simulations used in this project, 1) the large eddy simulation (LES) model of spray and combustion in an engine cylinder, and 2) the simulation of ignition delay during engine compression, were both in existence prior to the beginning of the project period. Details of these programs, including background mathematics, theory, and simulation method, are given in the publications listed above or are referenced in the above publications. Improvements made to the above models are described in the technical report in the appendix, where the background theory and solution approach are discussed. Those details are not reproduced here.

Hardware: The computational facilities for conducting large-scale simulations are provided by the High Performance Computing Center (HPCC) at MSU. The center resources include two 2048-processer PC clusters. For small-size simulations, flow visualization, software/algorithm model development, and post-processing of data, we used high end PCs in the CFD Laboratory at MSU.

The multi-step kinetics ignition model and the detailed CHEMKIN models used for predicting ignition delays in this project were run on a desktop computer (Windows with Intel Core 2 Quad Q9550 processor clocked at 2.83 GHz with 8GB of memory). The multi-step model was also linked to the Hierarchical Evolutionary Engineering Design System (HEEDS) software optimization method which used a genetic algorithm global search optimization to determine the optimal multi-level model constants.

APPENDIX

NOVEL BIOFUEL FORMULATIONS FOR ENHANCED VEHICLE PERFORMANCE

TECHNICAL REPORT OF PROJECT ACTIVITIES

APPENDIX TABLE OF CONTENTS

An exhaustive compilation of work performed on the project is reported in this section. Results are organized according to the major activities of the project, not specifically according to the task list or project objectives. Further details of work performed may be found in the publications resulting from the project effort.

I. Formulation of Biofuel Components

I.1 Catalytic Routes to Biofuel Components

I.1.1. Production of biodiesel and succinate esters

Components formulated included fatty acid ethyl esters (FAEE) and butyl esters (FABE), succinate esters including dimethyl succinate (DMS), diethyl succinate (DES), and dibutyl succinate (DBS). All were made by standard esterification methods.

I.1.2. Transesterification of fatty acid methyl esters (FAME) to butyl esters (FABE)

Transesterification:	Methyl Stearate + Butanol → Butyl Stearate + Methanol	(1)
Etherification:	2 n-Butanol → Dibutyl Ether + Water	(2)
	n- Butanol + Methanol → Butylmethylether+ Water	(3)

Preparation of butyl esters: Transesterification of methyl stearate with n-butanol was catalyzed by sulfuric acid and cationic exchange resins. Reaction was carried out in 20 ml screw cap glass vials. Vials were kept in an oil bath at desired temperature $\pm 0.5^0 C$ using a controller for 48 to 72 hours by which time chemical equilibrium is reached. The equilibrium constant was calculated from the final concentration of the components in the vial. Concentrations were replaced with activities to take care of nonideality of the liquid phase. The components' activity coefficients were calculated using UNIFAC group contribution method. Samples were diluted in 6:1 ratio by weight in 1-octanol and analyzed using gas chromatography. Ethyl caprylate was the internal standard.

Equilibrium constant for the transesterification of methyl oleate with n-butanol was carried out by same experimental procedure. Results shown in Table I.1 indicate that, equilibrium constant of both the reactions is in the order of 1.2 to 2. Reaction conditions and the results are shown in the following tables.

Kinetic study of methyl stearate to butyl stearate: Transesterification of methyl stearate to butyl stearate was carried out in a 75 ml Parr reactor using Amberlyst 15 cationic exchange resin as catalyst. The mole ratio of n-butanol to methyl stearate was fixed at 20:1 for all experiments. Catalyst loading ranged from 0.82 to 5.0 weight percent of solution. Experiments were carried out at 90°C and 100°C. The alcohol etherification reaction was not taken into account in this model.

Table I.1 Equilibrium constants for butyl ester production via transesterification

Methyl Sterate (MS) transesterification	Temperature (K)	n-Butanol to MS mole ratio	Equilibrium constant K
	362.15	20.5	1.26
	354.15	20.1	1.24
	345.15	19.9	1.16
	334.15	17.3	1.12
Methyl Oleate transesterification	Temperature (K)	n-Butanol to MS mole ratio	Equilibrium constant K
	344.15	33.7	1.37
	354.15	33.3	2.08

Development of Pseudo homogeneous model: For methyl stearate consumption, the rate equation can be written as follows:

$$r_{MS} = -k_{fwd} * W * \left(C_{MS} C_{BuOH} - \frac{C_{BS} C_{MeOH}}{K_{eq}} \right)$$

$$k_{fwd} : \frac{(gmsol)^2}{mole.time.(gmcatalyst)}$$

$$W : \left(\frac{gmcatalyst}{gmsolution} \right)$$

Similarly, four differential equations were written and were solved using Euler's numerical method. The forward rate constant (k_{fwd}) is calculated using both the initial rate method and root mean square error (RMS) method. The reverse rate constant is determined from the equilibrium rate constant.

$$RMS = \sqrt{\frac{\sum_{i=1}^{n} (error)_i^2}{N}}$$

where error = $(Ci)_{exp}$- $(Ci)_{model}$

The reaction kinetics of Amberlyst-15 catalyzed transesterification of methyl stearate, a model biodiesel compound, with n-butanol have been completed. After identifying conditions to minimize both internal and external mass transfer resistances, the effects of catalyst loading, temperature, and the mole ratio of n-butanol to methyl stearate in the transesterification reaction were investigated. The dependence of the transesterification equilibrium constant on temperature was also examined. Based on the experimental results, a second-order, activity-based kinetic model was developed and optimized to fit the data. UNIFAC group contribution method was used to determine activity coefficients of liquid components in the reaction mixture. To solve the differential equations fourth order Runge-Kutta method, ODE 23 in MATLAB 7.0 was used. Results from the kinetic model are presented in Table I.2. Figure I.1 shows the evolution of all species in transesterification over time; etherification of n-butanol with methanol to form butyl methyl ether causes the methanol mole fraction to fall below that of butyl stearate at longer times and even to decrease at 100^{o}C. Mole fractions of components calculated from the kinetic parameters are shown as continuous lines in Figure I.1. This model describes the

transesterification reasonably well over the range of 70 – 100°C, including the formation of ethers at higher temperatures.

Table I.2. Kinetic model parameters

Parameter	Value	Units
$k^0_{1,f}$	3.21×10^9	$kg_{soln}/(kg_{cat}.min)$
$E_{1.f}$	82500	kJ/kmol
k^o_2	1.56×10^{10}	$kg_{soln}/(kg_{cat}.min)$
k^o_3	3.12×10^{10}	$kg_{soln}/(kg_{cat}.min)$
E_2	98800	kJ/kmol
E_3	92500	kJ/kmol

$k^0_{1,f}$ = pre-exponential factor for forward reaction rate constant in transesterification reaction (kgsoln/(kgcat.min)
k^o_2= pre-exponential factor for rate constant for DBE reaction kgsoln/(kgcat.min)
k^o_3 = pre-exponential factor for rate constant for BME reaction kgsoln/(kgcat.min)
$E_{1,f}$ = Energy of activation for forward transesterification reaction, kJ/kmol
E_2 = Energy of activation for DBE reaction, kJ/kmol
E_3 = Energy of activation for BME reaction, kJ/kmol

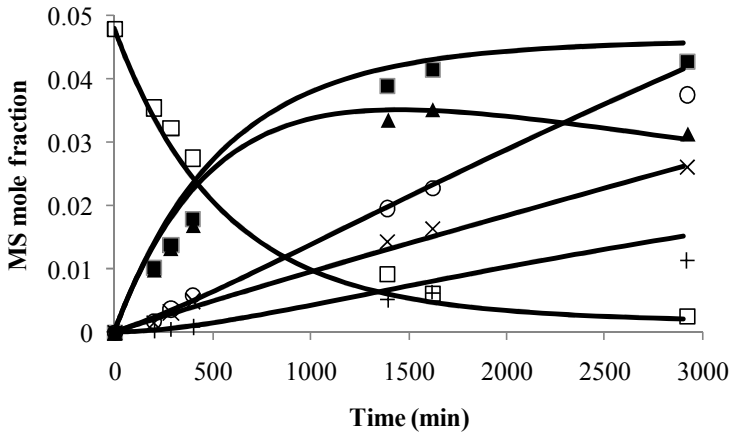

Figure I.1. Mole fraction profiles of species present in MS transesterification reactions at 100°C. Reaction conditions: initial mole ratio MS to BuOH = 1:20; catalyst loading = 4.8 wt%; (-□- - MS; -■- - BS; -▲- - MeOH; -×- - DBE; -+- - BME; -○- - W).

I.1.3. Formation of butyric acid esters

Synthesis of Butyrate Esters as Advanced Biofuel Components: Branched alcohol esters of butyric acid like isobutyl butyrate, 4-heptyl butyrate and 2-ethyl hexyl butyrate can modify the cold flow properties of biodiesel and can be potential biofuel components. This study focuses on

liquid phase esterification of butyric acid with alcohols of increasing chain length and branching catalyzed by p-toluene sulfonic acid and commercially available solid acid catalysts like Amberlyst-15, Amberlyst-36, Amberlyst-70 and Amberlyst BD 20. Butyric acid esterification reaction can be represented as follows:

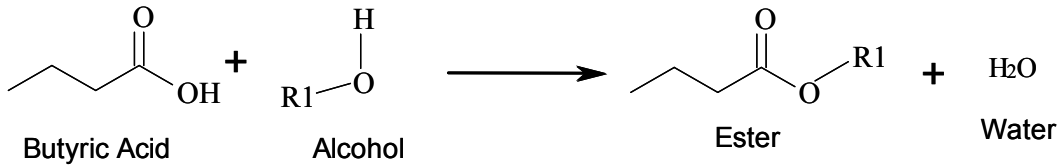

Butyric acid reactivity decreases with increasing alcohol chain length and exhibits a reactivity plateau for 1-heptanol and 1-octanol as shown in Figure I.2 for both homogeneous and heterogeneous catalysis. This is due to the steric effects resulting from the size of alcohol molecule and due to the dilution of –OH groups in the reaction system with the increasing chain length of the alcohol. It is also shows that on a per weight basis and per site basis, the homogeneous acid catalyst was much more active than the heterogeneous catalyst.

Among solid acid catalysts, on a per site basis, Amberlyst 70 is the best catalyst for butyric acid esterification (Figure I.3). This catalyst is used in kinetic experiments to develop a pseudo-homogeneous model for the esterification butyric acid with 2-ethyl hexanol.

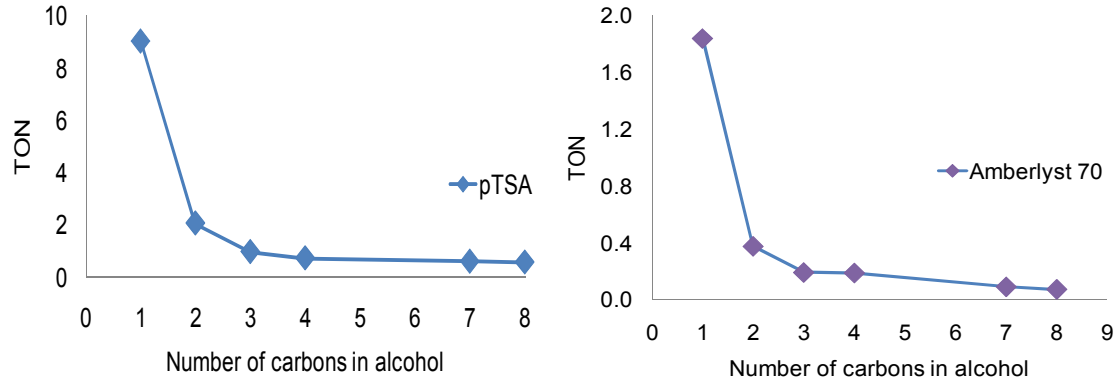

Figure I.2: Esterification of Butyric acid using homogeneous and heterogeneous catalysts. Reaction conditions: Temperature 60°C, mole ratio of alcohol to acid 3:1.

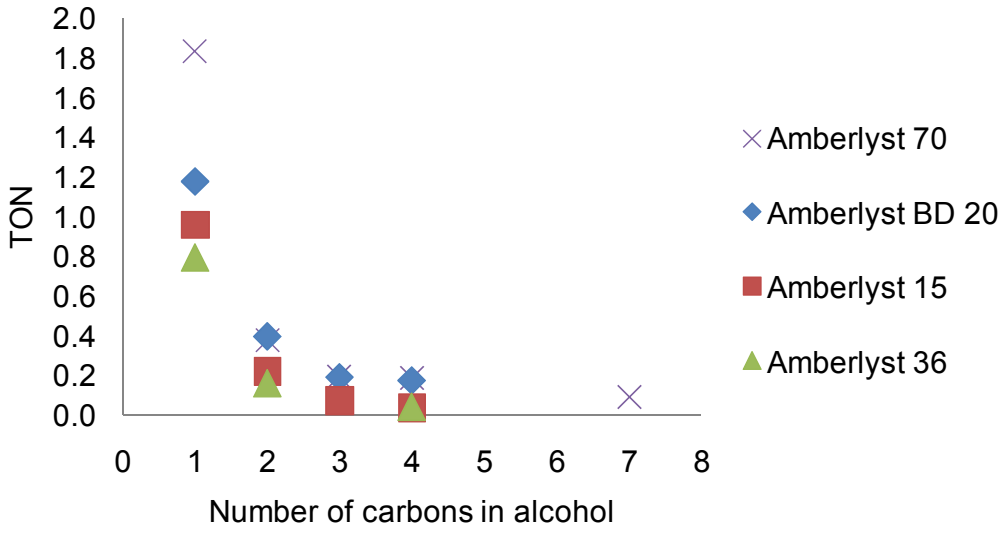

Figure I.3: Esterification of butyric acid using heterogeneous catalysts. Reaction conditions: Temperature 60°C, mole ratio of alcohol to acid 3:1.

Pseudo-homogeneous kinetic model: Using Weisz-Prater criteria, we conclude that internal mass transfer resistances are negligible for butyric acid esterification with 2-ethylhexanol. Therefore, a pseudo-homogeneous kinetic model can be applied to this system. To account for the thermodynamic non-ideality of the liquid solution in which reaction takes place, activity is used as a measure of species concentration instead of mole fraction. The UNIFAC group contribution method was used to calculate activity coefficients of butyric acid, 2-ethylhexanol, 2-ethylhexyl butyrate and water.

The effect of initial mole ratio of alcohol to acid, temperature, and catalyst loading were studied. A total of 19 experiments were conducted over a temperature range of 100°C to 150°C, catalyst loading of 0.3 to 3 weight% of the solution and an initial mole ratio of 3 to 15. Table I.3 summarizes the results obtained for kinetic parameters.

Table I.3: Optimized kinetic parameters for formation of 2-ethylhexyl butyrate

	Pre-exponential factor for forward reaction rate constant k_f (kgsoln/kgcat/min)	Activation energy E_a (J/mol)	Equilibrium constant K_{eq}
Mole fraction based model	1.46×10^6	59100	1.01
Activity based model	2.26×10^6	59900	12.2

The reaction rate of several alcohols containing from one to eight carbon atoms with butyric acid in the presence of either Amberlyst 70 ion exchange resin or sulfuric acid as catalysts has been correlated to several properties of the alcohols. First, rate is related to the overall –OH concentration of the neat alcohol, the value of which decreases with increasing chain length. Second, rate is correlated to the alcohol polarity, measured as $E_T(30)$, a property

quantifying the change in absorption of a pyridinium N-phenolate betaine dye as a function of surrounding solvent polarity. The relationship between $E_T(30)$ and rate is shown in Figure I.4 below; it is clear that $E_T(30)$ is a reasonable marker of esterification rate.

Finally, the rate constant for esterification with different alcohols can be correlated with polar susceptibility, or polarizability, according to the Taft Equation.

$$\log(k/ko)=\sigma^*\rho^*$$

k=forward rate constant
ko= forward rate constant of reaction with methanol
σ* = *polar substituent constant relative to CH3 group*
ρ*= *susceptibility of reaction series to polar substituents*

The resulting graph of the Taft Equation is given in Figure I.5 below.

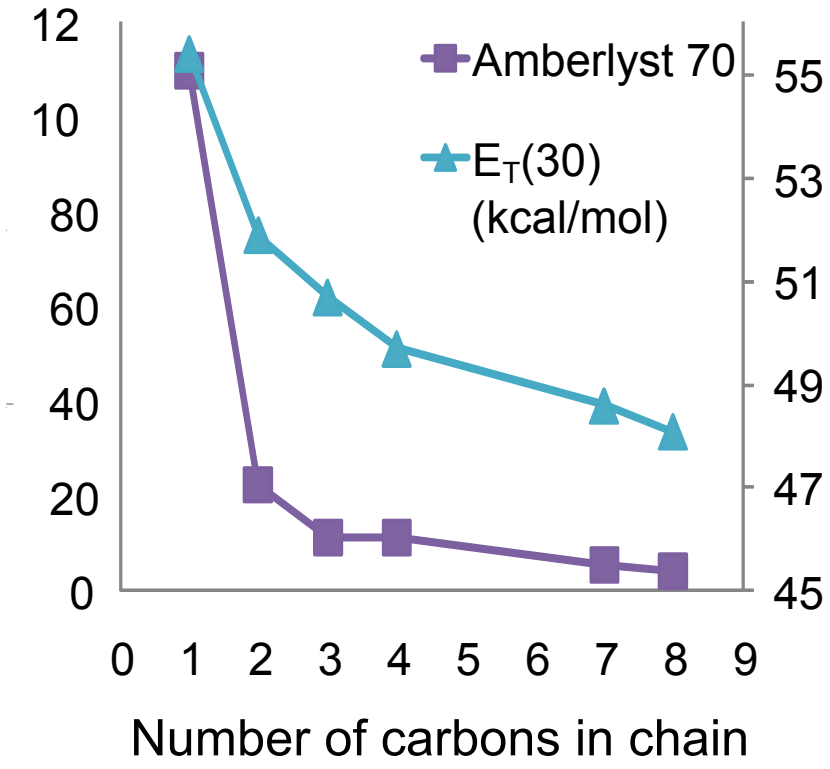

Figure I.4. Correlation of butyric acid esterification rate (TON, hr^{-1}) on Amberlyst 70 catalyst vs $E_T(30)$ polarity parameter. Rate is seen to correlate with alcohol polarity.

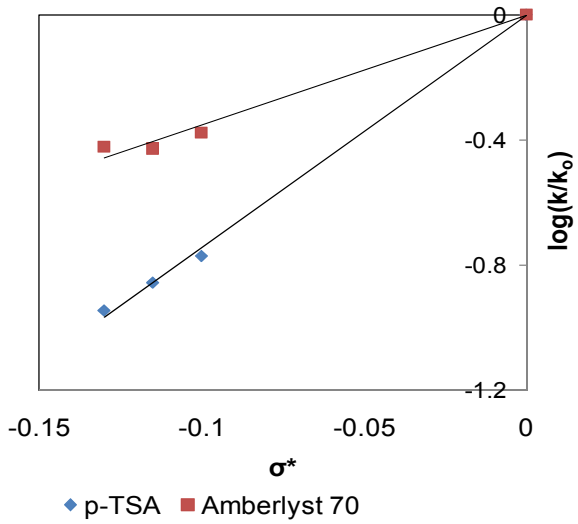

Figure I.5. Plot of the Taft Equation for different alcohols esterifying with butyric acid.

I.1.4. Ketonization of propionic and butyric acid

Catalyst Preparation:

MnO_x/CeO_2 (MC-CM prepared by co-precipitation): Cerium nitrate ($CeO_2(NO_3)_3.6H_2O$) and manganese nitrate ($Mn(NO_3)_2.4H_2O$) of the desired molar ratio were dissolved in de-ionized water and then hydrolyzed with aqueous ammonia. The hydrolyzed material was dried at 100 ^{0}C and calcined at 170^{0}C and 550^{0}C for 2h and 3hr, respectively, to obtain bulk MnOx/CeO_2.

Hexagonal Mesoporous Silica (HMS): HMS was prepared according to the method described elsewhere[1].

Mesoporous MnO_x/CeO_2 (Meso-MC): The catalyst was prepared by adding the desired molar ratios of citric acid and nitrates of manganese and cerium to a pre-calcined HMS. The material was dried at 170^{0}C for 2hr to obtain a metal citrate precursor. It was then calcined at 550^{0}C for 3hr to obtain active Meso-MC.

Catalyst characterization:

FTIR: Since the Meso-MC catalyst was prepared by the citrate process, it is helpful to evaluate the interaction between metal and citric acid in the precursor of Meso-MC. The FTIR spectra of citric acid and metal citrate precursor for Meso-MC in the region 2000-1000 cm^{-1} are shown in Fig. I.6A) and I.6B), respectively. The literature data[2] provide a reliable identification of the principle adsorption bands for citric acid: in the C=O stretching region a double carbonyl frequency is obtained. The peak at 1757 cm^{-1} is indicative of free carboxylic acid groups, whereas the peak at 1690 cm^{-1} represents the carbonyl frequency of the coordinated carboxyl groups, i.e. groups showing internal hydrogen bonds. The bands in the ranges 1350-1430 and 1166 -1258 cm^{-1} correspond, respectively, to the C-O stretching vibrations and to -OH in-plane deformation vibrations. The -OH stretching vibrations of the carboxylic groups occur as a broad

band with two superimposed peaks (-OH bonding at ~3500 cm^{-1} and intermolecular H-bond at ~3305 cm^{-1}, not shown). Finally, C-O stretching in C-OH group and tertiary -OH are represented by the bands at 1075 and 1110 cm^{-1}, respectively.

Figure I.6 corrupted and unavailable. Description in text.

Fig. I.6. FTIR spectra of A) citric acid and B) metal citrate precursor of Meso-MC

In the metal-citrate precursor of Meso-MC (Fig. I.6B), carboxylate salts are present. The resonance between the two C-O bonds of the COO^- groups results in appearance of bands near 1614 cm^{-1} and 1434 cm^{-1} that correspond to the asymmetric and symmetric vibrations of the COO^- group[3]. Many other skeleton vibrations occur in the range of 1437-1300 cm^{-1}, so the band at 1614 cm^{-1} best characterizes the carboxylate group attached to metallic ions. Thus, the absence of free carboxylic acid groups in the precursor (1690–1757 cm^{-1} in Fig. I.6B) indicates that the citric acid is forming a homogeneous mixture of metal citrates, the essential precursor for the formation of a homogeneous solid solution of mixed metal oxides. Other small bands in Fig. I.6B can be attributed to the C-O stretching of the C-OH group (1088 cm^{-1}) and to -OH bending (1226 cm^{-1}), respectively. The sharp absorption band of the nitrate ions occurs at 1385 cm^{-1}. The FT-IR absorption spectra of calcined HMS and Meso-MC samples are shown in Fig. I.7A) and I.7B), respectively. All samples show characteristic absorption bands at 3496 and 1687 cm^{-1} assigned to overlapping of the -OH stretching of adsorbed water and silanols. In the range of 400–1600 cm^{-1}, peaks at 480 cm^{-1}, 844 cm^{-1}, 1125 cm^{-1} and 1234 cm^{-1} correspond to the rocking, bending (or symmetric stretching), and asymmetric stretching of the inter-tetrahedral oxygen atoms in SiO_2, respectively. In Fig. I.7B, a new absorption band at ~963 cm^{-1} in Meso-MC is seen, suggesting formation of $Si–O–M^+$ (Ce or Mn) linkages and thus incorporation of MnO_X/CeO_2 into the silica framework of HMS. Such linkages are important for the formation of solid solutions of manganese and cerium oxides on HMS. The absence of carbonyl bands in the calcined Meso-MC suggests that all organic functionalities were decomposed during calcination.

BET Surface Area and Pore Size Analysis: The nitrogen adsorption isotherms of HMS and Meso-MC are shown in Fig. I.8A) and I.8B), respectively. The isotherms of both samples are type IV, according to the IUPAC classification[4], with a sharp step at intermediate relative pressures. The hysteresis loop for these materials starts at a relative pressure of $p/p_0 = 0.45$,

indicating the presence of mesoporosity. This hysteresis loop extends to a relative pressure of 0.80 - 1.0, implying that there is a textural inter-particle mesoporosity or macroporosity. The sharp inflection of the adsorption branch confirms the high quality of materials with uniform mesoporosity, and the appreciable type H1 hysteresis loops in both HMS and Meso-MC indicate the presence of textural and cylindrical mesopores. The BET surface area (S_{BET}) and average pore volume (V_p) of pure HMS and Meso-MC are listed in Table I.4. The average pore diameter of Meso-MC, calculated by the Barrett Joyner-Halenda (BJH) method, is 4.2 nm versus 5.4 nm for HMS. This reduction, as well as the reduction in BET surface area (S_{BET}) and pore volume (V_p) of Meso-MC relative to HMS, is due to incorporation of Ce/Mn oxides into the HMS pore structure. Some pore blockage is likely occurring, thus reducing access internal channels of HMS. Although there is a reduction in surface area and pore volume of Meso-MC, the surface area of Meso-MC is greater than that of unsupported MnO_x/CeO_2 prepared by co-precipitation method.

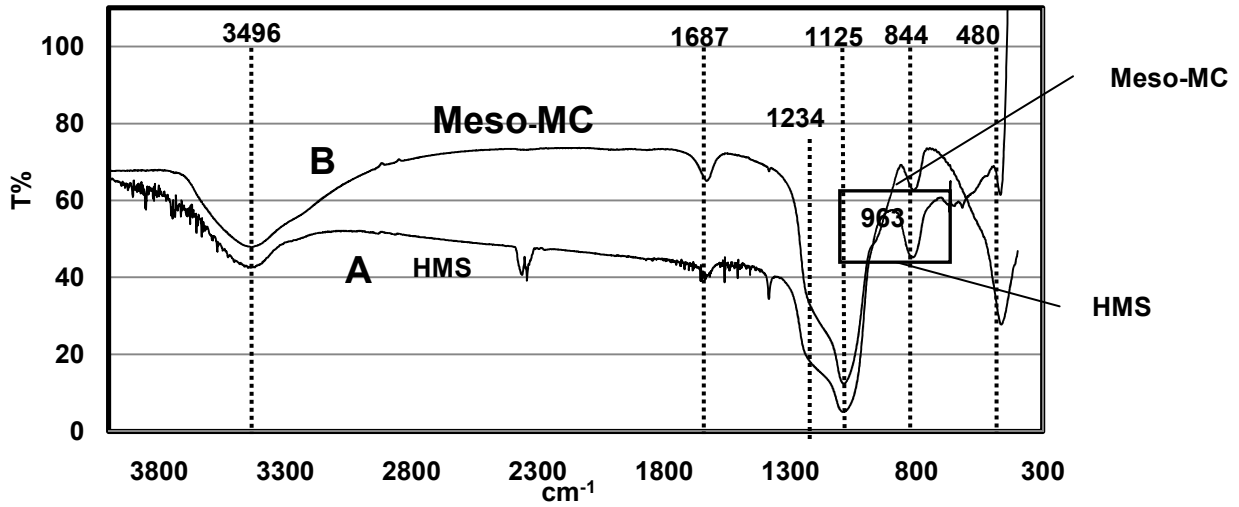

Fig. I.7. FTIR spectra of A) calcined HMS and B) Meso-MC catalyst.

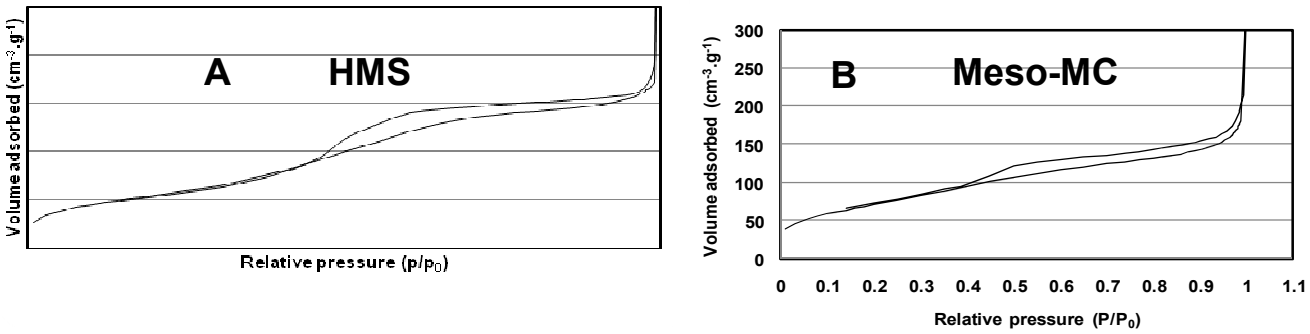

Fig. I.8. Nitrogen adsorption–desorption isotherms of A) HMS and B) Meso-MC

Table I.4. N_2 adsorption of MC-CM, HMS, and Meso-CM

Catalysts	BET surface area ($cm^3.g^{-1}$)	BJH Average Pore Diameter (nm)	Pore volume ($cm^3.g^{-1}$)

HMS	782	5.4	1.1
Meso-MC	**250**	**4.2**	**0.30**
MC-CM	106	10.3	0.29

Powder X-ray diffraction: The XRD patterns of HMS and Meso-MC are shown in Figures I.9A) and I.9B). In Fig. I.9A), HMS displays a strong, broad diffraction peak at $2\theta=1.8^{o}$, correspondng to the diffraction plane (100) of the typical hexagonal mesoporous silica wormhole structure assembled from long alkyl chain neutral amines as surfactants. This single, low-angle peak arises because of short-range hexagonal symmetry with uniform pore diameter[5]. Diffraction peaks of higher order are not observed, indicating that these materials do not possess significant long-range order. The absence of a long-range order can be attributed to the weak bonding forces (between the amine and silicates species) that govern the neutral (S^0I^0) pathway assembly. The Meso-MC shows a broad diffraction peak $2\theta=1.3^{o}$ in Fig. I.9A), indicating the deorganization of the mesoporous structure. Although the collapse of mesoporous channels could be one reason, we think that the incorporation of MnO_x/CeO_2 into the mesopores may cause such irregularity. This finding could be further evidenced by the facts that the diffraction peak shifted to lower angle, the intensity of (100) peak decreased, and the width of (100) peak became broader in the Meso-MC sample. The decrease of diffraction peak intensity of Meso-MC may be attributed to the decrease of the diffraction contrast between the pores and the walls as a result of mesopores partially filling with cerium and mangnese nanoparticles. This also suggests that the average size of the cerium and mangnese nanoparticles is close to the pore diameter of wormhole-like mesoporous structure.

The wide-angle XRD spectra of HMS in Fig. I.9B) shows only a broad peak of amorphous silica at $2\theta = 22^{o}$. The XRD peaks for Meso-MC are observed at $2\theta = 28.1^{o}$, 33.1^{o}, 47.5^{o} and 56.5^{o} corresponding to (111), (200), (220), and (311) planes, respectively. The diffraction peaks are characteristic of the cubic ceria phase with a fluorite structure. The concentration of MnO_X in Meso-MC is low and is thus not detected by XRD. The diffraction peaks of CeO_2 in the XRD spectrum of the Meso-MC indicate that large particles of CeO_2 are dispersed on the surface of HMS.

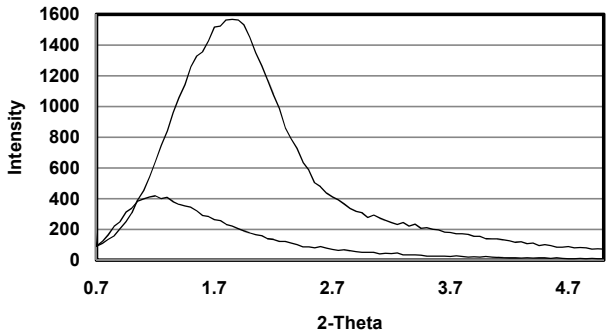

Fig. I.9. A) Low angle powdered XRD spectra of pure HMS and Meso-MC;
B) Wide angle powdered XRD spectra of pure HMS and Meso-MC (corrupted)

TEM: The high resolution TEM images of HMS and Meso-MC are displayed in Fig. I.10A and 1.10B. Pure HMS shows a wormhole-like mesoporous framework - although long-

range packing order is absent, a regular, uniform network of channels is observed[29]. The TEM image of Meso-MC (Fig. I.10B) confirms that MnO_X/CeO_2 particles are distributed over the surface of HMS and that some of the particles might be embedded into the HMS pores. The TEM images of the Meso-MC also suggest that average particle size of the MnO_X/CeO_2 are <10nm. It is clear from the low angle XRD, pore volume, and FTIR data that particles of MnO_X/CeO_2 are located in the pores of HMS and those larger particles are highly dispersed on the surface of HMS as confirmed by wide angle XRD and BET surface area results. The effects of MnO_X/CeO_2 loading on the structural integrity of HMS are still under study.

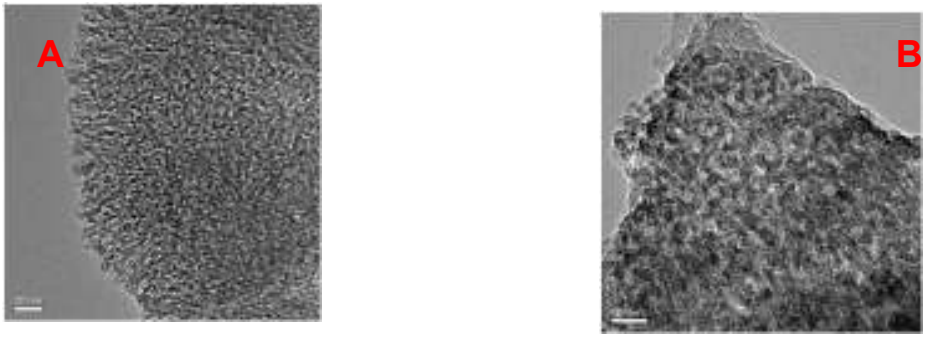

Fig. I.10. TEM images of A) HMS and B) Meso-MC

Catalytic Reactions: The catalytic activities of CM-MCM-41 and unsupported MnO_X(10%mol)/CeO_2 were tested for the ketonization of propionic and butyric acid at 410^0C at atmospheric pressure in a fixed bed reactor (Table I.5). The turnover number of CM-MCM-41 found to be greater than that of unsupported MnO_X(10%mol)/CeO_2. The material balance in all experiments closed to 100±5%. In both reactions, the selectivity to ketone formation is >98%, and no products other than water and carbon dioxide were observed.

The catalytic activity of CM-MCM-41 was further evaluated in the cross ketonization of propionic acid with butyric acid (Table I.6). In this reaction, three ketones are observed: 3-pentanone, 4-heptanone and 3-hexanone. Two symmetric ketones such as 3-pentanone and 4-heptanone produced via the homo-ketonization of propionic acid and butyric acid while an asymmetric ketone (3-hexanone) is produced by the cross-ketonization between propionic acid and butyric acid. As expected, an approximate binomial distribution is observed: the composition of the produced ketones is 1:2:1 for 3-pentanone, 3-hexanone, and 4-heptanone, respectively.

Table I.5. Activity tests of MnO_X (10%mol)/CeO_2 and CM-MCM-41

Catalysts	**Turnover number (TON)***	
	Ketonization of Propionic acid	Ketonization of Butyric acid
MnO_X (10%mol)/CeO_2	7	2
CM-MCM-41	18	5

*Reaction conditions: The catalyst charge: 1.5gm, N_2 flow: 15ml.min^{-1}, carboxylic acids flow: 0.1ml.ml^{-1}, Temperature: 410^0C, *TON= moles of acids reacted /moles of cerium and manganese in the catalyst/hr.*

Table I.6. Activity of CM-MCM-41 for cross ketonization of propionic acid and butyric acid.

Catalysts	**Conversion%**

	Propionic acid	Butyric acid
CM-MCM-41	66	56

Reaction conditions: The catalyst charge: 1.5gm, N_2 flow: 15ml.min^{-1}, Mole ratio of propionic acid: butyric acid: 1:1, mixed acids flow: 0.1ml.ml^{-1}, Temperature: 410^{0}C

Ketonization of butyl butyrate: The CM-MCM-41 was found to be active in ketonization of butyl butyrate and provides 4-heptanone and n-butanol together with small amount of n-butanal (Table I.7). In the n-butyl butyrate reaction over CM-MCM-41, only CO_2 was observed in the gaseous sample, indicating that the symmetric ketone (4-heptanone) is formed from the carboxylate part of the ester and n-butanol is formed from its alkoxy part (2RCOOR'→RCOR+2R'OH). It has been suggested that in an ester conversion to ketone, the most probable route is a carboxylate coupling which gives a β-ketoester that subsequently decomposes.

$$2RCH_2COOR' \rightarrow RCH_2(CO)CHRCOOR' + R'OH$$
$$RCH_2(CO)CHRCOOR' (+H_2O) \rightarrow RCH_2(CO)CH_2R + CO_2 + R'OH$$

If the ketoester decomposes without water, an olefin could be formed instead of alcohol. Thus, the absence of any type of olefins and presence of only CO_2 in an effluent gas n-butanol in a liquid phase effluent suggested that the formation of 4-heptanone from n-butyl butyrate over CM-MCM-41 proceeds via the β-ketoester route with the formation of n-butanol. Further work would be required to fully understand the mechanistic aspects of this reaction over CM-MCM-41.

Table I.7. Activity of CM-MCM-41 for ketonization of *n*-butyl butyrate.

Catalyst	**Conversion (mol %)**	**Yield (%)**		
	Butyl Butyrate	4-Heptanone	*n*-Butanol	*n*-Butanal
CM-MCM-41	40	24	16	0.4

Reaction conditions: Catalyst charge = 1.2 gm; N_2 flow = 15mlmin^{-1}; feed flow rate = 0.1mlmin^{-1}; T = 410^{0}C

I.1.5. Formation of allyl esters of biodiesel

Cloud point depressants for middle distillate fuels and biodiesel were prepared from copolymers of soy oil derivatives. These copolymers were prepared by transesterification of soy triglycerides with allyl alcohol (in a similar way biodiesel is prepared). The allylic double bond was then copolymerized by free radical initiation with vinyl monomers. Subsequent hydrogenation of the resulting copolymers is expected to produce biobased copolymers similar to currently used additives derived from copolymers of alpha olefins that are being used as cloud pour point depressant additives.

The underlying concept is based on current additives described in the literature to suppress or depress the onset of crystallization by disrupting the symmetry of the crystallizing species and thus preventing them from rearranging into an ordered structure. The most common

successful approach is based on additives derived from polymers containing alpha olefins as side chains [1] as shown in Figure I.11.

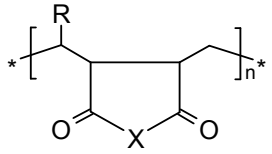

Figure I.11. Typical cloud point depressant additive

Similarly, large side chain acrylate copolymers, resembling fatty acids were shown to be effective cloud point depressant in biodiesel [2]. The large side chain species interact with the crystallizing species but due to the polymeric "tail" can't fit into a regular array and thus delaying crystallization.

To date, we have successfully prepared and characterized allyl soyate in high yields in a similar process used to prepare biodiesel (Figure I.12) and then copolymerize this soyate with styrene.

Two different synthetic methods were used: (1). Replacing allyl alcohol for methanol in a "conventional" biodiesel transesterification process, or (2). Starting with biodiesel and replacing methyl ester with allyl ester. Both these methods were evaluated and issues related to miscibility of allyl alcohol with glycerol (or methanol) were resolved. The allyl soyate was characterized by GC, FTIR, NMR, and iodine number and then copolymerized at different concentrations with styrene using conventional free radical initiation. The copolymers were then characterized by GPC, FTIR, DSC, TGA and NMR. Future work will focus on hydrogenation of the double bonds and then evaluating these coolymers as cloud point depressants in biodiesel.

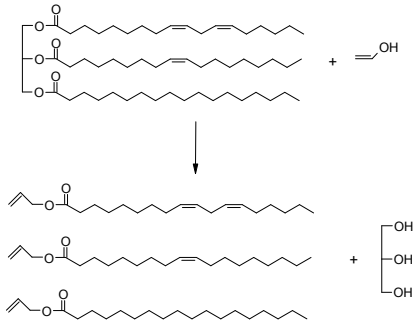

Figure I.12: Preparation of Allyl Soyate

Preparation and Characterization of Allyl Soyate – Styrene Copolymers: Since the terminal double bonds are much more active than internal double bonds, allyl soyate was copolymerized with styrene using conventional free radical initiation. Typical procedure was to add styrene and allyl soyate at a known ratio into a vial. The vial was flushed with nitrogen and placed in an bat at 120°C and the free radical polymerization was initiated with 1,1,4,4-Tetramethyltetramethylene Bis(Tert-Butyl) Peroxide. Various copolymers were prepared as shown in Table I.8.

Table I.8: Allyl Soyate – Styrene Copolymers

1. M.G. Botros, US Patent 6,143,043 (2000).
2. S. Clarke, Australian Provisional Patent 2008902610 (2008) and International PCT world patent WO/2009/143566 (2009).

Sample #	Styrene (mole %)	Styrene (moles)	Styrene (g)	Allyl Soyate (mole %)	Allyl Soyate (moles)	Allyl Soyate (g)
1	94%	0.0484	5.041	6%	0.0031	1.001
2	86%	0.0384	4.000	14%	0.0063	2.008
3	76%	0.0295	3.074	24%	0.0094	3.005
4	61%	0.0193	2.014	39%	0.0125	4.001
5	39%	0.0099	1.034	61%	0.0156	5.008

After the 5 hours polymerization time the samples were removed from the oil bath and allowed to cool. Each sample was then dissolved in 20mL toluene then precipitated by in methanol. The copolymer precipitates were then filtered using a Buchner funnel and placed in an oven overnight to dry.

Copolymers Characterization: The structure of the copolymers was verified by NMR (Figure I.13), which clearly shows the aromatic protons from styrene and the methylene protons from the fatty acids. The peak related to the terminal allyl soyate is significantly smaller (although not completely disappeared), indicating the formation of the desired copolymers.

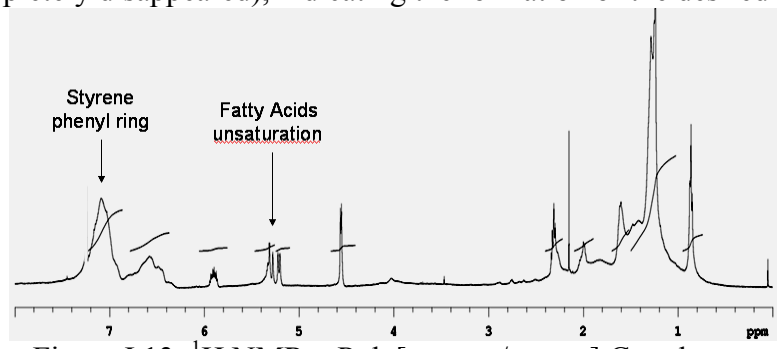

Figure I.13. ^{1}H NMR – Poly[styrene/soyate] Copolymer

I.2. Ozonolysis to Biofuel Components

I.2.1 Background

We introduce different alcohols (e.g. methanol, ethanol, n-propanol, and n-butanol) to the ozonolysis process to increase the energy density of the biofuels. These ester derivatives were prepared whereby air/ozone gas is mixed with the oil in a static mixer. The double bonds in the fatty acids are cleaved by the ozone and the new chain-ends react with the alcohol to form the desired esters. For example (Figure I.14) when ethanol is used as a reactant, oleic acid will be cleaved at the double bond to yield methyl ethyl nanoate diester and ethyl nanoate ester.

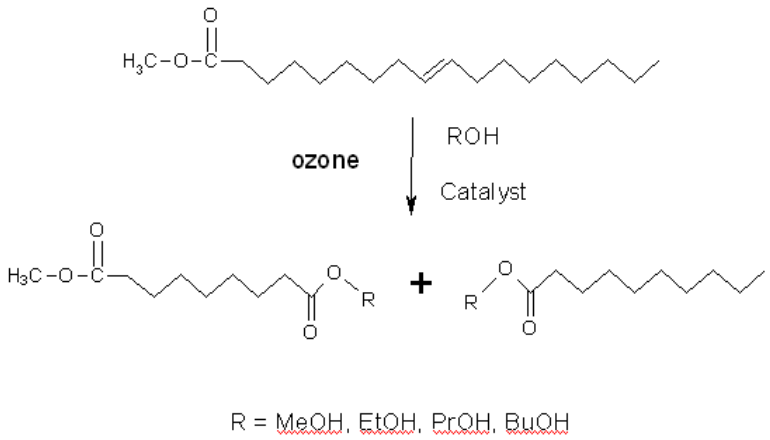

Figure I.14: Catalytic ozonation of methyl oleate with alcohols

The actual composition of the biofuel will depend on the type of oil used as given in Table I.9.

Table I.9: Composition of methyl esters starting materials

fatty acid	formula	mw	#C=C / mol FA	Canola Oil wt% in oil	Soy Oil wt% in oil	LowSat Soy Oil wt% in oil
linolenic acid	C18H30O2	292	3	9.6	6.6	8.1
linoleic acid	C18H32O2	294	2	20.1	54.3	60.6
oleic acid	C18H34O2	297	1	60.1	24.9	24.7
stearic acid	C18H36O2	299	0	1.5	4.7	2.7
palmitic acid	C16H32O2	270	0	3.5	9.5	3.9
misc			0.5	5.2	0	0
average FA mw (g/mol) =		279		292	293	
average FA C=C (mol/mol)=		1.32		1.53	1.70	

All these esters and di-esters are known and their boiling points are known. The new product distribution after the ozonation reaction is plotted in Figure I.15 and it can be clearly seen that the average molecular weight distribution is about half the original average molecular weight of the methyl soyate.

I.2.2 Materials and methods

Sodium hydroxide pellets, methanol, ethanol, propanol and butanol, all normal alcohols and ACS grade, were purchased from Sigma Aldrich. Building air was dried using Drierite, filtered with 0.6 um paper and used for the oxygen feed to the ozone generator. Fatty acid methyl

esters (FAMEs) from canola and soy oils were prepared by transesterification of the oils with methanol in an acidic medium.

A continuous stainless steel reactor (6.35 mm i.d. and 1 m long) was used for the catalytic ozonation (Figure I.16). The liquid and gas feeds were introduced from the bottom of the reactor and thoroughly mixed through in 5 cm static mixer. Stainless steel t-shaped connections were used to insert thermocouples at the bottom, middle and top of the reactor and a pressure gauge was inserted into the middle connection. Liquid feed was pumped using a Waters 501 HPLC pump and entered the bottom of the reactor column through a right angle pipe fitting. The ozone was produced by passing dry air through a Praxair-Trailgaz Ozone generator. The air/ozone atmosphere was then entered the column immediately below the liquid feed through the same t-shaped connection. The gas was vented through an aqueous potassium iodide solution to ensure destruction of excess (unreacted) ozone before venting it back to the atmosphere and the oil product was collected into a graduated separatory flask.

The feed to the reactor consisted of a mixture of oil FAMEs, 200 mol% of alcohol and 0.01% NaOH in the total feed. Sodium hydroxide in the feed acted as an alkaline catalyst for the reaction between alcohol and the ozonized fatty acid double bond. The feed was premixed with the FAMEs and alcohols. Flow rates for each oil-FAME-alcohol combination were determined by titration of the exiting gas with wetted potassium iodide filter paper for the presence of excess ozone to ensure complete removal of all double bonds.

Ozone was produced by passing dried, filtered building air through an electrical discharge tube at 675 watts. It was then fed into the reactor at 14 psi and 0.2 scfm flow rate. The concentration of ozone within the gas feed line varied between 2.5 to 3.6 wt% due to uncontrollable air supply conditions. This variation was countered by altering the liquid flow rate based upon the ozone titration method described above.

The reactor base and column were cooled using an ice bath and pumping the water through a cooling jacket surrounding most of the reactor column.

The biofuel products were characterized for their carbon double bond content and esters composition using both ASTM testing methods and FTIR analysis. Also, the reactor product was sampled throughout each run to determine the reactor stability using FTIR. Remaining carbon double bonds, measured in mg KOH/gm sample, were determined using the iodine value test, ASTM D 1959-97. FTIR chromatograms were collected using Perkin Elmer Spectrum One FT-IR Spectrometer and Spectrum 5.01 software. The FTIR chromatograms were evaluated for any existing carbon double bonds around 3000 cm-1 and ester composition around 1700 cm-1 wavenumbers. Prior to iodine value testing, all samples were stripped of any remaining alcohol via vacuum distillation using a 12 inch distillation column.

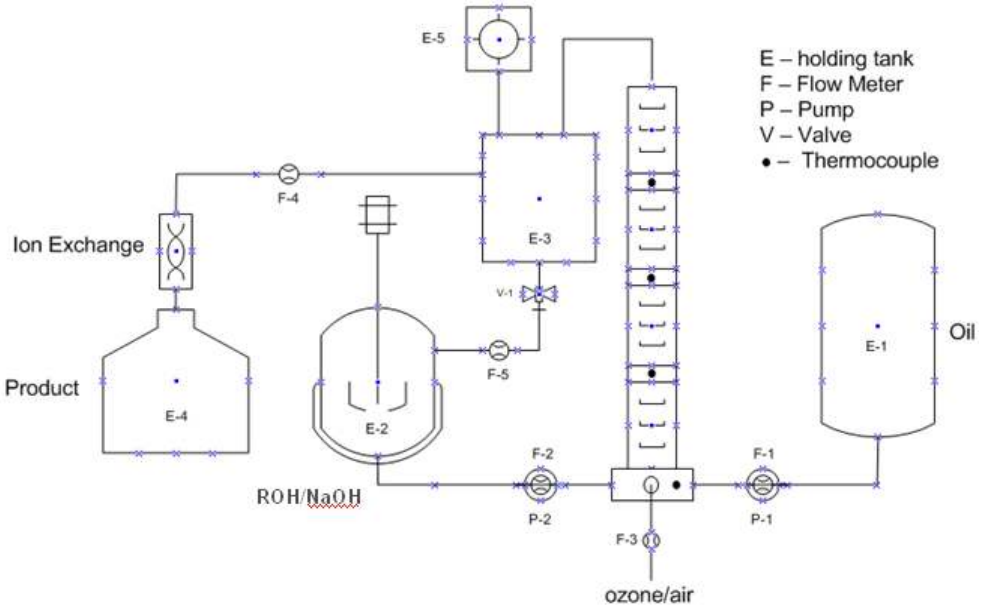

Figure I.16. Catalytic Ozonation Reactor

1.2.3 Results and discussion

Figure 1.17 is an example of the expected product distribution of esters and diesters from methyl soyate (conventional biodiesel) after its catalytic ozonation with methanol. It is apparent that the saturated fatty esters will not react (or will react to a very small extent) due to the much lower reaction rates of ozone with saturated C-C bonds or C-H bonds compared to its reaction with olefins.

It was found that the cleavage of double bonds and the subsequent formation of the desired methyl esters is highly dependent on the experimental conditions. The extent of cleavage increases through a maximum as shown in Fig I.18. Based on these results, the process was optimized.

Ester	MW	Wt%
methyl palmitate	270	11
methyl stearate	292	7
methyl linoleate	294	51
methyl oleate	296	23
methyl linilenoate	298	4

O_3 / MeOH

catalyst

Ester	MW	Wt%
methyl propanoate	88	3.0
methyl stearate	298	1.7
methyl nonanoate	172	9.8
methyl palmitate	270	4.7
methyl hexanoate	130	21.6
dimethyl propanoate	132	24.6
dimethyl nonanoate	206	34.5

Figure I.17. Expected composition of methyl soyate after catalytic ozonation with methanol

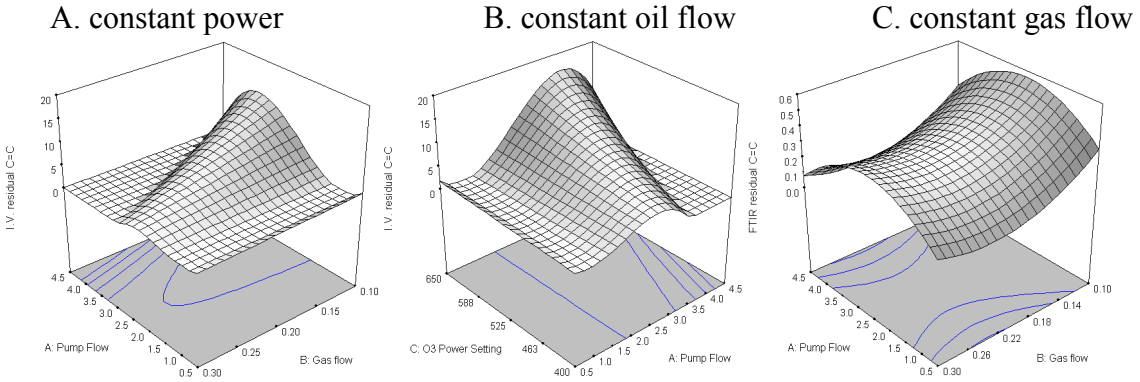

Figure I.18. Dependence of the cleavage of the double bonds on the reaction conditions

The esters and diesters product mixtures additional benefits compared with conventional biodiesel:

- The ozone treated biofuels do not contain unsaturation and are therefore expected to exhibit improved thermal and oxidation stability compared with biodiesel.
- The higher oxygen content is expected to lead to higher combustion temperature and therefore better and cleaner fuel.
- The overall molecular weight and viscosity of these biofuel are lower than biodiesel, thus increasing the volatility and allowing better mixing with the air in the combustion chamber.

An example showing the increase in the volatility of a biofuel prepared by catalytic ozonation of methyl soyate with methanol is shown in Figure I.19.

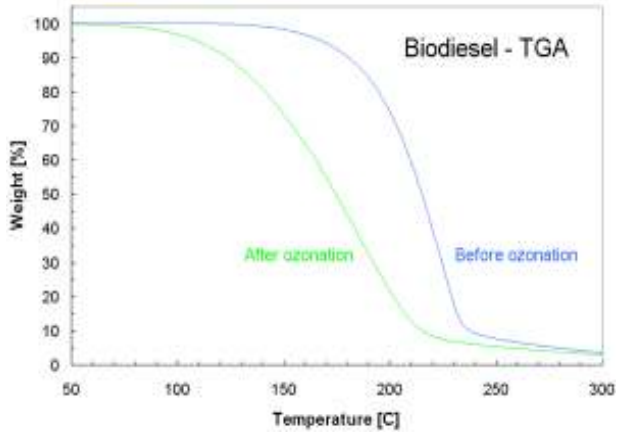

Figure I.19. TGA of Biofuel prepared by catalytic ozonation of methyl soyate with methanol

Typical FTIR spectra of methyl soyate and methyl canolate are shown in Figure I.20. The double bonds of the unsaturated methyl esters are readily visible around 3008 cm^{-1}. There are no apparent free hydroxyl groups (carboxylic acid, water, etc.) as evidence by the flat region around 3100-4000 cm^{-1}. The ester region appears as a sharp peak around 1600-1900 cm^{-1}.

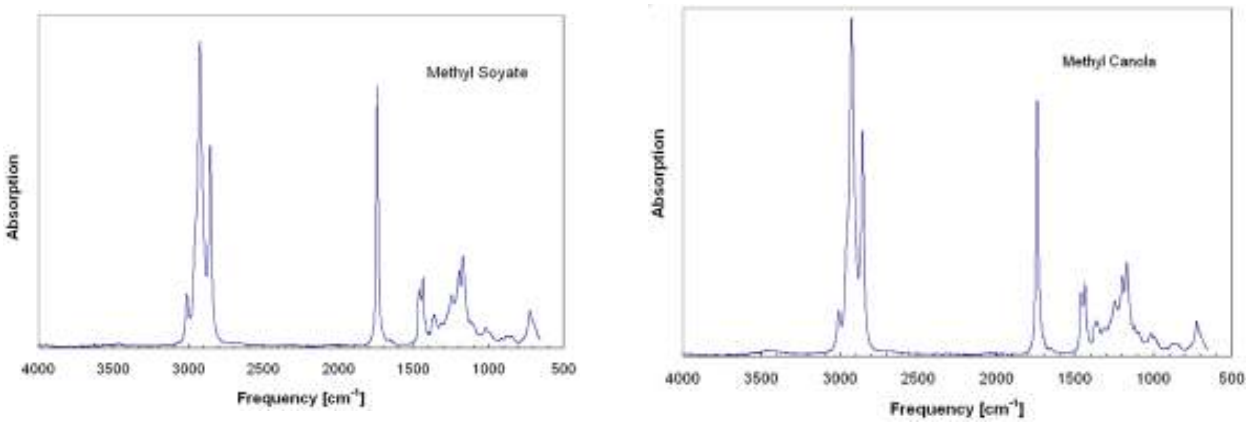

Figure I.20. Typical FTIR spectrum of methyl soyate (left) and methyl canolate (right)

Unfortunately, the OH region (3100-3500 cm-1) should have been characterized to determine possible side reactions (e.g. formation of carboxylic acid) or the presence of water. However, since excess alcohols were not removed from the products, this region shows the presence of alcohol, which inhibits further analysis of this region.

The disappearance of the double bonds as a result of the ozone attack on these sites is clearly evident in Figure I.21 (soy oil) and I.22 (canola oil). It is apparent that the catalytic ozonation of soy oil with methanol (upper right spectrum) did not proceed to completion and some double bonds are still present. This incomplete reaction can easily be corrected in the future by adjusting the oil flow rate slower such that the residence time in the reactor will be longer, allowing more complete reaction to take place. Although it is possible in theory to compensate and increase the air flow (instead of increasing the oil flow), it will not work in the set-up we currently use due to the limited ozone production from our relatively small ozone generator.

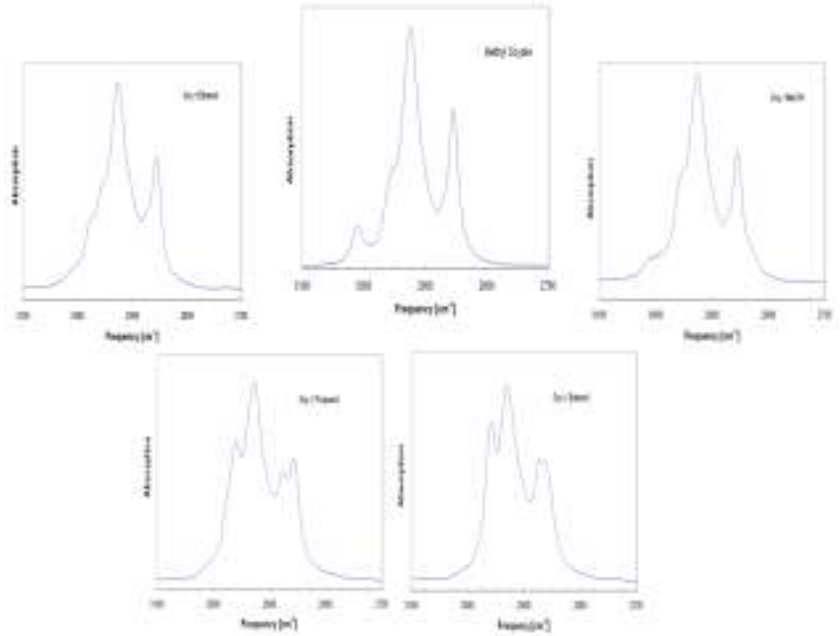

Figure I.21. Double bonds region of FTIR spectra of biofuels from soy oil

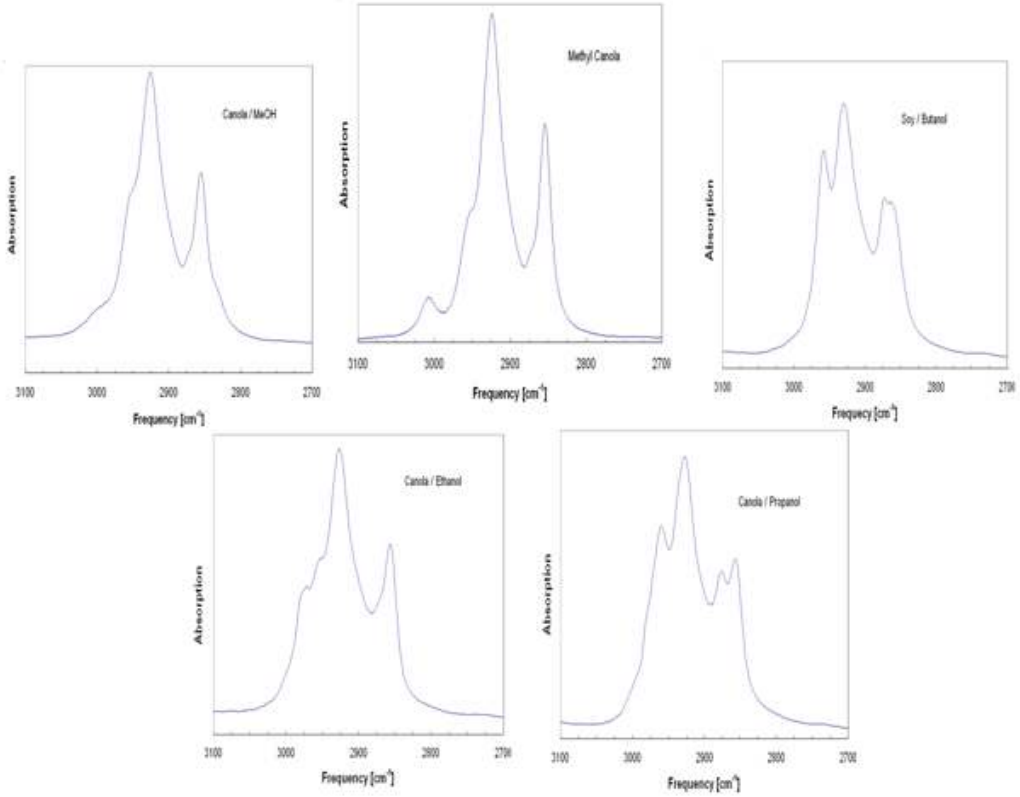

Figure I.22. Double bonds region of FTIR spectra of biofuels from canola oil

The ester formation of the products was investigated by expanding the ester region of the FTIR spectra (Figure I.23). Due to the new ester and di-ester groups the original ester peak is altered such that it appears as a shoulder on the original ester peak.

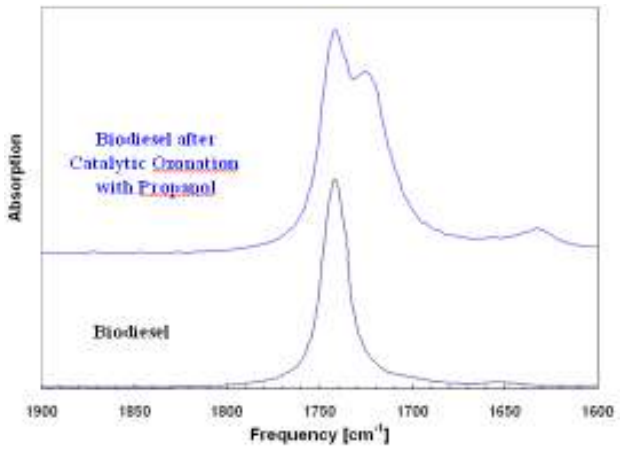

Figure I.23. The ester region in the FTIR spectra

We used a simple deconvolution method to approximate the contribution of the new peak after ozonolysis as for soy oils with methanol (Figure I.24), ethanol (Figure I.25), n-propanol (Figure I.26) and n-butanol (Figure I.27).

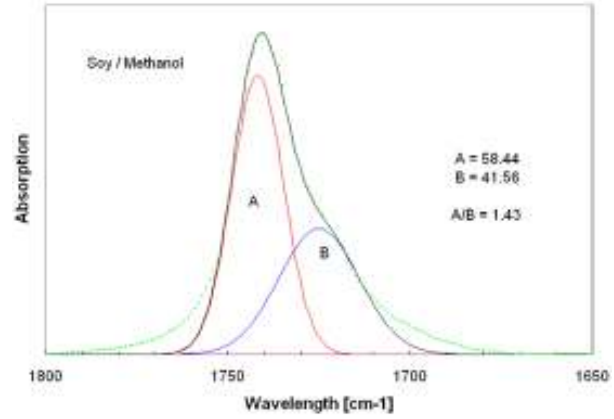

Figure I.24. Deconvolution of the ester peak of methanol + methyl soyate

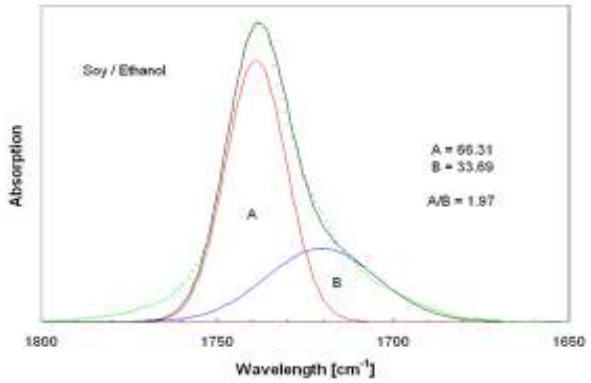

Figure I.25. Deconvolution of the ester peak of ethanol + methyl soyate

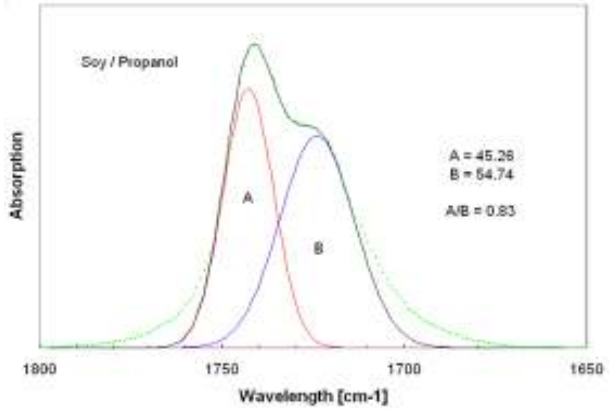

Figure I.26. Deconvolution of the ester peak of n-propanol + methyl soyate

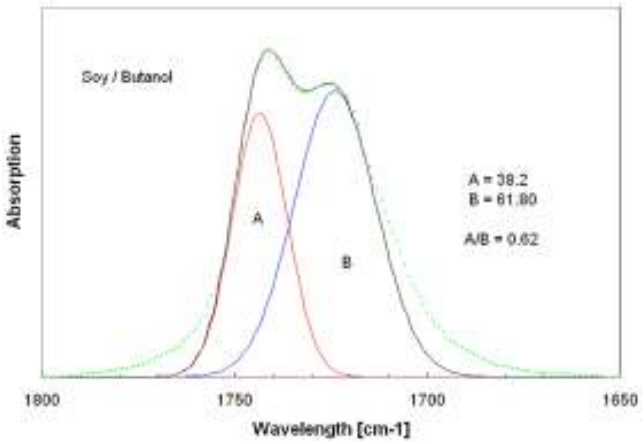

Figure I.27. Deconvolution of the ester peak of n-butanol + methyl soyate

Similarly, deconvoltion of canola base oils with methanol (Figure I.28), ethanol (Figure I.29), n-propanol (Figure I.30) and n-butanol (Figure I.31) are shown below:

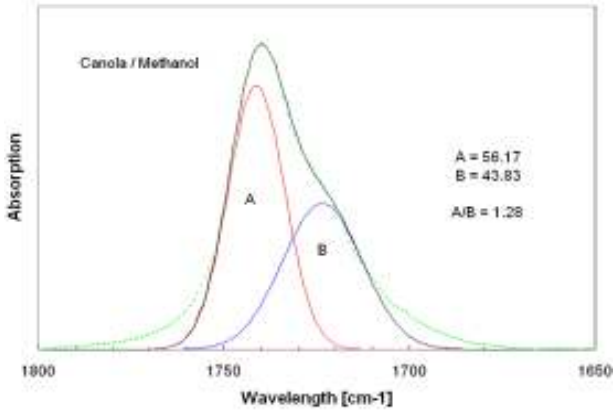

Figure I.28. Deconvolution of the ester peak of methanol + methyl canola

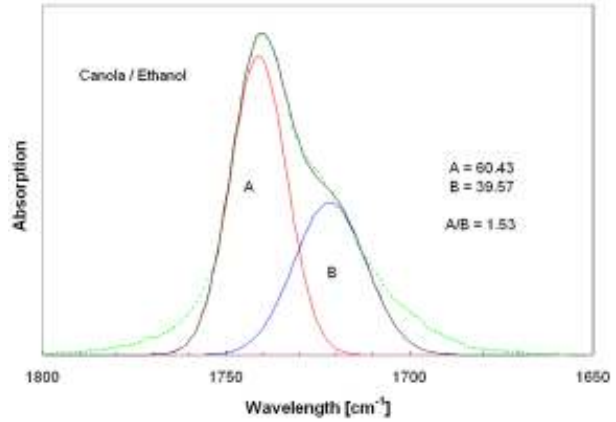

Figure I.29. Deconvolution of the ester peak of ethanol + methyl canola

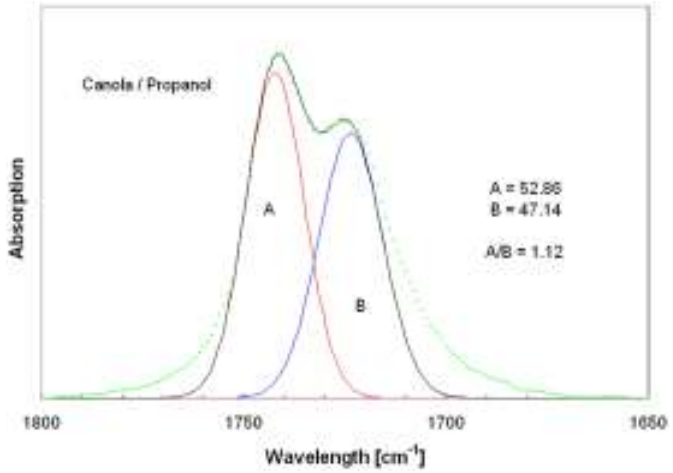

Figure I.30. Deconvolution of the ester peak of n-propanol + methyl canola

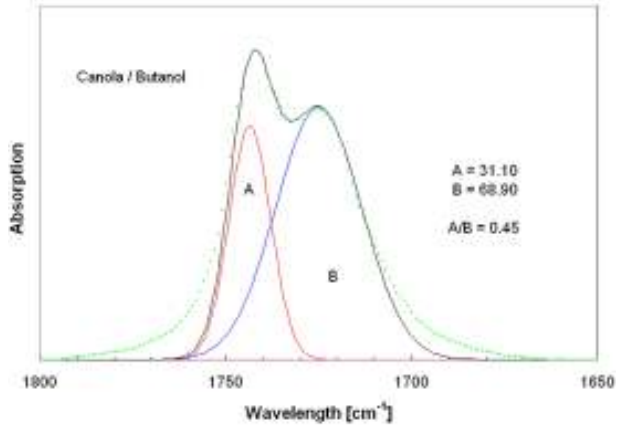

Figure I.31. Deconvolution of the ester peak of n-butanol + methyl canola

The ratio of the original ester peak of these oils to the "new" ester peak is plotted in Figure I.32. It is apparent the this ratio is independent of the type of oil and is inversely proportional to the size of the alcohol reactant.

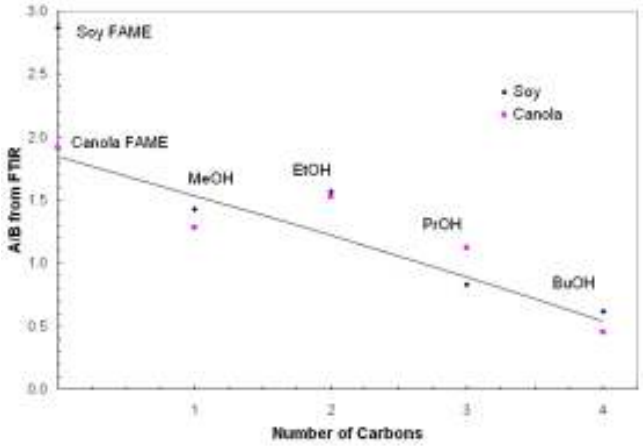

Figure I.32. The ratio of the areas of the original ester (A) to the new ester (B) as a function of the alcohols used.

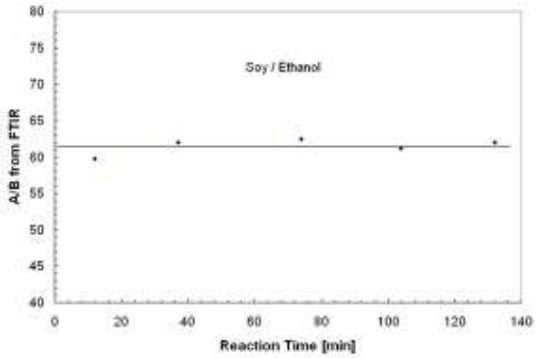

Figure I.33. Reactor stability during reaction of methyl soyate with methanol

It was important to determine the consistency and stability of the reactor throughout the run. This was done by taking samples periodically and examining the ester region (the product) as a function of time. Figure I.33 is a combined plot of the normalized ester region in the FTIR spectrum (left) and a deconvolution of the same region (right).

Similar data were obtained with the other alcohols as well as the reaction of methyl canolate with these alcohols. En example of the reactor stability with methyl canolate is shown in Figure I.34.

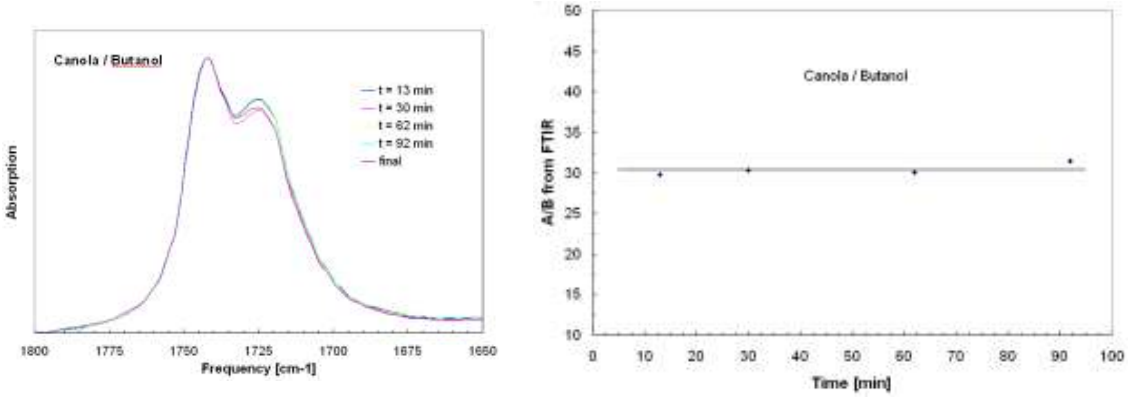

Figure I.34. Reactor stability of the run of methyl canolate and n-butanol

It appears that there is some variation during the run of the butanol methyl canolate (left panel of Figure I.34), however, these are minor deviation well within the experimental error.

It should further be pointed out here that the catalytic ozonation does not impact the saturated fatty acids. Thus, a DSC (Figure I.35) clearly indicates that the melting point associated with the unsaturated fatty acids (-65°C) disappeared but the higher melting point associated with the saturated fatty acids (around -10°C) remained and actually shifted to higher temperature (around 8°C).

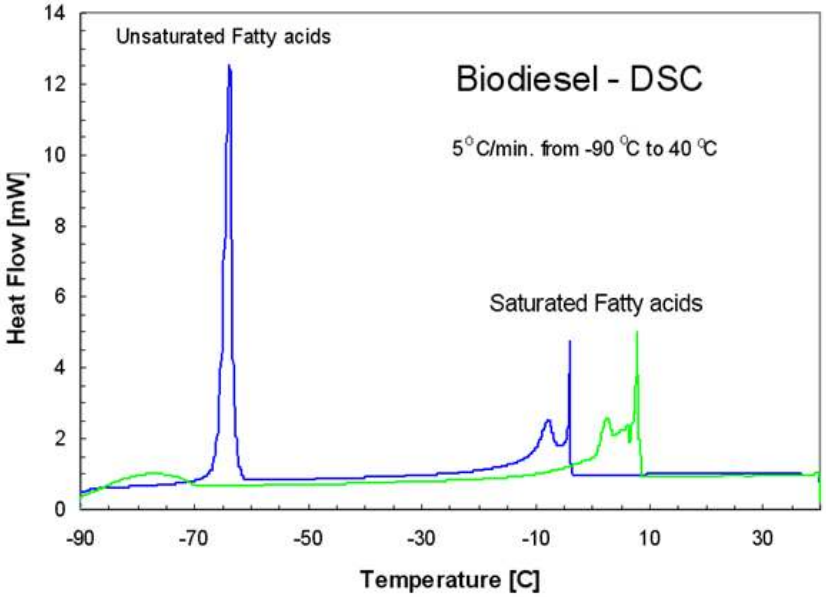

Figure I.35. DSC of methyl soyate before and after catalytic ozonation with methanol

1.2.4 Direct ozonolysis of triglycerides to advance biofuel compositions

Transesterification chemistry (reaction of triglyceride with methanol) is the standard approach to reducing the viscosity of the vegetable oils and makes them suitable for use as biofuel. However, the process results in a by-product glycerol that needs to be separated, and the resultant biodiesel (fatty acid methyl esters) still contains unsaturation with its attendant thermo-oxidative stability issues.

We have used out catalyzed ozonation process in the presence of methanol to produce low molecular weight (low viscosity) compositions suitable for use as transportation fuel. Our process does not produce waste glycerol, and the product mixture does not contain any unsaturation, thus, eliminating problems associated with thermal-oxidation stability of the biofuel. The general scheme is shown in Figure I.36 below.

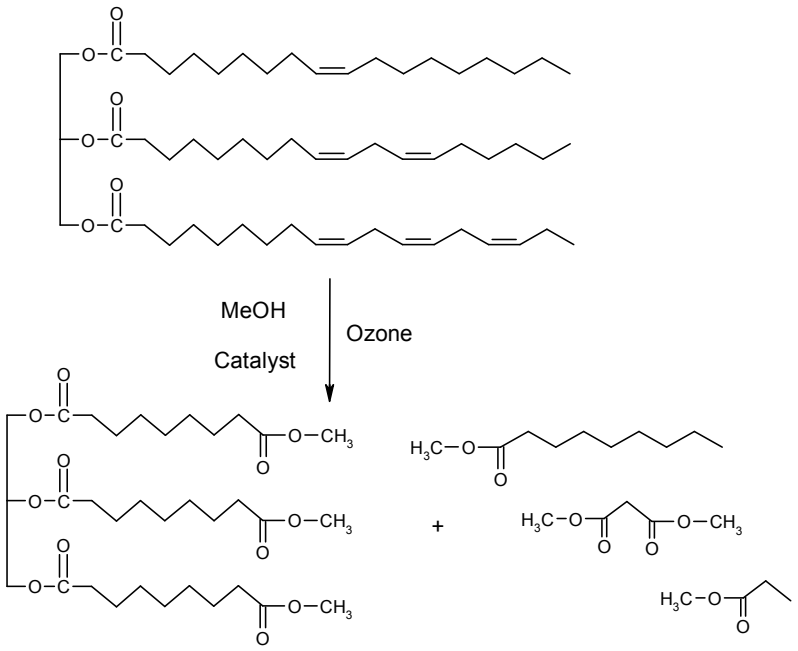

Figure I.36. Catalyzed ozonation of triglycerides in the presence of methanol

Using typical soy oil, about half the calculated composition mass is composed of low MW fragments and the other half is the residual shorter MW triglycerides (Figure I.37). Since the double bonds in all the unsaturated fatty acid occurs at the 9th carbon position, the primary component of this shorter triglyceride fraction is trinonanoate (NNN). The average calculated M_n is reduced from about 890 for soy oil to 350 for the product mixture. Our experiments indicate that the viscosity of soy oil is greatly reduced due to the lower molecular weight of the ozonized product mixture. Furthermore, we have found that the viscosity is decreased only if excess methanol (or ethanol) is present in the reaction mixture. Otherwise, the new chain-ends obtained by the cleavage of the double bonds as a result of the ozone attack recombine to form larger structures and higher molecular weights. Several varieties of soy oils were evaluated and, as expected, LowSat® oil appears most appropriate as it contains less than 1 wt% triglycerides composed of only saturated fatty acids.

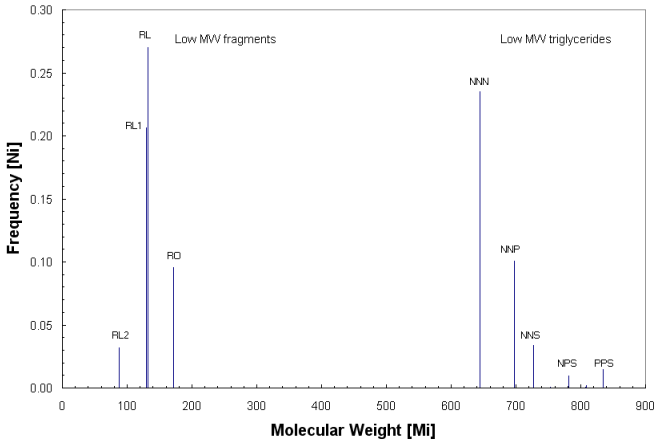

Figure I.37. Calculated MWD of catalyzed soy oil in methanol

1.2.5 Pilot-scale ozonation reactor

A schematic diagram of the reactor is shown in Figure I.38. Prime concerns were focused on the safety of the process. The core of the reactor is a small diameter (0.5") static mixer which is embedded in a larger (2") tube filled with cooling water. The oil/alcohol and ozone/gas lines are fed from the top of the assembly through the water to the bottom of the static mixer such that the temperature of the reactants is maintained at the same

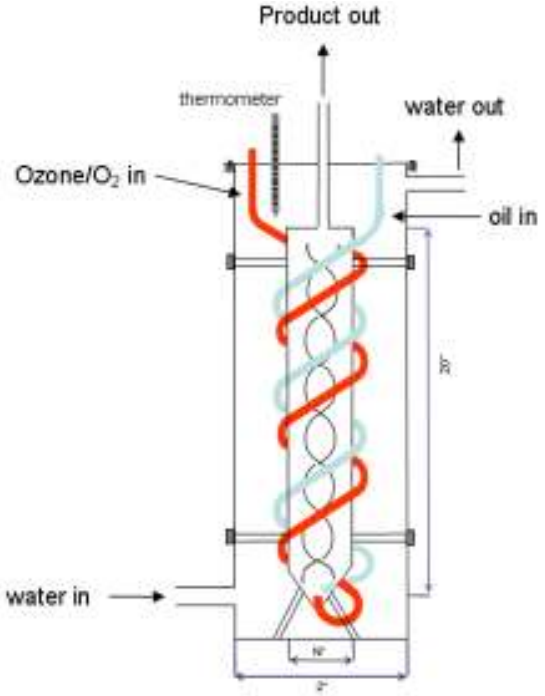

Figure I.38. Schematic of ozonation process

temperature of the reactor. The catalyst is dissolved in the alcohol prior to mixing it with the oil simplifying the construction and eliminating additional separate feeding line for this reactant. Furthermore, since a relatively large amount of cooling water is used, it was calculated that this volume will be sufficient to cool the exothermic ozonation reaction and maintain a constant temperature. As reported previously, the temperature of the reaction is critically important; the stability of the ozone in inversely proportional to the temperature, while the rate of the reaction is directly proportional to the temperature. Thus, the overall yield of the reaction has a complex dependency on the temperature, which must be controlled carefully.

Special attention was directed to the safe operation of the reactor. The design provides the weakest point to be at the top of the assembly such that if any problem will occur, any explosion will be directed upward away from the operator. Additionally, the reactor and all the peripheral equipment are placed behind a protective wall inside a hood away from other personnel in the lab. Fire extinguisher is nearby and only trained personnel are allowed to operate the reactor. Relatively large two ozone generators are used, each is capable of producing 0.25 Kg ozone per hour. In the current assembly, the ozone generators are fed separately with low pressure dry oxygen to provide ~8% ozone in the feed atmosphere. This ozone/oxygen

atmosphere is fed into the reactor in special lines that do not contain any ozone sensitive materials. The product is fed into a gas/liquid separator where oxygen is removed (the reaction parameters are set to ensure all ozone is being consumed in the reaction) and any unreacted alcohol is recycled back into the reactor. The input/output parameters are shown graphically in Figure I.39.

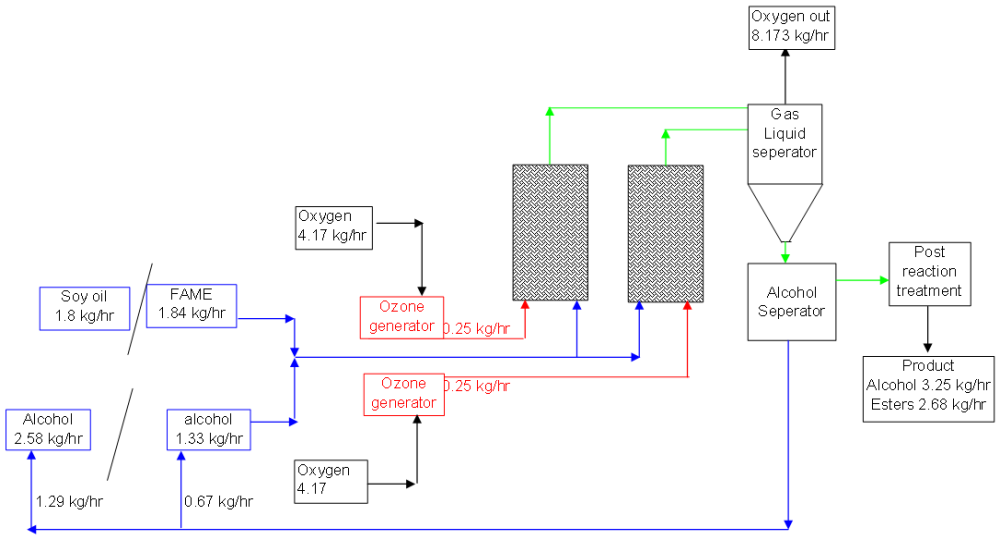

Figure I.39. General process parameters of the continuous ozonation reaction

Initial testing and optimization of the process went well. Figure I.40 is a typical example of the biofuel before (lower curve) and after (upper curve) ozonation. This FTIR clearly shows that the double bonds peak at 3008 cm^{-1} has almost disappeared. By calculating the area under this peak it is apparent that 96% of the double bonds were removed and replaced with a terminal ester functional group.

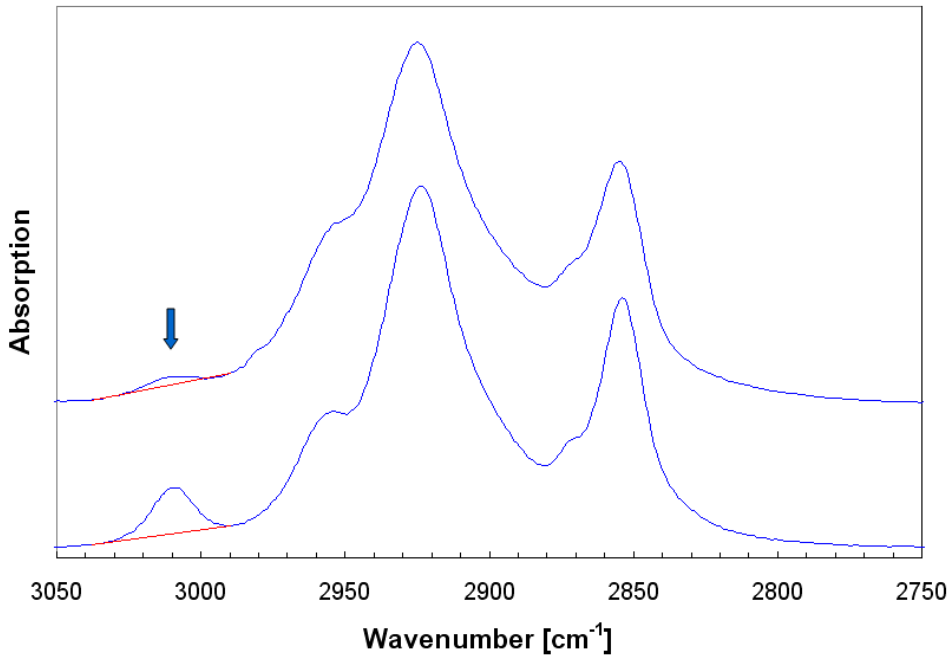

Figure I.40. Typical FTIR indicating cleavage of the double bonds

I.3 Biological Routes to Biofuel Components

The overall goal of this aspect of the project is to find improved ways and methods of using micro-organisms to ferment five and six carbon sugar containing feedstocks to biofuels. Crucial to economic feasibility are the energy and material requirements needed to separate the products from the fermentation broth. Therefore, the focus of the investigation up to the present has been on both, the fermentation process itself as well as separation techniques. The investigated microorganisms at this point include:

- *Clostridium Acetobutylicum* ATCC 55025, a mutant derived from the parent strain of *Clostridium Acetobutylicum* ATCC 4259, capable of an enhanced Acetone, Ethanol and Butanol (ABE) fermentation.
- *Chlostridium Tyrobutyricum* ATCC 25755, an anaerobic bacterium that can produce butyric acid as one of the products.

I.3.1. Production of acetone, butanol, and ethanol (ABE)

Fermentations were carried out in batch, fed batch and fed batch mode with product removal. In the case of ATCC 55025, the most successful experiments resulted in [g/l total solvent] 18.3, in batch mode and 26.5 in fed batch mode. These values represent about 90% of the values reported in the literature for the same organisms, indicating that the process is nearly optimized. The process of gas stripping was tested and found feasible for product removal. The stripping rate as a function of temperature and solvent concentration was determined for a mixture of ABE and acetate and butyrate. Solvent recovery from the stripped gas using resins, activated charcoal and silicalites is currently being investigated. So far, activated charcoal proved to be the most versatile and inexpensive adsorbent for both adsorption and desorption.

Research done by Lagier and Yang suggest suggests that immobilization of *Clostridium Acetobutylicum* is feasible and capable of increasing the productivity greatly. Immobilization of *ATCC 55025* was achieved successfully in a novel spiral tube reactor (STR). We were capable of boosting the overall productivity to 7 g/l/h while maintaining a relatively high species titer of about 6 g/l at a retention time of 51 min. The reactor was continuously operated over the course of 13 days. The first section of the reactor is characterized by acid productivities greater than 20 g/l/h. Total product formation, on the other hand, peaked at the beginning as well as at two-thirds of the reactor length at 10 g/l/h. These are remarkably high production rates.

A preliminary set of experiments concerned the use of the yeast *Pichia pastoris* for the conversion of butanol to butyraldehyde and ethanol to acetaldehyde. These results were promising to produce these aldehydes for numerous biofuel intermediates.

Table I.10. Fermentation yields of butyraldehyde

Date	Batch	Temp °C	EtOH added (g)	Acet-aldehyde produced (g)	BuOH added (g)	Butyr-aldehyde produced (g)	conversion %	Notes
3/25/2009	7	37	3.945	1.792	---------	---------	45.4	whole cells
3/27/2009	7	30	---------	---------	4.049	2.049	50.6	whole cells
3/27/2009	7	37	---------	---------	4.049	1.611	39.7	whole cells
4/3/2009	8	37	---------	---------	4.049	1.779	43.9	whole cells with condenser -2C
4/6/2009	8	37	---------	---------	4.049	2.566	63.3	whole and lysed cells with condenser -2C

I.3.2. Production of butyric acid

Butyrate fermentation: While investigating *Clostridium Tyrobutyricum (ATCC 25755)*, a contamination in the reactor lead to the discovery of a yet unidentified bacterial strain(s) capable of converting lactic acid to butyrate. A literature review did not yield any findings on this biological conversion. Initial investigations resulted in the following findings:

- Microscopic observation indicates the presence of a co-culture\
- The culture is facultatively anaerobic → initial sparging leads to rapid build-up of biomass
- Conversion of lactic acid to butyrate is most effective when the reactor operated in fed-batch mode with sugar concentrations in broth close to zero
- Highest achieved butyrate concentration was 37 g/l
- Lactic acid production does not cease when final butyrate concentration is reached

This finding may lead to ways to a pathway for butyrate production not previously known, and thus a previously undiscovered route for biofuels production.

Organic acid fermentation with Clostridium Acetobutylicum ATCC 824: Typically, the strain ATCC 824 is used to produce solvents in an ABE (**a**cetone, **b**utanol, **e**thanol) fermentation. Here, the pH is allowed to drop to in order to achieve a conversion of organic acids to the corresponding solvents. However, when keeping the pH close to neutral by neutralizing the organic acids (mostly butyrate, acetate and traces of lactate) one can prevent the culture from shifting to the solventogenic phase. These neutralized acids are less toxic to the organism. Thus, higher final titers are possible to achieve. The following Table I.11 gives an overview of the collected data.

Table I.11. Products from *Clostridium Acetobutylicum* ATCC 824 .

		butyrate	acetate	lactate	total acid	BuOH
run	**substrate**	**[g/l]**				
1	sucrose	9.2	4.8	0.3	14.3	0.1
2	sucrose	9.8	5.9	1	16.7	0.5
3	dextrose	21.8	6.1	5.1	33	1.4
4	maltodextrin	24.2	9.7	0.7	34.6	3.1
5	maltodextrin	26.1	11	0.5	37.6	1.7
6	maltodextrin	21.5	6.4	3.6	31.5	1.5
7	maltodextrin	20.6	6.8	2	29.4	1.5

The results imply that final acid-titers are approximately 10-15 g/l higher than for typical ABE fermentations. Additionally, small amounts of solvents are produced as well. Overall fermentation times ranged between four and seven days with the majority of the acids produced in the first three days.

A summary of results using *Chlostridia Acetobutylicum* is given in Table I.12 below. Specifically, we have achieved butyrate titers as high as 40 g/liter, as good as the best butanol fermentation and yet without optimization. Further, a new recovery scheme for alcohol recovery from continuous acetone-butanol-ethanol (ABE) fermentation wherein we use hot gas stripping to recover the alcohols from the fermentate is used. Concentrations exceeding 70 g/liter have been achieved in the condensate from this process, a marked improvement over the titers achievable in direct fermentation.

Table I.12. Results of fermentation studies to produce C4 biofuel intermediates

Strain	**Lab-name**	**ATCC/ DSM**	**main products**	**Cmax fed-batch [g/l]**	**Pfed-batch [g/l/h]**	**Cmax continuous [g/l]**	**Pconti [g/l/h] (average over reactor length)**	**Comments**
C. Acetobutyricum	824	824	ABE	15.6	0.3	unsuccessful		22/6 g/l butyrate/acetate when ph=6
mutant of C. Acetobutyricum	E604	55025	ABE	26.5	0.4	6	7	continuous operation for 14 days
C. Saccharobutylicum	262	13864DSM	ABE	7.3	<0.1	3.3	3.4	3 days of operation, then clogging
C. Beijerinckii	-	35702	ABE	6.1	0.1	unsuccessful		degenerated
C. Tyrobutyricum	Tyro	2637DSM	Butyrate, Acetate	16	0.2	4.8	1.5	no pH control with cont. culture
C.	Moorell	49707	Acetate	16	0.1	not tried		fermentation

thermoaceticum	a							@ 55 degC
Co-culture of Enterococcus faecalis, Klebsiella pneumoniae, Bacillus cereus	LA-BA	-	Butyrate	34	0.3	3.9	4.6	conti.-fermentation: feedstock = Lactic acid; culture=health hazard

Use of hemicellulose as a fermentation feedstock results in xylose as the primary sugar for fermentation. A preliminary study compared the ability of *Clostridium acetobutylicum* (ATCC 824) and *Clostridium tyrobutyricum* (ATCC 25755) for the consumption of xylose as opposed to dextrose as a carbon source for butyric acid production. Pre-conditioning the *C. acetobutylicum* for xylose consumption is necessary while with the *C. tyrobutyricum*, no pre-adaptation is required for them to readily consume dextrose. Also, as seen below in Table I.13, the *C. tyrobutyricum* fermentation with xylose as the feedstock produced more butyric acid than the fermentation with dextrose while for *C. acetobutylicum* there was no appreciable difference in butyric acid production between the two feedstocks.

A second compound, acetate, is present in fermentation feedstocks produced by hemicellulose hydrolysis. To test the effect of acetate on the fermentation, it was added in varying amounts. By adding acetate to the media at the beginning of the fermentation, the acetate producing metabolic pathway is inhibited and more butyrate is produced. Fermenting dextrose to acetate gives more ATP than fermenting to butyrate, which is the reason that the actetae producing pathway has to be inhibited if butyrate is to be produced. The data for these studies is presented below in Table I.13 – the highest level of acetate inhibition (36 g/L) produced the most butyric acid.

The one issue that develops with adding acetate to the start of a fermentation is that increases the lag period that the inoculum culture requires to enter into the log phase of cell division (production of biomass). The higher the acetate added for inhibition, the longer this lag period takes – data for this phenomena is presented in Table I.14.

All fermentations were performed using a batch-style 2L reactor with 950ml of media and 50ml inoculum culture. They all ran at 36^{o}C with 250 rpm of agitation under anaerobic conditions (some N_2 sparging in the beginning until enough CO_2 was produced by the organism). The starting concentration of sugar for each batch was 60g/L.

Table I.13. Results of Butyric Acid Fermentation with Different Feedstocks and Levels of Acetate Addition

Organism	**Feedstock**	**Butyrate concentration at end of batch (g/L)**	**Acetate added for inhibition at beginning (g/L)**
C. acetobutylicum	Dextrose	21.3	0
C. acetobutylicum	Xylose	20.8	0
C. tyrobutyricum	Dextrose	23.6	0
C. tyrobutyricum	Xylose	28.5	0
C. tyrobutyricum	Dextrose	22.5	6
C. tyrobutyricum	Xylose	24.8	6
C. tyrobutyricum	Dextrose	22.0	12
C. tyrobutyricum	Xylose	26.0	12
C. tyrobutyricum	Dextrose	24.5	24
C. tyrobutyricum	Xylose	27.5	24
C. tyrobutyricum	Dextrose	22.3	36
C. tyrobutyricum	Xylose	32.7	36

Table I.14. Lag time observed as a Function of Acetate Addition

Feedstock	**Acetate Inhibition (g/L)**	**Lag Period (hrs)**
Dextrose	0	0
Xylose	0	0
Dextrose	6	6
Xylose	6	6
Dextrose	12	20
Xylose	12	20
Dextrose	24	30
Xylose	24	45
Dextrose	36	118
Xylose	36	165

I.4 Production of Test Quantities of Biofuels

During the project the following batches of biofuels were produced for engine testing in the engine tests at MSU and at Ford Motor Company.

Biodiesel from MSU Canola: At our pilot-scale biofuel facility during the third quarter of the project, we processed over 300 gallons of canola oil to biodiesel (fatty acid methyl esters (FAME)). This biodiesel was used in an on-road diesel pickup truck and in diesel lawn equipment on the campus of Michigan State University.

Diethyl Succinate and Dibutyl Succinate: We prepared several batches of diethyl and dibutyl succinate in a 50 liter stirred batch reactor made of Pyrex. In the reactor, succinic acid was dissolved in butanol and esterified to make dibutyl succinate (DBS). Reactions were run by continually withdrawing water in a Dean-Stark trap to force the esterification reaction to proceed to completion. Purification was accomplished using the wipe film equipped with both internal

and new external condenser, yielding 20 kg high purity DBS (>98% pure). These biofuel components were used in MSU engine tests and as components in the blended biofuels used by Ford in their engine tests.

High Purity FAME and FABE for MSU Engine Testing: Purification of FAME (fatty acid methyl esters) made via standard methods from canola and soy oil was done by wiped film distillation. Optimized conditions were used to generate 4 kg of soy FAME and 4 kg of canola FAME that were essentially water white and odorless. These purified components were used in MSU engine testing. In another experiment, undistilled canola FAME was transesterified with butanol to produce 18 liters of canola FABE (Fatty Acid Butyl Esters). Conditions for wiped film distillation of FABE were optimized and used to produce 12 kg of highly purified FABE for use in MSU engine testing.

Butyl Nonanoate: A 100-kg batch of butyl nonanoate was prepared for a vehicle test at Ford Motor Company. N-butyl nonanoate has attractive properties both for blending with petroleum diesel and as a compression ignition engine fuel on its own accord. Butyl nonanoate was prepared by mixing nonanoic acid and n-butanol in a 3:1 alcohol:acid molar ratio in a 70 liter stirred batch reactor. Approximately 1 wt% Amberlyst 15 ion exchange resin was added as a catalyst, and the reaction was run at ~100^{o}C such that water formed during the esterification was continuously withdrawn from the reactor. At the end of reaction, noted by the absence of any remaining nonanoic acid, the reaction mixture was cooled and filtered to remove the solid acid Amberlyst catalyst. The mixture was then vacuum distilled in a wiped film apparatus to remove the excess butanol, which was recovered and recycled for the next batch. The butyl nonanoate produced was >98% purity. Four batches were produced of approximately 25 kg butyl nonanoate each; the 100 kg lot was delivered to Ford for testing.

II. Biofuel Blending and Characterization

II.1 Volatility Characterization

II.1.1 Vapor pressure and density

We have developed predictive SPEAD molecular simulations for cyclic hydrocarbons, cyclic ethers, and cyclic acetals, which are all potential components in multicomponent fuels. To optimize site parameters for the groups that compose these compounds, we found it necessary to differentiate between nearest neighbors in the ring compounds. For example, all the $>CH_2$ groups in 1,4-dioxane are next to one cyclic ether, while all the >CH2 groups in trioxane are next to two cyclic ethers. Using different parameters for such different environments provides good parameterization for all but the 4HMD, 5HD, 4HMMD, and 5HMD listed at the bottom of Table II.1. The comparisons with experimental data are approximate because the 'experimental' data are for blends of 4HMD + 5HD or 4HMMD + 5HMD and the errors are therefore listed in parentheses. The same experimental blend is used to compare with each of the compounds composing the blend.

Table II.1. Prediction of Vapor Pressure using current Group Parameters

Name	Structure	Pressure % AAD	Pressure % Bias	Pressure Max error %
cyclohexane		.7	.7	1.9
oxycyclohexane		7.3	7.3	11.7
1,3-dioxane		7.5	7.5	10.2
1,4-dioxane		2.8	-1.6	-9.4
trioxane		2.2	.3	-6.1
tetrahydrofuran		.4	.4	2.7
octahydrobifuryl	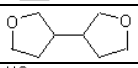	10.6	-.8	-34.1
tetrahydro-furfuryl alcohol		15.5	-3.7	-52.3
4-hydroxymethyl -1,3-dioxalane (4HMD)	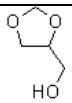	(6.7)	(2.0)	(23.7)
5-hydroxy-1,3-dioxane (5HD)	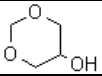	(58.2)	(58.2)	(62.0)

4-hydroxymethyl -2-methyl-1,3-dioxalane (4HMMD)	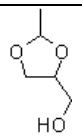	(69.8)	(-21.6)	(-91.5)
5-hydroxy-2-methyl-1,3-dioxane (5HMD)	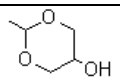	(70.5)	(-70.5)	(-70.5)

We have also worked to develop the MSU version of simulation which we call MSU-DMD-TPT to distinguish it from SPEAD. The advantage of MSU-DMD-TPT is that we are able to manipulate the source code. The vapor pressure modeling is excellent as shown in Figure II.1. We have initiated efforts to improve the density behavior of the model by adjusting the size of the functional groups. The predictions of the vapor pressure are excellent, but the density error is systematically off by about 5% (Figure II.2). Though the plot looks as though the errors are more significant for the heavier compounds, an adjustment of about 5% in size brings the density for all compounds into adjustment.

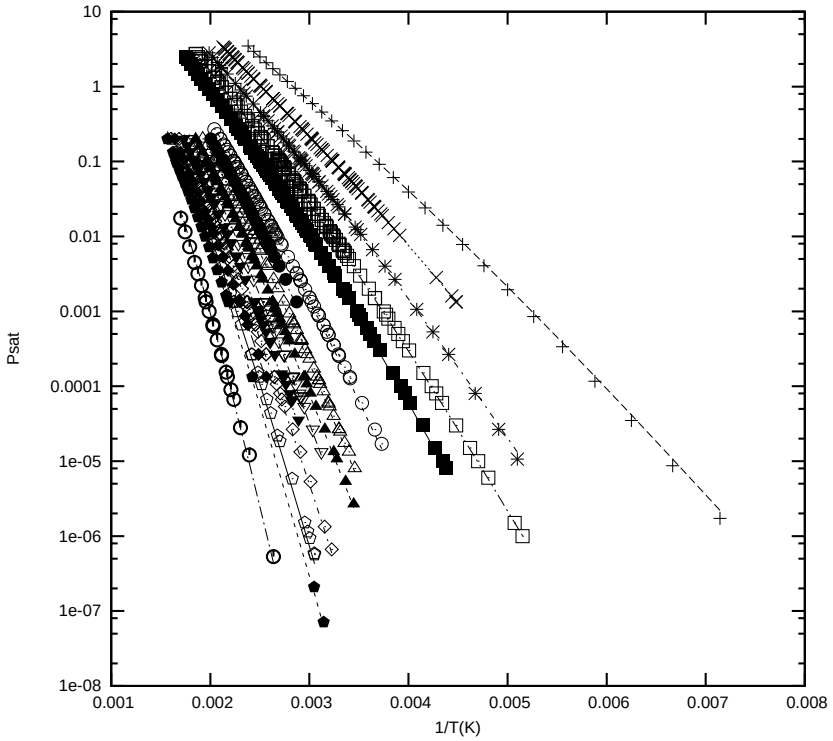

Figure II.1. MSU-DMD-TPT vapor pressure modeling for the following n-alkanes (L to R): C24, C19, C18, C17, C16, C15, C14, C13, C12, C11, C10, C8, C7, C6, C5, C4.

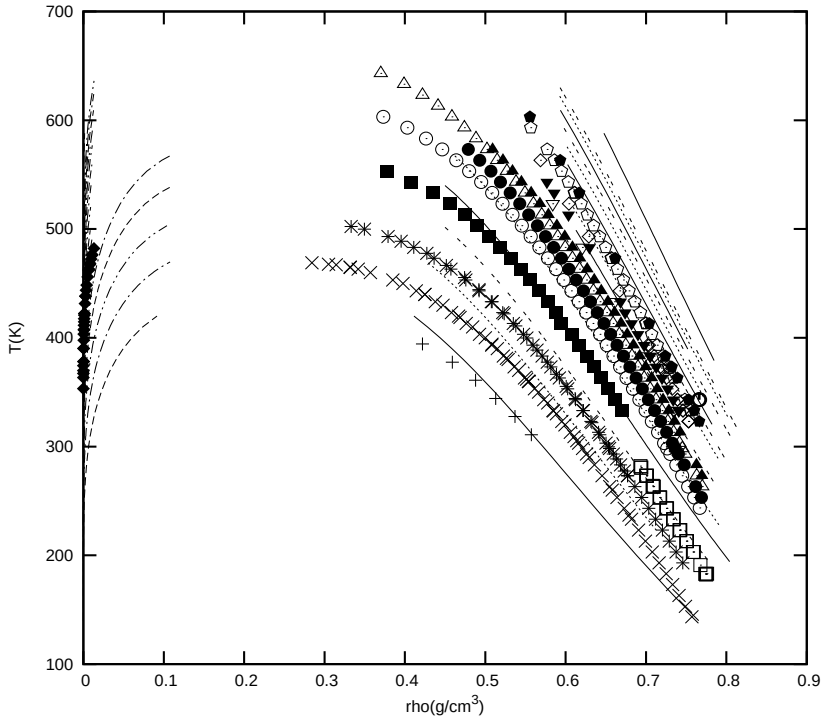

Figure II.2. MSU-DMD-TPT density modeling for the n-alkanes. The compounds are in the same order as the previous plot when viewed from the top to bottom.

In Figures II.3 and II.4 below, we show our vapor pressure and density predictions for primary alcohols. In Figure II.4, the densities of all the alcohols match the experimental values well, except for methanol. However, above room temperature, our predictions are almost same as the TRAPPE united atom Monte Carlo method. Below room temperature, no literature data is available for TRAPPE.

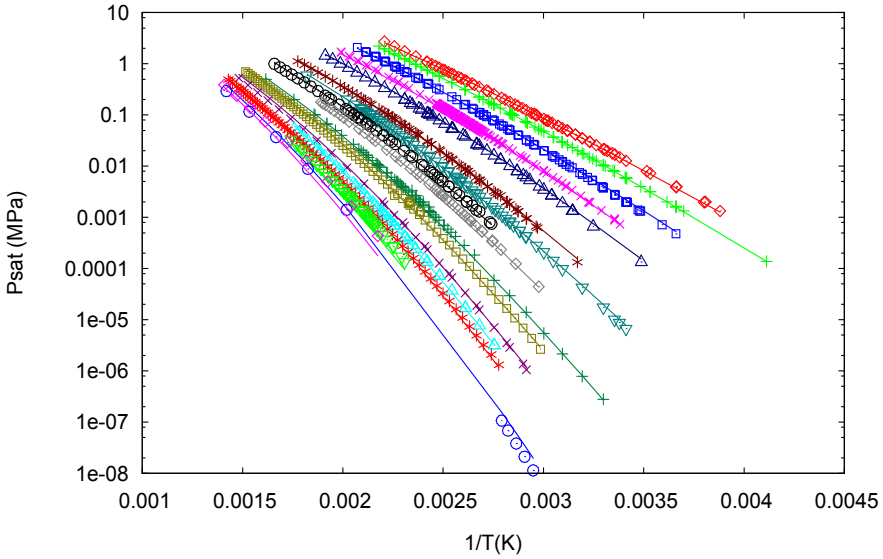

Figure II.3. Saturation pressures of primary alcohols. Lines are predictions from SPEAD and markers are experimental data from literature. From top to bottom, primary alcohol (1 ol) of : C1, C2, C3, C4, C5, C7, C8, C9, C10, C12, C13, C15, C16, C17, C18, C19, C20

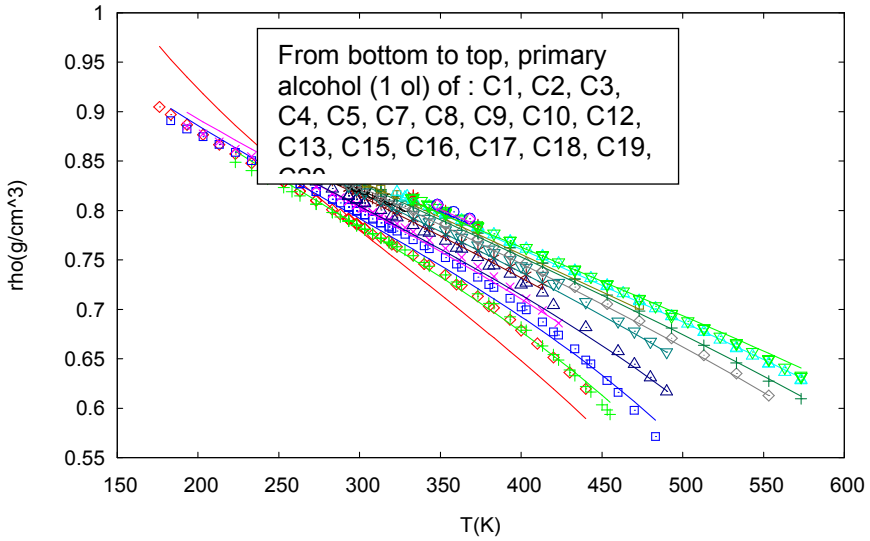

Figure II.4. Densities of primary alcohols. Lines are predictions from SPEAD and markers are experimental data from literature.

II.1.2 Flash point

Flash point is the minimum temperature at which an ignitable mixture of fuel vapor and air is formed. It is an important property that concerns safe storage and handling of fuels. It is calculated by noting the fact that the vapor mixture corresponds to the lower flammability limit of the fuel, and for a fuel blend it can be calculated by the following formula:

$$LFL_{mix} = \frac{100}{\sum C_i LFL_i}$$

where C_is are the component vapor phase concentrations and LFL_is are the component lower flammability limits. We have developed a flash point calculator which can provide the flash point temperature for a mixture, once the individual flash points of the components are known. The LFLs are available in databases, or can be calculated from correlations. Comparison of several mixture flash points with those predicted by the above relationship give excellent results. We thus have the capability to predict flash points of various fuel blends, an obvious advantage over direct measurements in time and savings of valuable sample (about 60 ml/test).

II.2 Low Temperature Properties

Cold flow properties of mixtures of biofuels (canola fatty acid methyl esters (FAME) biodiesel and dibutylsuccinate (DBS)) were characterized in binary blends with petroleum diesel fuel. Ternary mixtures of canola biodiesel, DBS, and petroleum diesel were also evaluated. Canola biodiesel was prepared by our MSU colleagues. DBS is a potential future biofuel (i.e., it can be produced from bio-derived feedstocks), but here was obtained commercially. Two petroleum diesel fuels (petrodiesel A and petrodiesel B; cetane 40.3), supplied by Haltermann

Products (Midland, MI), were used to make blends. Cold flow properties for these blends were measured using standard test methods for automated cloud point (CP; ASTM D2500-05) and automated cold filter plugging point (CFPP; ASTM 6371-05).

Canola biodiesel was blended with a petrodiesel over a range of blend ratios, ranging from 100% canola biodiesel to 100% petrodiesel and the CP and CFPP were measured. The CP of the biodiesel blends increased with increasing canola biodiesel content in a linear fashion (r^2>0.99). The CP of petrodiesel A was approximately 2 ^oC lower than the CP of petrodiesel B and this difference was reflected in the CP of the biofuel blends as the CP of petrodiesel A blends was consistently lower than the petrodiesel B counterparts (Figure II.5). The CFPP of petrodiesel A (-28.7 ± -1.5 ^oC) was higher than that of petrodiesel B (-37.0 ± -1.4 ^oC) (Figure II.6). For blend ratios less than 30% canola biodiesel, the observed relationship between blend ratio and CFPP were different. The CFPP remained fairly constant (a plateau region) up to 30% canola biodiesel in petrodiesel A. This phenomenon will be investigated further at a later date. The CFPP for biofuel blends containing petrodiesel B was nearly linear (r^2=0.95) with respect to blend ratio over the entire range of blends measured; no plateau region was observed for low-level blends.

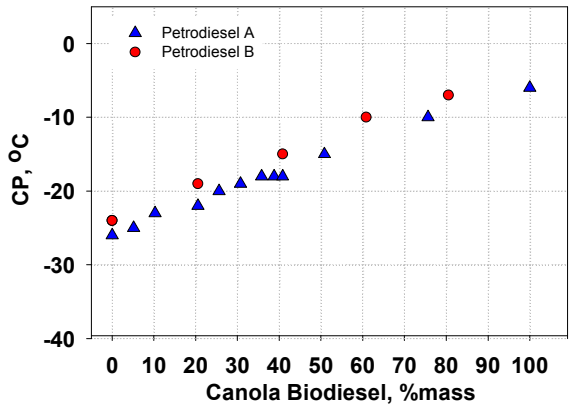

Figure II.5. Cloud point of canola biodiesel and petroleum diesel fuel blends.

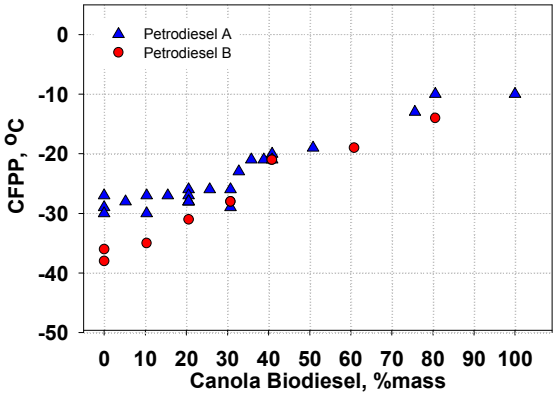

Figure II.6. Cold filter plugging point of canola biodiesel and petroleum diesel fuel blends.

Addition of dibutyl succinate to biodiesel provides improvements in cold flow properties. Similarly, DBS may provide improvements in cold flow properties of canola biodiesel/petroleum diesel blends. The CP was first measured for DBS blended only with petrodiesel A in ratios ranging from 0 to 100% DBS (Figure II.7). Interestingly, the CP of the DBS blends was often higher than the CP of either DBS or petrodiesel A measured individually. The reason for this is not understood but may be related to phase separation at cold temperatures.

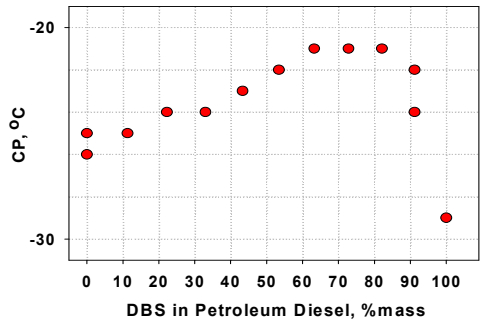

Figure II.7. Cloud point of DBS in petroleum diesel

The effect of DBS addition to canola biodiesel-petroleum diesel blends was evaluated by measuring CP and CFPP of the resulting blends. Ternary blends were prepared by addition of equal volumes of canola biodiesel and DBS to petrodiesel A. The CP or CFPP of the ternary blends was compared to those of binary blends containing canola biodiesel and petrodiesel. The CP of a ternary blend increased approximately linearly with the total biofuel content (r^2=0.90; Figure II.8). DBS blends generally had a lower CP and CFPP than blends where the biofuel fraction was comprised solely of canola biodiesel. This is due to the more favorable cold flow properties of DBS as compared to canola biodiesel. The effect was more pronounced at higher biofuel blend ratios. The CP of DBS (-29 ^{o}C) is similar to the CP of petrodiesel A (-27 ^{o}C) and is much lower than the CP of canola biodiesel (-6 ^{o}C). Due to the lower CP of DBS, the CP of the DBS blends deviated from that of the canola-petrodiesel A blend as the concentration of DBS in the blend increased. At higher blend ratios of DBS, the CP was noticeably lower than the equivalent canola biodiesel-petrodiesel A blend. The same effect is evident in CFPP data for binary and ternary blends in petrodiesel A (Figure II.9).

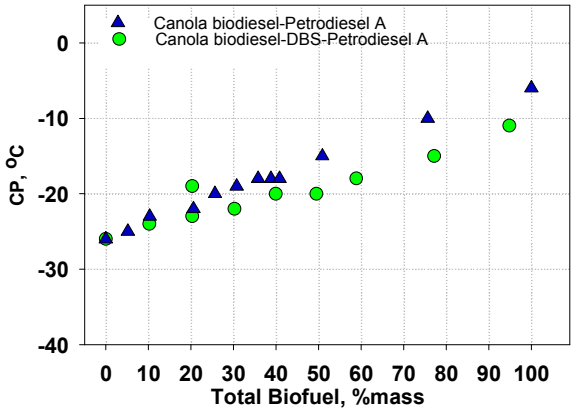

Figure II.8. Cloud point of binary and ternary biofuel blends in petroleum diesel fuel, expressed as total % biofuel (canola + DBS).

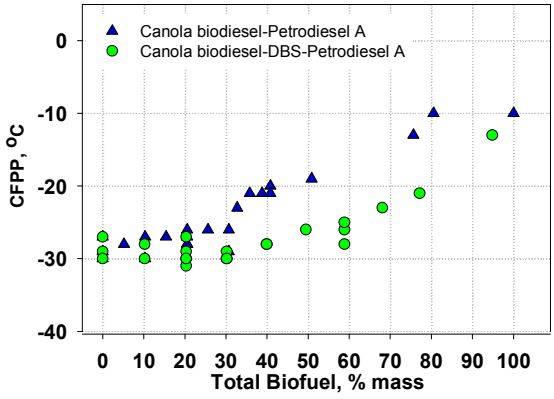

Figure II.9. Cold filter plugging point of binary and ternary biofuel blends in petroleum diesel fuel, expressed as total % biofuel (canola + DBS).

To evaluate the potential benefits of DBS addition to blends, the data in Figures II.8 and II.9 were replotted so that the x-axis expresses only the total % canola biodiesel in the blend and

not the sum of canola biodiesel and DBS. When plotted in this manner, the CP and CFPP of ternary blends containing DBS fall along the same line as the binary blends of canola biodiesel and petrodiesel A (Figures II.10 and II.11). These data show that with respect to cold flow properties, DBS provides a similar benefit to the petroleum diesel fraction that it replaces.

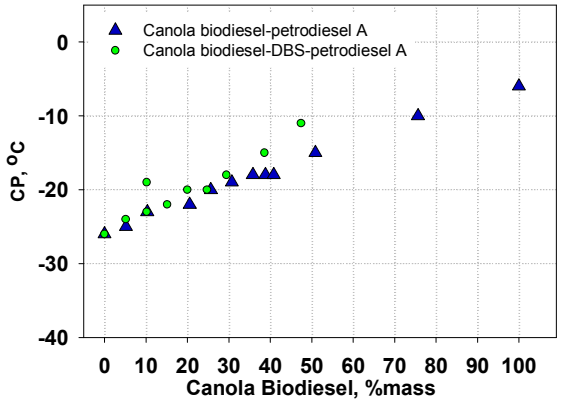

Figure II.10. Cloud point of blends of binary and ternary biofuel blends in petroleum diesel fuel, expressed as % canola biodiesel.

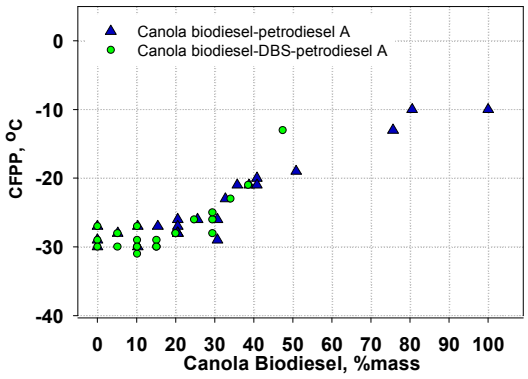

Figure II.11. Cold filter plugging point of binary and ternary biofuel blends in petroleum diesel fuel, expressed as % canola biodiesel.

Cold flow properties of blends of canola fatty acid methyl esters (FAME) biodiesel, dibutylsuccinate (DBS), and petroleum diesel fuel were characterized. Blends of a petroleum diesel and DBS were also evaluated. Cold flow properties were measured using standard test methods for automated cloud point (CP; ASTM D2500-05) and automated cold filter plugging point (CFPP; ASTM 6371-05). Canola biodiesel was prepared by our MSU colleagues. DBS is a potential future biofuel that was made at MSU. Two petroleum diesel fuels (petrodiesel A and petrodiesel B; both with cetane 40.3), supplied by Haltermann Products (Channelview, TX), were used in blends. The density, melting point, cloud point, and CFPP of the fuels used in the study are summarized in Table II.2.

Table II.2. Selected physical properties for biofuels and petrodiesel.

Fuel	Density at 20°C (g/ml)	Melting point (°C)	Cloud point (°C)	CFPP (°C)
Canola Biodiesel	0.882	nd[a]	0	-10
DBS	0.978	-29[b]	-29	-41
Petrodiesel A	0.857	nd	-26	-28.7 ± 1.53
Petrodiesel B	0.855	nd	-24	-37 ± 1.41

a – not determined b – The Merck Index, Merck & Co., Whitehouse Station, NJ, 1996.

The cloud point of DBS blended with petrodiesel A or B (0 to 100% DBS) was measured and the results are shown in Figure II.7. Interestingly, the cloud point of the DBS blends was often higher than the cloud point of either DBS or petrodiesel measured individually. The reason

for this is not understood, but may be related to phase separation of the fuel blend at cold temperatures.

The CFPP of these same blends of DBS with petrodiesel B was determined and are plotted in Figure II.12. The CFPP of petrodiesel B is approximately -37 ^{o}C and the CFPP of DBS is -41 ^{o}C. The addition of 10% DBS to the petrodiesel B lowered the CFPP by 4 degrees to -41 ^{o}C. Additional DBS slightly lowered the CFPP to a minimum of -43 ^{o}C observed for a 50:50 blend of DBS in petrodiesel B. Blends containing greater than 50% DBS in petrodiesel had slightly higher CFPPs than the 50:50 blend, but the values were still lower than for the petrodiesel alone.

The effect of DBS addition to blends of canola biodiesel and petrodiesel was evaluated by measuring the cloud point and CFPP of the resulting ternary blends. These blends were prepared by addition of equal volumes of canola biodiesel and DBS (ranging from 0 to 50 %) to petrodiesel B. The cloud point or CFPP of these blends was compared to that of binary blends containing canola biodiesel and petrodiesel in Figures II.13 and II.14. For easier comparison, the x-axis expresses only the mass percent canola biodiesel in the ternary blend and not the sum of the canola biodiesel and DBS. For example, a ternary blend represented by a point at 40 % on the x-axis refers to a blend of 40 % canola biodiesel, 40% DBS, and 20% petrodiesel. When plotted in this manner, the cloud point and CFPP of the ternary blends containing DBS generally fall along the same line as the binary blends of canola biodiesel and petrodiesel B, implying that DBS is acting similar to petrodiesel in terms of these two cold temperature properties.

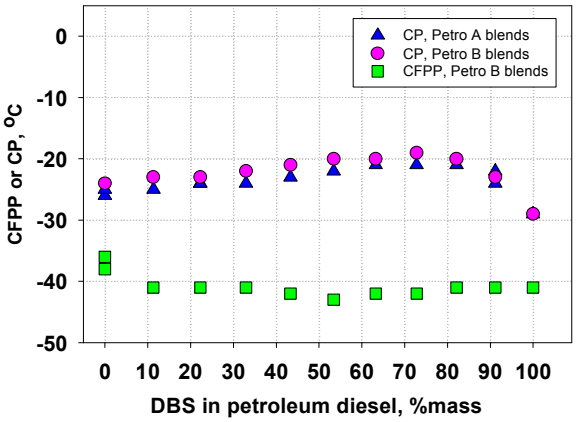

Figure II.12. Cold flow properties of petroleum diesel blended with DBS

The cloud point of blends containing DBS increased approximately linearly with the total biofuel content as shown in Figure II.13 (r^2=0.98). The CFPP of a ternary blend was comparable to the CFPP of the binary blend, from 0 to 40% canola biodiesel, as shown in Figure II.14. The blend containing equal volumes of canola biodiesel and DBS (shown in Figure II.14 as containing 48% mass canola biodiesel) with no petrodiesel had a CFPP about 5 ^{o}C higher than expected for a blend of canola biodiesel and petrodiesel with a similar mass fraction of biodiesel. This is likely because of the absence of cold flow improvers in the maximum binary blend containing no petrodiesel; cold flow improvers are normally added to petrodiesel. Results reported earlier with petrodiesel A showed this same phenomenon. These data show that with respect to cold flow properties, DBS provides a similar benefit to the petroleum diesel it replaces. However, despite the fact that DBS has CP and CFPP lower than the petrodiesel, no additional benefit was observed.

Figure II.13. Cloud point of petroleum diesel blended with canola FAME and DBS.

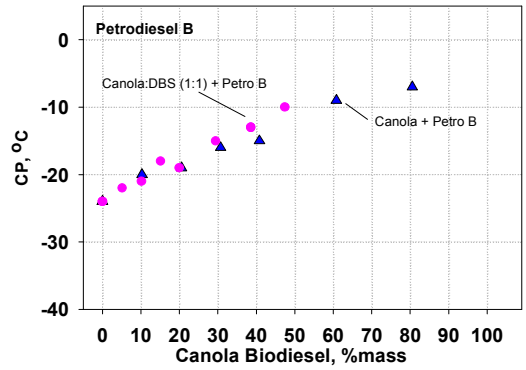

Figure II.14. Cold filter plugging point of blends of petroleum diesel, canola FAME, and DBS.

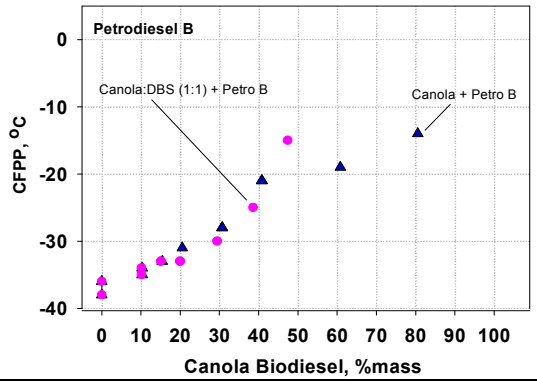

The effect of several biofuel constituents on the cloud point of petroleum diesel fuels was evaluated. Diisobutyl succinate (DIBS) has a freezing temperature of -55˚C, where DBS is only -29˚C, so it is possible that the DIBS could be a better additive than DBS. It was anticipated that DIBS would exhibit different cloud points due to the change in the end groups on the succinate. Instead, we found that DIBS had almost the exact same cloud points as DBS in mixtures with two of the diesel fuels, the 727 and 720 types. It was then decided to evaluate the cloud points for compounds with different functional groups. Hexanes (a mixture of 6 carbon containing molecule isomers) and butyl butyrate (an ester with 4 carbon length chains on either side) have similar freezing points, but behave differently when in mixtures with the diesel fuels (Figures II.15 and II.16). Both diesel fuels exhibit the same trend in mixtures with all the different additives, despite having different cloud points and different ratios of aromatics and saturated components. The hexanes mixtures (triangles on both graphs) show the cloud point decreasing almost linearly when up to 80 mass percent hexanes is added. The butyl butyrate mixtures (circles on both graphs) also behave similarly, but the cloud point is not suppressed as much. Because the monoester butyl butyrate does not exhibit the hump we speculate that the immiscibility of the DBS and DIBS caused by the diester group. The longer chain esters had the same effect on the cloud point as the shorter ones. Even though their melting temperatures were approximately 40˚C warmer than those for the butyl butyrate, the cloud point temperatures are almost the same for all concentrations. In addition, it is noticeable in Figure II.17 that even though the end groups differ, the cloud point temperatures are almost identical for all additives. This further supports the conclusion that it is either the ester group, or the carbonyl portion of the ester, that contributes the most to determining miscibility in earlier work.

Table II.3 shows the different additive types, their structures and their freezing points. These different additives were evaluated in 3 different fuels (two diesel fuels and a jet fuel). The results are shown in Figure II.15, Figure II.16, and Figure II.17.

Table II.3. All bio-based molecule additives used to date in cloud point evaluation.

Name	*Structure*	*Freezing Point (˚C)*
Dibutyl succinate	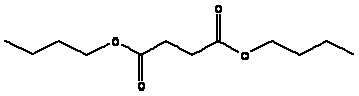	*-29*
Diisobutyl succinate	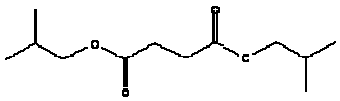	*-55*
Hexanes (mixture of isomers)	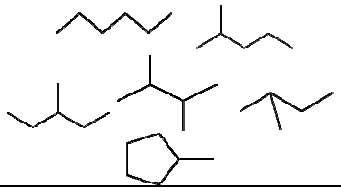	*-95*
Butyl butyrate	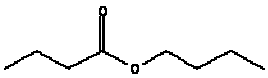	*-92*
4-Heptanone	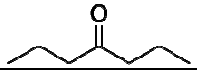	*-32.5*
Butyl nonanoate	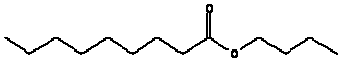	*-38*
Isobutyl nonanoate	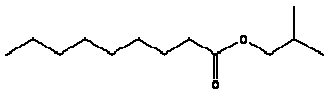	*-48*
Butyl ethyl hexanoate	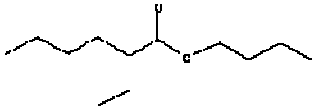	*unknown*
Ethyl hexyl nonanoate	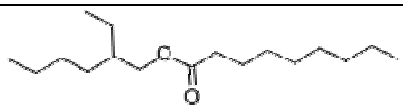	*unknown*

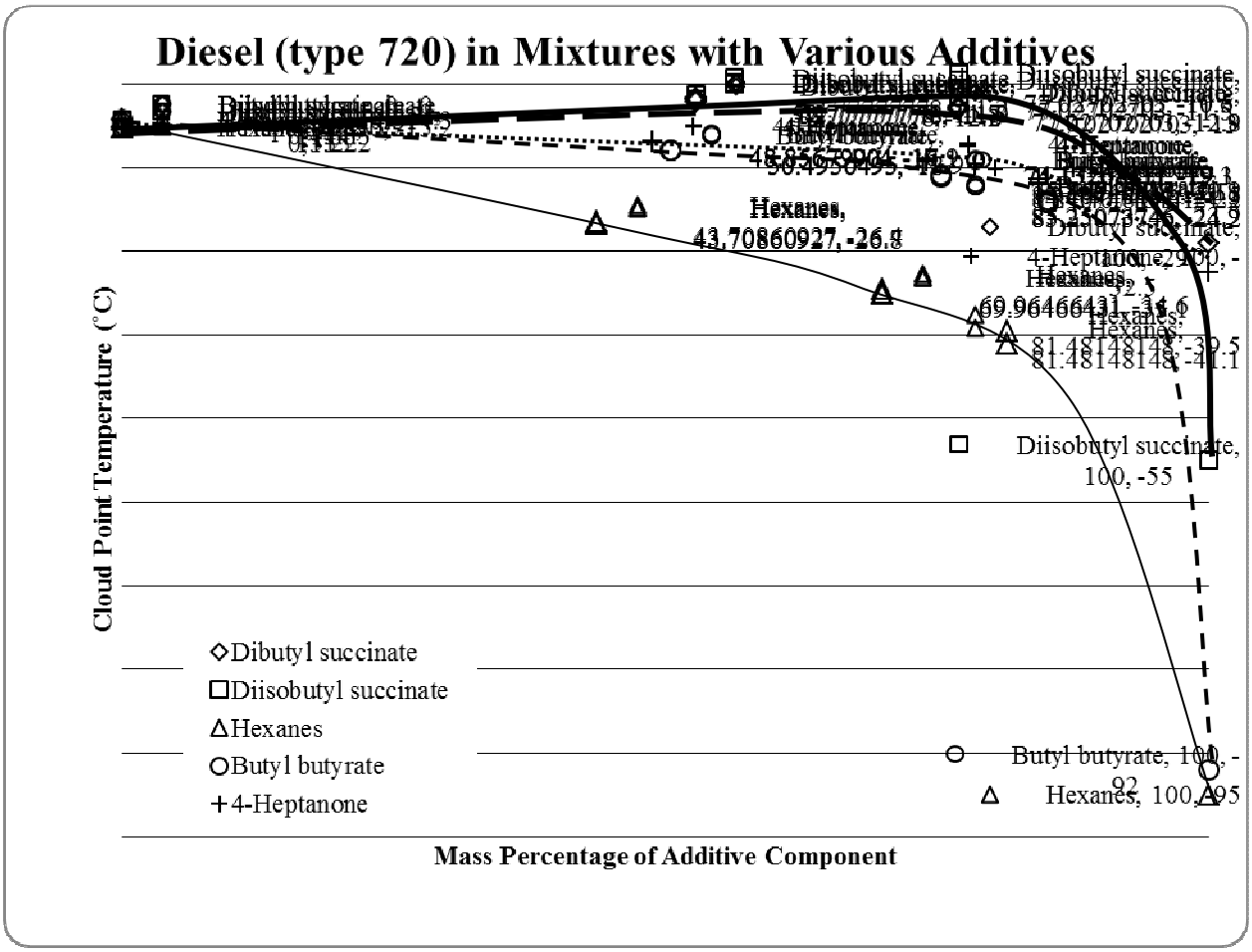

Figure II.15: Cloud point of diesel type 720 in mixtures with various bio-molecule additives.

The three different fuels show interesting overall trends. For the 720 type (Figure II.15) and 727 type (Figure II.16) diesel fuels, the heptanone and butyl butyrate show very similar improvement in the cloud points of the diesel, despite having a difference in freezing temperature of approximately 60˚C. However, when the heptanone is used in concentrations above 50% by volume in JP-8, the mixtures subcool and warm quickly after the cloud point is reached and crystallization begins. This causes the cloud points to become random, depending on the number of nucleation sites which are available. Various methods were attempted to prevent subcooling, such as stirring, addition of boiling chips and addition of activated carbon, but no methods succeeded.

It appears that both heptanone and butyl butyrate do not separate into two liquid phases when mixed with fuels at low temperature. The consistent decrease in cloud point and the presence of warming upon crystallization imply that these mixtures are exhibiting solid-liquid phase behavior at these low temperatures. In addition, these components could help to increase the cetane number of a fuel mixture, since the dibutyl succinate has a lower cetane number. This can increase the efficiency of combustion of the fuels and decrease the difficulty of an engine to start while using these fuels.

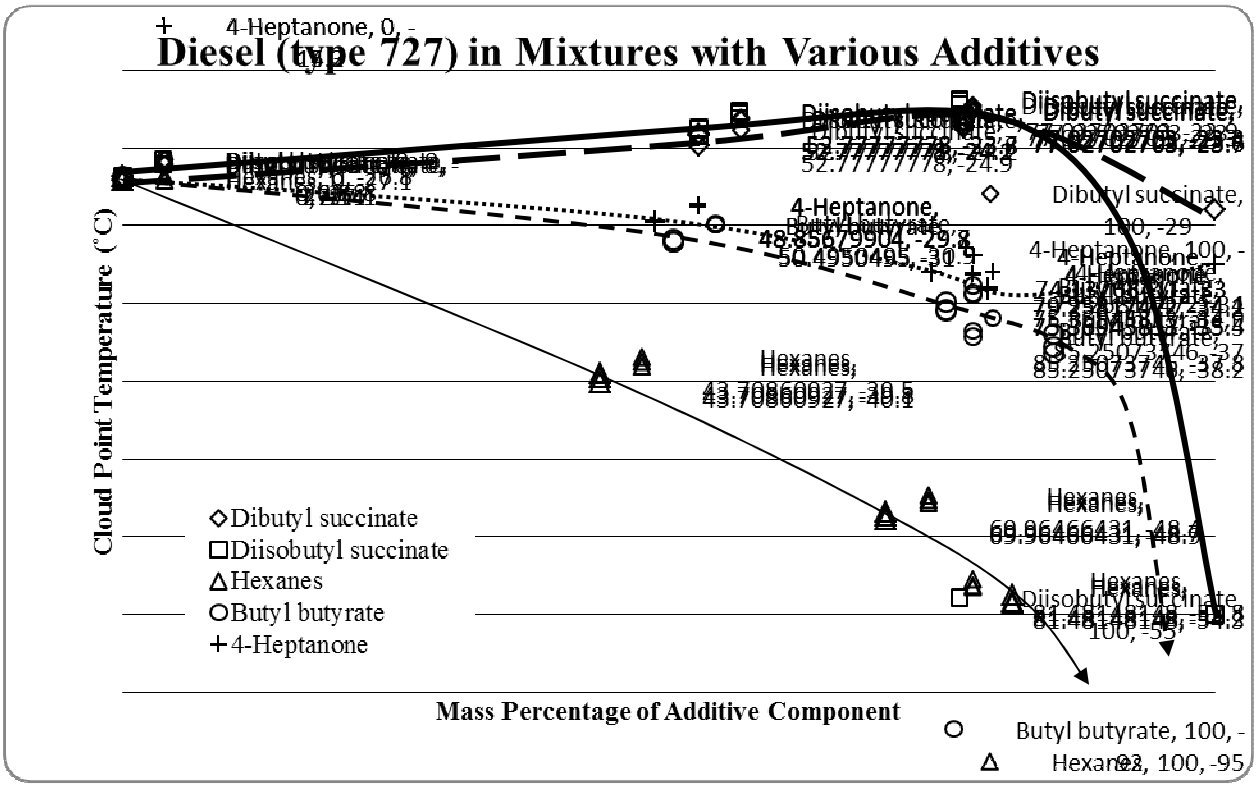

Figure II.16: Cloud point of diesel type 727 in mixtures with various bio-molecule additives. The pure component melting points of hexane and butyl butyrate are not shown in order to show detail.

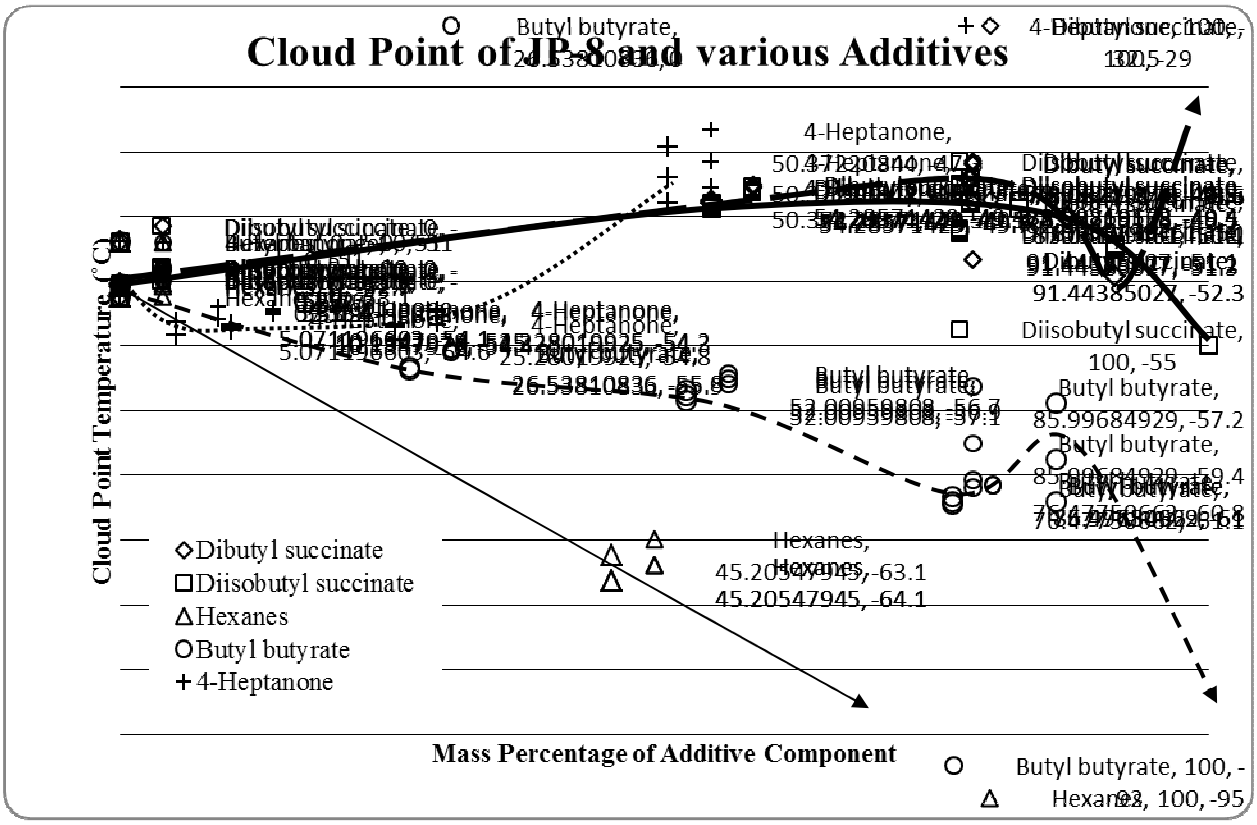

Figure II.17: Cloud point of military jet fuel JP-8 in mixtures with various bio-molecule additives. The pure component melting points of diisobutyl succinate, hexane, and butyl butyrate are not shown in order to show detail.

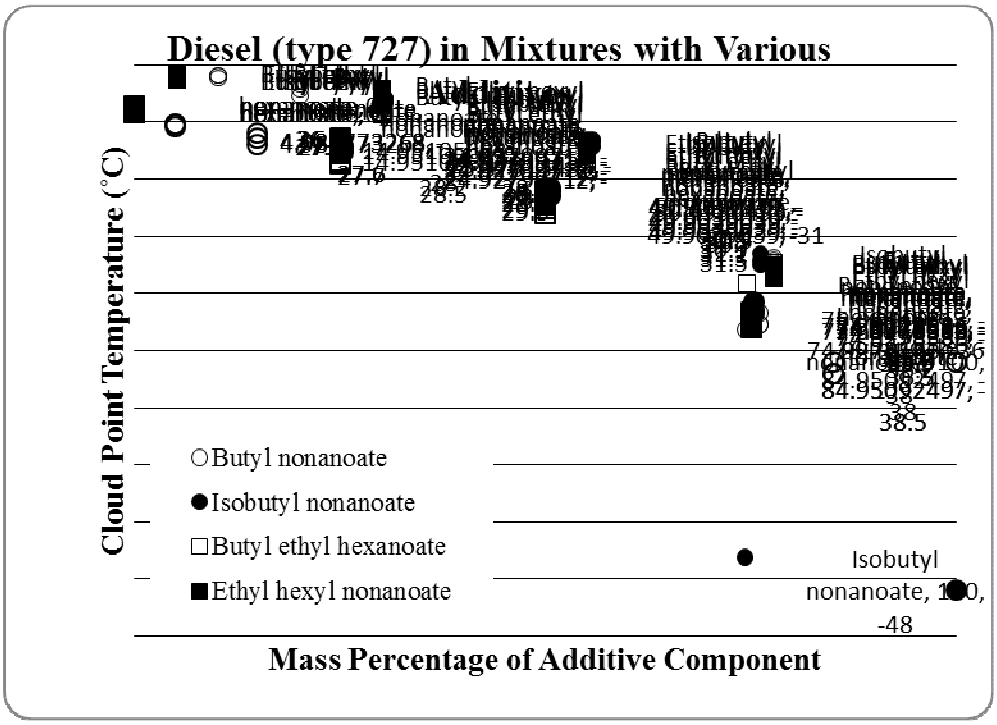

Figure II.19. Cloud points of diesel type 727 in mixtures with various higher cetane potential fuel additives. Melting temperatures for pure butyl ethyl hexanoate and ethyl hexyl nonanoate are unknown.

II.3 Cetane Number of Biofuels

A test fuel consisting of 50% dibutyl sucincate (DBS) 50% canola fatty acid methyl esters (FAMES) was analyzed for cetane value. The resulting cetane value of 35.6 was significantly lower than standard diesel (~42); as a result, we examined the effects of blending ratio of DBS/FAMES on cetane values. Cetane values vary linearly with DBS/FAMES ratios as shown in Figure II.20. Addition of dibutyl ether (DBE) as a cetane enhancer to the original 50/50 test fuel showed only a small increase in cetane value as seen in Figure II.21.. Using more than 20% DBE results in a flashpoint that is lower than that specified by ASTM for #2 diesel. Addition of the industrially accepted cetane enhancer 2-ethylhexyl nitrate (2-EHN) to our 50/50 test fuel was thus also examined. It can be seen in Figure II.22 that addition of 1000 ppm 2-EHN increases the fuel cetane number to the minimum ASTM value of 40, while the addition of 4000 ppm 2-EHN results in a cetane value comparable to #2 diesel.

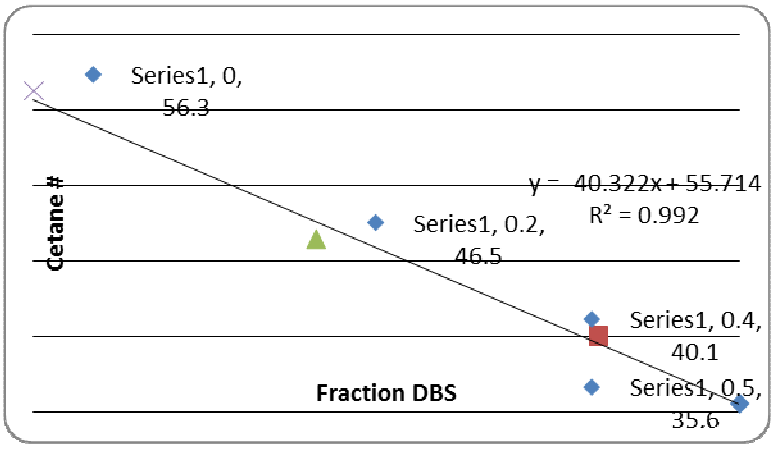

Figure II.20. Cetane value vs. DBS fraction in canola FAMES

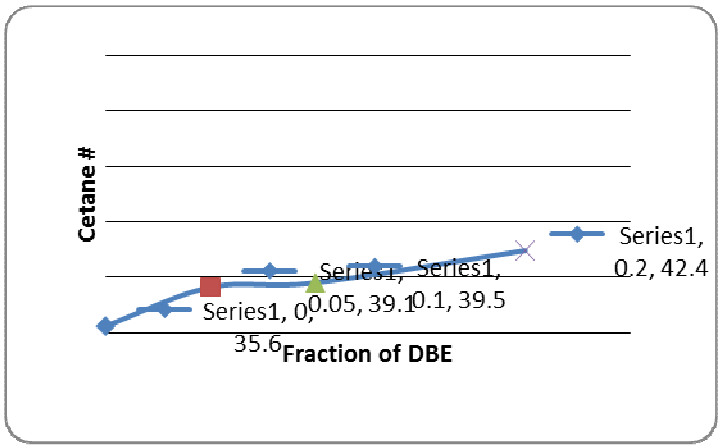

Figure II.21. Cetane value vs. DBE fraction in test fuel consisting of 50%DBS and 50% canola FAMES.

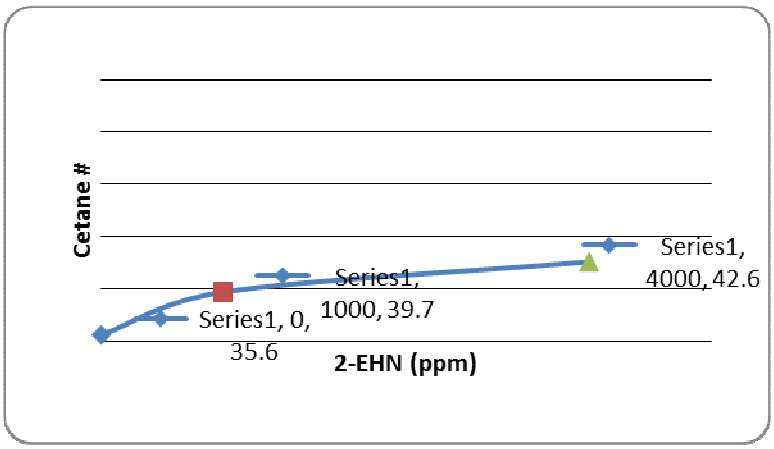

Figure II.22. Cetane value vs 2-EHN fraction in test fuel consisting of 50%DBS and 50% canola FAMES.

II.4 Properties Prediction for Combustion Simulations

The following physical properties have been examined and calculation methods developed during the reporting period. These calculators will be applied in simulation studies to produce a more accurate physical picture of spray dispersion and combustion than has been previously possible.

II.4.1 Surface tension

Surface tension evaluation methods for pure compounds are either based on corresponding state theory, or Macleod-Sugden parachors. The corresponding state theory methods need critical property information, which may not always be readily available. More accurate methods involve thermodynamic models, which are more complex and need more parameters. We have used the Macleod-Sugden method to create our surface tension calculator. The parachors are temperature independent, and have been tabulated for practically all functional groups. The parachor and the surface tension are related according to the following formula [1],

$$\sigma^{1/4} = P(\rho_L - \rho_V)$$

where P is the compound parachor, $\sigma^{1/4}$ the surface tension and ρ_L, ρ_V the liquid and vapor molar densities. Table II.4 shows a comparison of the surface tensions of some compounds calculated with our model with experimental values. The experimental values, unless specified, have been obtained from DIPPR.

Table II.4. Surface tensions of pure components

Compound	Calculated	Experimental
Heptane	20.48	20.14
Methyl laurate	27.99	27.68
Methyl oleate	33.48	31.3
Methyl stearate	31.82	29.0

II.4.2 Enthalpy of formation and combustion

The ideal gas heat of formation model developed in our group uses Verma and Doraiswamy (VD) method [2]. The other common methods are the Joback, and Gani and Constantinou models, which require more parameters for each group. The VD method on the other hand uses just two parameters, and the heat of formation is calculated according to the relation,

$$(\Delta H_f^0)_T = A + BT,$$

where T is the absolute temperature. The constants A and B can be calculated for each compound based on the groups forming it. For example, for an ester, A and B can be calculated by summing up the contributions from methyl, methylene and the ester groups.

The model predicted the heats of formations for alkanes within a few percent, but a correction factor was needed for esters. The correction factors were calculated based on Gaussian

results from Osmont et al's work [3]. Once the heat of formation is known, the heat of combustion can be calculated according to the relation,

$$\Delta H_c = -393.78 N_C - 121 N_H - \Delta H_f$$

where N_C is the number of C atoms and N_H is the number of H atoms in the compound. The coefficients of N_C and N_H are the heats of formations of CO_2 and H_2O respectively in J/mol. Table II.5 below shows a comparison of the model predictions against experimental values.

Table II.5: Heats of formation and combustion of pure compounds

Compound	Heat of formation (g) (kcal/mol)		Heat of combustion (kcal/mol)	
	Calculated	Experimental	Calculated	Experimental
Heptane	45.20	44.89	1077.40	1068.10
Methyl laurate	149.95	146.50	1827.36	1810.24
Methyl stearate	179.60	184.1	2710.34	---
Methyl oleate	147.44	149.76	2684.56	2655.50

II.4.3 Enthalpy of vaporization

In order to get an estimate of the enthalpy of vaporization, the Clausius-Clapeyron equation can be integrated to get a relation between vapor pressure and temperature, as shown below,

Integrating, we get,

$$\frac{dp}{p} = \frac{\Delta H}{RT^2} dT, where \quad \Delta H = A + BT + CT^2$$

$$\ln p = \frac{1}{R}\left[-\frac{A}{T} + B \ln T + CT \right] + D$$

The constants A, B, C and D can be evaluated from vapor pressure – temperature data. We are working on getting good estimates of the constants, so that the enthalpy of vaporization can be calculated more precisely.

II.5 Lubricity of Biofuels and Biofuel Blends

II.5.1 Background

Lubricity is an important property for diesel fuel used in modern diesel engines, as the fuel itself provides some or all of the lubrication between contacting surfaces [1,2]. Modern petroleum-based diesel fuels (ultra-low sulfur diesel, ULSD) are known to have poorer lubricity than earlier diesel fuels due to chemical changes from refinery operations (hydrotreatment) used to provide lower sulfur content and lower aromatic content. As such, additives are commonly required to bring lubricity to within industry specifications. One attractive feature of biodiesel (typically methyl esters of fatty acids from plant or animal oils/fats) is that it has relatively high

lubricity compared to ULSD. Nearly all of the lubricity benefit is realized upon adding relatively small amounts (1-5% v/v) of biodiesel to diesel fuels [3].

Industry specifications for lubricity [4-7] of diesel fuels are defined in terms of results from a High Frequency Reciprocating Rig (HFRR). HFRR measures wear caused by friction under the boundary lubrication regime as determined by rubbing a steel ball against a flat steel disk. The size of the resulting wear scar is an indication of fuel lubricity. To provide a preliminary evaluation of the effect of DBS on fuel lubricity, HFRR lubricity measurements were made for the following three fuels:

- ULSD
- Canola B100 (canola biodiesel or canola methyl ester)
- 50:50 blend (v/v) of DBS and canola biodiesel

II.5.2 Methods and materials

Lubricity was measured according to ASTM D6079-04 [8] using a HFRR from PCS Instruments. In this test, a non-rotating steel ball (AISI E-52100 steel, 66 HRC) rubs against a stationary steel disk (AISI E-52100 steel, 190-210 HV 30). The interface is submerged in 2 mL of fuel at 60 ^{o}C. The steel ball is forced against the disk with a 200-g load (resulting in 260 MPa initial contact stress), oscillating at 50 Hz with a 1-mm stroke length. The test duration is 75 minutes. Prior to testing, steel balls and disks are rinsed with hexane, then ultrasonically cleaned in hexane for 5 minutes, then rinsed again with hexane. After completion of each test, the steel ball is rinsed with hexane to remove fuel and wear debris and dried with a Kimwipe tissue and dry nitrogen gas. The minor and major wear axes of the wear scar are measured with an optical microscope and digital imaging software. The reported wear scar diameter of the steel ball is the average length of the minor and major axes. Tests were conducted in duplicate or in triplicate. During the tests, two additional parameters were measured: average coefficient of friction and electrical contact resistance. Coefficient of friction was not measured for the ULSD fuel due to a calibration issue.

II.5.3 Results and discussion

To summarize, the canola B100 showed the highest lubricity. When DBS was blended with canola biodiesel (50% v/v each), the lubricity was reduced, but to a level still considerably higher than that of the ULSD test fuel. The lubricities of all three fuels were within industry specifications for diesel fuel.

The wear scar diameter results are shown in Figure II.23, with smaller wear scar diameter signifying higher lubricity. All results met industry standard maximum allowable values (ranging from 400 microns [7] to 520 microns [4]). The canola B100 sample had the smallest wear scar diameters, and thus greatest lubricity, of the three samples. The 50:50 blend yielded somewhat larger wear scar diameters than the canola B100, but still considerably smaller those with ULSD.

Coefficient of friction results measured during the HFRR tests are provided in Figure II.24. Lower friction coefficient indicates higher lubricity. As with the wear scar results, the higher friction coefficient measured for the 50:50 blend indicates that it has lower lubricity than the canola B100. No data were available for the ULSD sample.

Electrical contact resistance measured during the HFRR test is shown in Figure II.25. Greater resistance generally indicates higher lubricity. Consistent with the other indicators, electrical contact resistance for the 50:50 blend was similar to that of ULSD and lower than the canola B100, indicating lower lubricity compared to the B100. All three indicators from the HFRR tests show that blending of DBS into canola biodiesel decreases its lubricity compared to pure canola biodiesel. When mixed in a 50:50 volumetric ratio, the resulting lubricity met industry specifications for diesel fuel, however. It is expected that the 60:40 blend (60% canola biodiesel, 40% DBS) used in engine dynamometer testing at Ford will have lubricity that is marginally better than the 50:50 blend. Additional testing would be needed to determine the lubricity of DBS/canola biodiesel blended into ULSD (e.g., at 5% or 20% concentration levels, B5 or B20).

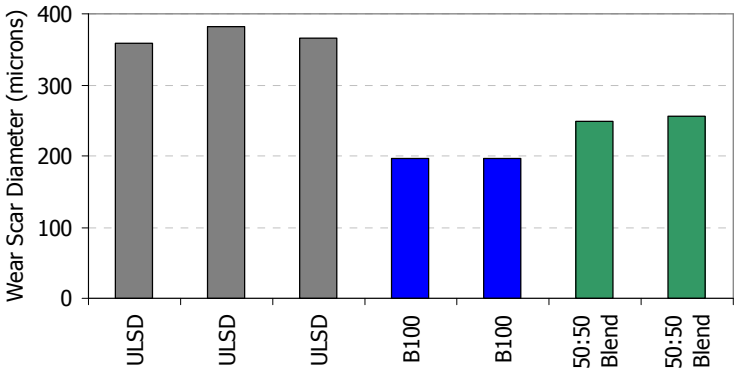

Figure II.23. Wear scar diameter resulting from HFRR tests

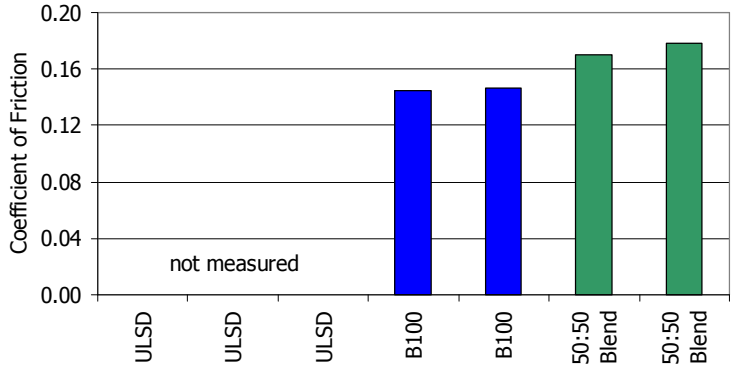

Figure II.24. Coefficient of friction during HFRR tests.

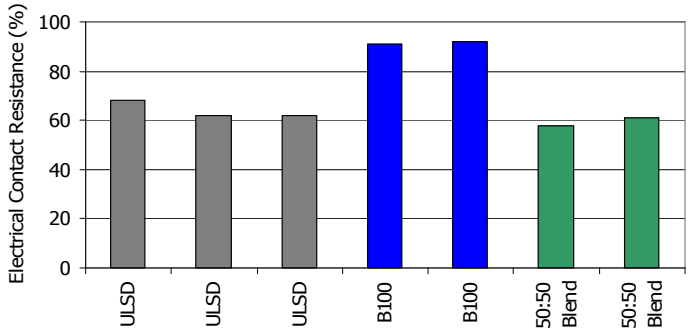

Figure II.25. Electrical contact resistance during HFRR tests.

References

1. Barbour, R., Rickeard, D., Elliott, N., 2000. "Understanding diesel lubricity", SAE Technical Paper Series, 2000-01-1918.

2. Matzke, M., Litzow, U., Jess, A., Caprotti, R., and Balfour, G., 2009. "Diesel lubricity requirements for future fuel injection equipment", SAE Technical Paper Series, 2009-01-0848.

3. National Biodiesel Board, undated. "Lubricity benefits", citing data from Stanadyne Automotive Corporation, http://www.biodiesel.org/pdf_files/fuelfactsheets /Lubricity.PDF, accessed on 12/18/09.

4. ASTM D975-09b, "Standard specification for diesel fuel oils".

5. EN 590. "Automotive fuels—diesel—requirements and test methods".

6. Worldwide Fuel Charter, 4th Edition, September 2006, p. 49.

7. "Fuel Requirements for Diesel Fuel Injection Systems, Diesel Fuel Injection Equipment Manufacturers Common Position Statement 2009", Signed by Delphi Diesel Systems, Robert Bosch GmbH Diesel Systems, Continental Automotive GmbH, Denso Corporation, and Stanadyne Corporation, issued September 2009. http://www.globaldenso.com/en/topics/files/common_position_paper.pdf

8. ASTM D 6079-04, "Standard test method for evaluating lubricity of diesel fuels by the High Frequency Reciprocating Rig (HFRR)".

III. Rapid Compression Machine (RCM)

III.1 Design and Construction of RCM

The Michigan State University RCM (Figure III.1) is capable of measuring auto-ignition parameters for a variety of temperatures, pressures, and equivalence ratios. Additionally, the RCM provides insight into chemical species formation during the combustion process. These measurements are used to characterize the novel biofuel blends and to develop global chemical kinetics models.

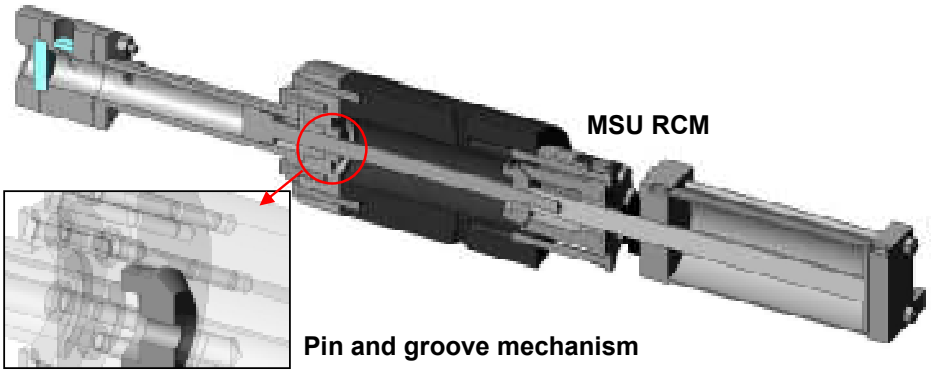

Figure III.1. Cross section of MSU RCM

Two common challenges encountered when designing an RCM are vibrations during the piston deceleration process and decoupling the combustion chemistry from the complex fluid dynamics during the compression stroke. A hydraulic pin-and-groove system is commonly used to quickly decelerate the piston, but harsh vibration issues are observed in most existing machines. The MSU RCM uses an advanced stepped pin and groove mechanism which slows the piston down in increments to ensure a smooth deceleration profile. The design of the steps in the pin and groove mechanism is based on numerical calculations of fluid dynamics between the viscous oil and grooves of the hydraulic piston. In the combustion chamber, a creviced piston design is incorporated to ensure that the fluid dynamics are decoupled. Figure III.2 shows the completed RCM.

There are other design features which are unique to the MSU RCM. The windows for optical access have been given a unique sealing design to prevent leaks during high pressure operation. The windows are able to withstand pressures in access of 200 bar. The combustion chamber itself has improved and uniform heating for better control of the test fuel temperature. Adjustment of the stroke in the machine is made easier by using screw driven assemblies and external shims to lock it into position.

The RCM is capable of burning aerosols which are introduced through a Sono-Tek ultrasonic nozzle. The generated aerosol flows through a poppet valve before filling the combustion chamber of the RCM. To promote charge homogeneity we have completed a series of computational fluid dynamics (CFD) simulations to optimize the

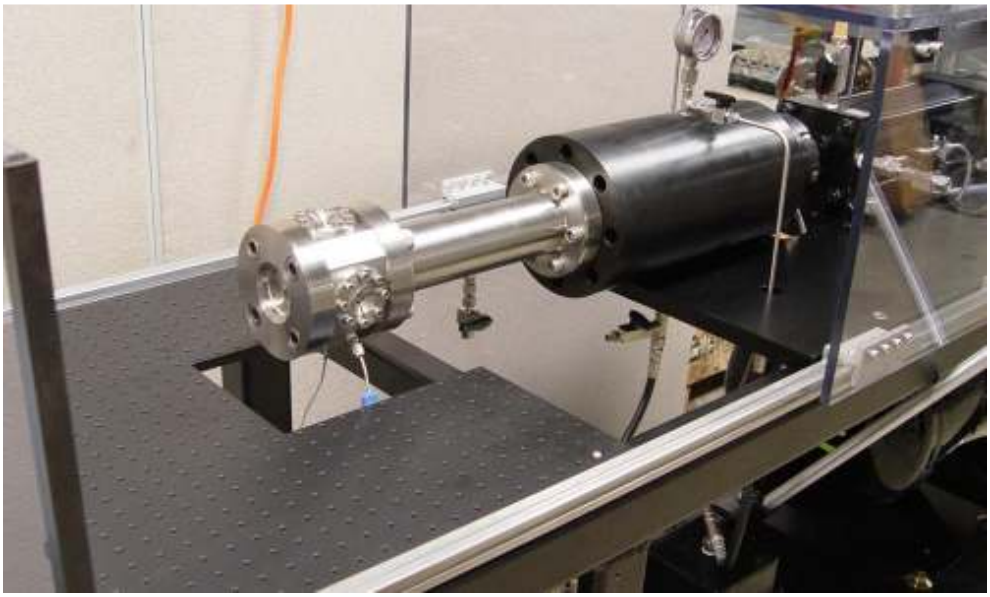

Figure III.2. Rapid compression machine and mounting assembly at MSU

poppet valve geometry. Figure III.3 shows a subset of these CFD results. The results of the CFD have been used to design a poppet valve that maximizes turbulent mixing in the combustion chamber and minimizes surface area where the aerosol may settle.

Additional efforts are being focused on modeling the RCM compression and droplet evaporation process. To model the chemical kinetics of a reaction in the RCM, we must develop a numerical model that accurately describes the conditions within the combustion chamber. For a creviced piston, Mittal et al. [1] have previously demonstrated that an adiabatic core of reacting gases exists within the RCM. Within this core, the compressed temperature may described by

$$\int_{T_0}^{T_{ac}} \frac{1}{\gamma - 1} \frac{dT}{T} = \ln\left(\frac{V_i}{V_f}\right) = \ln(CR),$$

where γ is the specific heat ratio and the compression ratio, *CR*, is expressed as the ratio of initial (V_i) and final volumes (V_f). Outside of the adiabatic core, heat is lost to the walls, making the overall compression process non-adiabatic. The degree of non-adiabaticity of the compression may be determined using pressure data from the RCM, leading to the definition of an effective volume during compression.

$$V_{eff}(t) = V_g(t) + V_{add}$$

where V_g is the volume calculated through piston velocity and V_{add} is an empirically-determined parameter. After compression, the effective volume may be modeled as

$$V_{eff}(t) = V_{eff}(0) v_p(t)$$

where v_p is determined by curve-fitting a volume expansion trace of a non-reactive RCM test. $V_{eff}(0)$, is the effective volume at the end of the compression stroke ($t = 0$).

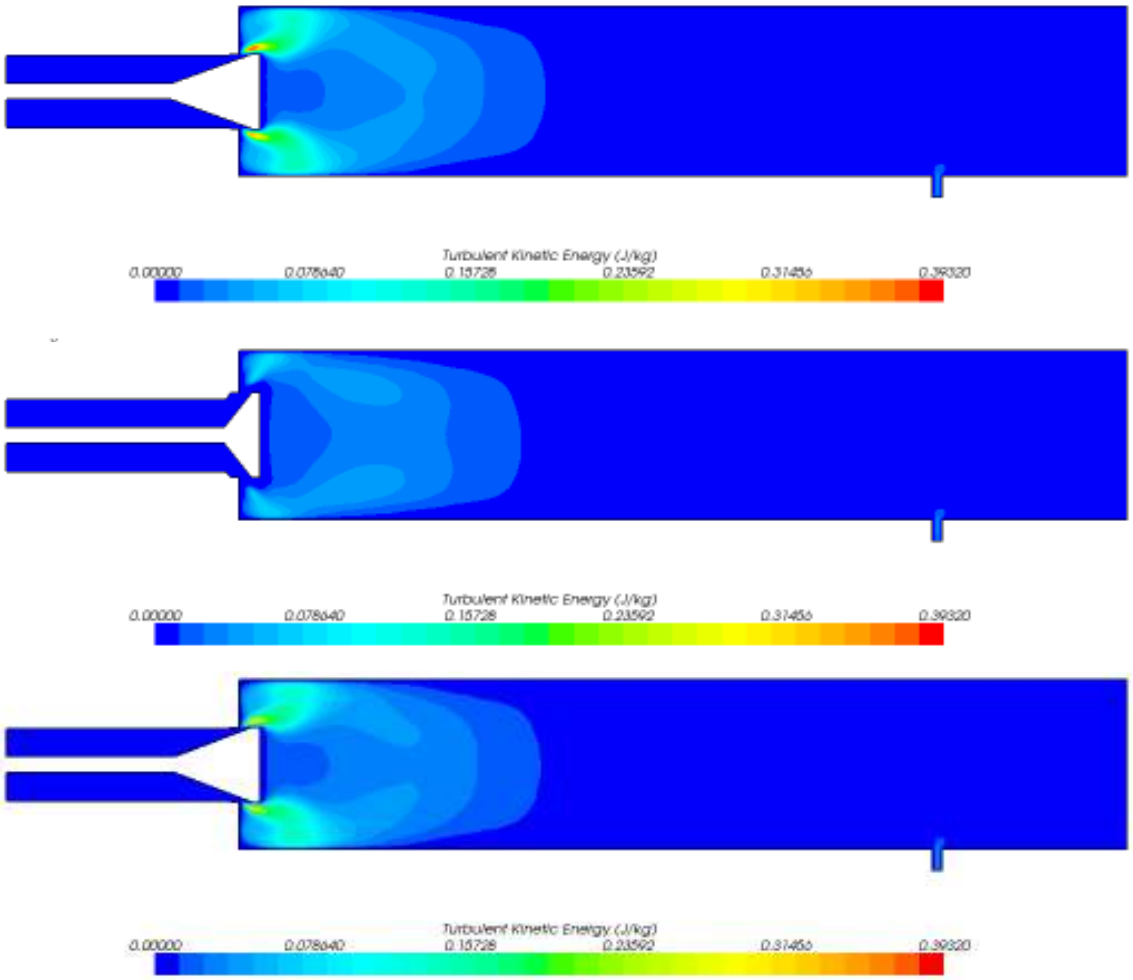

Figure III.3. Turbulent kinetic energy for various poppet valve geometries

As shown in Figure III.4, preliminary tests demonstrated the reproducibility of RCM tests. For a given set of initial conditions and fluid composition, the RCM consistently generates the same compressed temperature and pressure.

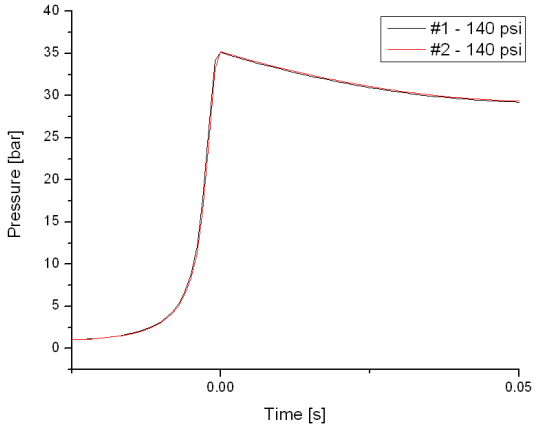

Figure III.4 Pressure trace in RCM showing reproducibility

In addition to the ability to test fuels as premixed vapor charges and aerosol-gas mixtures introduced through the poppet valve, the RCM has now been equipped with a fuel injector (gasoline direct injection). The injector enables fuel introduction in accurate quantities, and the injection may be accurately timed with the occurrence of TDC. A schematic of the setup appears in Figure III.5 and highlights the use of a fused silica window that may be installed for imaging of the fuel spray and combustion.

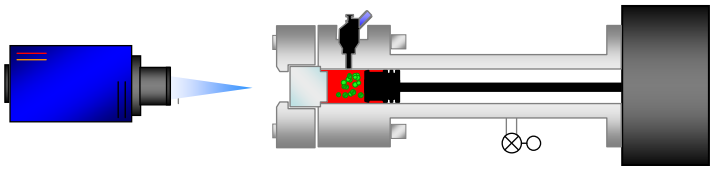

Figure III.5. Schematic of RCM with injector mounted and CCD camera used for imaging the fuel spray.

The fuel injector is operated with 100 bar of fuel line pressure which can lead to spray speeds in excess of 25 m/s. At these speeds, and given the relatively small volume of the RCM combustion chamber (2" diameter, 0.75" clearance), the potential exists for significant fuel impingement on the side of the test chamber. To characterize the degree of impingement, we completed two imaging experiments. First, as an initial test, we imaged the spray of ethanol emerging from the fuel injector. The injection for these tests started at TDC and lasted for 1 ms (9 mg of fuel injected). One image was obtained from each run of the RCM, and with each new run, the image time after the start of injection was incremented by 100 μs. In this manner, we obtained a time progression showing the development of the spray. A sample image from these tests appears in Figure III.6a), where the image was taken 1.5 ms after the start of injection, and the camera exposure lasted 100 μs. In the second experiment, the same approach was used, but ethanol was replaced with canola B100. Figure III.6(b) shows a canola B100 spray image taken at 1.5 ms after the start of injection (100 μs exposure). Both the ethanol and canola B100 were sprayed into an inert nitrogen environment at 710 K and 25 atm. One obvious difference between the ethanol and canola B100 tests is the spray angle. This is simply a result of changing the

injector orientation. Additional tests demonstrated that impingement begins to occur near 2 ms after the start of injection, and when the complete time progression of images is compared, it is seen that a significant portion of the liquid fuel is vaporized prior to reaching the test chamber wall.

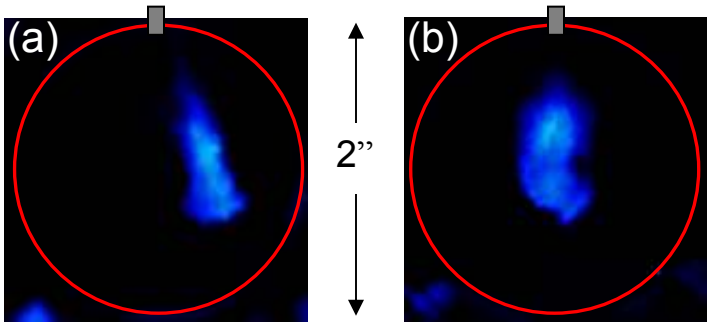

Figure III.6. Fuel spray at 1.5 ms after the start of injection for (a) ethanol and (b) canola B100.

A further RCM improvement for low volatility fuels is to prepare the test mixture directly in the test chamber of the rapid compression machine (RCM). For convenience, this approach is referred to as the direct test chamber (DTC) charge preparation protocol. The advantage of this approach is that initial pressures for testing in the RCM are much lower (e.g. 0.5 – 1 bar) than those of the mixing vessel. This reduces the partial pressure requirement of the fuel, and therefore the initial temperature may be reduced to a region where fuel cracking concerns are minimized. However, the preparation of a test charge directly in the RCM requires the ability to accurately load a very small quantity of fuel (e.g. 5 mg). We have developed an approach which uses a high-resolution, high-accuracy fuel injector to meet this requirement. In the test approach, the oxidizer and diluent gases are added to the test chamber of the RCM which is preheated to an elevated temperature. The chamber is subsequently isolated, and the fuel injector is activated to spray the desired fuel quantity into the test chamber. The fuel is provided sufficient time (~15 min) to evaporate and mix in the chamber before the test is initiated.

Before the fuel injector can be used with a fuel, it must be calibrated. A calibration curve is constructed that describes the injected mass as a function of the pulse width. A sample of this calibration curve appears in Fig. III.7. Several pulse widths are selected as calibration points, and for each point, a series of injections ($\geq$ 100) are collected in a container. The total mass of the injections is determined by weighing the container before and after the test which allows direct calculation of the fuel mass per injection.

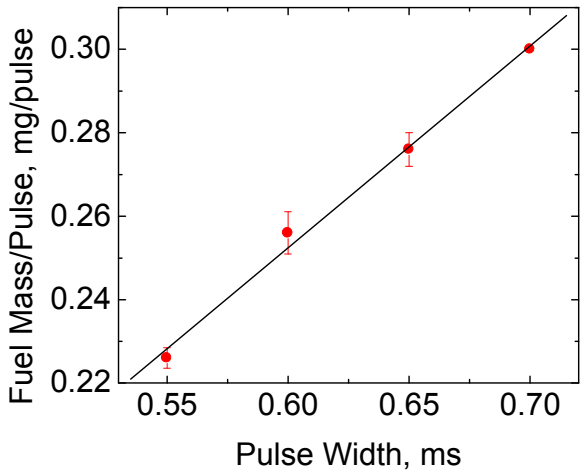

Figure III.7**.** Sample fuel injector calibration data

Care is taken to select calibration points in the linear operating region of the injector so a linear fit can be safely applied to the data. The fit is used to calculate the number and duration of the injections for each test. It should be noted that relatively short pulse widths are selected for the calibration points so that multiple injections are required for each test (typically 5 – 10). This eliminates the effect of any shot-to-shot variation that could influence test results where a single injection is used.

As an initial test of the approach, JP-8 ignition delays were measured in the RCM using the DTC approach. JP-8 is slightly more volatile than biodiesel and serves as a good fuel for a proof-of-concept test of the DTC approach. Figure III.8 illustrates the typical experimental repeatability observed for these tests, where nine raw pressure history curves are shown for three different unique test conditions. It is clear that that the experimental repeatability is good, and that the DTC approach is capable of measuring high-fidelity gas-phase ignition delays of non-volatile fuels. Figure III.9 shows several ignition delay measurements plotted as a function of inverse temperature. These measurements were taken at a compressed pressure of p_c = 7 bar and an oxidizer to fuel mass ratio of *O/F* = 14.4. A clear negative temperature coefficient (NTC) region can be identified in the data where the overall ignition delay ($\tau_1 + \tau_2$) becomes longer with increasing temperature. The ability to distinguish this feature is further evidence that the DTC approach is viable for measuring ignition delays of non-volatile fuels.

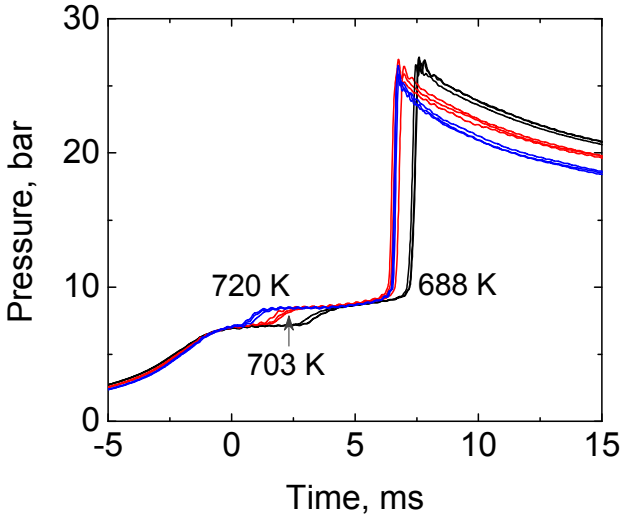

Figure III.8. Pressure history data illustrating experimental repeatability using DTC approach

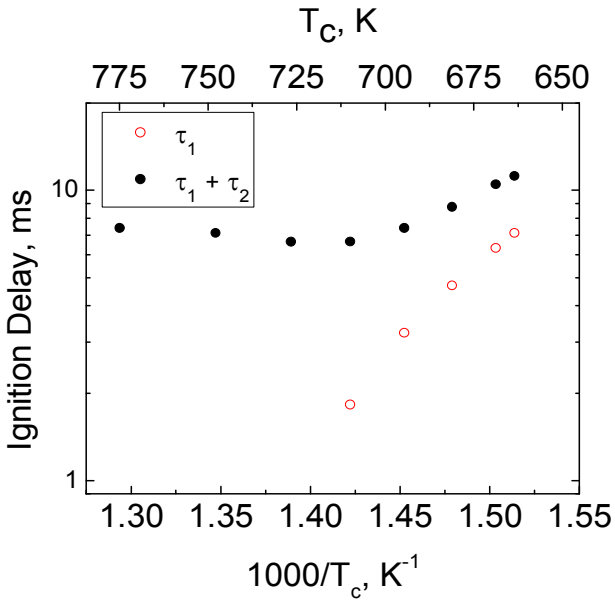

Figure III.9. JP-8 ignition delay measurements (p_c = 7 bar, O/F = 14.4)

III.2 Modeling of kinetics and ignition delay in RCM

III.2.1 Methyl butanoate combustion

A detailed kinetic and multi-step model of the RCM have been generated and applied to oxygenated fuels. The multi-step modeling concept is aimed at capturing the ignition behavior of

new oxygenated fuel blends, for which detailed or reduced chemical kinetics data is not available. The predicted ignition delays from the multi-step auto-ignition model using the biodiesel surrogate fuel methyl butanoate were validated against results attained using a detailed chemical kinetic mechanism in conjunction with CHEMKIN [1]. Once the multi-step model constants were calibrated for methyl butanoate, the model showed good agreement with the detailed mechanism ignition delays, but with significantly reduced computational time. The multi-step model was tested over a compressed temperature range of 750-925 K, compressed pressures from 10-46 atm and equivalence ratios from 0.5 to stoichiometric.

The multi-step kinetics ignition model used for this work is based on the Shell Model of Halstead et al. [2,3], which was originally designed to predict hydrocarbon auto-ignition (knock) in gasoline engines. Since this time, the model has also been shown applicable to diesel and biodiesel ignition in compression ignition engines [4-8]. The model developed by Halstead et al. [3] is shown in Table III.1 and consists of 7 species (5 generic, O_2 and N_2) and eight reactions that are based on the degenerate chain branching characteristic of hydrocarbon auto-ignition. In addition, the model contains 26 constants that are unique to a particular fuel. The model was modified to accommodate oxygenated hydrocarbons such as alcohols and esters. As a first step, the model was applied to the biodiesel surrogate fuel, methyl butanoate since a detailed kinetic mechanism for this fuel is available [1].

The species involved in the multi-step kinetic model for oxygenated hydrocarbons are

RH, the hydrocarbon fuel of composition $C_nH_{2m}O_k$
O_2, oxygen
R*, the radical formed from the fuel
B, the branching agent
Q, the intermediate species
P, the products (CO, CO_2 and H_2O)
N_2, nitrogen

Table III.1. Auto-ignition Reaction Mechanism [3]

	Step	Reaction	Rate Coefficient
1	Initiation	$RH + O_2 \longrightarrow 2R^*$	k_q
2	Propagation	$R^* \longrightarrow R^* + P + Heat$	k_p
3	Propagation	$R^* \longrightarrow R^* + B$	$f_1 k_p$
4	Propagation	$R^* \longrightarrow R^* + Q$	$f_4 k_p$
5	Propagation	$R^* + Q \longrightarrow R^* + B$	$f_2 k_p$
6	Branching	$B \longrightarrow 2R^*$	k_b
7	Termination	$R^* \longrightarrow$ termination	$f_3 k_p$
8	Termination	$2R^* \longrightarrow$ termination	k_t

The intermediate species (Q), formed in Reaction 4, represents oxygenated compounds such as aldehydes (RCHO) during the first induction period and the alkylperoxy radical (HO_2) and its isomerization products during the second induction period [5]. These intermediate species are capable of enhancing the rate of formation of the degenerate branching intermediate (B) in

Reaction 5 [9]. The branching intermediate is related to hydroperoxide (RO_2H) at low temperature and hydrogen peroxide (H_2O_2) at high temperature [10].

Over thirty CHEMKIN simulations of methyl butanoate RCM ignition were completed in order to attain sufficient data with which to calibrate the multi-step model. The pressure, temperature and equivalence ratio of the simulations were chosen to be similar to those tested by Dooley et al. [1], in order to ensure that the model could correctly predict the ignition delay and in all cases, results were comparable. The conditions tested with the CHEMKIN model are shown in Table III.2.

Table III.2. Mixture Composition, Temperature and Pressure of CHEMKIN Simulations

Mix	Φ	MB (mole fraction)	O_2 (mole fraction)	N_2 (mole fraction)	T_c (K)	P_c (atm)
1	1	0.0313	0.2034	0.7653	738-940	23
2	0.5	0.0159	0.2067	0.7774	760-950	5.75, 11.5, 23, 46

Methyl butanoate multi-step model pressure trace results together with those attained using CHEMKIN with the detailed methyl butanoate mechanism at Φ =1 and a compressed pressure of 23 atm are shown in Figure III.10. The multi-step results show good agreement with those achieved with CHEMKIN, with the computational time reduced by more than two orders of magnitude.

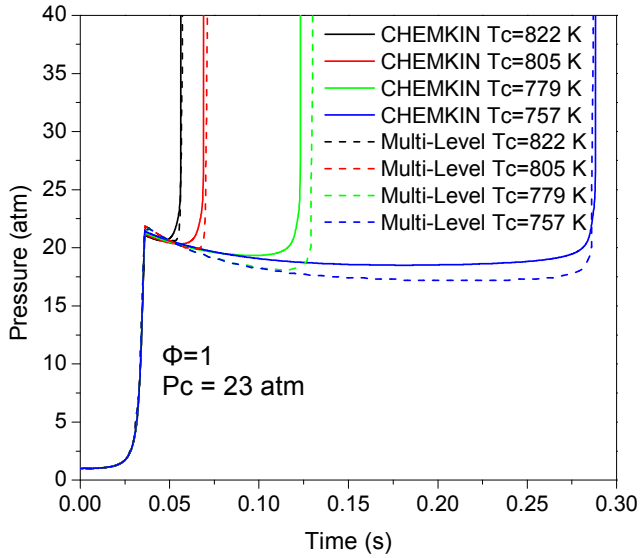

Figure III.10. Pressure traces of the multi-step and CHEMKIN modeling runs at different compressed temperatures (Φ = 1 and Pc = 23 atm).

A comparison between the ignition delay achieved with the multi-step model and that using CHEMKIN is shown in Figure III.11. In Figure III.11 (upper) the effect of increasing

compressed pressure on ignition delay is visible at a constant equivalence ratio of 0.5. It can be seen that the multi-step model correctly simulates the increase in ignition delay that occurs with increasing compressed pressure for an equivalent compressed temperature. Figure III.11 (lower) shows the effect of different equivalence ratios on ignition delay at a compressed pressure of 23 atm. In this case, it is observable that the multi-step model adequately predicts the increased ignition delay that arises as the equivalence ratio changes from 0.5 to stoichiometric for a given compressed temperature. In all cases shown in Figure III.11, the ignition delay decreases with increasing compressed temperature.

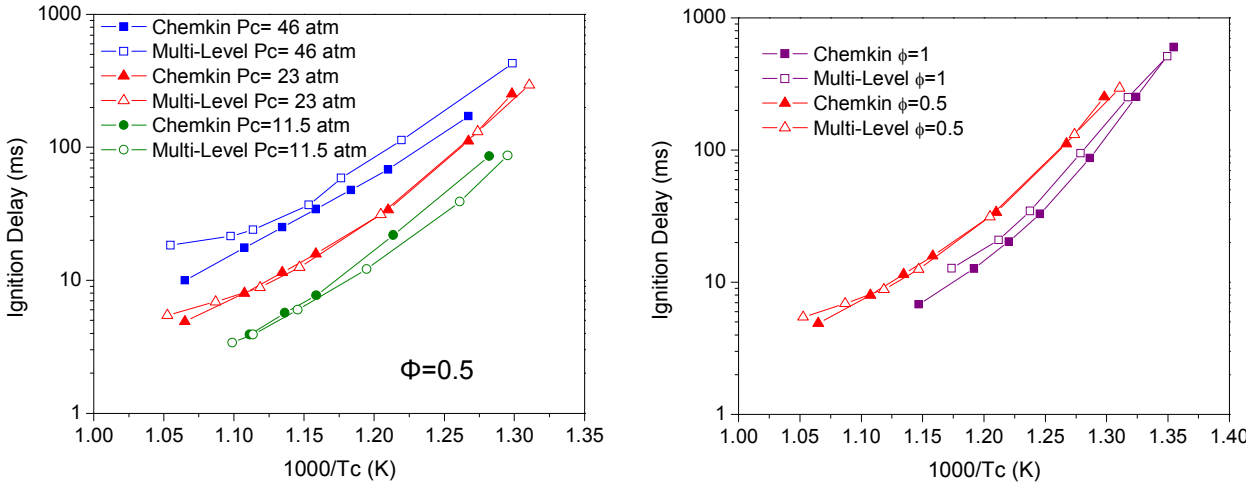

Figure III.11. Methyl butanoate auto-ignition delay times with CHEMKIN (solid) and the multi-step model (hollow) at $\Phi = 0.5$ (upper) and $P_c = 23$ atm (lower)

The results of using the adapted multi-step model with the 26 model constants fitted specifically for methyl butanoate compared well with the CHEMKIN modeling using the detailed kinetic model. Over the range of conditions tested, the percent relative error in the ignition delay between the multi-step and CHEMKIN modeling was less than 15 %. Discrepancies between the multi-step modeling and CHEMKIN results were largest at the highest and lowest compressed temperatures. It is anticipated the error could be further reduced by optimizing the model constants using an optimization code, with such a process currently in the development stage. Optimization will be critical, when determining constants for biofuels, the majority of which are two-stage ignition fuels. The availability of multi-step model constants for a range of oxygenated fuels based on experimental rapid compression machine results will be a valuable tool in dramatically reducing the computational time of auto-ignition modeling, especially in CFD applications.

References

1. Dooley, S., H.J. Curran, and J.M. Simmie, *Autoignition measurements and a validated kinetic model for the biodiesel surrogate, methyl butanoate.* Combustion and Flame, 2008. 153(1-2): p. 2-32.
2. Halstead, M.P., L.J. Kirsch, A. Prothero, and C.P. Quinn, *A Mathematical Model for Hydrocarbon Autoignition at High Pressures.* Proc. R. Soc. Lond. A, 1975. 346: p. 515-538.

3. Halstead, M.P., L.J. Kirsch, and C.P. Quinn, *The autoignition of hydrocarbon fuels at high temperatures and pressures--Fitting of a mathematical model.* Combustion and Flame, 1977. 30: p. 45-60.
4. Yuan, W., A.C. Hansen, and Q. Zhang. *Computational Study of Biodiesel Ignition in a Direct Injection Engine*. in *ASAE Annual International Meeting*. 2003. Las Vegas, Nevada, USA.
5. Kong, S.-C., Z. Han, and R.D. Reitz, *The Development and Application of a Diesel Ignition and Combustion Model for Multidimenstional Engine Simulation.* SAE Paper 950278, 1995.
6. Kong, S.-C. and R.D. Reitz, *Multidimensional Modeling of Diesel and Combustion Using a Multi-step Kinetic Model.* Journal of Engineering for Gas Turbines and Power, 1993. 115: p. 781-789.
7. Yuan, W., A.C. Hansen, M.E. Tat, J.H. Van Gerpen, and Z. Tan, *Spray, Ignition and COmbustion Modeling of Biodiesel Fuels for Investigating NOx Emissions.* Tranactions of the ASAE, 2005. 48(3): p. 933-939.
8. Sazhina, E.M., S.S. Sazhin, M.R. Heikal, and C.J. Marooney, *The Shell autoignition model: applications to gasoline and diesel fuels.* Fuel, 1999. 78(4): p. 389-401.
9. Griffiths, *Reduced Kinetic Models and their Application to Practical Combustion Systems.* Prog. Energy Combust. Sci., 1995. 21: p. 25-107.
10. Benson, S.W., *The Kinetics and Thermochemistry of Chemical Oxidation with Application to Combustion and Flames.* Prog. Energy Combust. Sci., 1981. 7: p. 125.

III.2.2 Dimethyl ether (DME) combustion

We have coupled the multi-step model with a genetic algorithm optimization routine for the prediction of two-stage auto-ignition of oxygenated fuels in the rapid compression machine (RCM). The main application of the model is for predicting auto-ignition of new and future oxygenated fuel blends where detailed or reduced chemical kinetics models are not available.

Experimental data for the ignition of DME/O_2/N_2 mixtures at more than 60 different conditions were used by the optimizer to determine the 26 kinetic parameters of the multi-step model that are unique to each individual fuel or fuel blend. The optimization was performed for conditions with compressed pressures in the range of 10-20 bar, compressed temperatures from 615-735 K and at equivalence ratios of 0.43, 0.75 and 1.5, summarized in Table III.3.

Table III.3. Molar composition, equivalence ratio, temperature and pressure of simulated mixtures

□□	DME (molar composition)	O_2 (molar composition)	N_2 (molar composition)	Compressed Temperature (K)	Compressed Pressure (bar)
0.43	1	7	27	615-723	10, 15
0.75	1	4	30	617-736	10, 15, 20
1.5	1	2	32	618-728	10, 15

Figure III.12 shows a comparison of experimental,[1] multi-step modeling and detailed kinetic modeling (model 1[2], model 2[3, 4]) pressure traces for the ignition of a DME/O_2/N_2 mixture at an equivalence ratio of 0.75 and a compressed pressure of ~15 bar. For this research, ignition delay is defined as the time elapsed from the end of the compression stroke (t = 0) to the time where the maximum pressure rise rate occurs. Using this definition the first and overall ignition delay for the CHEMKIN detailed model 2 pressure trace are shown in Figure III.12.

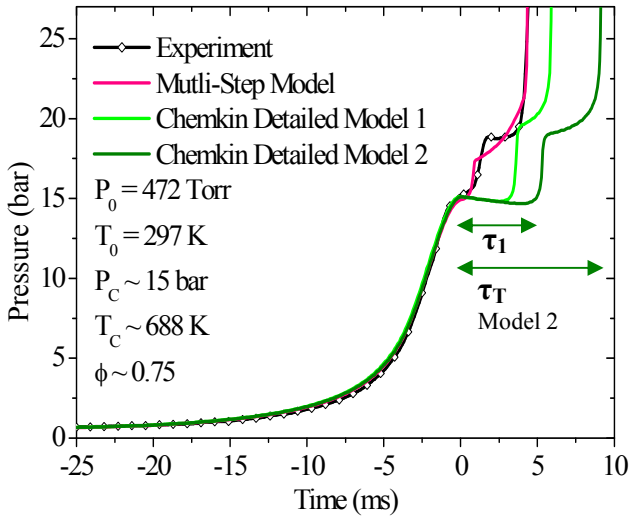

Figure III.12. Multi-step model, CHEMKIN detailed model 1[2], model 2[3, 4] and measured[1] pressure traces together with definitions of the first-stage and overall ignition delays shown for the CHEMKIN detailed model 2 case.

Figure III.13 shows a comparison between the first-stage (upper) and overall ignition delay (lower) results attained with the multi-level modeling (open-symbols) and experimental results of Mittal et al.[1] (filled-symbols) at varying equivalence ratio and compressed pressure as a function of compressed temperature. The first and overall ignition delay characteristics predicted by the multi-step model with the 26 optimized dimethyl ether model constants show good agreement with the experimental data for the majority of conditions tested. The overall percent relative error between the multi-step modeling and experimental results for both the first-stage and overall ignition delay was

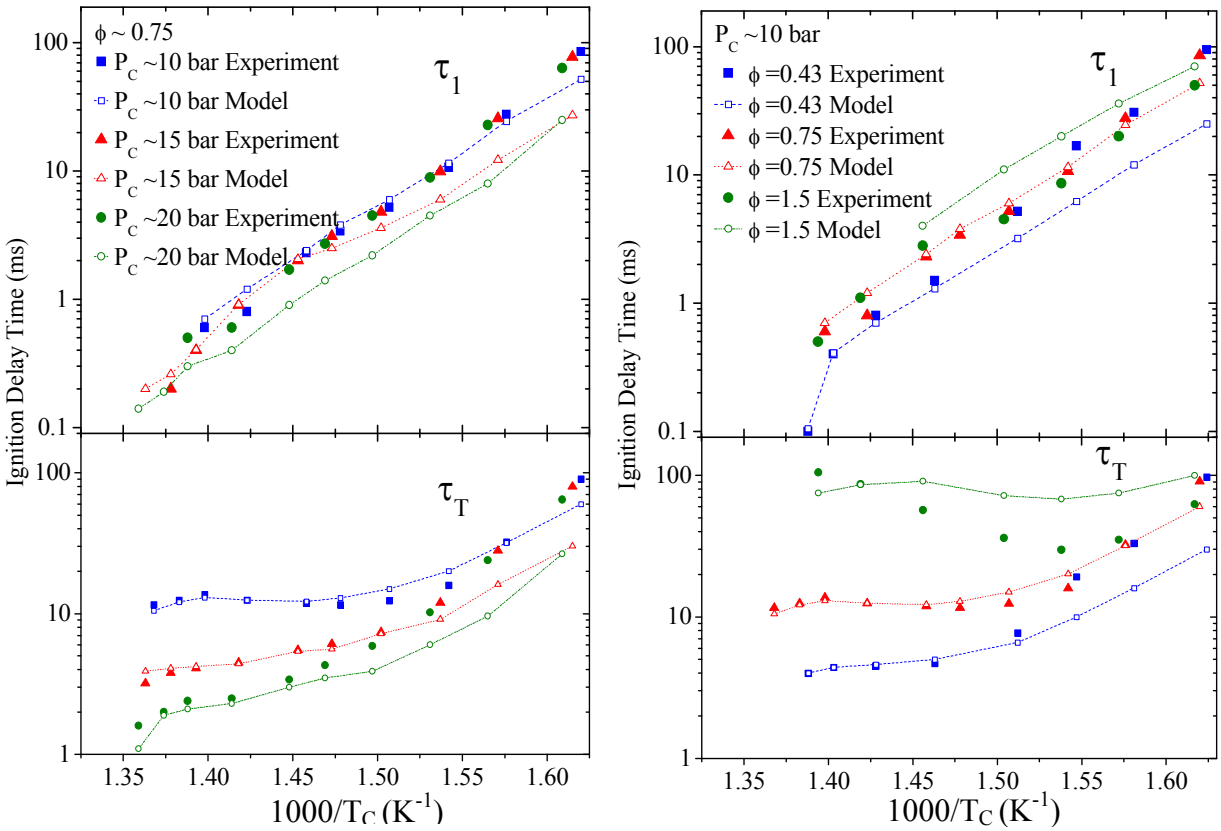

Figure III.13. Multi-level model and experimental[1] first-stage (upper) and overall (lower) ignition delays at an equivalence ratio of 0.75 and varying compressed pressure (Left) and at 10 bar compressed pressure and varying equivalence ratio (Right).

less than 30%. It is anticipated that the optimization procedure could enable the determination of multi-step modeling constants for biofuels and their blends through the use of rapid compression machine experimental data. The main benefit of this type of modeling is to capture the ignition behavior of novel blends of oxygenated compounds, for which no detailed kinetics data are available. The availability of multi-step model constants for a range of oxygenated fuels and blends will be a valuable tool in dramatically reducing the computational time of auto-ignition modeling, especially in CFD applications.

References

1. Mittal, G., et al., *Dimethyl ether autoignition in a rapid compression machine: Experiments and chemical kinetic modeling.* Fuel Processing Technology Dimethyl Ether Special Section, 2008. **89**(12): p. 1244-1254.
2. Zhao, Z., et al., *Thermal decomposition reaction and a comprehensive kinetic model of dimethyl ether.* International Journal of Chemical Kinetics, 2008. **40**(1): p. 1-18.
3. Curran, H.J., S.L. Fischer, and F.L. Dryer, *The reaction kinetics of dimethyl ether. II: Low-temperature oxidation in flow reactors.* International Journal of Chemical Kinetics, 2000. **32**(12): p. 741-759.

4. Fischer, S.L., F.L. Dryer, and H.J. Curran, *The reaction kinetics of dimethyl ether. I: High-temperature pyrolysis and oxidation in flow reactors.* International Journal of Chemical Kinetics, 2000. **32**(12): p. 713-740.

III.2.3 Combustion of methyl butanoate – n-heptane blends

A detailed n-hetpane and methyl butanoate mechanism was generated by combining the detailed n-heptane mechanism (ver. 3) developed at Lawrence Livermore National Laboratory[3] (3827 reactions, 654 species) and the methyl butanoate mechanism published in 2008 by Dooley et al.[4] (1545 reactions, 275 species). Following this, all of the duplicate reactions originating from the methyl butanoate mechanism were removed leaving the blended mechanism with 3073 reactions and 678 species.

The multi-level model constants for the neat methyl butanoate and n-heptane were used to determine those of the fuel blends. The methyl butanoate model constants have previously been published [5], and the n-heptane model constants were determined using the optimization procedure outlined in[6]. As some of the constants are very large in magnitude and others small, the weighted geometric mean was used to calculate the constants for the blends as the arithmetic mean is biased towards the larger constant. The weighted geometric mean is calculated as:

$$\bar{x} = \exp\left(\frac{\sum_{i=1}^{n} w_i \ln x_i}{\sum_{i=1}^{n} w_i}\right)$$

where x_i is the multi-level constant and w_i is the corresponding weight of the constant in terms of mole fraction of that component in the mixture. Using this approach, the multi-level constants for methyl butanoate, n-heptane and several blends are shown in Table III.4.

Figures III.14 and III.15 show a comparison of the ignition delay results attained with the multi-level model (hollow symbols) and the detailed CHEMKIN model (filled symbols) with varying compressed temperature, at a compressed pressure of approximately 22 atm, and equivalence ratios of 1 and 0.5 respectively. The ignition delays predicted by both the detailed CHEMKIN model and Multi-Level model follow similar trends and it can be clearly seen with both models that the ignition delay decreases with increasing concentrations of n-heptane in the mixture.

Table III.4. Multi-step model constants for methyl butanoate [5], n-Heptane (optimized using the technique described in [6]) and for mixtures using the weighted geometric mean method.

Parameter	**Methyl Butanoate (MB)**	**n-Heptane**	**2-n-Heptane: 1-MB**	**1-n-Heptane: 1-MB**	**1-n-Heptane: 2-MB**
$\mathbf{A_{p1}}$	1.0×10^{12}	1.0×10^{12}	1.0×10^{12}	1.0×10^{12}	1.0×10^{12}
$\mathbf{E_{p1}}$	0	0	0	0	0

A_{p2}	1.0×10^{11}	1.0×10^{11}	1.0×10^{11}	1.0×10^{11}	1.0×10^{11}
E_{p2}	1.5×10^{4}	1.5×10^{4}	1.5×10^{4}	1.5×10^{4}	1.5×10^{4}
A_{p3}	1.0×10^{13}	1.0×10^{13}	1.0×10^{13}	1.0×10^{13}	1.0×10^{13}
E_{p3}	8.5×10^{2}	8.5×10^{2}	8.5×10^{2}	8.5×10^{2}	8.5×10^{2}
A_q	1.5×10^{10}	3.52×10^{13}	2.65×10^{12}	7.27×10^{11}	1.99×10^{11}
E_q	5.0×10^{4}	3.74×10^{4}	4.12×10^{4}	4.32×10^{4}	4.54×10^{4}
A_b	6.51×10^{15}	2.0×10^{19}	1.38×10^{18}	3.61×10^{17}	9.47×10^{16}
E_b	6.0×10^{4}	5.7×10^{4}	5.80×10^{4}	5.85×10^{4}	5.90×10^{4}
A_t	3.0×10^{5}	3.2×10^{12}	1.45×10^{10}	9.8×10^{8}	6.6×10^{7}
E_t	0	0	0	0	0
A_{f1}	9.3	1.6×10^{-5}	1.3×10^{-3}	1.2×10^{-2}	1.1×10^{-1}
E_{f1}	-1.5×10^{4}	-1.5×10^{4}	-1.5×10^{4}	-1.5×10^{4}	-1.5×10^{4}
A_{f2}	1.8×10^{2}	1.8×10^{2}	1.8×10^{2}	1.8×10^{2}	1.8×10^{2}
E_{f2}	-7.0×10^{3}	-7.0×10^{3}	-7.0×10^{3}	-7.0×10^{3}	-7.0×10^{3}
A_{f3}	1.205	2.89	2.16	1.87	1.61
E_{f3}	1.5×10^{4}	1.0×10^{4}	1.14×10^{4}	1.22×10^{4}	1.31×10^{4}
A_{f4}	1.88×10^{4}	8.0×10^{5}	2.29×10^{5}	1.23×10^{5}	6.56×10^{4}
E_{f4}	4.0×10^{4}	3.0×10^{4}	3.30×10^{4}	3.46×10^{4}	3.63×10^{4}
x_1	1.5	1.0	1.14	1.22	1.31
y_1	0	-0.5	-0.33	-0.25	-0.17
x_3	0	0	0	0	0
y_3	0	0	0	0	0
x_4	-0.3	1.3	-0.80	-0.62	-0.49
y_4	0.35	1.0	0.70	0.59	0.50
A_i (cm,mol,s units), E_i (cal/mole), R=1.9872cal/mole K					

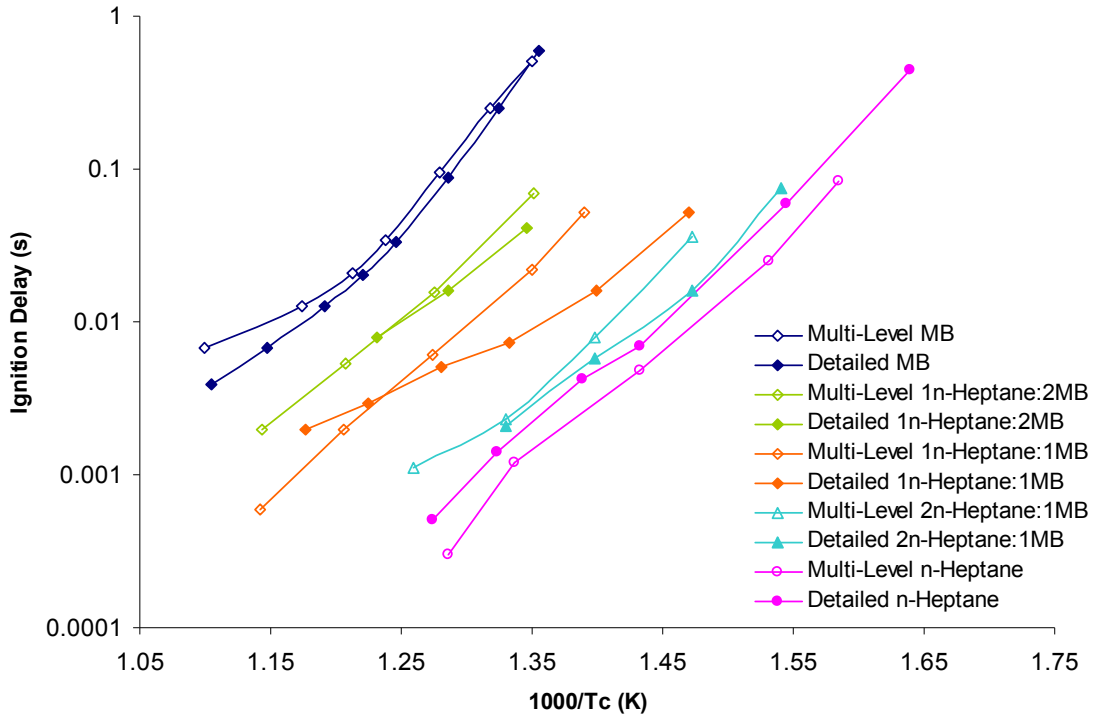

Figure III.14. n-Heptane – methyl butanoate mixture autoignition delay times with the CHEMKIN detailed model (solid) and the multi-level model (hollow) at a compressed pressure of 22 atm, φ= 1 and varying compressed temperature.

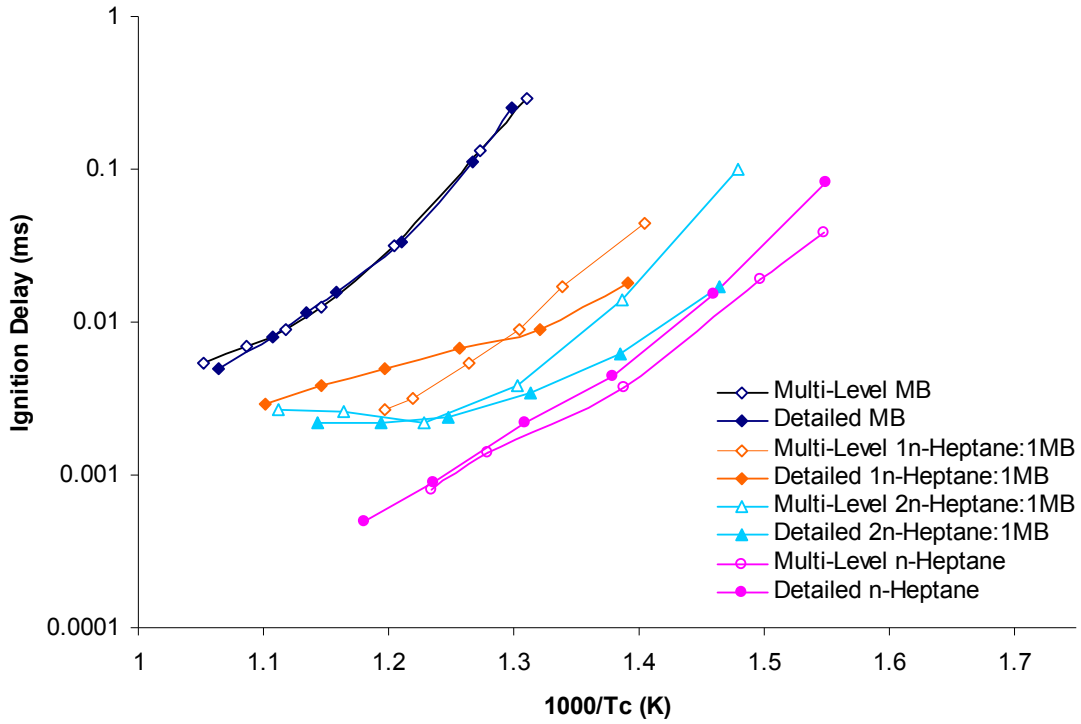

Figure III.15. n-Heptane – methyl butanoate mixture autoignition delay times with the CHEMKIN detailed model (solid) and the multi-level model (hollow) at a compressed pressure of 22 atm, φ= 0.5 and varying compressed temperature.

References

1. S. Um and S. W. Park, "Modeling effect of the biodiesel mixing ratio on combustion and emission characteristics using a reduced mechanism of methyl butanoate", Fuel. In Press, Corrected Proof.
2. J. L. Brakora, Y. Ra, R. D. Reitz, J. McFarlane and C. S. Daw, "Development and Validation of a Reduced Reaction Mechanism for Biodiesel-Fueled Engine Simulations", SAE 2008-01-1378, **2008**.
3. M. Mehl, W. J. Pitz, M. Sjoberg and J. E. Dec, "Detailed kinetic modeling of low-temperature heat release for PRF fuels in an HCCI engine", SAE 2009-01-1806, **2009**.
4. S. Dooley, H. J. Curran and J. M. Simmie, "Autoignition measurements and a validated kinetic model for the biodiesel surrogate, methyl butanoate", Combustion and Flame, **2008**. 153(1-2), 2-32.
5. E. Toulson, C. M. Allen, D. J. Miller and T. Lee, "Modeling the Auto-Ignition of Oxygenated Fuels using a Multistep Model", Energy & Fuels, **2009**. 24(2), 888-896.
6. E. Toulson, C. M. Allen, D. J. Miller, H. J. Schock and T. Lee, "Optimization of a Multi-step Model for the Auto-ignition of Dimethyl Ether in a Rapid Compression Machine", Energy & Fuels, **2010**. 24(6), 3510-3516.

III.3 LES Simulations of Spray and Combustion in RCM

III.3.1 Description of simulations and initial results with ethanol fuel

We present the development and application of turbulence, spray and combustion models for large-eddy simulation (LES) of the MSU rapid compression machine. The simulations are conducted with the two-phase LES/FMDF methodology and high-order numerical schemes which can handle complex geometries, moving valves, moving piston, spray and various types of flames (premixed, non-premixed, partially-premixed, slow, fast,……..).

Flow inside the Rapid Compression Machine: Extensive large-eddy simulations of flows in the MSU's rapid compression machine (RCM) were conducted. The stroke and bore of this RCM is 25.4 and 5 cm, respectively. The operational compression ratio is 17.147. In order to have a uniform temperature distribution in the cylinder, a creviced piston head is included. For numerical computation, the RCM is modeled with a 4-block grid system; the 3D and 2D views of the grid is shown in Fig. III.16.

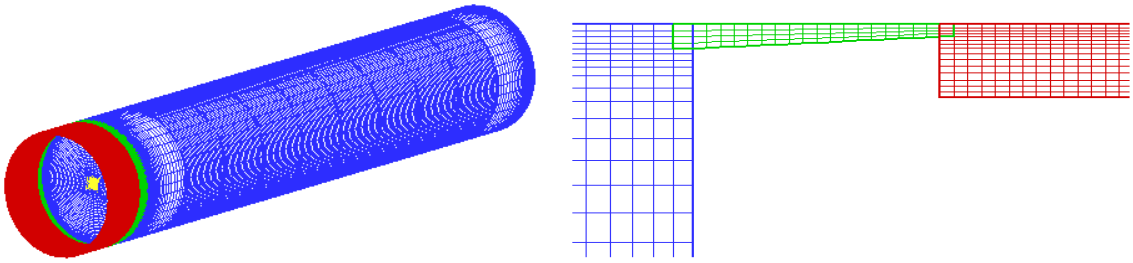

Fig. III.16. 3D and 2D views of the 4-block computational grid used for LES of RCM.

During the compression, we keep the same number of grids, but compress them as the piston moves. Compression time is about 30 milliseconds. Here, it is assumed the time = -30ms to be the beginning of compression and time = 0 is the termination of compression. At the beginning of compression, it is assumed that the in-cylinder mixture is either a homogeneous charge of evaporated ethanol with equivalence ratio of 1.237 or pure nitrogen at specific initial temperature and pressure condition. The walls are assumed to be isothermic equal to initial temperature. Here, we are interested in fluid dynamics and (single-phase) combustion in RCM. One important goal in RCMs is having uniform temperature distribution at the end of compression. In order to study the effect of piston shape on the temperature field inside the cylinder two types of piston were considered: I) flat piston, II) creviced piston.

I) Flat piston - In this simulation, the grids which cover the creviced section of piston (green and red blocks in Fig. III.16 are excluded from the computation. The working fluid is pure Nitrogen with initial temperature and pressure of 297 K and 0.93 bar, respectively. With the acceleration of piston, the boundary layer grows on the walls of cylinder. Radial component of the fluid flow velocity in the boundary layer at the corner of piston head and cylinder wall transfer colder fluid in the vicinity of the piston head into the cylinder and generates a circulation in the temperature field. By further movement of piston, this circulation is moved towards the

cylinder center axis. Temperature contour plots, 15 milliseconds before the termination of compression are shown in Fig. III.17. In this figure, the temperature circulations are moving towards the center of the cylinder.

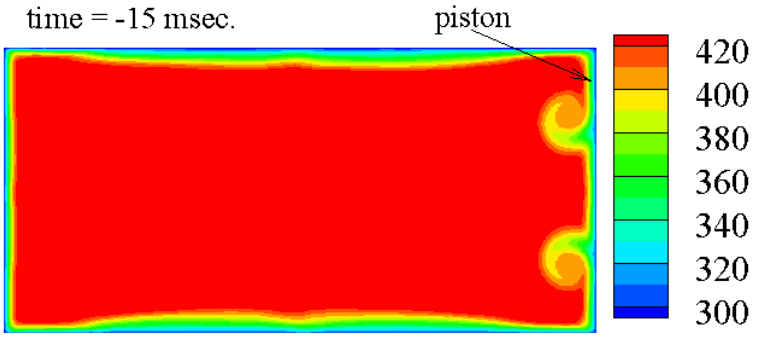

Fig. III.17. Temperature contour plots, 15 milliseconds before termination of compression for the flat piston case.

As piston moves further, the generated circulated flow/temperature moves close to the cylinder axis and stay over there until the compression termination. Fig. III.18(a) shows the temperature field 5 milliseconds before the termination of compression. At the end of compression the circulating flow makes the core of cylinder a colder zone, while a warmer region between cold cylinder region and cold flow near the cylinder wall remains. This phenomenon is shown in Fig. III.18(b). Dissipation of warm region after termination of compression is shown in Fig. III.18(c). It can be concluded that the flow in the cylinder is not uniformly distributed for the case with flat piston.

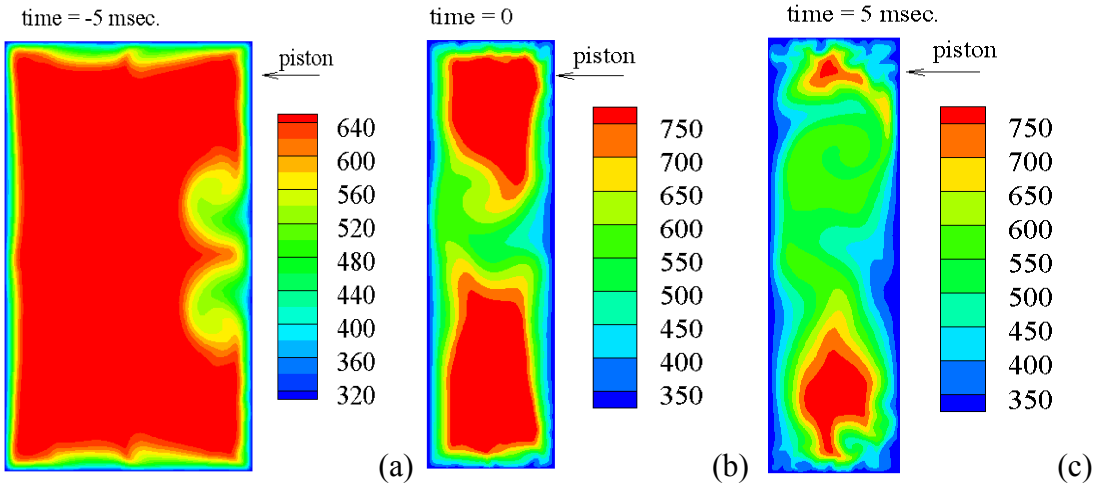

Fig. III.18. Temperature contour plots, (a) 5 milliseconds before termination of compression, (b) at the end of compression and (c) 5 milliseconds after termination of compression for the flat piston.

II) Creviced piston - In this simulation, all grids in Fig. III.16 are included in the computation. The working fluid, similar to previous one, is pure nitrogen with initial temperature and pressure of 297 K and 0.93 bar, respectively. Acceleration of piston makes the in-cylinder

flow moves from piston head toward the cylinder head and also in-cylinder flow in the corner of piston and cylinder wall moves into the nozzle-shape crevice. This affects the generation and growth of boundary layer on the wall of cylinder. Radial component of the fluid flow velocity in the boundary layer at the corner of piston head and cylinder wall is not as large as that in the case with flat piston. Weaker radial velocity generates weaker temperature circulation and cannot move the circulation to the cylinder axis. Figure III.19 shows the temperature contour plots 15 milliseconds before termination of compression. In comparison with temperature contours for the case with flat piston (Fig. III.17) the size of circulation zone is much smaller and the location is farther away from the cylinder axis.

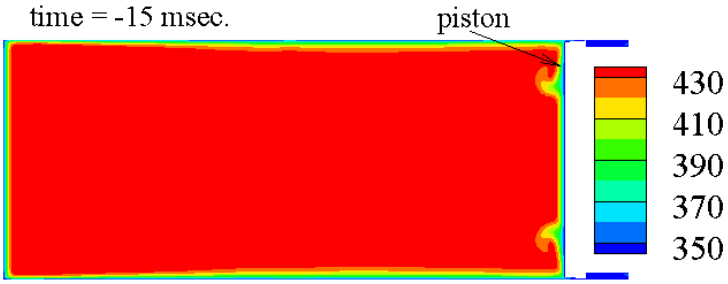

Fig. III.19 Temperature contour plots, 15 milliseconds before termination of compression for the creviced piston.

In Fig. III.20(a) and (b), temperature contours 5 milliseconds before termination of the compression and at the end of compression are shown. Again in comparison with the temperature contours for the case with flat piston (Fig III.18 (a) and (b)) the circulation zone is small and never gets closer to the cylinder center line. This makes the in-cylinder flow temperature to be more uniform than that observed for the flat piston. Temperature distribution 5 milliseconds after compression are shown in Fig. III.20(c). Again temperature distribution and diffusion occur more uniformly than those observed for the flat piston. Based on these results, one may conclude that with the creviced piston, more uniform temperature distribution in the cylinder may be achieved.

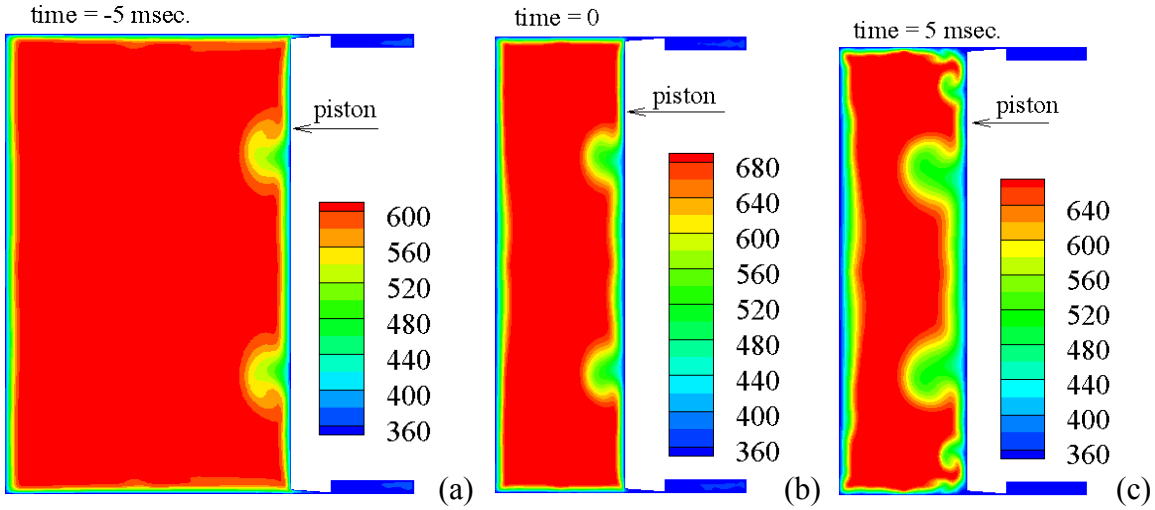

Fig. III.20 Temperature contour plots, (a) 5 milliseconds before termination of compression, (b) at the end of compression and (c) 5 milliseconds after termination of compression with creviced piston.

Combustion inside Rapid Compression Machine: Reactive flow simulations based on experiment conducted at MSU are also considered. In these simulations, it is assumed that the initial fluid is a uniform mixture of ethanol and air with equivalence ratio of 1.237 and initial temperature and pressure of 343 K and 0.6 bar, respectively. The fluid flow simulation is similar to that for nonreactive flow with creviced piston. For simplicity and affordability, a one step global mechanism of ethanol was considered at this moment. However, more complex kinetics models may be used and will be considered in future studies. Temperature, fuel mass fraction and CO_2 mass fraction contours plots during the ignition of ethanol are shown in Fig. III.21(a), (b) and (c), respectively. It is observed that the reaction is nonuniform and starts in the warmer zones in the cylinder. The induced flow by the cylinder wall is cold and has higher fuel and lower CO_2 mass fraction. This is consistent with the experimental observation.

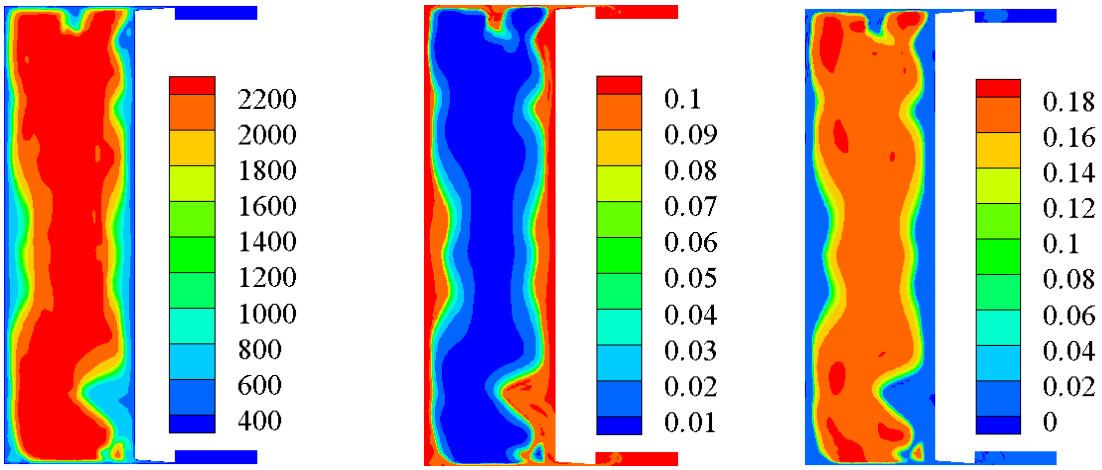

Fig. III.21 (a) Temperature, (b) fuel mass fraction and (c) CO2 mass fraction contours plots during the ignition of ethanol for the creviced piston.

Figure III.22 shows the predicted volume-averaged pressure during the compression and combustion are compared with the MSU's experimental data. Predicted pressure is in good agreement with the experimental data. Some deviations of numerical results from the experimental data are observed which can be attributed to inaccurate initial condition, heat transfer and chemistry model. These are being carefully examined at this moment.

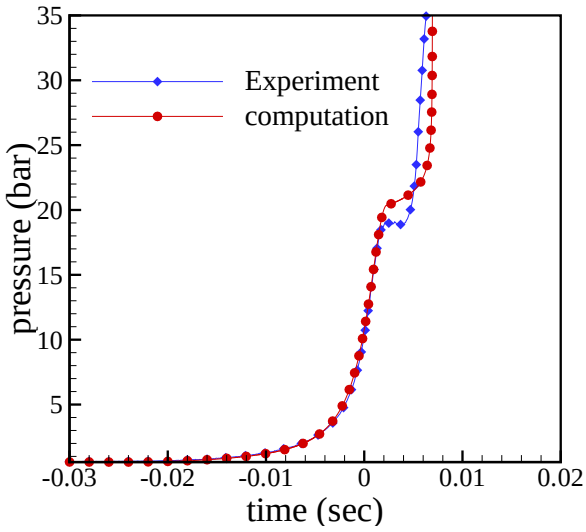

Fig. III.22. Predicted Volume averaged pressure during compression and combustion as compared with the experimental data.

III.3.2 Simulation of spray combustion inside RCM

We have simulated reacting and non-reacting flows with spray inside the RCM with the LES/FMDF for four different spray conditions. The injection of fuel at the end of compression stroke in the MSU's RCM is performed at different compression ratios. For the compression ratio of 17.147, the injector is located halfway between the piston and the cylinder head. In this simulation, it is assumed that the initial fluid is nitrogen or air with a uniform initial temperature and pressure of 423 K and 1.38 bar, respectively. Using these initial conditions and the creviced piston, the final temperature and density in central region of the cylinder reaches to $950 \pm 30K$ and $13.8 \pm 1.0 Kg/m^3$. There are some differences in the thermodynamic conditions in comparison to the experiment. In the experiments, the stagnant temperature and density are 1000 K and 14.8 Kg/m^3. Figure III.23 shows the two-dimensional (2D) contour of the gas temperature before the injection in two center line plates. The gas temperature in the central region of the cylinder is almost uniform. Four experimental flow conditions, (referred to as cases 1-4 in Table III.5), are simulated. The first three cases are all non-reacting. Figure III.24 shows the 3D iso-levels and 2D contours of the temperature inside the RCM together with the injected fuel droplets for Case 1. In the Sandia experiment, injection continues for about 2 msec. We use similar injection features in the RCM simulation.

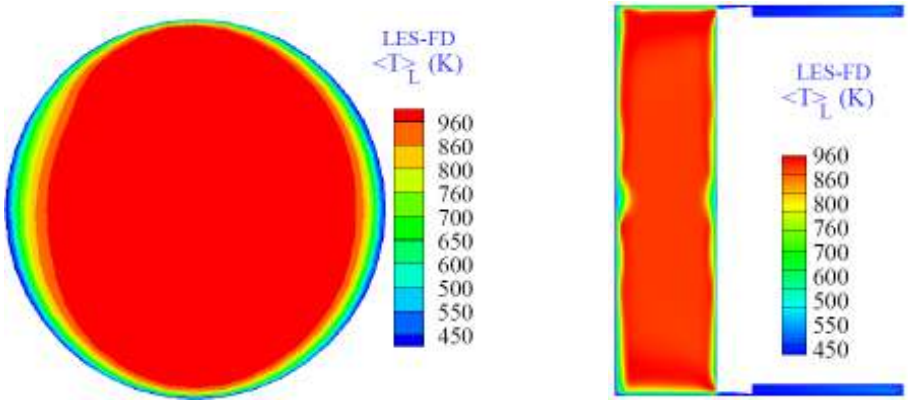

Figure III.23. Two-dimensional contours plots of temperature in two planes parallel and perpendicular to the piston at the end of compression and before the fuel injection.

Table III.5. Four spray experimental conditions used in the RCM. For all cases, gas phase temperature and density are 1000 K and 14.8 Kg/m3, respectively.

Case #	Nozzle Dia. μm	Inj. Press. MPa	Fuel Type	Fuel Temp. K	O_2 %	penetration Exp. LES	lift-off Exp. LES
1	246	138	n-Hexadecane	436	0	31.6 31.3	-
2	100	138	n-Hexadecane	436	0	13.4 14.4	-
3	100	150	n-Heptane	373	0	9.2 9.3	-
4	100	150	n-Heptane	373	21	-	12.2 17.0

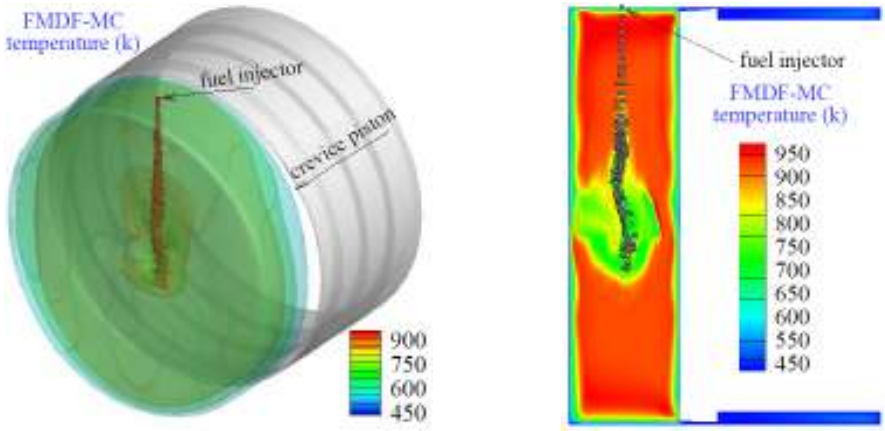

Figure III.24. Iso-levels and contours of temperature with fuel droplets during the injection for Case 1 described in Table III.5.

The 2D contours of the evaporated fuel mass fraction and temperature as predicted by the LES-FD and FMDF-MC for the Cases 1, 2, 3 and 4 are shown in Figure III.25 (a), (b), (c) and (d), respectively. The liquid droplets with the values of penetration and flame lift-off are also shown in comparison with the experiment. In Cases 1 and 2, two different injector diameters of 246 and 100 μm are used with other injection and thermodynamic conditions identical. Similar to the Sandia's experiment in stagnant environment, the liquid penetration decreases as the

injector diameter decreases. The predicted liquid penetrations for Cases 1 and 2 are 30.3 and 13.1 mm, which are close to the experimental values (31.6 and 13.4). In Case 3, n-heptane is injected in the cylinder with different injection pressures and fuel temperatures. The shorter penetration length, compared to Case 2, is predicted well with the LES/FMDF. For the Cases 1, 2 and 3, the LES-FD and FMDF-MC results for the deficit in the gas temperature and the evaporated fuel mass fraction are also shown to be consistent (Figures III.25 (a), (b) and (c)). The reacting spray is simulated with conditions used in Case 3 with 21 % oxygen. The 2D contours of LES-FD and FMDF-MC temperatures and the fuel mass fraction plus spray droplets are shown in Figure III.25 (d). The calculated flame lift-off is about 12.2 mm, which is lower than the experimental value of 17 mm. The underprediction can be due to simple chemical kinetics model or some differences in the initial conditions. However, the predicted LES-FD and FMDF-MC flame temperatures and fuel mass fractions remain consistent.

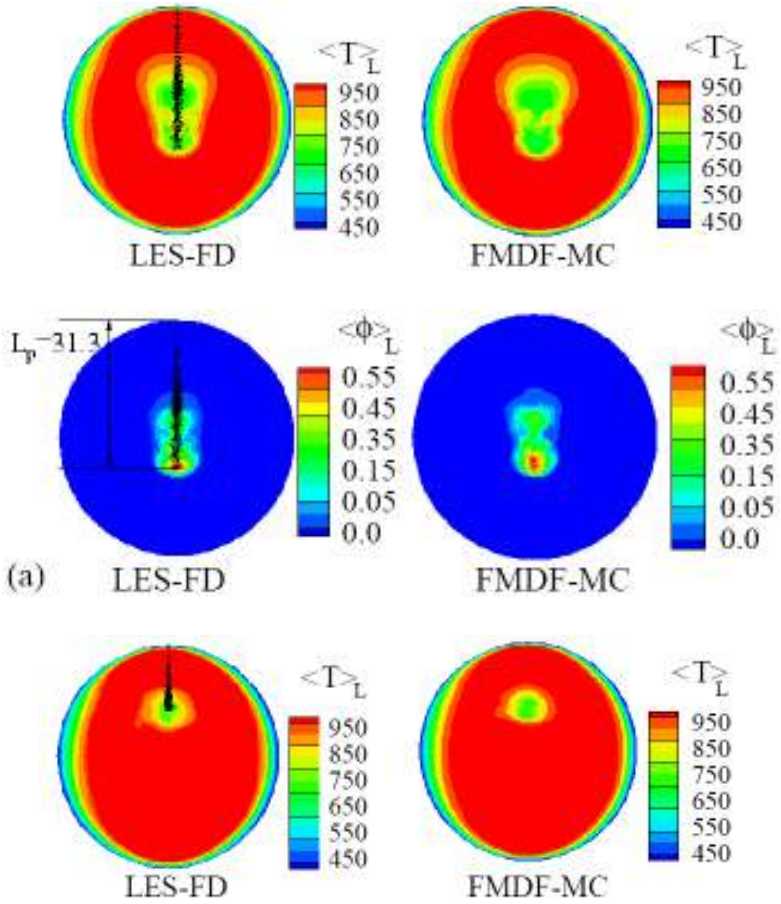

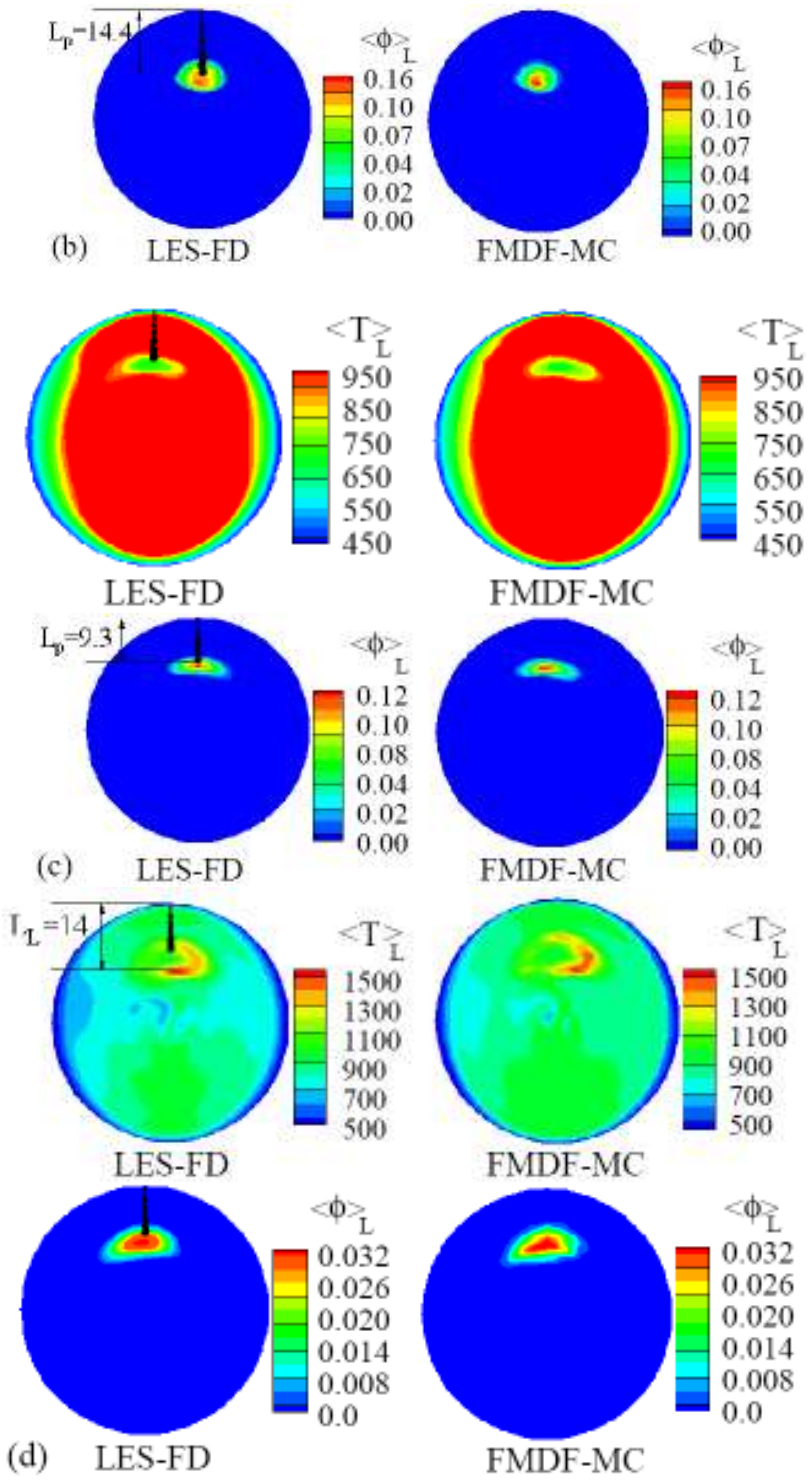

Figure III.25. Evaporated fuel mass fraction and temperature contours as predicted by the LES-FD and FMDF-MC for (a) Case 1, (b) Case 2, (c) Case 3 and (d) Case 4 described in Table 2. Predicted liquid penetration and flame lift-off are also indicated.

III.4 Experimental Studies of Biofuel Combustion in RCM

III.4.1 Ignition delays of biodiesel and petroleum diesel

Use of the fuel injector is a practical approach for testing non-volatile fuels such as fatty acid methyl esters (FAMEs) and diesel. Ignition delay measurements are taken in the RCM by injecting a small quantity of fuel at or after top dead center, and measuring the period of time for ignition to occur, which we identify by the maximum rate of pressure rise due to combustion. Using this definition, ignition delays have been measured for canola B100, canola fatty acid butyl esters (FABEs), a reference #2 diesel, and soy FAMEs. The purpose of these tests is two-fold. First, it is important to validate our approach of comparing fuel ignition properties via spray ignition studies where details of the chemical ignition process may be difficult to isolate from the physical evaporation process. Traditionally, ignition delay measurements are taken in the gas phase where a homogeneous charge of reactants is exposed to autoignition conditions and all physical disturbances (i.e. evaporation and turbulent flows) are minimized. This approach isolates the chemical ignition process, and reveals subtle ignition features such as negative temperature coefficient (NTC) regions where fuel reactivity decreases as temperature increases. For our spray ignition measurements, it is important to confirm features such as NTC are visible. The second purpose of studying these fuels is to provide baseline ignition delay measurements in the RCM for fuels that are currently used in production diesel engines.

Figure III.26 shows sample ignition profiles for the four fuels at compressed temperatures of 730 K and 770 K. For each of these tests, a unique time was chosen to inject after TDC, corresponding to the desired compressed temperature. The time scale on the plots is set so that the injection begins at $t = 0$. The compressed pressure for all these test is 30 bar, and the injection mass was chosen to satisfy $\varphi = 0.30$ with $X_{O2} = 0.12$. For both test conditions, the relative reactivity among the fuels is consistent, with the canola B100 igniting first and the reference diesel fuel showing the longest ignition delay. Changing the temperature by 30 K between the two cases leads to an obvious change in ignition delay.

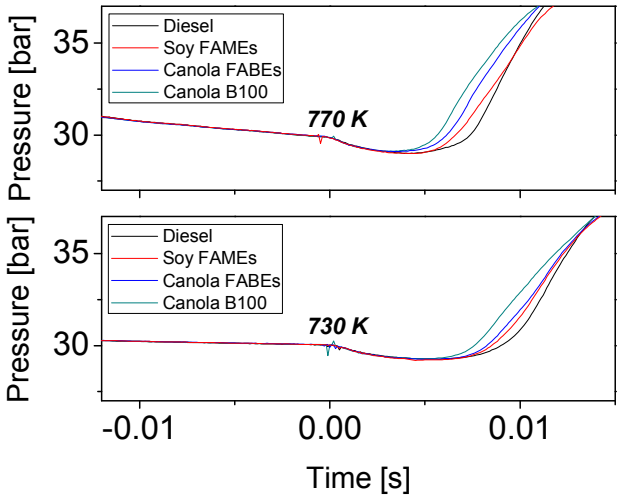

Figure III.26. Pressure traces during injection and ignition of diesel and biofuels.

Additional ignition delay measurements were taken for a larger set of temperatures and oxygen mole fractions, and the results appear in Figures III.27 and III.28. Figure III.27 shows

ignition delays taken at a variety of compressed temperatures, with φ = 0.25 and p_c = 30 bar, and X_{O2} = 0.12. Based on preliminary cetane number testing, we expected the canola B100 to ignite the earliets, which is true at nearly all conditions tested. An NTC region is clearly visible for the canola B100 and the soy FAMEs near compressed temperatures of 820 – 980 K, and to a lesser extent for the reference diesel. These results support the use of our spray ignition system for comparing ignition delays for fuels.

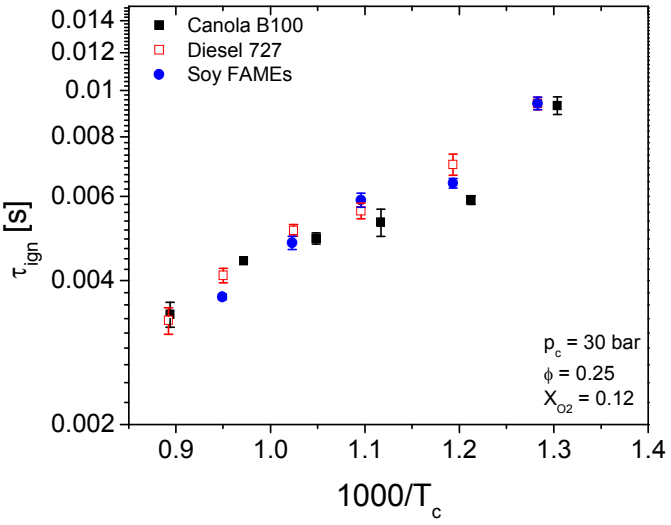

Figure III.27. Ignition delays at p_c = 30 bar, f = 0.25 and X_{O2} = 0.12.

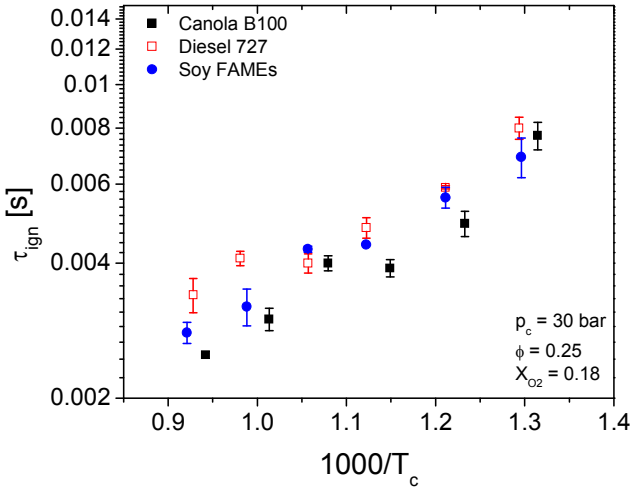

Figure III.28. Ignition delays at p_c = 30 bar, f = 0.25 and X_{O2} = 0.18.

Figure III.28 shows ignition delay measurements for the same fuels as Figure III.27, but with the oxygen mole fraction changed to X_{O2} = 0.18. These results show the same general trend seen for the X_{O2} = 0.12 case, where the fuels may be listed in order of increasing reactivity as

diesel, soy FAMEs, canola B100. By comparing Figures III.27 and III.28, which are shown with the same y-axis scales, it is clear that increasing the oxygen concentration leads to faster ignition. The results also indicate that the ignition delay of each fuel exhibits a different sensitivity to changes in oxygen concentration. The canola B100 ignition delay is decreased more substantially by the increased oxygen concentration than the diesel fuel.

Detailed ignition delay measurements are reported below for these fuels for compressed temperatures between 700 K and 840 K. Two different ignition delay periods were measured, as illustrated in Figure III.29. As the injection of the fuel in the RCM begins at $t = 0$, there is a clear reduction in pressure as energy is absorbed by the fuel for heating and vaporization. Soon after, the first exothermic reaction of the fuel is visible when the reactive pressure trace is compared with a pressure trace where the fuel is sprayed into an inert environment with the same specific heat. At this point, denoted by τ_1, the reactive and inert traces diverge. The overall ignition delay, $\tau_1 + \tau_2$, is identified as the point at which the reactive test pressure exceeds the pressure of a test where no fuel is injected.

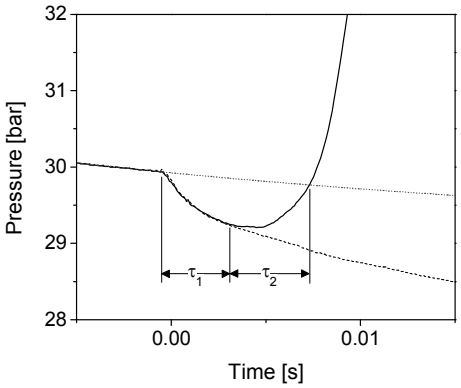

Figure 19. Definition of ignition delay periods

The elevated temperatures are created by compressing a gas mixture in the RCM, and the exact temperature may be altered by varying the diluent ratio (nitrogen:argon) which influences the specific heat of the mixture. Tests were performed by first compressing a gas charge to top dead center (TDC) and then allowing the charge to cool until the pressure reached 30 bar, at which point the fuel injection was started. By varying the initial pressure, the time required to reach 30 bar is altered and so is the core temperature, offering a mechanism to test ignition delays at different core temperatures. An illustration of this approach appears in Figure III.30. Before testing fuels in this fashion, we took precaution because it is known that significant velocity variations may influence the ignition delay. With the outlined approach, gas velocity in the RCM is near a maximum at TDC and steadily dissipates afterward. To test the influence of injection timing, we created various gas mixtures that would reach a core temperature of 727 K and pressure of 30 bar at different times after TDC. The results of this test appear in Figure III.31. It can be seen that changing the timing for start of injection (SOI) has no noticeable influence on the ignition delay. The small changes we observe are within the standard error.

Figures III.32 – III.35 show ignition delays (τ_1 and $\tau_1 + \tau_2$) for canola FAMEs, canola FABEs and reference #2 diesel for different test conditions. Figure III.32 compares the two different ignition delay periods for compressed temperatures between 700 K and 840 K, with oxygen mole fraction of $X_{O2} = 0.12$. Both show an overall decreasing trend in ignition delay as

the temperature increases and a negative temperature coefficient (NTC) region near 750 – 780 K, where an increase in temperature leads to a longer ignition delay. Figure III.33 shows $\tau_1 + \tau_2$ for two different oxygen mole fractions, $X_{O2} = 0.12$ and $X_{O2} = 0.18$. We see that by increasing the oxygen concentration, ignition occurs earlier, and the presence of the NTC region is suppressed. Figures III.34 and III.35 compare canola FAME ignition delays with diesel 727 (reference #2 diesel) and canola FABE, respectively. The ignition delays for the canola FAMEs are shorter than the diesel ignition delays, as we would expect based on the higher cetane number of the canola FAMEs. The canola FAMEs also exhibited a shorter ignition delay than the canola FABEs, as shown in Figure 25. Intuitively, we may expect that the growth in the alkyl chain length from a methyl group to a butyl group would lead to greater reactivity and

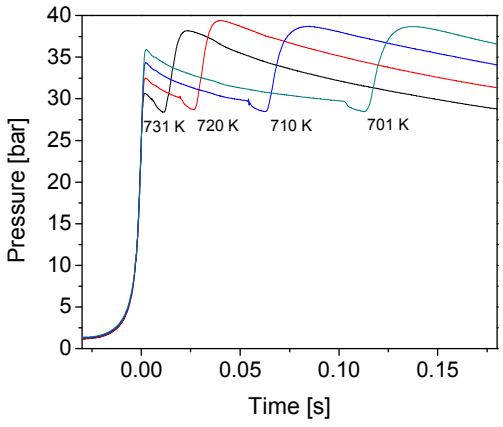

Figure III.30. Approach for altering test temperature for spray ignition.

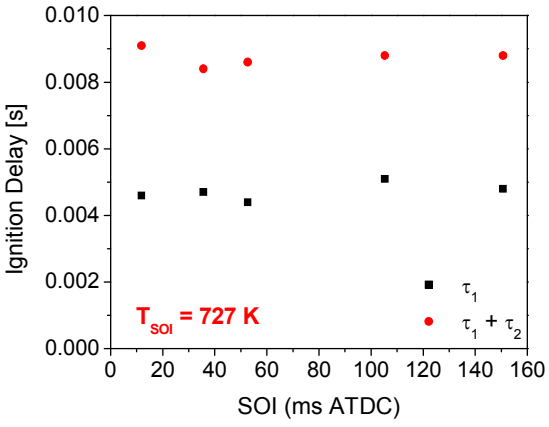

Figure III.31. Investigation of influence of injection timing on ignition delay.

shorter ignition delays for the canola FABEs, however, this is not the case. In fact, prior research of cetane numbers has shown that in some cases, growth of the alkyl chain leads to a decrease in cetane number [1]. Our data supports this finding. As a check for

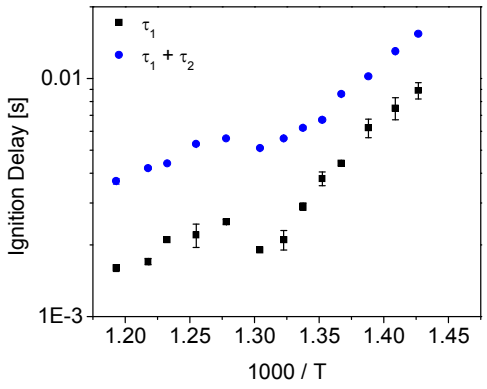

Figure III.32. Canola FAMEs Ignition Delays ($X_{O2} = 0.12$)

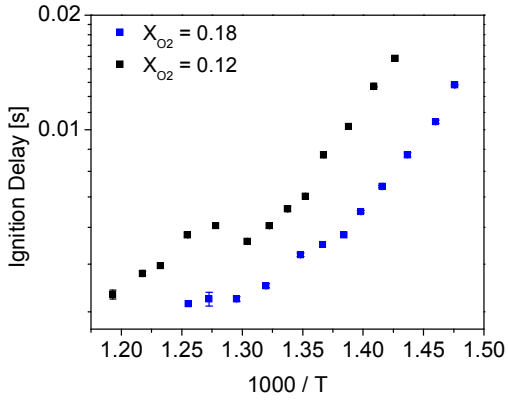

Figure III.33. Canola FAMEs Ignition Delays ($\tau_1 + \tau_2$)

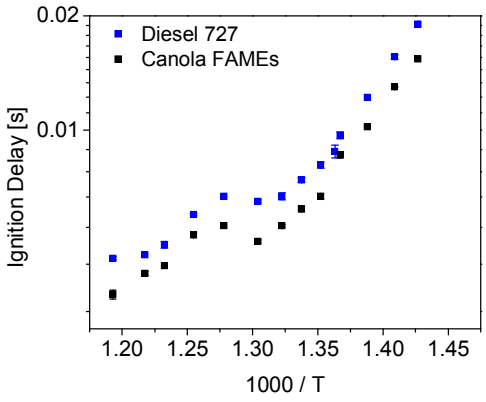

Figure III.34. Ignition delays ($\tau_1 + \tau_2$), $X_{O2} = 0.12$

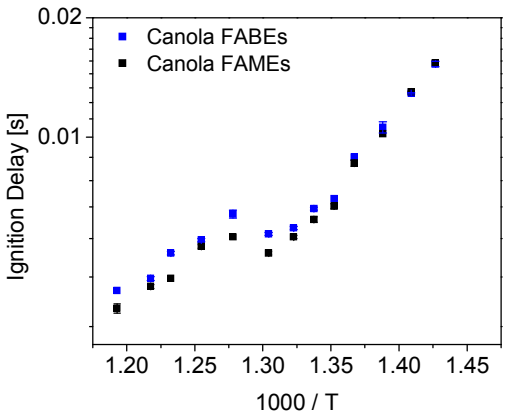

Figure III.35. Ignition delays ($\tau_1 + \tau_2$), $X_{O2} = 0.12$

logical consistency, the diesel ignition delay results were compared with data published in the literature [1-5]. A comparison of this data appears in Fig. III.36. The data for these tests have been scaled to a 30 bar test condition assuming the ignition delay depends linearly on the inverse pressure (*1/p*). The results indicate good general agreement with other studies. Our measured ignition delays appear to be near the upper limit of what other researchers have measured, but all other studies have used 21% oxygen, while our measurements were completed using 12% and 18% oxygen.

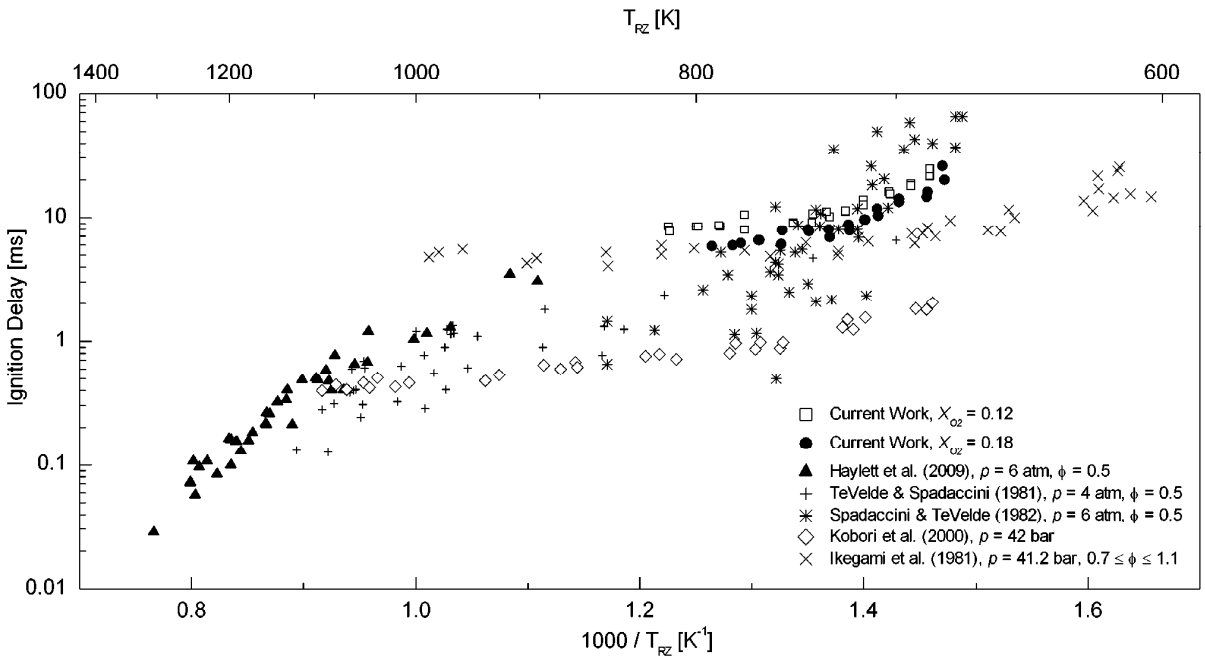

Figure III.36. Comparison of measured diesel ignition delays with data published in the literature.

Figure III.37 shows a comparison of the canola BD and D2 ignition delays, where we define the ignition delay, τ, to be the time from the start of injection to the time required to reach the peak heat release rate. The results indicate that for any given reaction zone temperature and oxygen concentration, the canola BD ignites more readily than D2. This result is not unexpected given that cetane numbers for canola BD and D2 have been reported as 47.9 – 56 [6-8] and as 47 [9], respectively. However, these measurements provide new useful data in a regime where temperatures are lower than used in cetane number measurements (~ 820 K). Both fuels exhibit negative temperature coefficient behavior (NTC) where increasing temperature leads to increasing ignition delays over a given temperature region. The onset of NTC behavior is near 770 K for the canola BD, and near 740 K for the D2.

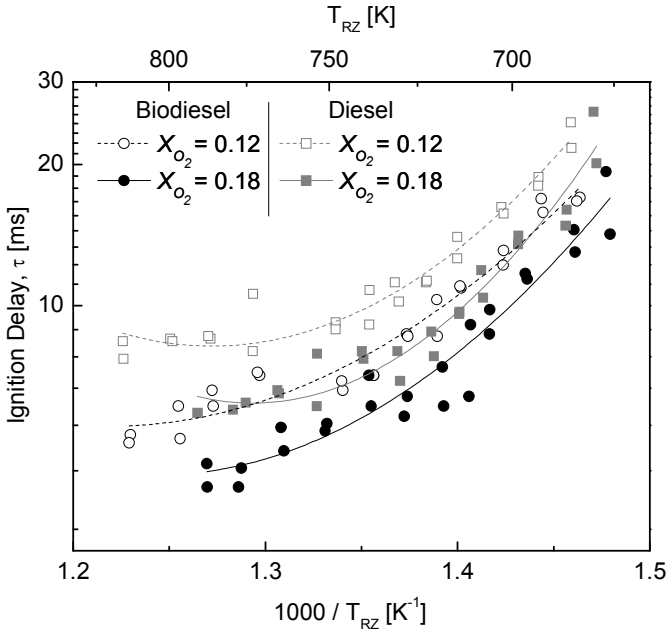

Figure III.37. Comparison of ignition delay period τ for canola BD and D2 fuel sprays in oxidizing environments with X_{O2} = 0.12 and X_{O2} = 0.18.

The ignition properties of three different biodiesels: soy methyl esters (SME), canola methyl esters (CME), and canola butyl esters (CBE) are compared to investigate the influence on ignition behavior imparted by changes in the alcohol moiety chain length (CME vs. CBE) and by changes in molecular unsaturation in the fatty esters (SME vs. CME). The tests for these fuels were also conducted over the same test region as described previously for the canola BD (*i.e.* CME) and D2. Ignition delays for the fuels using 12% and 18% oxygen appear in Fig. III.38 and Fig. III.39, respectively. An additional ignition delay period, τ_1, appears in these results which corresponds to the timing of first fuel heat release. With the increased availability of oxygen in the 18% test cases, the fuels are nearly indistinguishable over the entire set of tested reaction zone temperatures. However, by decreasing the oxygen content to 12%, some variation among the fuels is observed, as shown in Fig. III.39. We hypothesize that within the overall ignition delay, the chemical delay plays a secondary role to the physical transport processes of spray breakup and evaporation. For the 18% oxygen tests differences in fuel kinetics cannot be observed amid the physical ignition delay. In the 12% cases, chemical kinetic effects become visible for the fuels because the chemical delay begins to have a more substantial influence on the overall ignition delay.

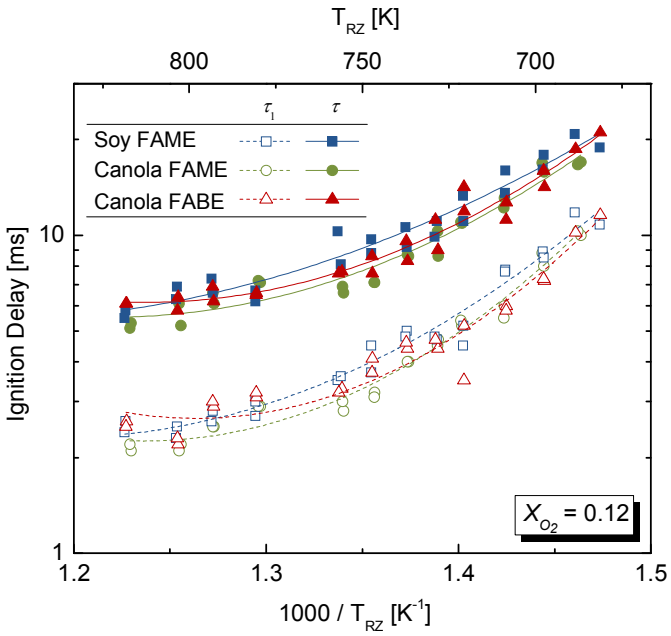

Figure III.38. Ignition delay measurements (τ_1 and τ) for SME, CME and CBE fuel sprays in an oxidizing environment with $X_{O2} = 0.12$.

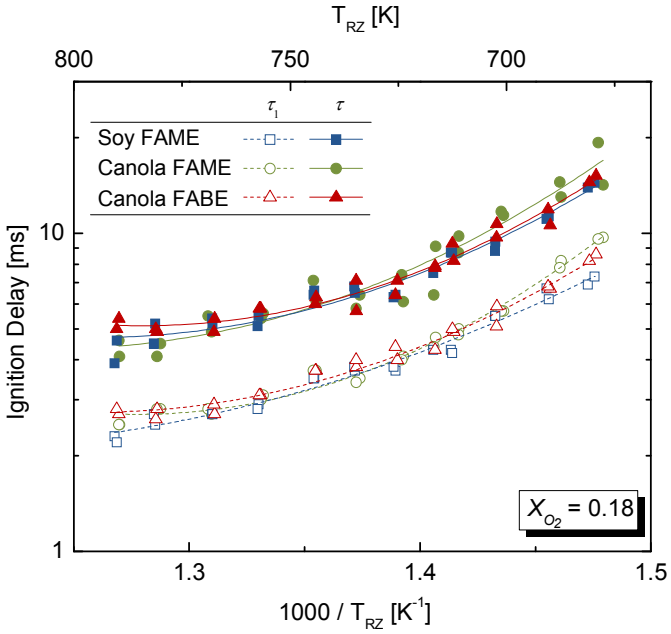

Figure III.39. Ignition delay measurements (τ_1 and τ) for SME, CME and CBE fuel sprays in an oxidizing environment with $X_{O2} = 0.18$.

II.4.2 Soot production from diesel and biodiesel in RCM

Our concluding work related to the rapid compression machine (RCM) has been the implementation of an optical system for measuring soot temperatures and quantitative soot volume fractions. Tests at equivalence ratios of φ = 4.0 and an oxygen mole fraction of 21%

indicated this was possible with both the biodiesel surrogate methyl decanoate (MD) and with blends of MD and dibutyl succinate (DBS). A schematic of the optical setup appears in Figure III.40. A prism is placed in front of the RCM to duplicate the image. Each of the duplicated images is filtered using a unique bandpass filter before being captured on a high-speed camera. The pixel-by-pixel intensities of the duplicated images may be compared to provide estimates of soot temperature and soot volume fraction. This is an implementation of the well-known two-color pyrometry approach, and Figure III.41 illustrates the measurement principle. The shape of the spectral distribution of the light being radiated from the soot is a function of the soot temperature. The ratio of the intensities of the filtered light at a set of wavelengths is characteristic of a given temperature. Once the temperature is calculated, the soot volume fraction may be determined using the approach documented by Cignoli et al[10].

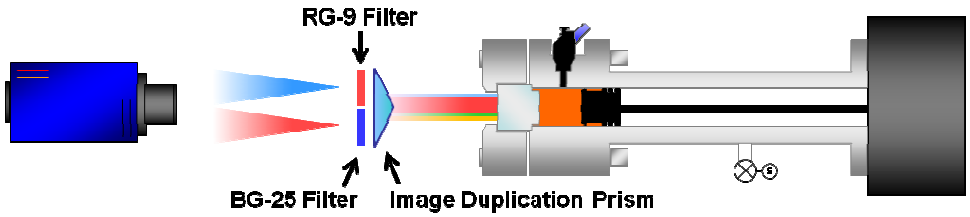

Figure III.40. Optical diagnostics setup for measuring soot temperature and soot volume fraction in RCM

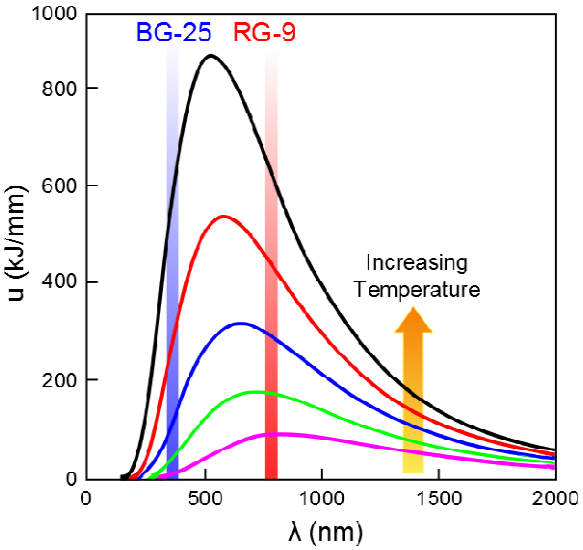

Figure III.41. Two-color pyrometry measurement principles showing spectral distribution for soot radiation at increasing soot temperature.

References

1. Haylett, D.R., et al., *Application of an aerosol shock tube to the measurement of diesel ignition delay times.* Proceedings of the Combustion Institute, 2008. **32**.

2. Tevelde, J.A. and L.J. Spadaccini, *Autoignition Characteristics of No. 2 Diesel Fuel*, N.L.R. Center, Editor. 1981.
3. Spadaccini, L.J. and J.A. Tevelde, *Autoignition characteristics of aircraft-type fuels.* Combustion and Flame, 1982. **46**: p. 283-300.
4. Kobori, S., T. Kamimoto, and A.A. Aradi, *A study of ignition delay of diesel fuel sprays.* International Journal of Engine Research, 2000. **1**(1): p. 29-39.
5. Ikegami, M., K. Miwa, and M. Inada, *A Study on Ignition and Combustion of a Diesel Spray by Means of a Rapid Compression Machine.* Bulletin of the JSME, 1981. **24**(195): p. 1608-1615.
6. Avella, F., A. Galtieri, and A. Fiumara, *Characteristics and utilization of vegetable derivatives as diesel fuels.* Rivista dei combustibili, 1992. **46**(6): p. 181-188.
7. Bouché, T., et al., *Optimising tractor CI engines for biodiesel operation*, in *SAE Paper*. 2000.
8. Krahl, J., et al., *Gaseous Compounds, Ozone Precursors, Particle Number and Particle Size Distributions, and Mutagenic Effects Due to Biodiesel* Trans. ASAE, 2001. **44**(2): p. 179-191.
9. Goering, C.E., et al., *Fuel properties of eleven vegetable oils.* Trans. ASAE, 1982. **25**(6): p. 1472-1477.
10. F. Cignoli, S. De Iulliis, V. Manta, G. Zizak, *Applied Optics* 40 (2001) 5370-5378.

IV. Simulation of Combustion in Single Cylinder Engines

The MSU computational group has applied turbulence, spray, and combustion models for large-eddy simulation (LES) of internal combustion (IC) engines. The simulations are conducted with the two-phase LES/FMDF methodology and high-order numerical schemes which can handle complex geometries, moving valves, moving piston, spray and various types of flames (premixed, non-premixed, partially-premixed, slow, fast,……..). The group's research efforts on the spray simulations, multi-component droplet evaporation models, and combustion in single cylinders are described below.

IV.1 Simulation of Spray Injection

The fuel spray characteristics and parameters affecting the fuel mixing in diesel engine environment are numerically studied. The numerical simulations are conducted for conditions close to experiments performed at Sandia National Laboratory. In these experiments, the fuel spray evaporation and combustion in a closed combustion chamber are studied with hexadecane as fuel. Figure IV.1 the shows interior picture, schematic cross section and fuel injector in this experiment. The characteristic size of the combustions chamber is 108 mm**.** The gas pressure, density and temperature in the vessel are changed via an intake valve.

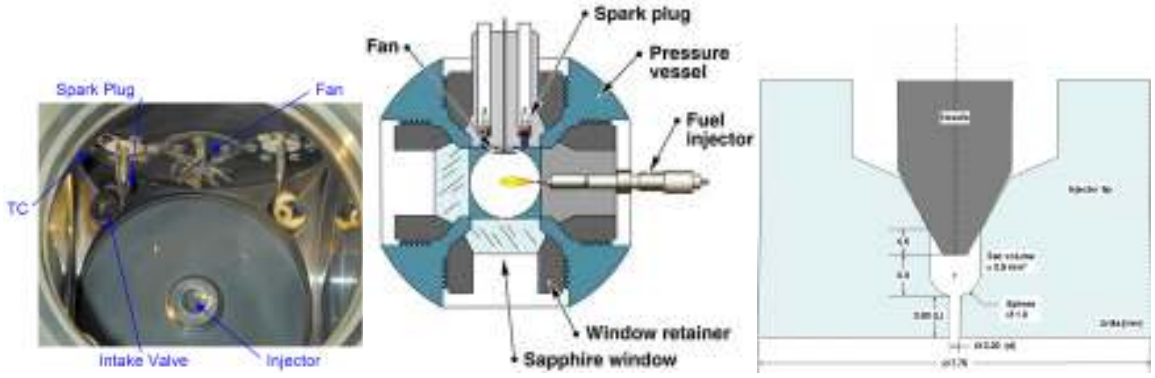

(a) (b) (c)

Figure IV.1. (a): Combustion vessel interior photo, (b): Schematic cross section of the vessel, (c) The fuel injector of the vessel. [*Photo and schematic drawings are taken from Sandi National Laboratory engine combustion network website https://share.sandia.gov/ecn/index.php*]

Also in the experiment, the gas temperature, density and oxygen concentration vary from 450 K to 1300 K, 3 to 60 kg/m^3 , 0% to 21%, respectively. The fuel injector is located in one side of the engine, and the nozzle diameter ranges from 0.05 to 0.5 mm with the fuel injection pressures between 40 to 200 MPa. This combustion vessel has been operational at Sandia National Laboratory since 1997 (Siebers, SAE 980809).

The effect of ambient temperature, density, injector pressure and nozzle diameter on the liquid penetration in non-reacting cases and the flame lift-off in reacting cases were studied by

the LES/FMDF code/models. The liquid penetration depth is the maximum extent of liquid-phase spray penetration during the injection and the flame lift-off is the axial distance from the injector to the location of high-temperature reaction zone.

The numerical simulation is conducted via large-eddy simulation together with Blub/Kelvin–Helmholtz/Rayleigh-Taylor instability droplet breakup models. A cubic computational domain with uniform grids (dx=dy=dz=2 mm) is employed. Initial gas phase conditions are set uniformly based on experimental conditions. The fuel droplets
Are injected into the domain from the center point of the left face. The 3D and 2D views of the computational domain with sample sprayed fuel droplets are shown in Figure IV.2.

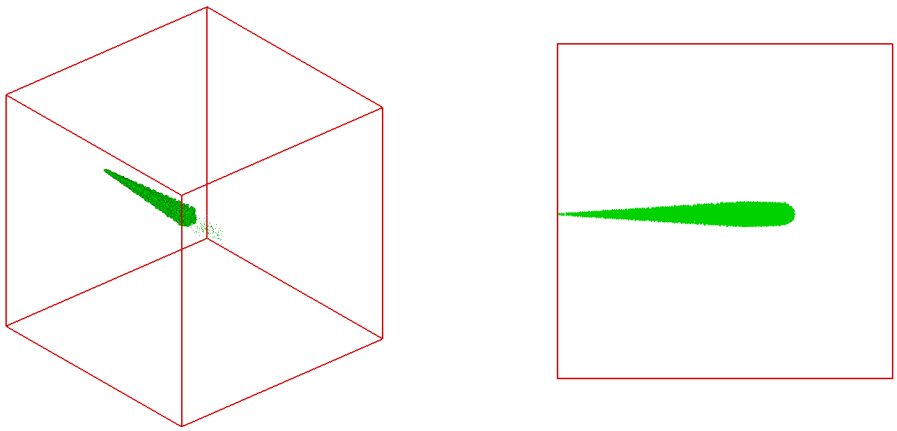

(a) (b)

Figure IV.2. (a) 3D, (b) 2D views of the computational domain and fuel spray.

Initial droplet velocity is calculated from the Bernoulli's equation with a correction coefficient as $V = C\sqrt{2\Delta P_{inj} / \rho_{fuel}}$. The coefficient (C) varies from 0.7 to 1.0. The initial diameter of droplets is calculated by using the nozzle diameter and its area-contraction coefficient. LES results and experimental data for liquid penetration in the non-reacting cases at different ambient densities and temperatures are shown in Figure 3. In these simulations, the fuel temperature, the injector pressure and the nozzle diameter are fixed at 436K, 138 MPa and 246 mm, respectively, consistent with the experiment. The oxygen concentration is zero. In Figure IV.3, the solid and dashed lines represent the isothermal experimental data and the LES results, respectively. Evidently, the liquid jet penetration decreases by increasing the ambient temperature or density. This decrease in penetration is significant at low temperatures or densities, but it is small at high temperatures or densities. The numerical results are shown to be consistent with the experiment.

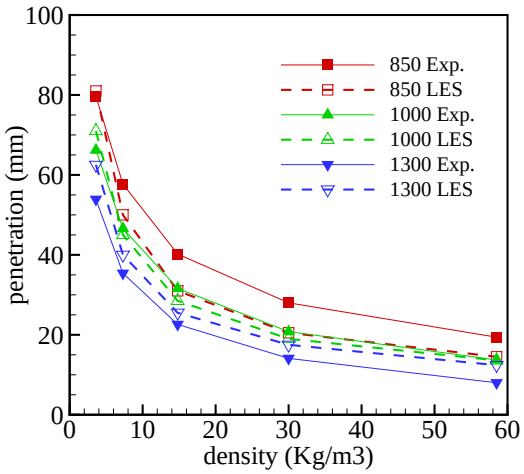

Figure IV.3. Liquid penetration depth at different ambient gas densities or temperatures.

The effect of injection pressure on liquid penetration in non-reacting cases is shown in Figure IV.4. In these simulations/experiments, the fuel temperature and nozzle diameter are fixed at 436K and 246 mm. Again the oxygen concentration is zero. The solid and dashed represent the experimental and LES results similar to Figure IV.5. By increasing the injection pressure, while keeping the ambient temperature and density constant, the liquid penetration is shown to remain nearly constant. Again, the numerical results are consistent with the experiment and show very similar trends, despite some quantitative differences.

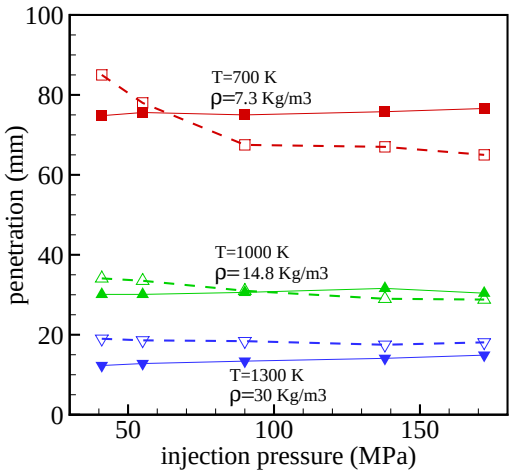

Figure IV.4. Liquid penetration depth at different injection pressures.

Figure IV.5 shows the effect of injector nozzle diameter on the liquid jet penetration in non-reacting conditions. In these simulations/experiments, the fuel temperature and the injector pressure are fixed at 436K and 138 MPa, respectively and the Oxygen concentration zero. Similar to Figures IV.3 and IV.4, solid and dashed lines represent experimental and numerical

data. Unlike the results obtained for varying injector pressure, by increasing the injector diameter, while keeping the ambient temperature and density constant, the liquid jet penetration increases. However, the rate of change in the penetration depth is much higher at low temperatures or densities as opposed to that in high temperatures or densities. Again, the numerical results are consistent with the experiment and show very similar trends, despite some small quantitative differences.

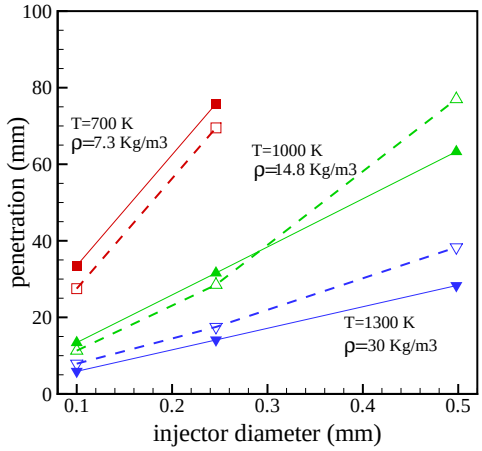

Figure IV.5. Liquid penetration depth at different injection diameters.

The effects of liquid density, viscosity and surface tension are reported below using a similar numerical set-up. The fuel is normal-hexadecane and its initial temperature, the injector pressure and the nozzle diameter are fixed at 436K, 138 MPa and 246 mm, respectively. The oxygen concentration is zero. In these simulations, the fuel density, viscosity and surface tension are increased and decreased artificially by 20 and 40 per cent from their physical values to investigate their effects in the liquid penetration. This is important and can help us in the development of "better" biofuels.

LES results for liquid penetration in the non-reacting cases at different liquid densities and ambient temperatures are shown in Figure IV.6. In this figure, each solid line represents the isothermal ambient condition for the LES simulations. Evidently, while keeping all liquid and ambient variables constant and equal to their physical values at average temperature, the liquid jet penetration increases/decreases by increasing/decreasing the liquid density.

The effect of liquid viscosity on liquid penetration in non-reacting cases is shown in Figure IV.7. Each solid line represents the isothermal ambient condition for LES similar to that shown Figure IV.6. On increasing/decreasing the liquid viscosity, while keeping all liquid and ambient variables constant and equal to their physical values at average temperature, the liquid penetration is shown to remain nearly constant.

Figure IV.8 shows the effect of liquid surface tension on the liquid jet penetration in non-reacting conditions. Unlike the results obtained for viscosity variations, on increasing/decreasing the liquid surface tension, while keeping all liquid and ambient variables constant and equal to their physical values at average temperature, the liquid jet penetration increases/decreases. By comparing the slope of isothermal lines in Figures IV.6 and IV.8, is can be concluded that the effect of fuel density in liquid penetration is more significant than the effect of surface tension.

Nevertheless, the change in liquid penetration due to viscosity variation of about 40 per cent is negligible.

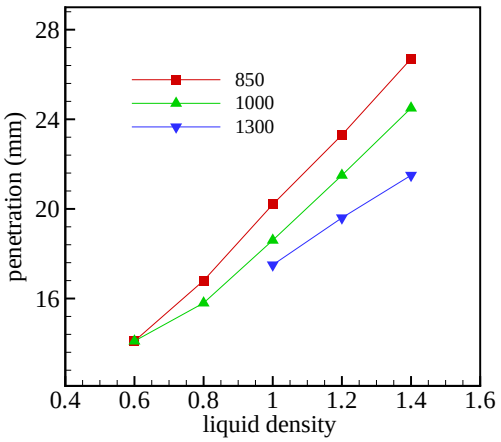

Figure IV.6. Liquid penetration depth at different liquid density.

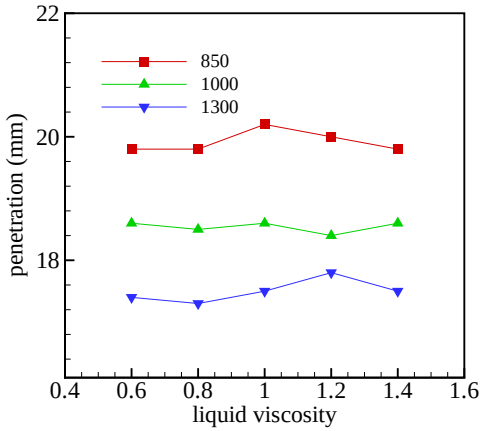

Figure IV.7. Liquid penetration depth at different liquid viscosity.

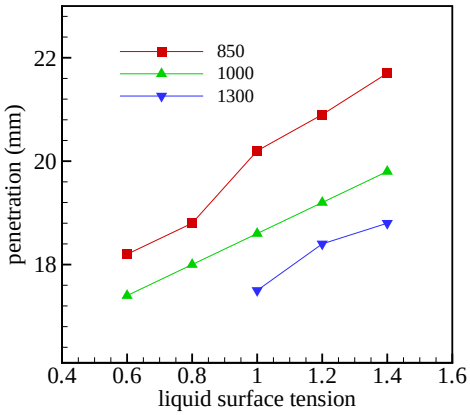

Figure IV.8. Liquid penetration depth at different liquid surface tension.

IV.2 Modeling and Simulations of Multi-component Evaporation: Model fuels

A multi-component evaporation model has been developed for simulating the evaporation of a single, spherically symmetric fuel droplet in a stagnant environment. This model solves for the non-monotonic and one-dimensional fuel and temperature distributions inside a fuel droplet and for the continuity, momentum, species conservation and energy equations in the gas phase. The model was used for simulating the mass fraction and the temperature profiles in the liquid and gas phases for a single bi-component (50 % ethanol-50 % iso-octane by weight) droplet in an ambient environment. Simulation results for a simple 2-valve engine geometry utilizing the already existing multi-component evaporation model in KIVA4 were also presented earlier.

The multi-component evaporation model has now been incorporated into the LES code. The model solves the conservation equations in the liquid phase and at the liquid-gas interface while the gas phase heat and mass transfer are modeled using Nusselt number and Sherwood number correlations. In order to test the implementation of the model in the LES code, simulations have been performed for the closed combustion chamber used in the Sandia experiments as described above (Figure IV.1). The simulations have been carried out for a single-component fuel, n-hexadecane, using both the multi-component evaporation model and the existing single-component evaporation model, with the same operating conditions (injection pressure 41 MPa, gas temperature 700 K, and gas pressure 1 atm.). In both the simulations, a series of droplets of n-hexadecane with a temperature of 293 K were injected into the combustion chamber and their evolution with time was tracked. The multi-component model is capable of utilizing temperature dependent physical properties for the fuel. However, in order to compare the results of the multi-component model with the existing evaporation model, constant physical properties, evaluated at the average temperature of the droplet, have been used. Also, the liquid velocity inside the droplet is not solved and liquid thermal conductivity is increased artificially to very high values to simulate infinite thermal conductivity, which is an assumption in the lumped model.

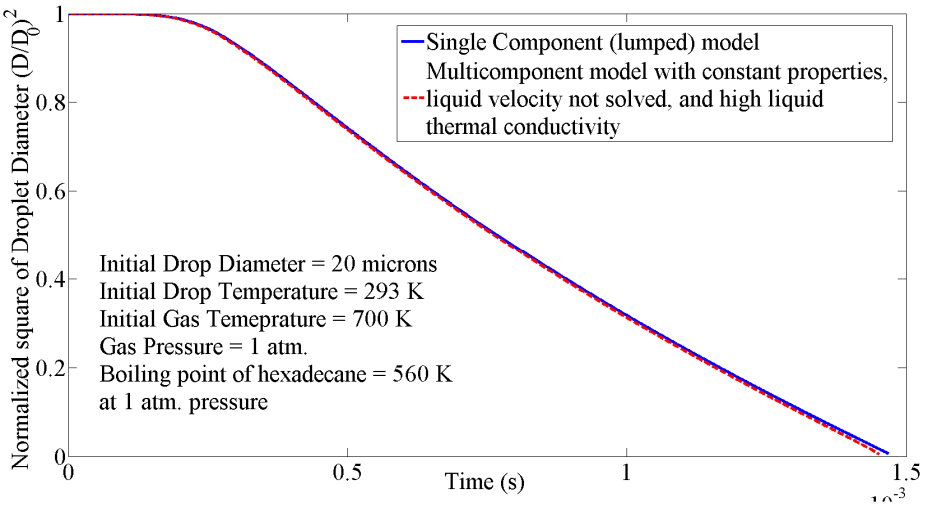

Figure IV.9. Square of normalized diameter with time.

Figure IV.9 shows the time variation of the square of the droplet diameter normalized by the square of the initial droplet diameter, for a drop of diameter 20 μm. Both models predict a

similar rate of evaporation. As expected for single-component fuels, both the models predict a 'D-square' law behavior – the square of the droplet diameter varies linearly with time after the initial heating period.

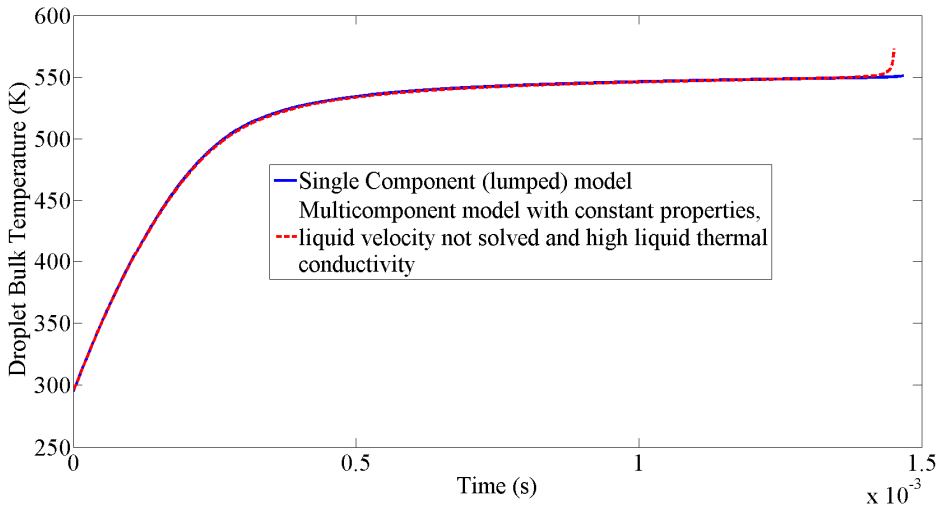

Figure IV.10. Variation of droplet bulk temperature with time.

Figure IV.10 shows the evolution of the droplet bulk temperature with time for the two models. Both the models predict similar droplet temperature evolution. Hence the multi-component model's predictions in the limit match the lumped model's predictions.

IV.2.1 Effect of fuel properties on droplet evaporation

In order to study the effect of various liquid fuel properties on evaporation, the properties were added step-by-step to the multi-component model (Baseline model) used in Figures IV.9 and IV.10. Figure IV.11 shows the effect of variable finite thermal conductivity on the droplet lifetime while Figures IV.12 and IV.13 show the effect of variable liquid C_p and latent heat of vaporization on the droplet lifetime and droplet temperature respectively. While, finite thermal conductivity does not have a significant effect on the droplet lifetime, variable C_p leads to a much faster evaporation rate caused by the lower specific heat and consequently higher droplet temperature achieved initially as seen in Figure IV.13.

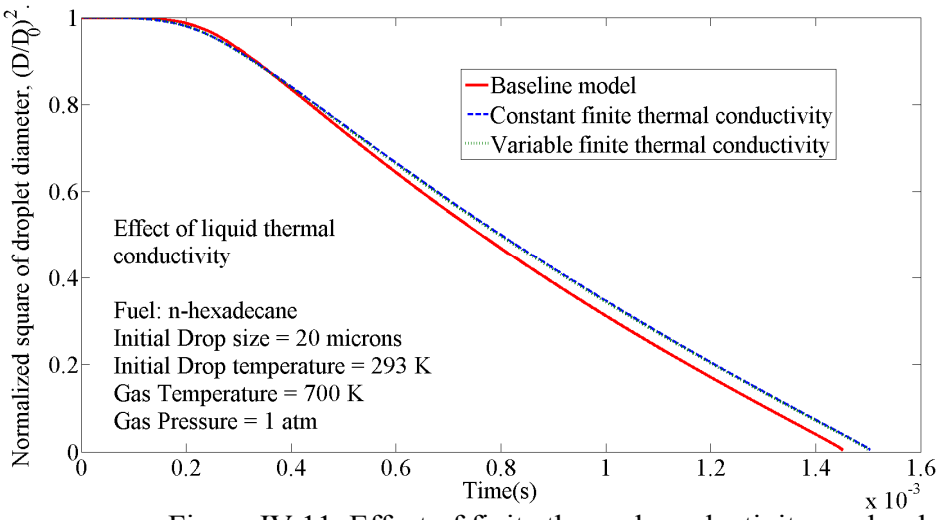

Figure IV.11. Effect of finite thermal conductivity on droplet life time.

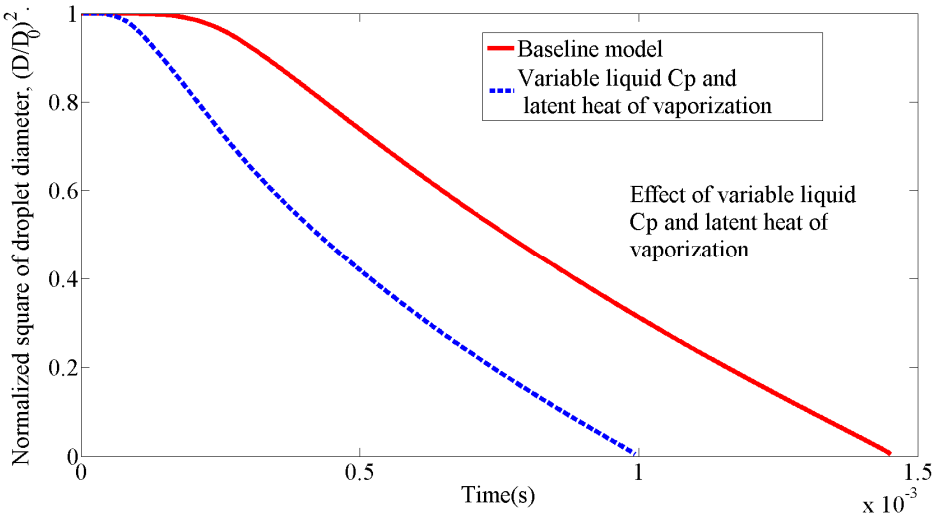

Figure IV.12. Effect of variable Cp and latent heat of vaporization on droplet lifetime.

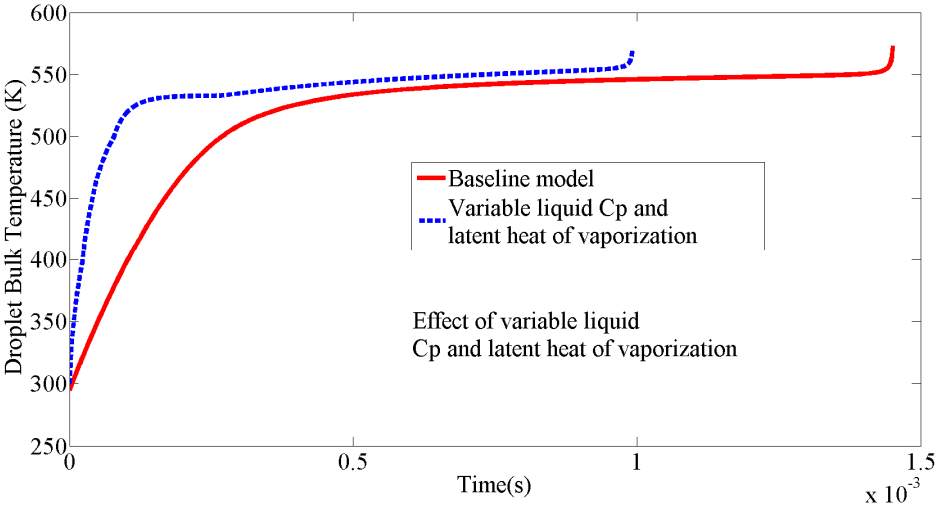

Figure IV.13. Effect of variable Cp and latent heat of vaporization on droplet temperature.

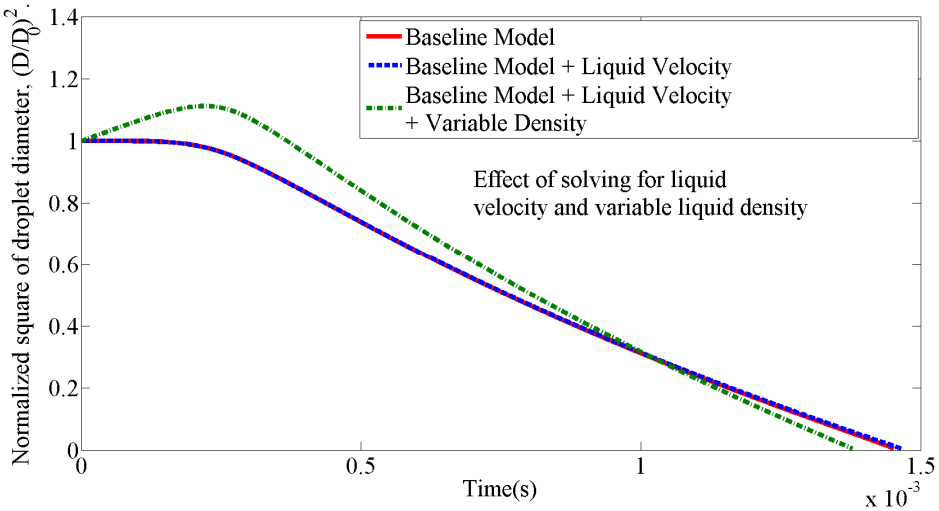

Figure IV.14. Effect of liquid velocity and variable liquid density on droplet lifetime.

Figure IV.14 shows the effect of variable liquid density on the droplet evaporation and captures the phenomenon of thermal expansion of the droplet during the heating phase of the droplet, although there is no significant change in droplet lifetime.

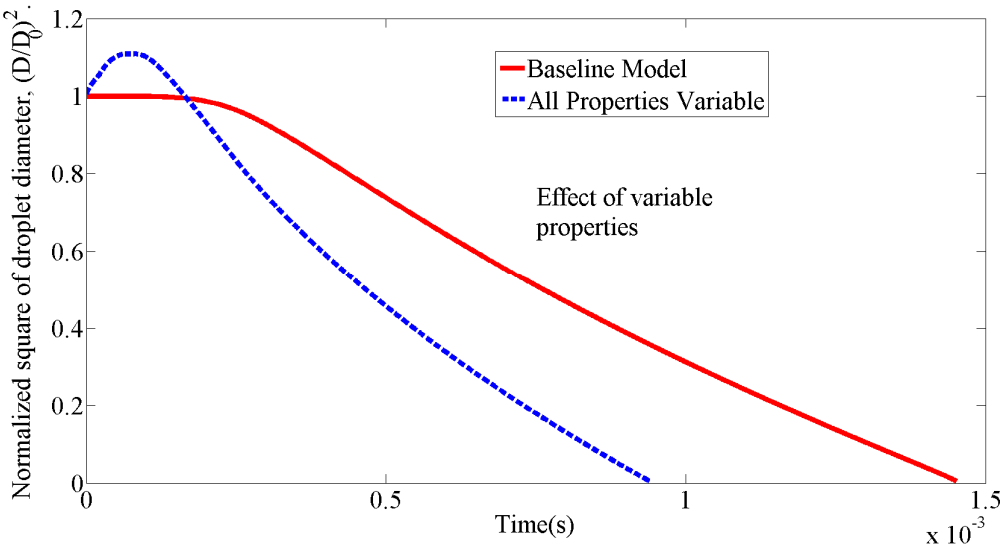

Figure IV.15. Effect of variable properties on droplet lifetime.

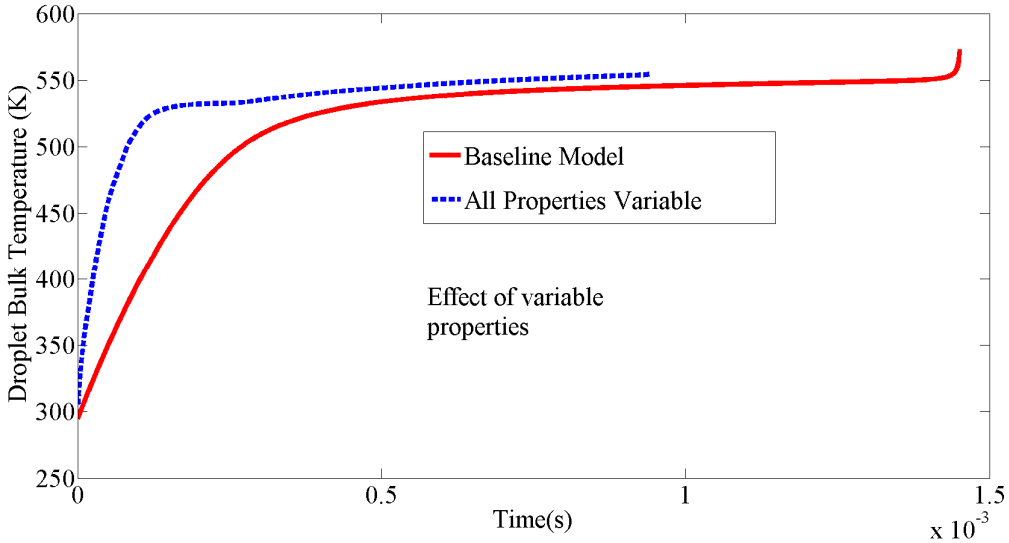

Figure IV.16. Effect of variable properties on droplet bulk temperature.

Figures IV.15 and IV.16 indicate the effect of fully variable liquid properties on the droplet lifetime and temperature. The droplet evaporates at a much faster rate than the baseline model with constant properties and at a slightly higher temperature, thus signifying the importance of using variable properties in droplet evaporation models.

Figure IV.17 shows the effect of increasing and decreasing the liquid density and latent heat of vaporization from their actual values. This is useful as it suggests a direction in which fuel/fuel properties might be modified to improve vaporization and hence mixing. Observing the slopes of the two curves, it can be concluded that changes in the liquid density have a more significant effect on the droplet lifetime as compared to latent heat of vaporization, as expected.

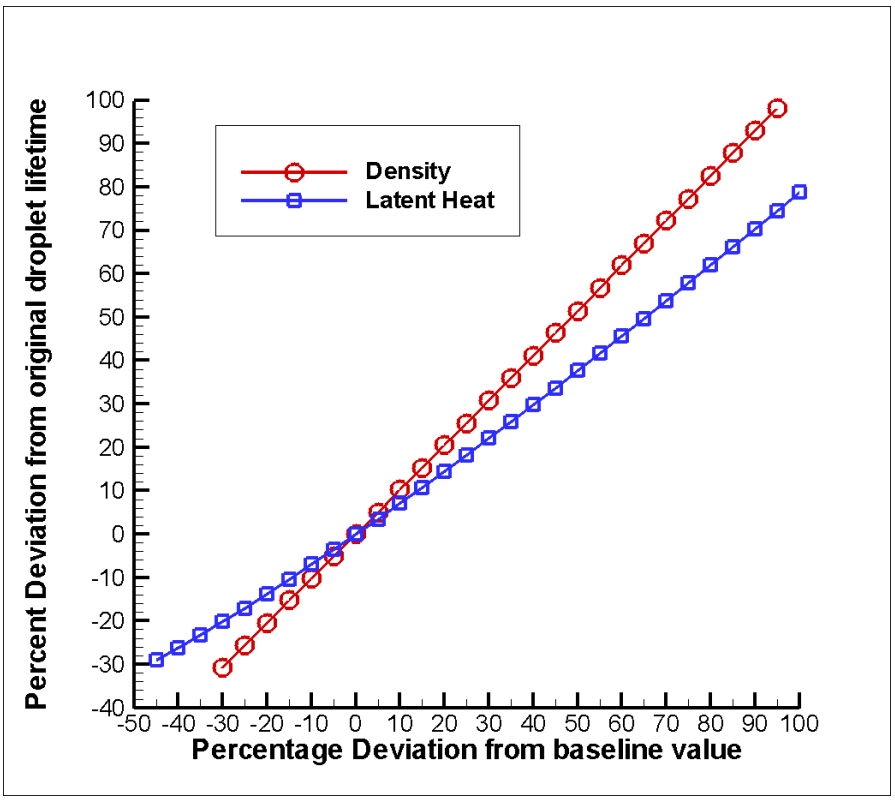

Figure IV.17. Effect of increasing and decreasing liquid density and latent heat of vaporization on droplet lifetime.

The Sandia penetration length experiments for Diesel #2 fuel were also simulated using the multi-component evaporation model. Diesel2, which is chemically complex, was simulated using a 2-species 70% n-decane + 30% α – methylnaphthalene mixture.

The results (Figure IV.18) indicate that the penetration lengths for the lower core gas temperatures are under-predicted, especially at higher gas densities. This might be accounted by the absence of heavy, less volatile diesel fuel components in the diesel surrogate model. As the gas temperature is increased, the numerical penetration length predictions compare well with the experimental results, particularly when the gas temperature is 850 K/1000 K.

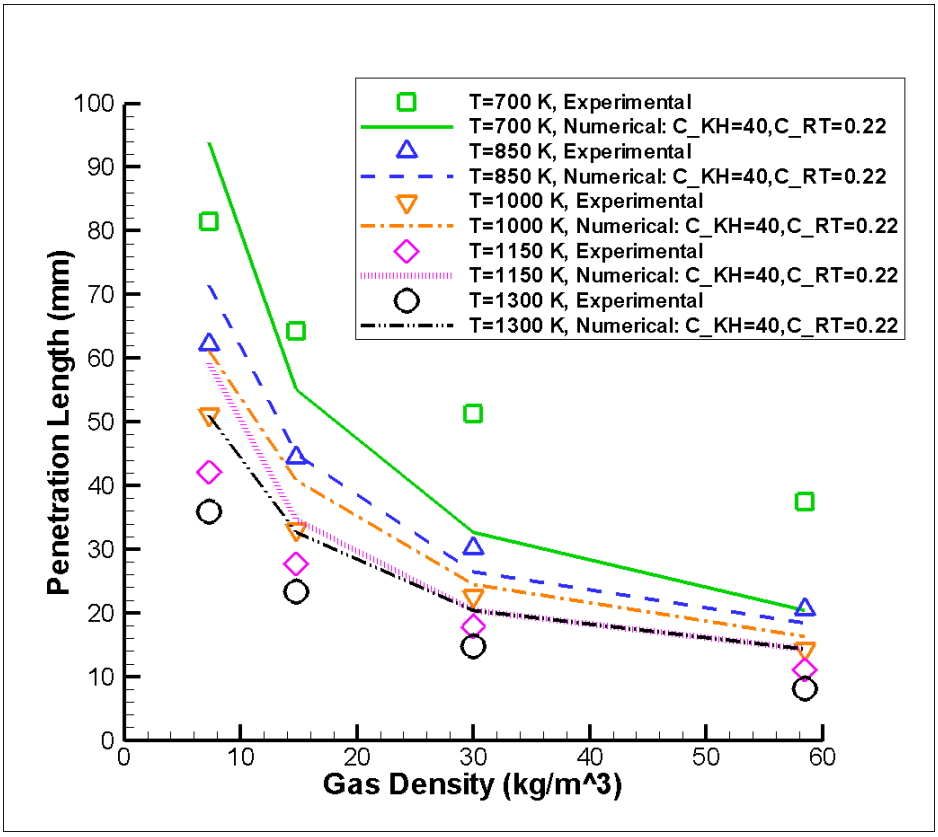

Figure IV.18. Comparison of Penetration lengths for Diesel2 surrogate fuel

IV.2.2 Radiation absorption model

Thermal radiation has a pronounced effect on the vaporization rate of diesel fuel. In order to incorporate radiation effects, a radiation absorption model based on [1] and [2] is being implemented along with the evaporation model. The model takes into account the distribution of thermal radiation absorption inside droplets and is based on an approach known as the modified DP_0 approximation, wherein spherical symmetry of thermal radiation inside the droplet and its boundary is assumed. This approach relies on the geometrical optics approximation and is valid only for droplets much larger than the wavelengths of thermal radiation. The droplet's own thermal radiation is ignored and external thermal radiation is assumed to be that of a black body. The effect of radiation on evaporation is comparatively small to other effects and can be dependent on the choice of the liquid-phase model. Also, the radial distribution of absorbed radiation inside the droplet is not uniform and has two maxima, one at the surface and another at one-third the distance to the core. Hence, the model is being implemented both for the infinite-conductivity lumped model and the more detailed finite-conductivity multi-component model.

According to the radiation model [1] and [2], the radiative power absorbed in the unit volume inside the droplet is given by

$$Q(\eta) = \frac{3\pi}{R_d} \int_{\lambda_1}^{\lambda_2} w(\eta, \lambda) E_a B_\lambda (T_{ext}) d\lambda$$

where $\eta = r/R_d$, $B_\lambda(T_{ext})$ is the Planck function given by

$$B_\lambda(T_{ext}) = \frac{C_1}{\pi\lambda^5\left[\exp\left(C_2/(\lambda T_{ext})\right)-1\right]},$$

C_1 and C_2 are known constants, λ is the wavelength in μm, E_a is the efficiency factor for absorption, $w(\eta,\lambda)$ is the normalized spectral power of radiation per unit volume absorbed inside the droplet, and λ_1 to λ_2 constitute the spectral range of thermal radiation which contributes to droplet heating. E_a depends on the spectral optical properties of the liquid fuel: index of absorption $\kappa(\lambda)$ and refractive index $n(\lambda)$. $w(\eta,\lambda)$ is obtained from the geometrical optics model combined with the MDP_0 approximation and is a complex function of η and λ.

Figure IV.19 shows the variation of the thermal radiation power absorbed in an n-dodecane droplet due to an external radiation temperature of 1000 K and indicates the two maxima, one at the droplet surface and another at one-third the distance to the core.

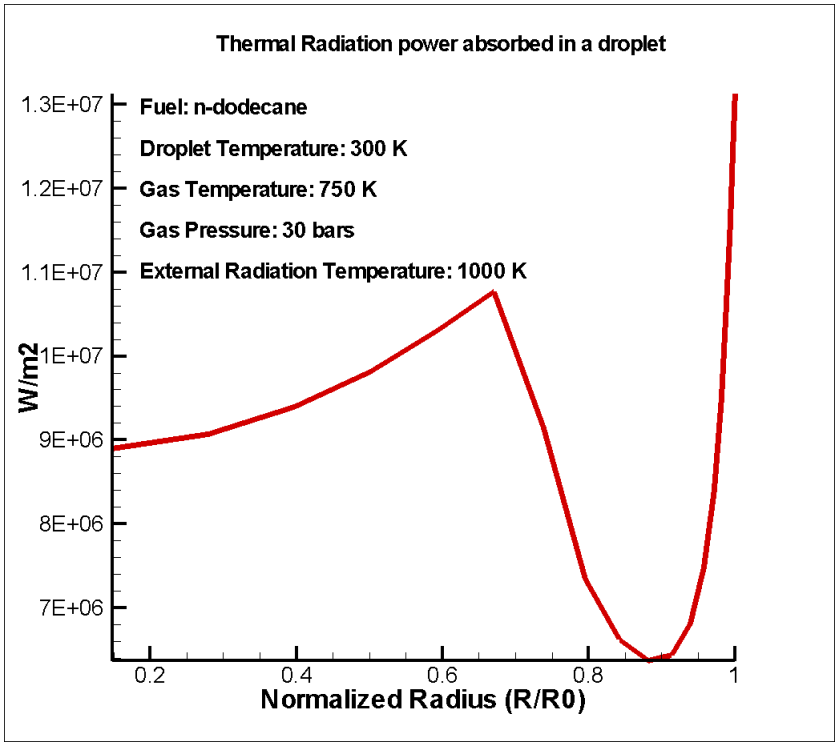

Figure IV.19. Radial variation of thermal radiation power absorbed in a droplet.

IV.2.3 Stochastic breakup model and finite-size effects

An advanced secondary breakup model for the simulation of sprays has been developed. The main notion is that the probability to break each parent particle into a given number of fragments is independent of the parent particle size. The liquid sheet injected into the computational domain is represented by large particles called primary particles. These individual

drops undergoing breakup produce a broad range of smaller drops that have a distribution *T(x), x=lnr* given by the Fokker-Planck equation.

$$\frac{\partial T(x,t)}{\partial t} = -\nu\langle\zeta\rangle\frac{\partial T(x,t)}{\partial x} + \frac{1}{2}\nu\langle\zeta^2\rangle\frac{\partial^2 T(x,t)}{\partial x^2}$$

Solving the Fokker-Planck equation involves determining statistical properties $\langle\zeta\rangle$; $\langle\zeta^2\rangle$ based on local droplet radius and Weber number. The breakup frequency ν is associated with the fastest growth rate of Rayleigh Taylor waves in the high speed limit, so for the droplet with size r_j, $t_{bu} = B\sqrt{\frac{\rho_l}{\rho_g}}\frac{r_j}{|u_{rel\ j}|}$. The relative velocity is based on the interaction of viscous dissipation and droplet time scale, $\langle u_{rel\ j}^2\rangle \approx \varepsilon\tau_{stokes}$.

The child droplets are grouped into bins to form parcels corresponding to their size and other properties such as velocity, temperature, etc. by conservation of mass, momentum and energy. The location is mass weighted averaged. The parcels thus created then undergo breakup, but do not create new parcels.

Since the relative velocity fluctuation calculation needs more accurate estimate of droplet motion, the wake effect of an upstream droplet on the seen relative velocity of the other droplet in the breakup region is of prominent importance. To capture the effect of nearby droplets on a specific droplet, three possible upstream droplets among the droplets in the same cell or neighboring cells are found which have either the lowest relative angle, or the minimum distance or the maximum relative size with respect to the concerned droplet. The effects of these three droplets on the concerned droplet are taken into account by using a correction factor for the relative velocity of the droplet. By this correction, not only droplet drag is influenced, but also heat and mass transfer are also modified implicitly due to modification of Reynolds number based on relative velocity.

It should be pointed out that stochastic breakup model gives a more physical spray evolution compared to KH RT breakup, giving a distribution of droplet size as a result of breakup, compared to almost mono dispersed outcome of KH RT model. In this case heat and mass transfer are more influential on the penetration length. Also in this model, some assumptions like small Reynolds number assumption for droplets in the spray are relaxed.

Figure IV.20 shows the comparison of the two breakup models while using the same lumped evaporation model with experimental data. As illustrated by the figure, the stochastic breakup model behaves better compared to KH RT breakup model and the difference with the experimental results can be attributed mostly to non-detailed evaporation model (compared to multi-component evaporation model) as well as lack of collision model. Meanwhile a temperature dependent trend can be deduced by comparing the results at different temperatures. The overall model (stochastic breakup and lumped evaporation) under predicts results in lower temperatures and over predicts at the higher temperature (Tgas=1300 K). At Tgas=850 K, the

model under predicts the penetration length significantly, compared to KH RT model. Efforts are being made to overcome this issue.

The evaporation model is modified to take into account for variable thermo-physical properties and the effect of Stefan flow on heat and mass transfer between the droplet and the gas, using Abramzon & Sirignano model (1989). Even with these modifications, the penetration lengths at lower temperatures are still under predicted compared to experimental results. This can be attributed to the absence of a collision model. The statistical accuracy of the stochastic breakup model is being improved by introducing more parcels with lower weightage compared to classical parcel approach.

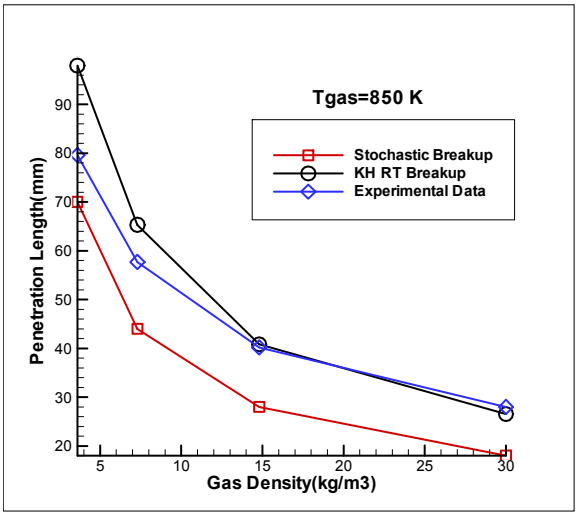

(a)

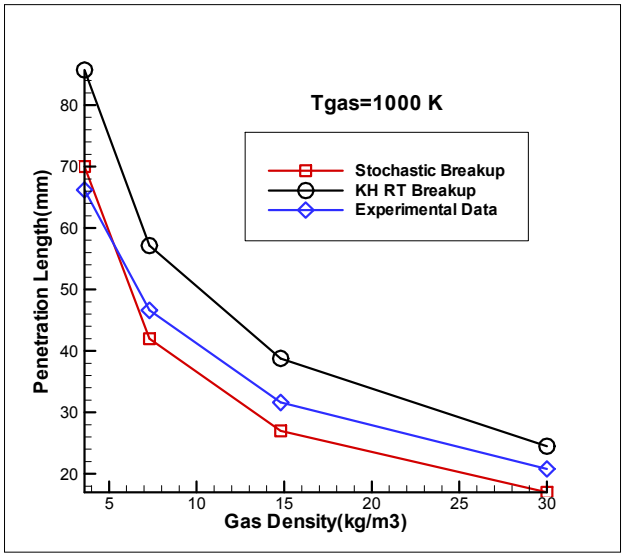

(b)

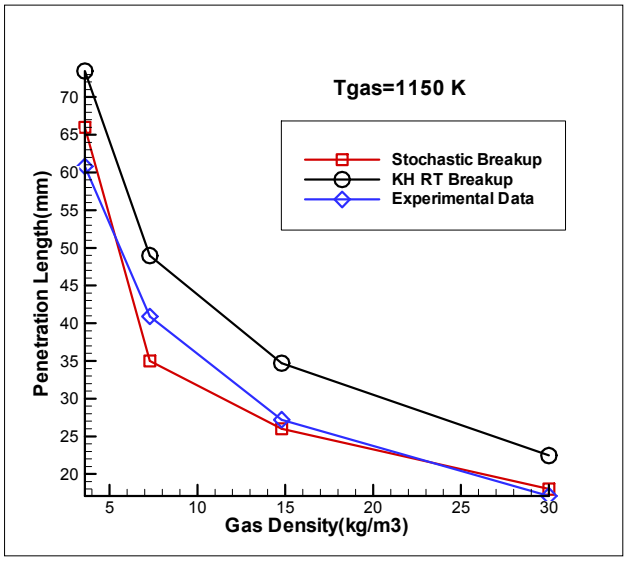

(c)

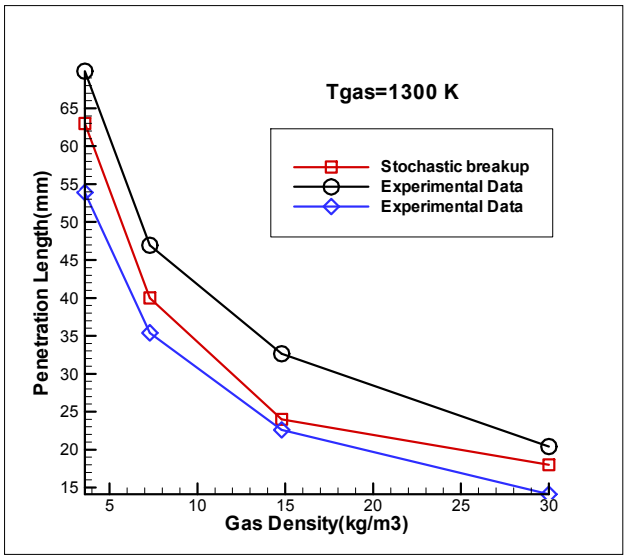

(d)

Figure IV.20. Effect of ambient gas temperature and density on penetration length of n-hexadecane. Comparison of experimental data with two different Breakup model using lumped evaporation model, (a) Gas Temperature = 850 K, (b) Gas Temperature = 1000 K, (c) Gas Temperature = 1150 K, (d) Gas Temperature = 1300 K.

IV.2.4 Collision and coalescence model

In the dense regions of the spray, collisions and coalescence of droplets becomes a vital phenomenon as it affects the size distribution of the droplets and consequently the evaporation, mixing and combustion of fuel, and needs to be modeled appropriately. A collision and coalescence model is currently being implemented in the LES code. The model is based on Munnannur and Reitz's model ([2], [3]), with suitable modifications for high pressure and multicomponent fuel systems.

The model has two major components:

1. **Collision probability prediction –** The reliable prediction of the collision probability is a numerical problem and should be independent of the gas phase mesh density and time step.

   - Radius of influence – A radius of influence approach is used to locate the potential collision partners for a parcel. In this approach, a collision is possible only if the distance between two parcels is less than the radius of influence of the larger parcel. For a candidate collision pair, collision occurs only if $X > P_{nocol}$. Here X is a random number in the interval (0,1) and P_{nocol} is the probability of not having a collision in a time step dt and is given by $P_{nocol} = e^{-\lambda dt}$, where $\lambda = \frac{n_{mp}\pi(r_{lp} + r_{mp})^2 U}{V_{col}}$ is the collision frequency, n is the number of drops in the parcel, r is the drop radius, U is the relative velocity, V_{col} is the spherical control volume and the subscripts np and mp refer to parcels with less number and more number of parcels, respectively.

   - Resolution improvement – In order to maintain the statistical accuracy of the collision process, the adequate number of parcels required in a control volume is determined statistically and selective parcel splitting or merging is carried out to maintain the desired number of parcels.

2. **Collision outcome prediction** – The type of outcome and the resulting characteristics of the colliding parcels is a physical aspect of the collision model, depending mainly on the relative Weber number ($We = \rho_L U^2 d_s / \sigma$), impact parameter ($b$, Figure IV.21) and the drop size ratio ($\Delta = d_s / d_l$).

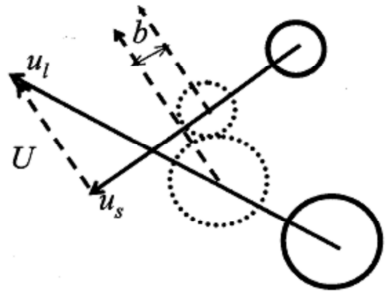

Figure IV.21. Definition of the impact parameter in a binary droplet collision. The smaller drop's diameter is d_s and the larger drop's diameter is d_l.

Figure IV.22 shows a schematic of the collision regimes as a function of We and the non-dimensional impact parameter *B*.

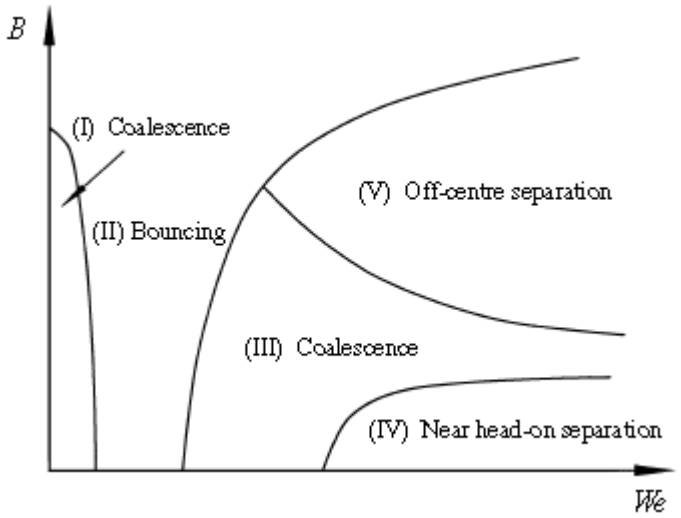

Figure IV.22. Schematic of various collision regimes of hydrocarbon droplets in 1 atm. Air [4].

The following outcomes are possible after a droplet collision:

- Bouncing - If the layer of gas trapped between the drops is not expelled at collision, bouncing occurs. The droplets bounce if the following criterion is met:

  $We < \frac{\Delta(1+\Delta^2)(4\Theta'-12)}{\chi_1\{\cos[\sin^{-1}(B)]\}^2}$, where Θ' is a shape factor and χ_1 is a function of the drop-sizes and the impact parameter. The velocities of the droplets after collision are determined based on a method given by Pischke et al. [5]. The critical We for bouncing varies with the ambient gas pressure, and a correction, accounting for the gas pressure, is applied based on Post and Abraham's [6] approach.

- Coalescence – At Weber numbers higher than the critical We for bouncing, the droplets coalesce to form a single droplet. The criterion for coalescence to occur is $B \le \sqrt{e_{coal}}$. Here e_{coal} is the collision efficiency given by

  $e_{coal} = \min\{1.0, [2.4(\gamma^3 - 2.4\gamma^2 + 2.7\gamma).We\}, \gamma = 1/\Delta$.

- Off-centre or stretching separation – Droplets colliding at moderate to high impact parameters combine temporarily, but finally separate into two or more drops due to the kinetic energy of the non-contacting portion overcoming the surface energy of the interacting region. Stretching separation occurs if $B > \sqrt{e_{coal}}$. The size of the child droplets is obtained by solving the non-linear equation for the ligament radius at breakup:

  $\frac{0.75}{\sqrt{2}}(k_1\alpha)We^{1/2}{}_0\overline{r_{bu}}^{7/2} + \overline{r_{bu}}^2 - 1 = 0$.

- Near head-on or reflexive separation – Near head-on collisions i.e. collisions with low impact parameters result in reflexive separation, in which the droplets form a torus whose outer part stretches and breaks to produce drops. The Weber number criterion for reflexive separation is:

$$We > \frac{3[7(1+\Delta^3)^{2/3} - 4(1+\Delta^2)]\Delta(1+\Delta^3)^2}{(\Delta^6\eta_1 + \eta_2)}$$, where η_1 and η_2 are functions of B and Δ.

IV.2.5 Complete evaporation model results for biofuel components

Penetration lengths for biofuels: Simulations were performed for single stationary droplets suspended in a stagnant environment. Different amounts of these components were mixed to n-hexadecane, which acts a single-component surrogate for diesel. The droplet lifetime results for these simulations are shown in Figure IV.23. The initial droplet temperature for these simulations was 400 K and the droplet diameter was 50 μm. The gas pressure was maintained at 1 atm. and the gas temperature was 850 K. In Figure IV.23, the y-axis corresponds to the droplet lifetime normalized by the droplet lifetime of a pure n-hexadecane droplet. The x-axis indicates the mass percentage of the biofuel mixed with n-hexadecane. In the case of methyl oleate, the droplet lifetime increases for all mass compositions since it is both heavier and less volatile than n-hexadecane. For the other four components, which are more volatile than n-hexadecane, the droplet lifetime increases when these components comprise 25% by mass. This is due to evaporative cooling of the gas near the droplet which reduces the rate of evaporation of the still significant amount of n-hexadecane. As the mass fraction of the biofuels is increased, the droplet lifetime starts decreasing due to lesser amount of n-hexadecane in the droplet evaporating in shorter time despite the cooling effect of the more volatile components. This is only a preliminary study of the evaporation of biofuels and biofuel blends. In the future, more studies would be carried out to characterize the behavior of these components, including penetration length studies, allowing us to tailor biofuel blends for different operating conditions.

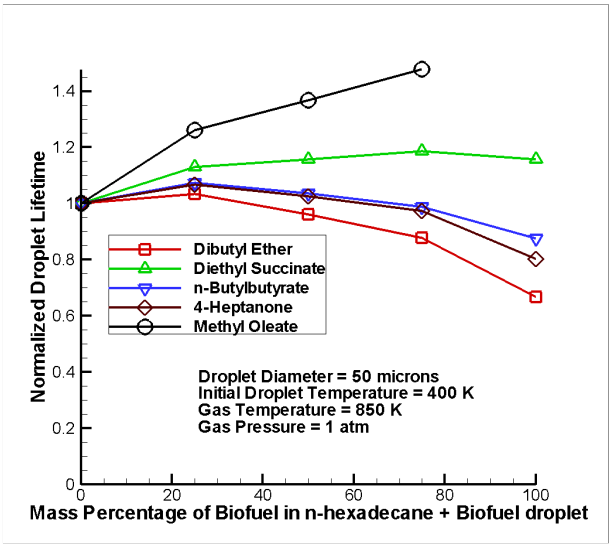

Figure IV.23. Droplet lifetimes for biofuel-blends

Single drop and penetration length studies have been carried out to characterize the behavior of blends of methyl oleate (canola biodiesel), Dibutyl succinate (DBS), 2-ethylhexyl nonanoate, butyl nonanoate, isobutyl nonanoate, 2-ethylhexyl butyrate and a diesel surrogate (n-hexadecane).

The physical properties of these components have been calculated using suitable correlations and methods given in Poling et al. [1]. Table IV.1 gives a list of the methods and expressions used to calculate the properties and Table IV.2 lists some of the properties of the various fuel components. Figures IV.24 – IV.29 show the variation of the physical properties important for evaporation, with temperature.

Methyl oleate has the highest liquid specific heat (Figure IV.24), highest vapor specific heat (Figure IV.25), highest latent heat of vaporization (Figure IV.26), lowest vapor pressure (Figure IV.27), and lowest thermal conductivity (at lower temperatures, Figure IV.28). This implies that a higher concentration of methyl oleate would require higher heat input for droplet heating and evaporation. On the contrary, 2-ethylhexyl butyrate lies at the other end of the spectrum with the lowest liquid specific heat and latent heat of vaporization and the highest vapor pressure and is the most volatile of the components considered here. Butyl nonanoate and isobutyl nonanoate have properties similar to 2-ethyl hexyl butyrate and similar results can be expected. The specific heat and vapor pressure of 2-ethylhexyl nonanoate are closer to methyl oleate as compared to other components and its volatility should be similar too. dibutyl succinate has intermediate properties but its density (Figure IV.29) is also the highest. Consequently, droplets with DBS would take longer to evaporate due to the higher mass.

In order to understand the evaporation and spray characteristics of the bio-fuel components, two sets of studies have been done. The first set of simulations consists of stationary droplets, suspended in a stagnant environment. The droplets are composed of two components, with methyl oleate as the base fuel and a second component. The initial droplet size and temperature are 50 μm and 400 K, respectively. The gas pressure and temperature are 1 atm. and 700 K, respectively. The second set consists of spray simulations, with the droplets having the same composition as the stationary droplets. The gas temperature and density are 700 K and 14.8 kg/m3, injection pressure is 138 MPa, the nozzle dia is 0.246 mm and injected liquid temperature is 436 K. Table IV.3 shows the droplet composition for the various simulations.

Table IV.1: Methods used to calculate the physical properties of biofuel components [1]

Property (Method)	Expression
Critical Temperature	$T_c(K) = 181.128 \ln \left[\sum_k N_k(tc1k) + W \sum_j M_j(tc2j) \right]$ (2-2.5)
Critical Pressure	$P_c(bar) = \left[\sum_k N_k(pc1k) + W \sum_j M_j(pc2j) + 0.10022 \right]^{-2} + 1.3705$ (2-2.6)
Critical Volume	$V_c(cm^3\ mol^{-1}) = -0.00435 + \left[\sum_k N_k(vc1k) + W \sum_j M_j(vc2j) \right]$ (2-2.7)
Acentric Factor	$\omega = 0.4085 \left\{ \ln \left[\sum_k N_k(w1k) + W \sum_j M_j(w2j) + 1.1507 \right] \right\}^{(1/0.5050)}$ (2-3.4)
Liquid Density (Rackett Equation)	$V_s = V_c^R(0.29056 - 0.08775\omega)^{\phi}$ (4-11.4a) $\phi = (1 - T/T_c)^{2/7} - (1 - T^R/T_c)^{2/7}$ (4-11.5)
Liquid Specific Heat (Corresponding States Method)	$\frac{C_p^r}{R} = \frac{C_p - C_p^o}{R}$ $= 1.586 + \frac{0.49}{1 - T_r} + \omega \left[4.2775 + \frac{6.3(1 - T_r)^{1/3}}{T_r} + \frac{0.4355}{1 - T_r} \right]$ (6-6.4)
Vapor Specific Heat (Joback Method)	$C_p^o(T) = \left\{ \sum_k N_k CpAk - 37.93 \right\} + \left\{ \sum_k N_k CpBk + 0.210 \right\} T + \left\{ \sum_k N_k CpCk - 3.91E-04 \right\} T^2 + \left\{ \sum_k N_k CpDk + 2.06E-07 \right\} T^3$ (J mol^{-1} K^{-1}) (3-3.3)
Vapor Pressure (Riedel Corresponding States Method)	$\ln P_{vp_r} = A^+ - \frac{B^+}{T_r} + C^+ \ln T_r + D^+ T_r^6$ (7-5.4) where $A^+ = -35Q$ $B^+ = -36Q$ $C^+ = 42Q + \alpha_c$ $D^+ = -Q$ $Q = K(3.758 - \alpha_c)$ (7-5.5) $\alpha_c = \frac{3.758K\psi_b + \ln(P_c/1.01325)}{K\psi_b - \ln T_{br}}$ (7-5.6) $\psi_b = -35 + \frac{36}{T_{br}} + 42 \ln T_{br} - T_{br}^6$ (7-5.7)
Enthalpy of Vaporization (Law of Corresponding States)	$\frac{\Delta H_v}{RT_c} = 7.08(1 - T_r)^{0.354} + 10.95\ \omega(1 - T_r)^{0.456}$ (7-9.4)
Surface Tension (Sastri and Rao Method)	$\sigma = KP_c^x T_b^y T_c^z \left[\frac{1 - T_r}{1 - T_{br}} \right]^m$ (12-3.12)

Table IV.2: Properties of Biofuel Components

Species\Property	Molecular Weight (kg/kmol)	Critical Temperature, Tc (K)	Critical Pressure, Pc (bars)
Dibutyl Succinate ($C_{12}H_{22}O_4$)	230.3	715.4418	47.6475
2-EthylHexyl Nonanoate($C_{17}H_{34}O_2$)	270.46	745.4561	26.5212
Butyl Nonanoate ($C_{13}H_{26}O_2$)	214.34	703.4173	41.9401
iso-Butyl Nonanoate ($C_{13}H_{26}O_2$)	214.34	698.6097	41.9401
2-EthylHexyl Butyrate ($C_{12}H_{24}O_2$)	200.32	684.7253	48.0276

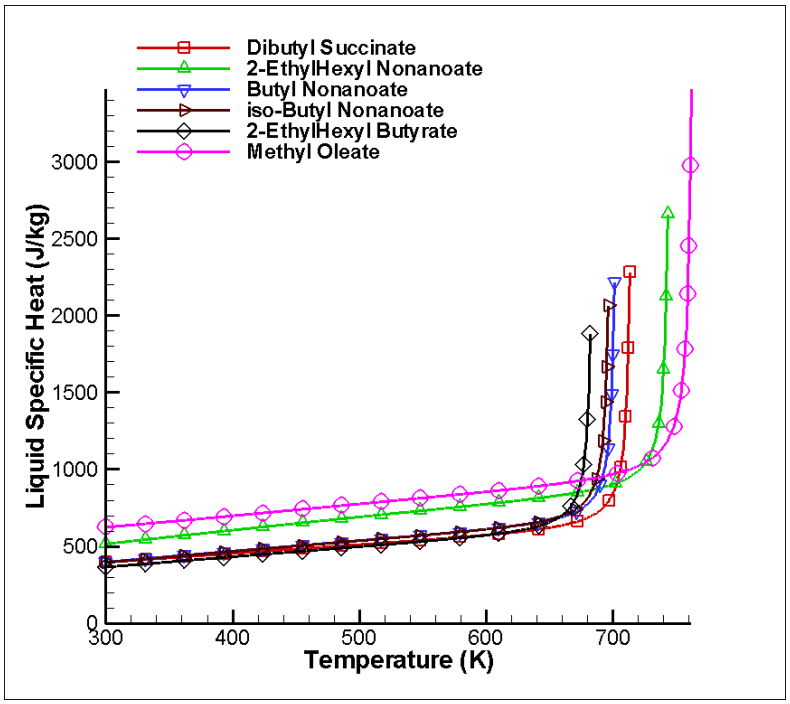

Figure IV.24. Liquid Specific Heat

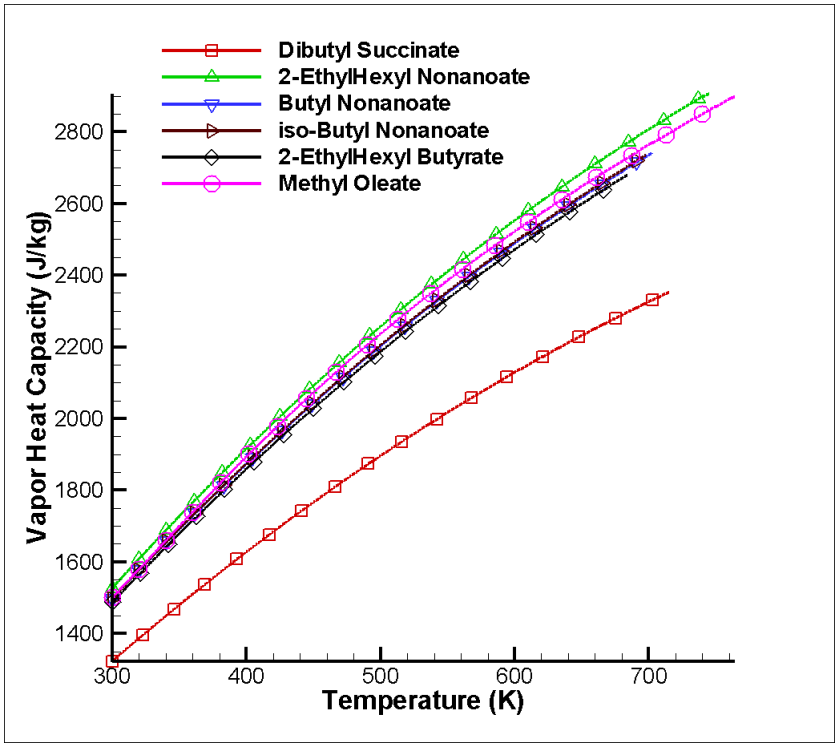

Figure IV.25. Vapor Heat Capacity

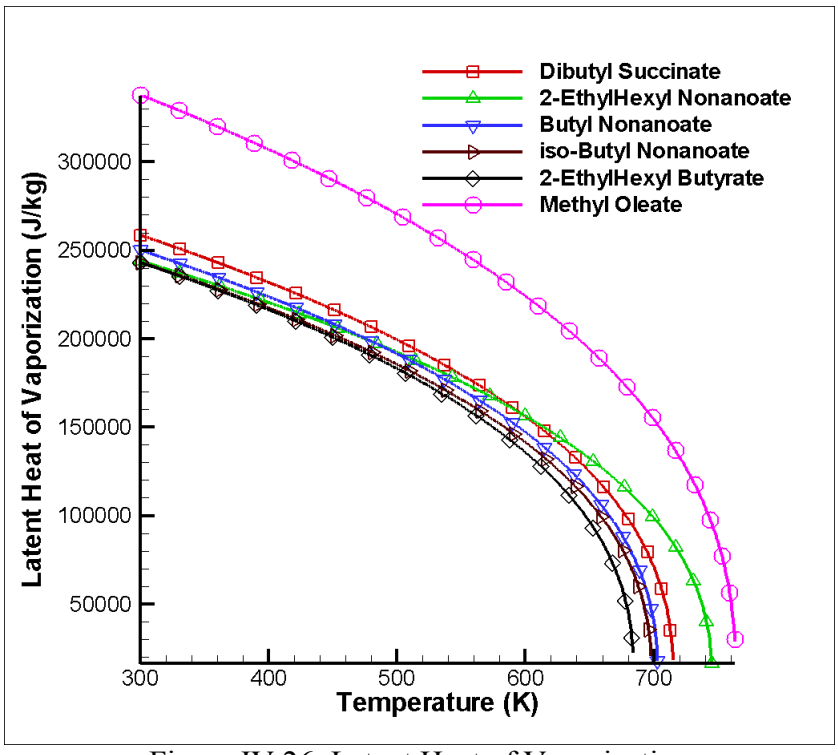

Figure IV.26. Latent Heat of Vaporization

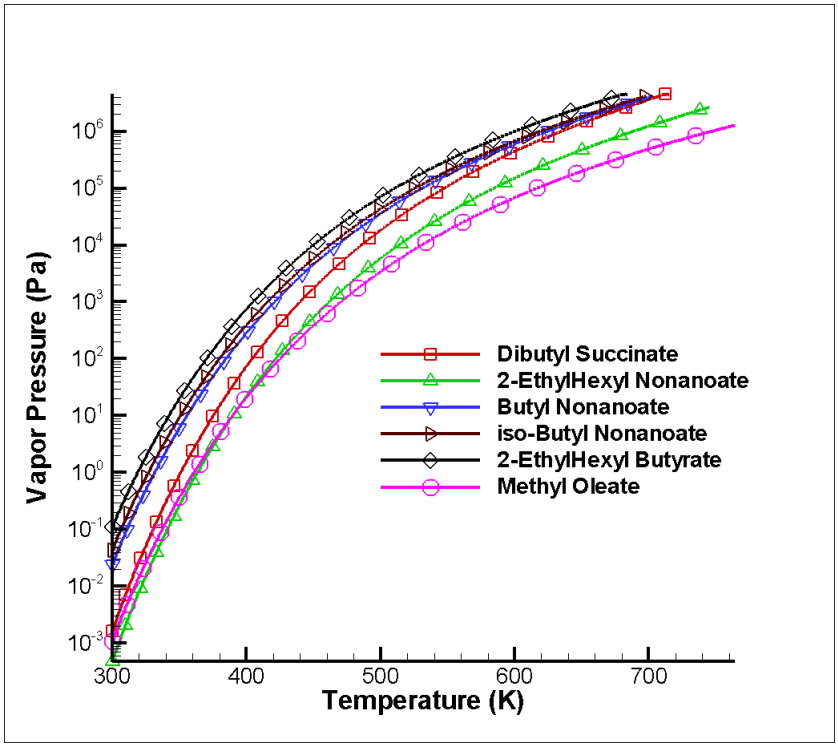

Figure IV.27. Vapor Pressure

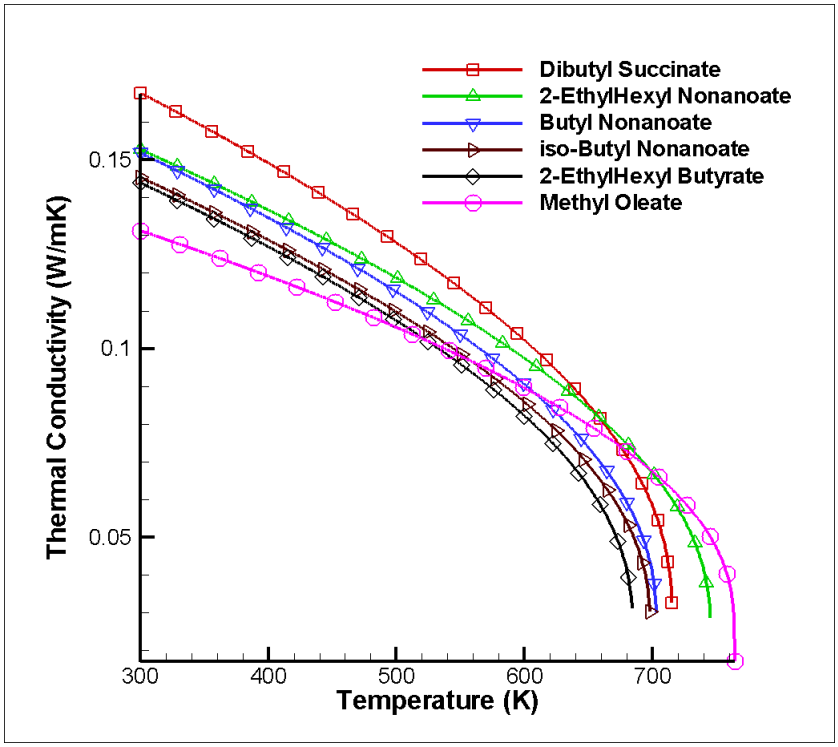

Figure IV.28. Thermal Conductivity

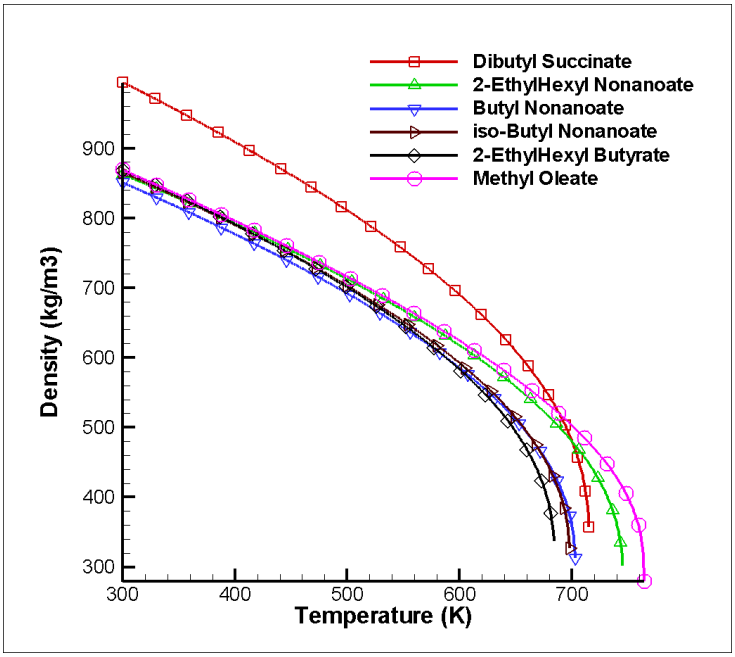

Figure IV.29. Liquid Density

Figure IV.30 shows the droplet lifetimes for stationary droplets of compositions given in Table IV.3. As expected, the shortest droplet lifetimes are for bi-component droplets with 2-ethylhexyl butyrate due to its higher volatility. Since methyl oleate is the least volatile of all the species considered, the droplet lifetimes decrease as the mass fraction of the second, more volatile component, is increased. The highest droplet lifetimes are for methyl oleate + dibutyl succinate droplets, due to their higher mass and higher latent heat of vaporization.

Figures IV.31 and IV.32 show the normalized droplet area and bulk temperatures for droplets with 50% methyl oleate and 50% of the second component by mass, respectively. The droplet with 2-ethylhexyl nonanoate has the highest increase in temperature and longer heating time, but the rate of evaporation increases with time and the droplet evaporates earlier than the dibutyl succinate droplet. The area and temperature trends for the droplets with butyl nonanoate, isobutyl nonanoate and 2-ethylhexyl butyrate are similar. Figure IV.33 shows the gas phase mass fractions of the second component in the evaporated fuel vapor in the vicinity of the droplet, for the case with 50% by mass composition. Initially, there is no evaporation of methyl oleate and the fuel vapor consists entirely of the second component. As methyl oleate starts evaporating, the mass fraction of the other components decreases, but starts increasing as the droplet starts heating and the more volatile component evaporates faster. After the initial heating of the droplet, the rate of evaporation of the components reaches a maximum value and remains constant for most of the lifetime. As the second component mass fraction decreases in the droplet, most of the newly evaporated fuel is now composed of methyl oleate and thus, the mass fraction of the second component in the vapor decreases.

Table IV.3. Fuel Composition for the single droplet and spray simulations

S. No.	Fuel Composition (Mass Percentage)					
	Base Fuel - Canola (Methyl oleate)	**Dibutyl Succinate**	**2-ethylhexyl nonanoate**	**Butyl Nonanoate**	**Isobutyl Nonanoate**	**2-ethylhexyl butyrate**
1	90	10	0	0	0	0
2	80	20	0	0	0	0
3	70	30	0	0	0	0
4	60	40	0	0	0	0
5	50	50	0	0	0	0
6	40	60	0	0	0	0
7	30	70	0	0	0	0
8	20	80	0	0	0	0
9	10	90	0	0	0	0
10	90	0	10	0	0	0
11	80	0	20	0	0	0
12	70	0	30	0	0	0
13	60	0	40	0	0	0
14	50	0	50	0	0	0
15	40	0	60	0	0	0
16	30	0	70	0	0	0
17	20	0	80	0	0	0
18	10	0	90	0	0	0
19	90	0	0	10	0	0
20	80	0	0	20	0	0
21	70	0	0	30	0	0
22	60	0	0	40	0	0
23	50	0	0	50	0	0
24	40	0	0	60	0	0
25	30	0	0	70	0	0
26	20	0	0	80	0	0
27	10	0	0	90	0	0
28	90	0	0	0	10	0
29	80	0	0	0	20	0
30	70	0	0	0	30	0
31	60	0	0	0	40	0
32	50	0	0	0	50	0
33	40	0	0	0	60	0
34	30	0	0	0	70	0
35	20	0	0	0	80	0
36	10	0	0	0	90	0
37	90	0	0	0	0	10
38	80	0	0	0	0	20
39	70	0	0	0	0	30
40	60	0	0	0	0	40
41	50	0	0	0	0	50
42	40	0	0	0	0	60
43	30	0	0	0	0	70
44	20	0	0	0	0	80

45	10	0	0	0	0	90

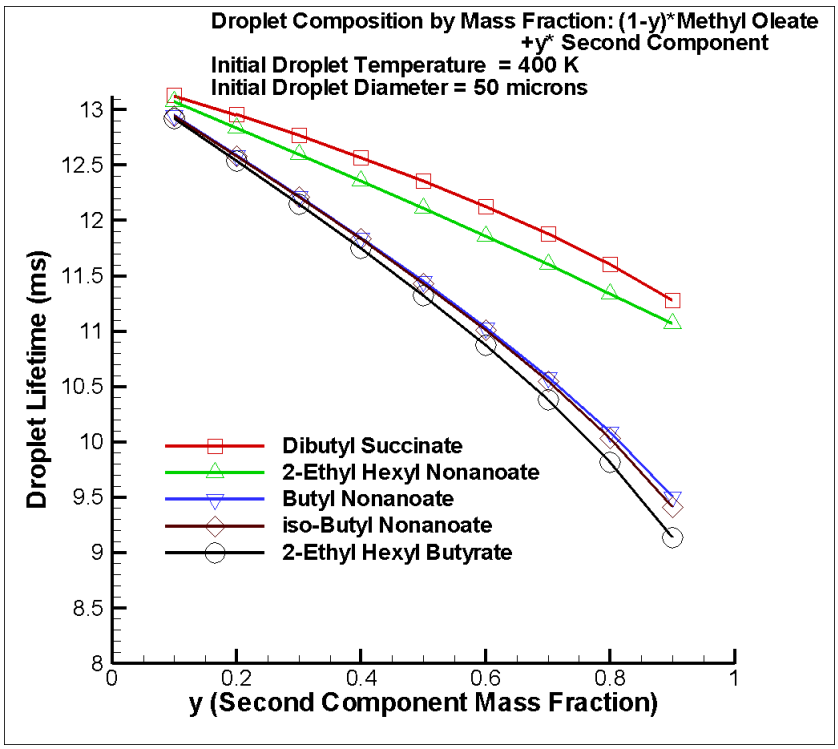

Figure IV.30. Droplet Lifetime

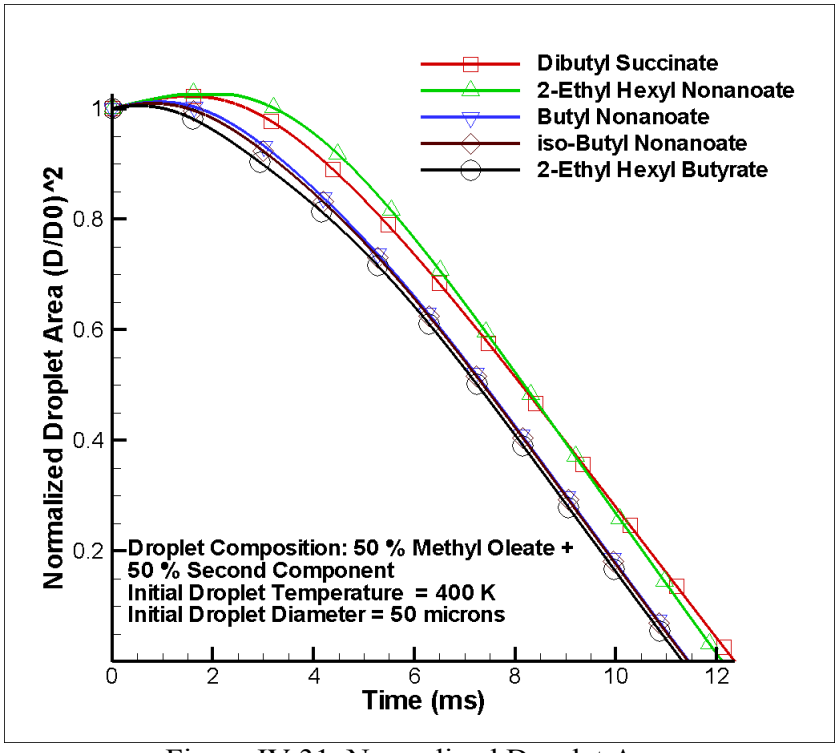

Figure IV.31. Normalized Droplet Area

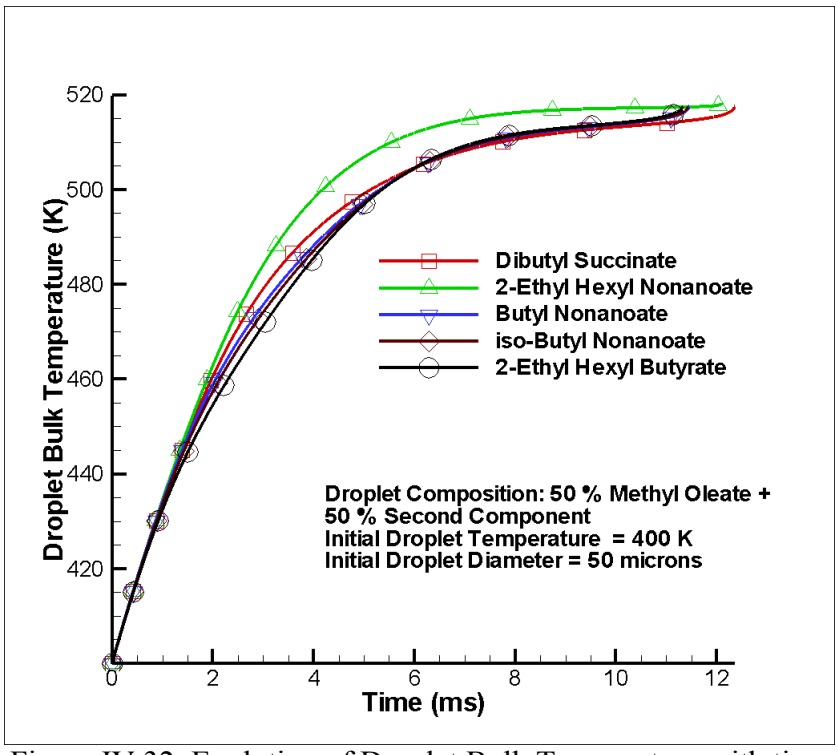

Figure IV.32. Evolution of Droplet Bulk Temperature with time

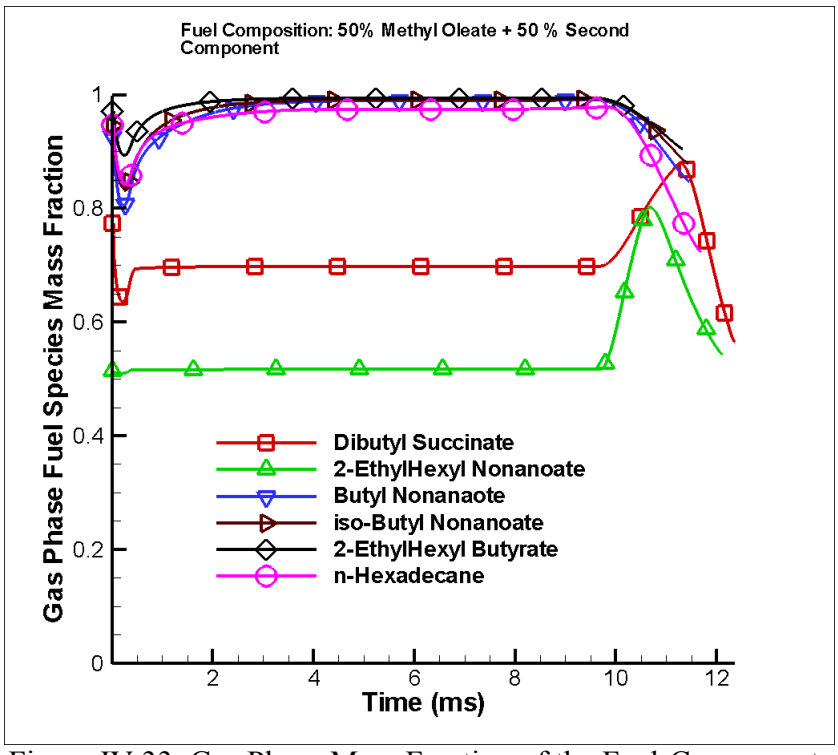

Figure IV.33. Gas Phase Mass Fraction of the Fuel-Components

Figure IV.34 shows the spray penetration lengths of fuels with different compositions. The penetration length is a measure of the length of the evaporating liquid jet injected into the

combustion chamber. A smaller penetration length indicates that the jet breaks up and evaporates faster and this might allow better mixing of the evaporated fuel with the air/oxidizer. Along with the fuel species considered above, the figure also shows the penetration lengths for mixtures of methyl oleate and n-hexadecane. The trends in Figure IV.34 indicate that as the mass fraction of the second component is increased the penetration length decreases. This is expected as the second components are more volatile than methyl oleate and the evaporation is faster. However, the penetration length reaches a minimum when the mass fraction of the second species is around 0.5-0.7 and increases when the mass fraction is increased further. A possible reason for this trend is the lower surface tension of methyl oleate at lower temperatures (Figure IV.35). For droplets with a higher concentration of methyl oleate, the breakup is faster, but the droplets evaporate slowly, leading to higher penetration lengths. As the mass fraction of methyl oleate is decreased the surface tension of the droplet increases and breakup is slower, but the droplets are more volatile, decreasing the penetration length. But as the mass fraction of methyl oleate is further decreased, the increase in volatility is countered by the higher surface tension and slower breakup, and consequently the penetration length increases. Figure IV.34 also shows that the lowest penetration lengths are for droplets with methyl oleate and n-hexadecane. The penetration lengths for the sprays with methyl oleate and dibutyl succinate are the highest, while the penetration lengths of other mixtures lie in between.

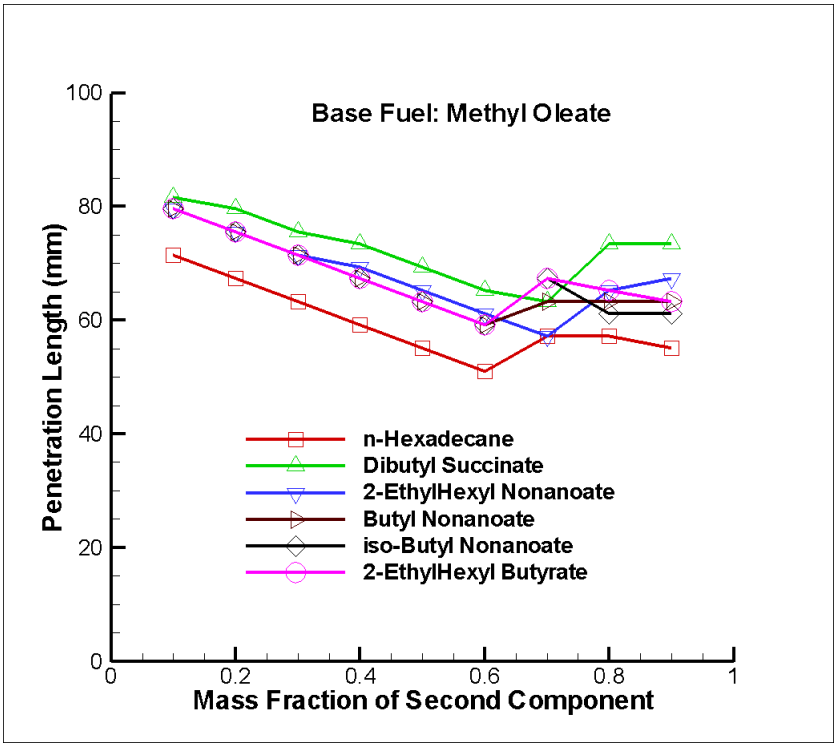

Figure IV.34. Penetration Length

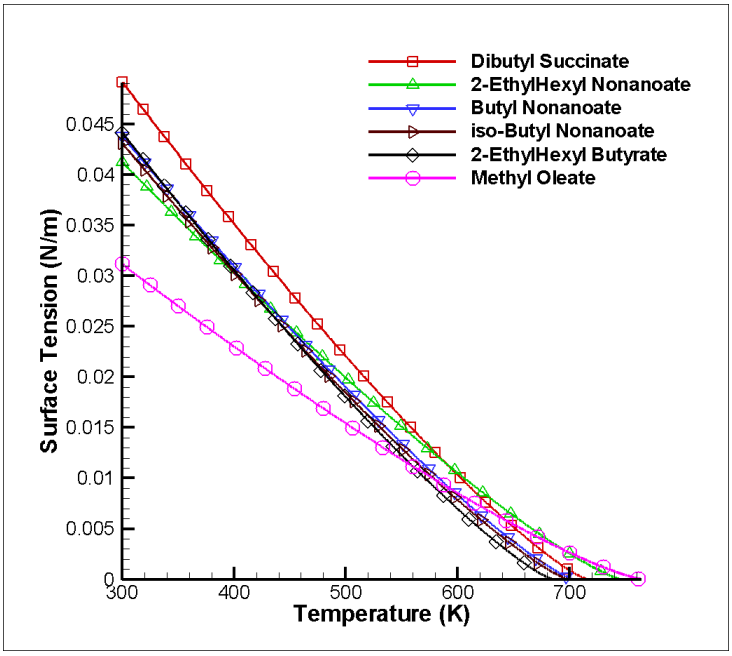

Figure IV.35. Surface tension

Figure IV.36 shows the mean mass fractions of the fuel vapor at different cross-sections of the domain at the end of the evaporation process. The trends for the different species are similar, although the mass fraction of dibutyl succinate is higher at the end of the domain due to the higher penetration length of the spray.

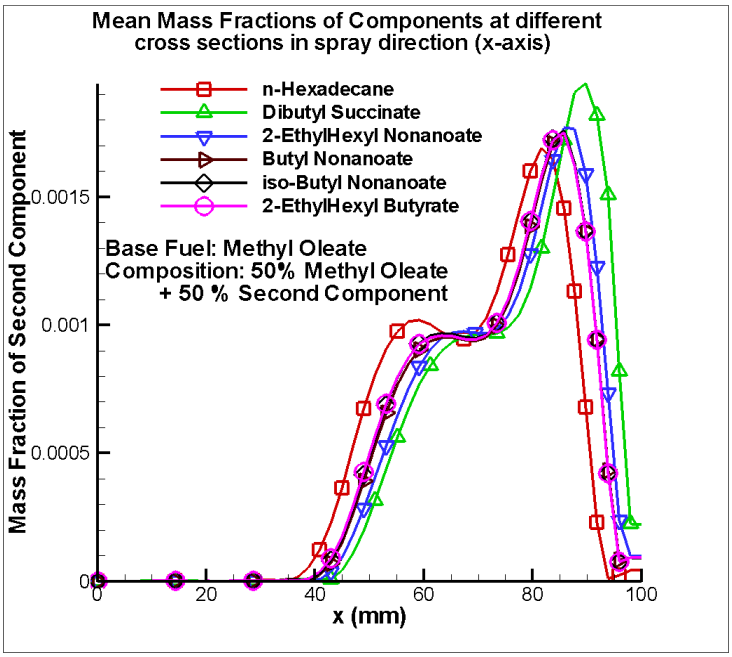

Figure IV.36. Mean mass fractions of components at different cross-sections in spray direction.

Figure IV.37 shows the evolution of dibutyl succinate vapor mass fraction of in the z=0 plane for the composition 50 % Methyl oleate and 50 % dibutyl succinate. Due to the high penetration length, the maximum concentration of the fuel is near the end of the domain.

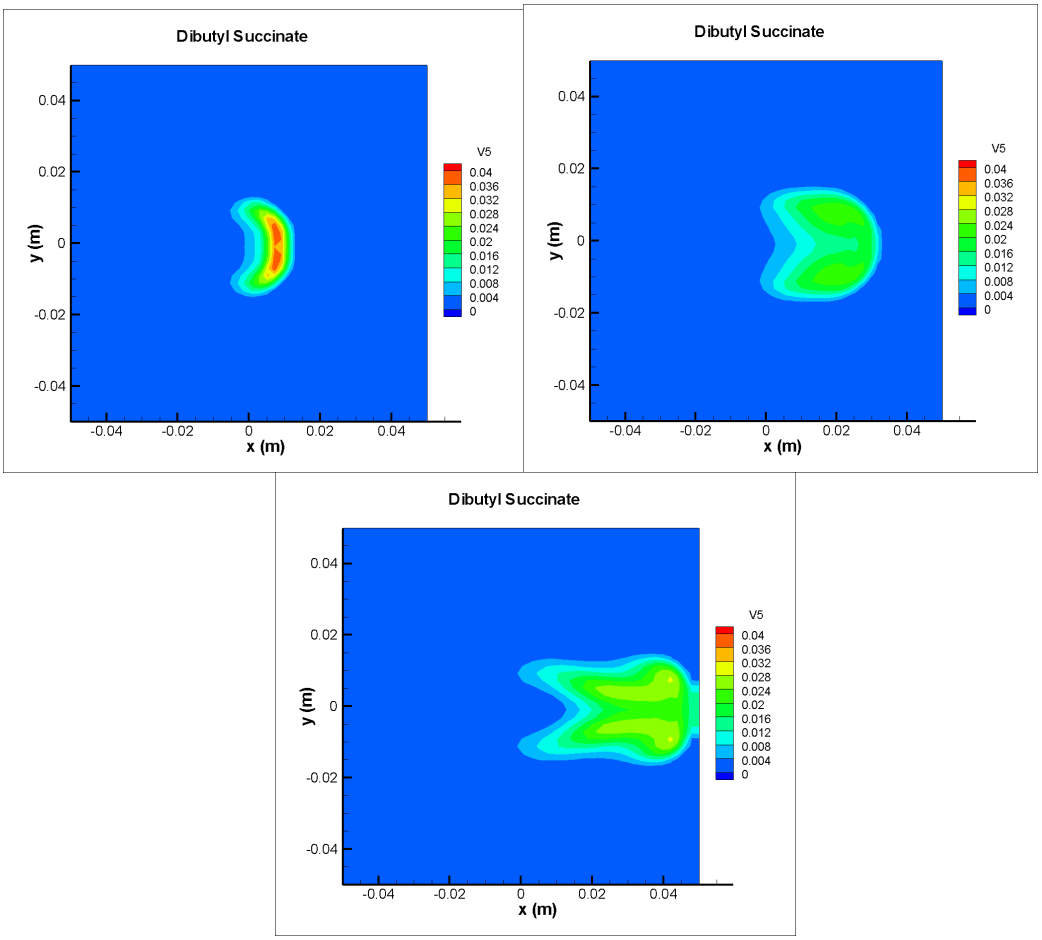

Figure IV.37. Evolution of dibutyl succinate vapor mass fraction of in the z=0 plane.

V. Experimental Engine Studies

V.1 Description of Single Cylinder MSU Engine and Components

V.1.1 Fuel delivery system

We have revised the fuel delivery system on the MSU optical engine in order to facilitate combustion testing of small quantities of biofuels. To do this, we have purchased and installed a pressure transfer vessel (Figure V.1 and V.2) that uses the present fuel delivery system to drive biofuels through the engine injectors. The pressure transfer vessel is a machined cylinder with a fitting on each end and a movable piston that serves as a seal between the two sides of the cylinder. As pressure is applied by one fluid, force is transferred across the piston to the other side of the cylinder. Thus, it is possible to drive biofuels into the optical engine using regular diesel in the main pressure system.

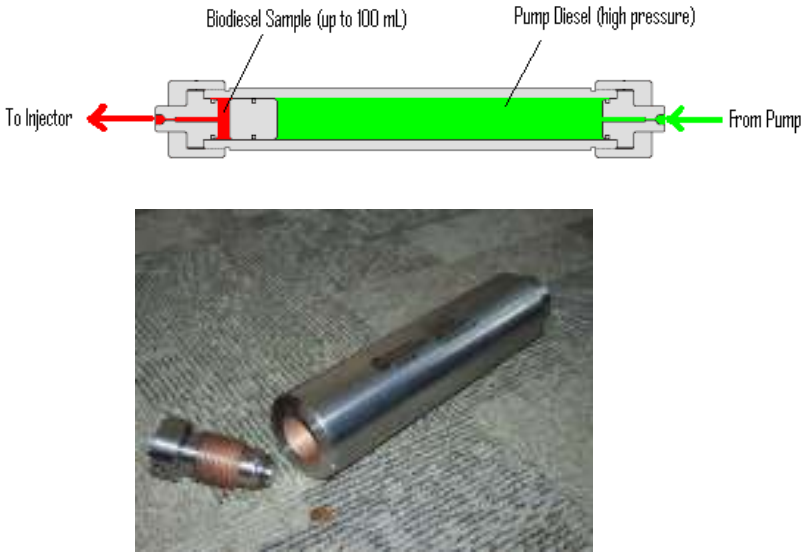

Figure V.1. Cylinder and piston for biofuel delivery to optical engine.

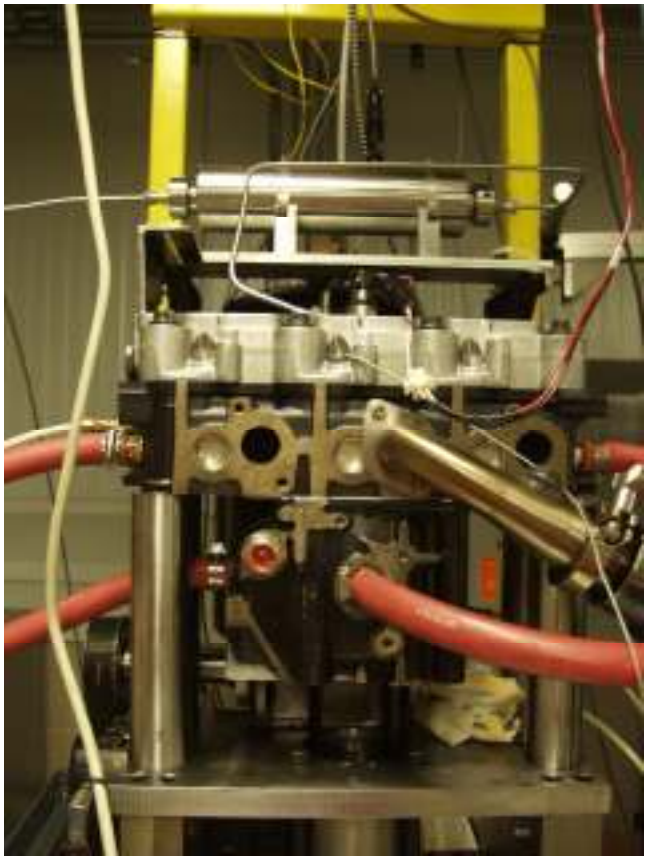

Figure V.2. Front view of the engine and FSC setup installed above the engine.

V.1.2 Optical engine control system

In order to gain proper insight into the events occurring inside an engine, boundary conditions must be maintained between experiments. An Opal RT based engine controller system connected to a PC interface was thus installed. The PC interface allows for altering of certain important parameters. The control system controls several subsystems important to the creation and continuance of proper boundary conditions. The control system allows for repeatable boundary conditions of the engine, which translates to comparable in-cylinder results within and between experiments.

The controller programming is based mainly on a setup that was previously used for a single-cylinder Diesel engine experiment at the research laboratory. This non-optical engine has similar geometry to the optical engine, meaning little modification of the program was required. Head temperature and intake charge control schemes were added to this program. A user interface is run on the PC, with direct communication with the controller, which allows changing of the outputs of the system. The PC updates the Opal-RT in real time, such that the parameters controlled can be varied. The sensors inputted into the controller are also communicated and displayed via the PC.

The controller system consists of several subsystems that need to be controlled in order to achieve proper, consistent boundary conditions. The subsystems controlled by the Opal-RT are as follows:

- Fuel Rail Pressure Subsystem
- Intake Oxygen Percentage, Gas Temperature and Plenum Pressure Subsystem
- Engine Head and Coolant Tank Temperature Subsystem
- Injector Subsystem

The fuel rail pressure is controlled using a PWM (Pulse Width Modulation) board with two output signals to control the pressure valve solenoid and the volume valve solenoid of the fuel pressure pump. The resulting pressure is mapped to the outputted PWM signals in order to ensure proper behavior of the system. If a solenoid signal commands too small of an opening of its valve, a drop in rail pressure may be seen when the injector begins firing; too large an opening could mean that the pressure will not be able to achieve the commanded injection pressure. A Kistler piezo-electric pressure transducer is mounted in the common rail for feedback of this subsystem. The controller uses this feedback to ensure an accurate fuel rail pressure.

The intake charge subsystem controls intake oxygen percentage, plenum pressure, and gas temperature. The intake plenum pressure and intake oxygen percentage are controlled using two electronically actuated butterfly valves. There is a valve placed in the compressed air supply line and another valve in the compressed nitrogen supply line. Controlling these valves allows for independent variation of the flow of air and nitrogen into the intake system. Together, this valve system allows for changes in oxygen percentage while varying the plenum pressure. A results mapping of the actuated butterfly valves are necessary to relate valve position to plenum pressure and oxygen percentage. A Kistler piezo-resistive pressure sensor is mounted in the intake plenum to provide feedback for the plenum pressure. An AFR sensor provides an output of the oxygen percentage flowing through the primary intake runner. Downstream of the butterfly valves, a heater is controlled and used to heat the intake air charge. A thermocouple is used to sample the intake temperature downstream of the heater for feedback to the controller. This subsystem yields similar in-cylinder motoring pressures, oxygen concentrations, and temperatures such that comparisons can be made between experiments.

The engine head and coolant tank temperatures are controlled using a single subsystem. The hardware includes a heating element inside a slightly modified home hot water heater tank to heat “coolant” that flows through pipes, through the coolant passages of the engine head, and back to the tank. This is done to preheat the head in order to simulate steady-state over-the-road operating conditions. The system samples two thermocouples: one just downstream of the engine head and one inside the heater tank itself. The subsystem is set such that the tank can preheat without heating the head. This allows for cleaning of the engine head and piston assembly while the system begins heating the coolant without heating the engine head. When the engine is cleaned and ready, a pump can be turned on with a valve opened, allowing for the system to circulate hot coolant to the head, and thereby preheating the engine head. This subsystem setup this way reduces the amount of time required between experiments, as the head can be cooled and cleaned between experiments without the need to reduce the temperature of the coolant.

The fuel injector system is controlled by the Opal-RT controller as well. A pulse per cycle, pulse per revolution, and crank angle signal is needed for the Opal-RT to determine the correct placement of the injector pulse in the engine cycle. It is possible to set the injector pulse width and crank angle of injection using the PC interface and, therefore, the controller. A TTL (transistor-transistor logic) signal is outputted from the controller to the injector driver.

The Opal-RT controller system creates more repeatable in-cylinder conditions in the single-cylinder optical Diesel engine. A PC interface allows for modification of parameters. The

PC communicates these changes to the controller as well as display outputs of the controller. Several subsystems are controlled by the Opal-RT system.

V.2 Combustion of Petroleum Diesel and Biofuel Components

V.2.1 Early experiments with diesel and canola biodiesel

Biofuel Combustion in MSU Test Engine Facility: Figure IV.3 shows in graphic form a sequence of infrared images of combustion in an operational compression ignition engine. The top sequence of images shows a canola derived methyl ester (biodiesel) synthesized at Michigan State University, and the bottom normal pump diesel fuel. Injection started at 9° BTDC in both configurations; however, the details of mixing and subsequent combustion are quite different. Experience has shown that there is at least a 10% difference in efficiency when timing of the combustion event has the variability shown in this figure. Our goal is to develop a scientific understanding of why these differences occur and what can be done to optimize combustion efficiency while decreasing NOx and particulate emissions.

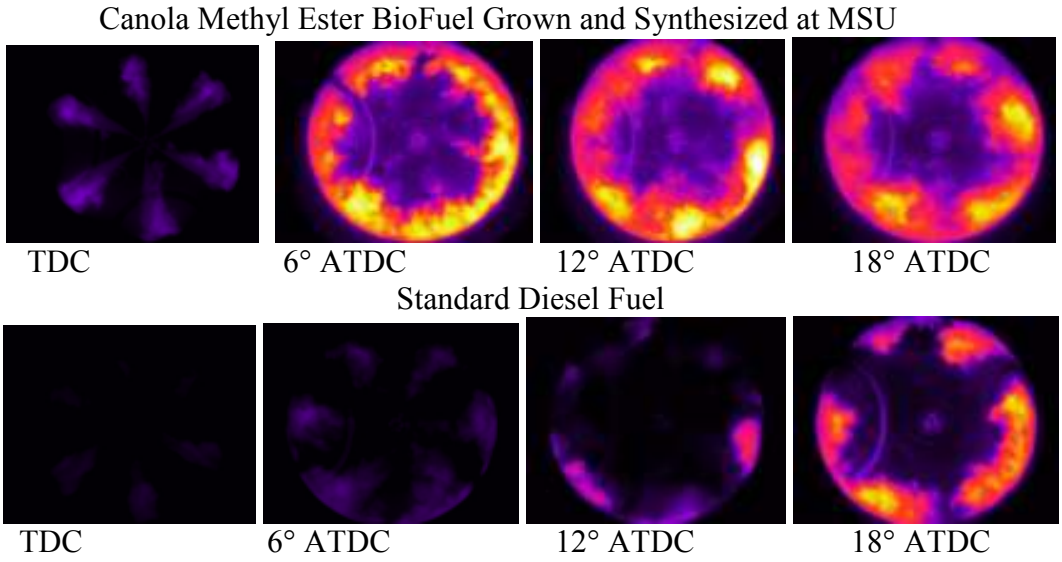

Figure V.3. Images of Compression Ignition in MSU's Optical Engine
Turbocharged diesel engine CR=18:1, 0.35 bar boost,
1500 RPM, light load, 2000 bar injection pressure

V.2.2 Detailed biofuel combustion testing with controlled optical engine

A data acquisition and control systemfor the optical engine were installed. Infrared and high-speed, visible images were recorded of combustion using pump Diesel, B100 Canola, and a 60/40 blend of Canola and DBS (Can/DBS). Only the infrared images are presented here for conciseness and the lack of information provided by the visible images. Three operating conditions were selected for running of these fuels. The results show trends which were expected from the Ford experiments. The pure canola fuel showed the shortest ignition delay, while the DBS caused a large delay in combustion.

The engine controller described above is an Opal-RT based system with a PC interface. This system is set to control the auxiliary systems of the engine, including intake oxygen percentage and boost pressure, coolant temperature, injection timing and pulse width, as well as fuel rail pressure. The system is capable of five injections per cycle. Currently the system is not set to control either intake or fuel temperature. Modifications are currently being made to control these parameters, as testing showed these parameters to be possible sources of variation between tests. Also important is the installation of electronically controlled valves in the intake system. These valves allow for the control of intake pressure and oxygen percentage when used with the controller.

The operating points used in these experiments were chosen from the representative operating conditions supplied by Ford. Three combustion strategies were examined: One low temperature combustion (LTC) strategy as well as two conventional combustion strategies. The operating conditions corresponding to these points can be seen in Table V.1. Important to note in these cases is that the IMEPs are attempted to be matched between fuels. Matching the IMEPs required that pulse widths between the fuels be modified. That is, because the biofuels are less energy dense, more fuel needed to be injected. It was also found that the Can/DBS mixture would not ignite under the Conventional Combustion 2 operating point and these results are therefore not presented. It was also necessary to advance the main injection timing for the mixture case under Conventional Combustion 3 cases in order to achieve the targeted IMEP. All experiments were run at 1500 rpm, a cylinder and head temperature of 190˚F, and with a fuel rail pressure of 30000 psi.

Table V.1: Operating conditions used in these experiments.

Case	Goal IMEP	Pilot PW (ms)	Pilot PW CAD	Main PW (ms)	Main PW CAD	Intake (bar)	O2%
Diesel LTC 1	3.5	N/A	N/A	0.36	15 BTDC	1.2	13
Diesel Conv Comb 2	3.5	0.22	15 BTDC	0.305	0	1.2	17
Diesel Conv Comb 3	6.4	0.22	20 BTDC	0.4	0	1.3	17
Canola LTC 1	3.5	N/A	N/A	0.36	15 BTDC	1.2	13
Canola Conv Comb 2	3.5	0.22	15 BTDC	0.305	0	1.2	17
Canola Conv Comb 3	6.4	0.22	20 BTDC	0.4	0	1.3	17
Can/DBS LTC 1	3.5	N/A	N/A	0.4	15 BTDC	1.2	13
Can/DBS Conv Comb 2	N/A	N/A	N/A	N/A	N/A	N/A	N/A
Can/DBS Conv Comb 3	6.4	0.25	20 BTDC	0.45	5	1.3	17

The images produced from these experiments show similarities to trends seen in the pressure data recorded from these experiments. Selected infrared images, at every 9 CAD after the commanded injection, can be seen in the images found in Figures V.4, V.7, and V.10. The pressure traces from each of these operating cases are in Figures V.5, V.8, and V.11. In these figures the heat release can be examined. The IMEPs of each operating point were used to determine the combustion consistency. If there is a variation on the order of 25% between cycles

in IMEP, the combustion strategy is said to be inconsistent. The IMEP for each cycle is plotted in Figures V.60, V.9, and V.12. It was seen in each operating case that certain conditions produce inconsistent combustion of the different fuels. The trends, seen in these Figures, show that an earlier ignition could lead to more consistent combustion. Startup effects are also seen through these plots, as the IMEP values initially grow as the cycles continue, before reaching a level value. It was seen through examination of these figures that an earlier start of combustion is correlated with more consistent combustion and for those combustion cases which were more consistent, startup effects were also less noticeable.

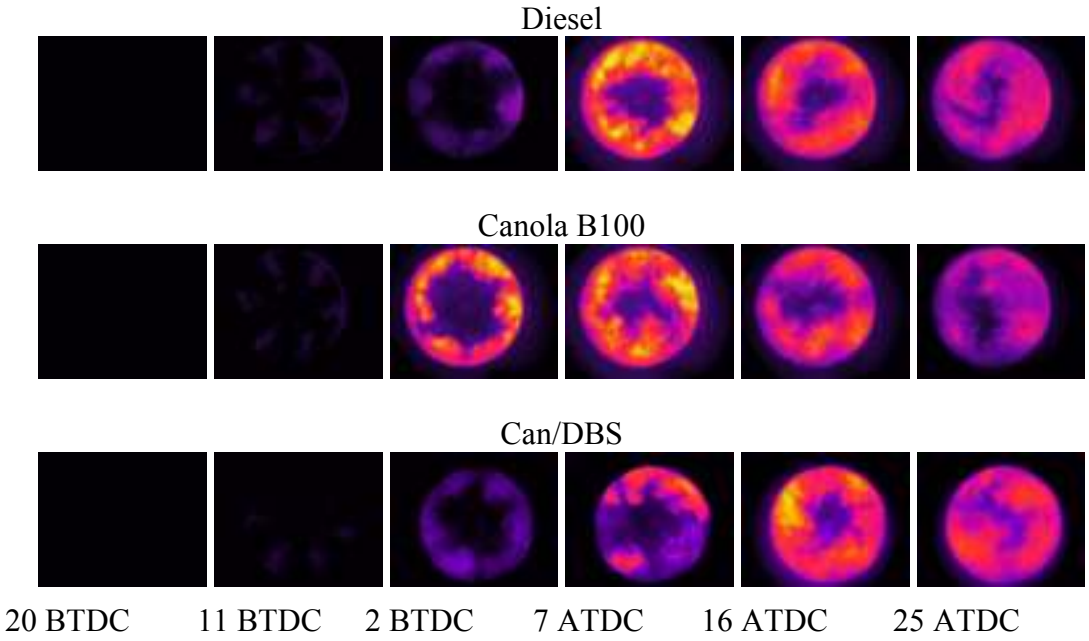

Figure V.4: Infrared images of the different fuels under LTC 1 operating condition illustrating the advanced combustion of the B100 and delayed combustion of the Can/DBS mixture.

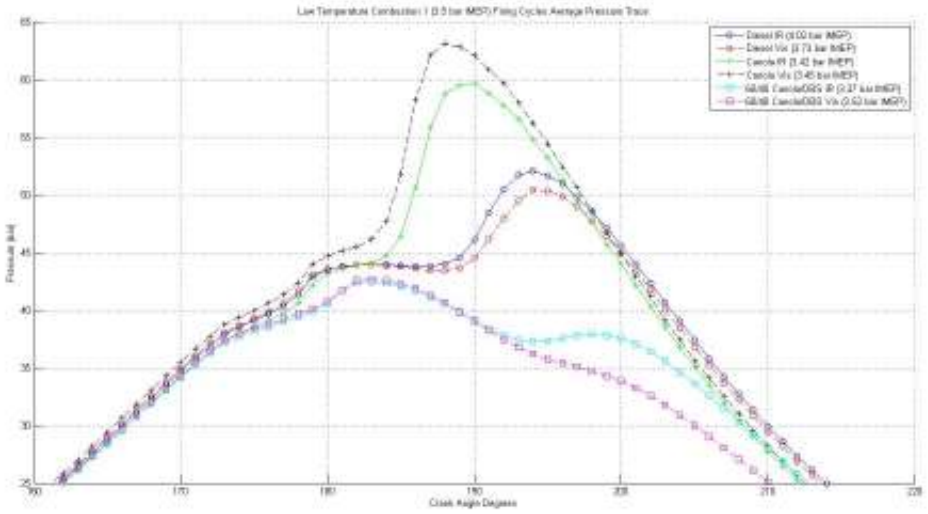

Figure V.5: Pressure traces produced from the LTC 1 operating condition showing the same trends as seen in the infrared images.

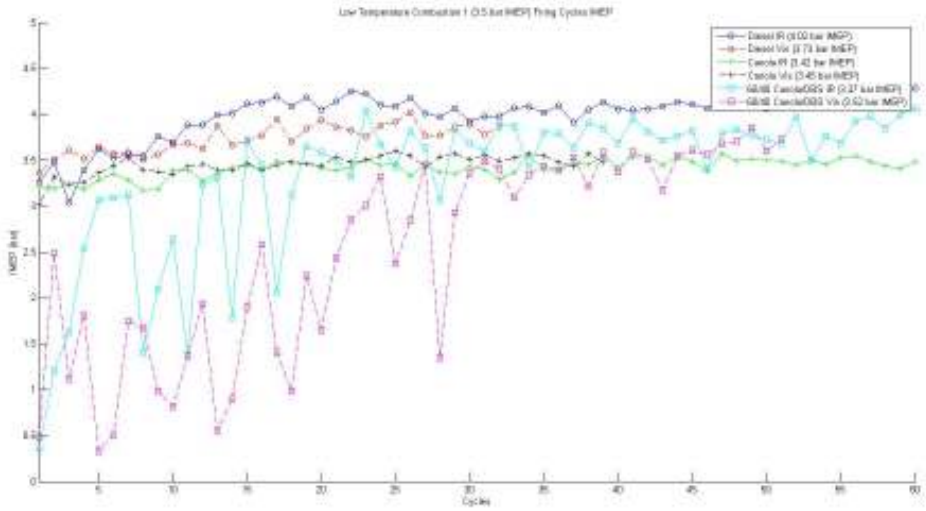

Figure V.6: IMEP data of the LTC 1 operating condition showing the inconsistency of the Can/DBS mixture.

Under the LTC strategy, the shortest ignition delay was seen to come from the B100 Canola fuel. This ignition delay was delayed greatly by mixing the fuel into a 60% Canola B100, 40% DBS mixture. These trends are seen both in pressure data and through the images acquired. The LTC 1 operating point showed the later combustion of the Can/DBS mixture to be inconsistent. The IMEPs for both the B100 and pump Diesel were seen to be consistent. Startup effects are seen in this figure, as well. It is most evident in the Can/DBS mixture case, but is also seen in the Diesel case and to a smaller amount in the B100 case. For those conditions which contain startup effects, it should be noted that the later, more stable cycles should be used during analysis.

Diesel

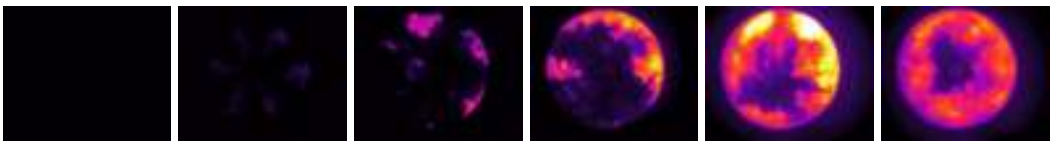

Canola B100

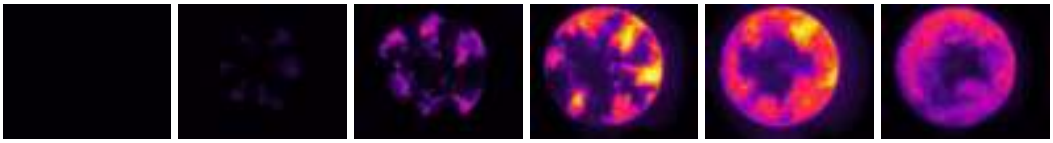

15 BTDC 6 BTDC 3 ATDC 12 ATDC 21 ATDC 30 ATDC

Figure V.7: Infrared images of the different fuels under Conventional Combustion 2 operating condition illustrating a slightly earlier combustion of the B100.

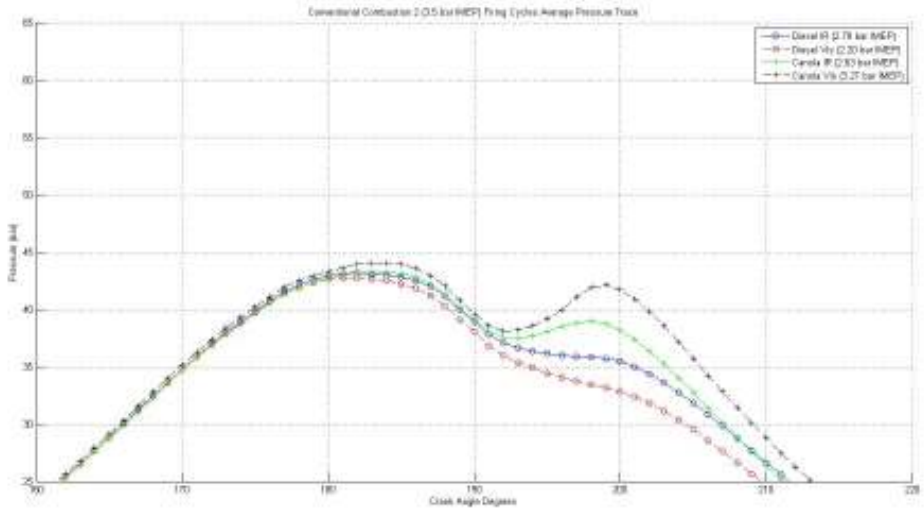

Figure V.8. Pressure traces produced from the Conventional Combustion 2 operating condition showing the earlier combustion of the B100.

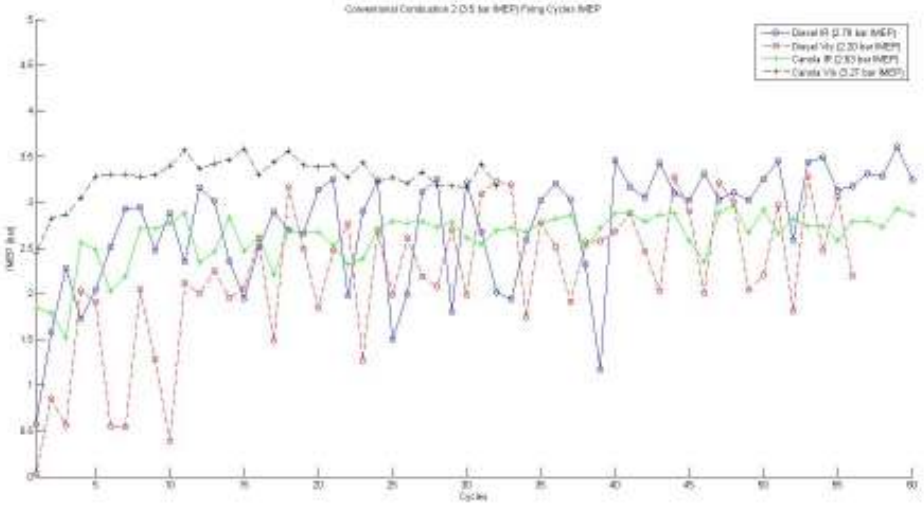

Figure V.9. IMEP data of the Conventional Combustion 2 operating condition showing the inconsistency of the pump Diesel.

The results from the LTC operating point are echoed in the Conventional Combustion 2 operating point. The B100 shows less of an ignition delay, while the pump Diesel shows a longer delay, as seen in Figures V.7 and V.8. Again, the Can/DBS mixture would not combust enough to achieve the correct IMEP for this operating point. The IMEP data produced by the Conventional Combustion 2 operating point showed both the inconsistency and startup trends seen in the LTC 1 cases. Both fuels were seen to be more inconsistent at this operating point than the LTC 1 point. Startup effects were also more prominent than in the previous experiment.

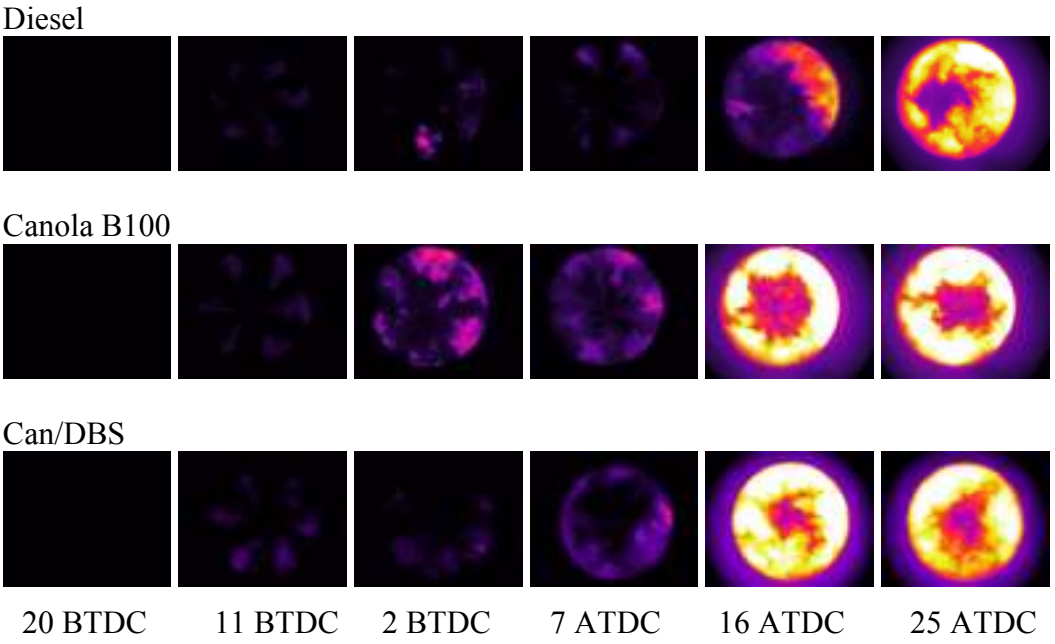

Figure V.10. Infrared images of the different fuels under Conventional Combustion 3 operating condition illustrating the advanced combustion of the B100 and the Can/DBS mixture.

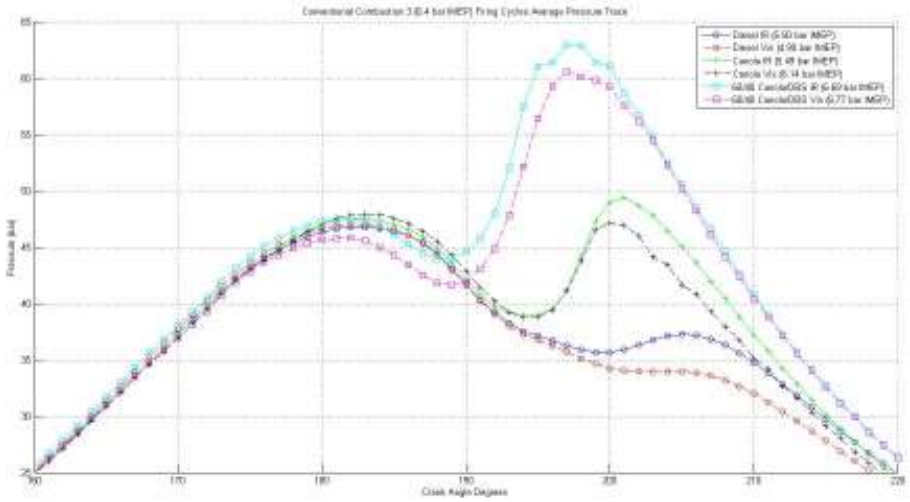

Figure V.11. Pressure traces produced from the Conventional Combustion 2 operating condition showing the earlier combustion of the B100 than Diesel as well as the advanced timing of the Can/DBS.

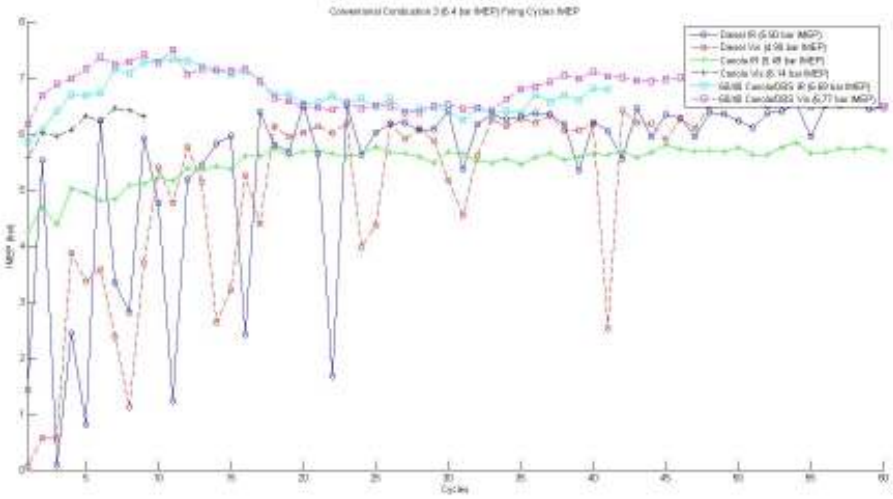

Figure V.12. IMEP data of the Conventional Combustion 3 operating condition showing the inconsistency of pump Diesel under these conditions.

The difference in the Conventional Combustion 3 operating point is the advanced main injection timing for the Can/DBS mixture. This injection advance causes an earlier heat release as well as higher in-cylinder pressures. The B100 again shows a shorter ignition delay than the pump Diesel. Pump Diesel in the Conventional Combustion 3 case also showed inconsistency and startup effects as the combustion timing was latest of the fuels for this case. The advancement of the Can/DBS mixture led to the most consistent combustion for this fuel of any operating condition.

V.2.3 Characterization of biofuel combustion properties in optical engine

The operating conditions which were verified above have been tested and filmed using an infrared (IR) camera and a high-speed visible camera. The operating conditions used in these experiments are tabulated in Table V.2. A major difference in these cases versus those supplied by Ford is the reduced actual oxygen content of the intake charge. This was due to an incorrect reading from the oxygen sensor used in the early part of these experiments. A newer oxygen sensor model, a Lambda 5220 from ECM, with pressure compensation has been installed and the true oxygen percentage was read for these conditions. The manifold pressures were modified in order to match pressures at TDC (top dead center) with the pressure traces supplied by Ford. Of note are also the optimized operating conditions for the biofuels, which is the conditions under which the 10% burn points and IMEPs are matched between the fuels. To this point, the LTC2 condition has not been able to be tested due to combustion inconsistency with the Canola/DBS blend.

Table V.2. Operating conditions including optimized timings and pulse widths.

Fuel	Case	Pilot PW (ms)	Pilot CAD	Main PW (ms)	Main CAD	Intake Temp (deg C)	MAP (bar abs)	Meas. O2 % (actual)	Goal IMEP (bar)
Diesel	LTC 1	-	-	0.38	-12	60	1.31	13.5 (11.5)	4
Diesel	LTC 2	-	-	0.5	-4	60	1.44	13.5 (11.5)	6.9
Diesel	CC 2	0.24	-20	0.3	0	90	1.31	17 (14.5)	4
Diesel	CC 3	0.255	-22	0.375	-2	50	1.44	17 (14.5)	7.2
Canola	LTC 1	-	-	0.38	-12	60	1.31	13.5 (11.5)	4
Canola	LTC 2	-	-	0.5	-4	60	1.44	13.5 (11.5)	6.9
Canola	CC 2	0.24	-20	0.3	0	90	1.31	17 (14.5)	4
Canola	CC 3	0.255	-22	0.375	-2	50	1.44	17 (14.5)	7.2
Can/DBS	LTC 1	-	-	0.38	-12	60	1.31	13.5 (11.5)	4
Can/DBS	LTC 2	-	-	0.5	-4	60	1.44	13.5 (11.5)	6.9
Can/DBS	CC 2	0.24	-20	0.3	0	90	1.31	17 (14.5)	4
Can/DBS	CC 3	0.255	-22	0.375	-2	50	1.44	17 (14.5)	7.2
Canola (opt)	LTC 1	-	-	0.4	-10	60	1.31	13.5 (11.5)	4
Canola (opt)	LTC 2	-	-	0.53	-2	60	1.44	13.5 (11.5)	6.9
Canola (opt)	CC 2	0.24	-19	0.32	1	90	1.31	17 (14.5)	4
Canola (opt)	CC 3	0.26	-22	0.4	-2	50	1.44	17 (14.5)	7.2
Can/DBS (opt)	LTC 1	-	-	0.42	-11	60	1.31	13.5 (11.5)	4
Can/DBS (opt)	LTC 2	-	-	0.54	-1	60	1.44	13.5 (11.5)	6.9
Can/DBS (opt)	CC 2	0.25	-20	0.33	0	90	1.31	17 (14.5)	4
Can/DBS (opt)	CC 3	0.27	-22	0.43	-2	50	1.44	17 (14.5)	7.2

Operating conditions were repeated once for each condition. This allowed both cameras(IR and high speed video cameras) to film piston and valve views. When one camera would film the piston view, the other would record images through the valve window. The camera positions would switch for the repeated test. This method of filming would give representative imaging through both the piston and valve windows. A sample of images from these experiments is given in Figure V.13. For brevity, only the images from the piston view of the LTC1 operating condition are presented, and only for the optimized biofuel injection timings and amounts. The visible images in this figure are from the first cycle of the test and are consecutive images from every 4.5 CAD. The IR images are from every fifth cycle (one image per cycle) and are also presented every 4.5 CAD. The main trends seen in these images come in the reduced amount of luminosity seen from combustion in the visible images for the 60/40 Can/DBS mixture, with only a small amount seen in the frames recorded at 13.5 and 18 CAD (crank angle degree) ASOIc (after start of injection commanded) for this fuel. This can be interpreted as a reduced soot production under these conditions, as the luminosity in the visible range is dominated by soot. Canola and Diesel fuels show similar natural luminosity. The infrared images taken under these conditions show little differences between the fuels, showing that similar temperatures are likely experienced in the engine between these cases. The frames taken from the other operating conditions depicted similar trends as seen in this operating condition.

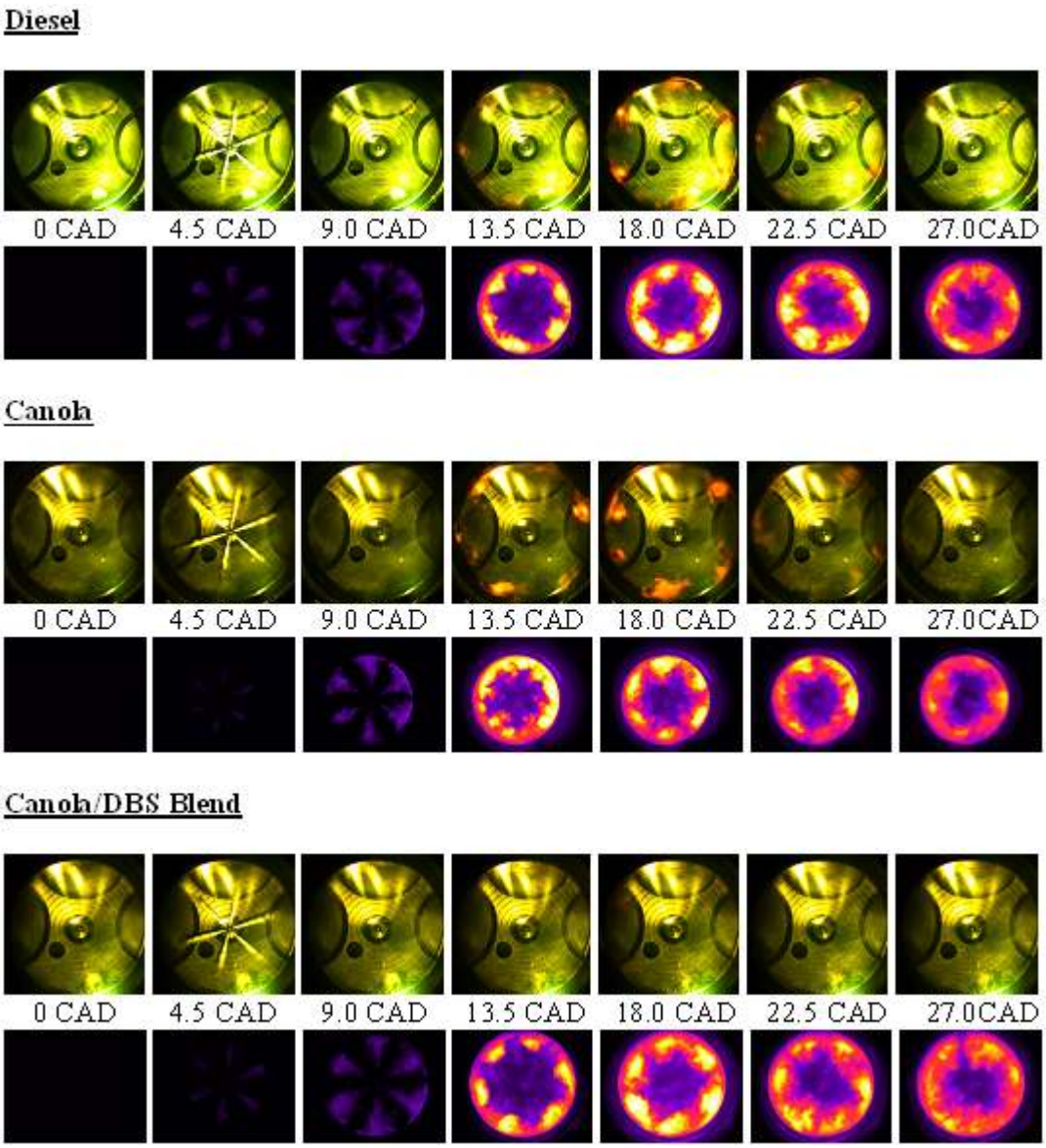

Figure V.13. Optimized LTC1 operating condition for the different fuels. The delays between the images are the crank angle after the commanded start of injection.
Visible images are above the CAD delays, IR below.

Pressure Data (including MFB): A sample of the average in-cylinder pressure data recorded from these experiments is seen in Figures V.14-V.16. These data are taken from the fired engine cycles, approximately 50 cycles. From these data, the need to optimize the pulse widths and timings of the biofuels is evident, as the non-optimized combustion is phased much away from the baseline diesel. The mass fraction burned data (MFB) are also shown here in order to show the agreement with MFB 10% points between these fuels. The MFB curves initially decrease largely due to blowby. It was therefore necessary to match the points at a value of .1 above the minimum of the diesel baseline case. The best agreement was found between the optimized fuelling cases with the given resolution of the injection system. In all cases, it is seen

that less than one CAD is seen between the fuels at the MFB10 point for the optimized fuel conditions with the baseline diesel.

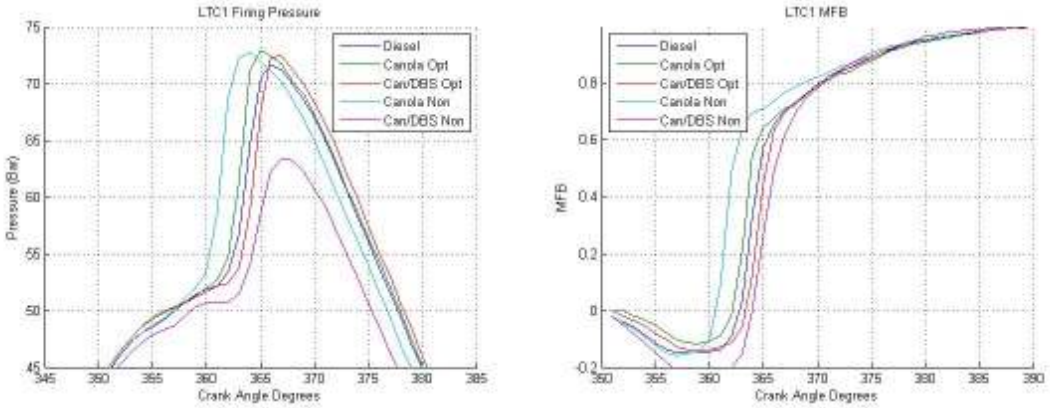

Figure V.14. Pressure data and MFB curves for the LTC1 operating condition.

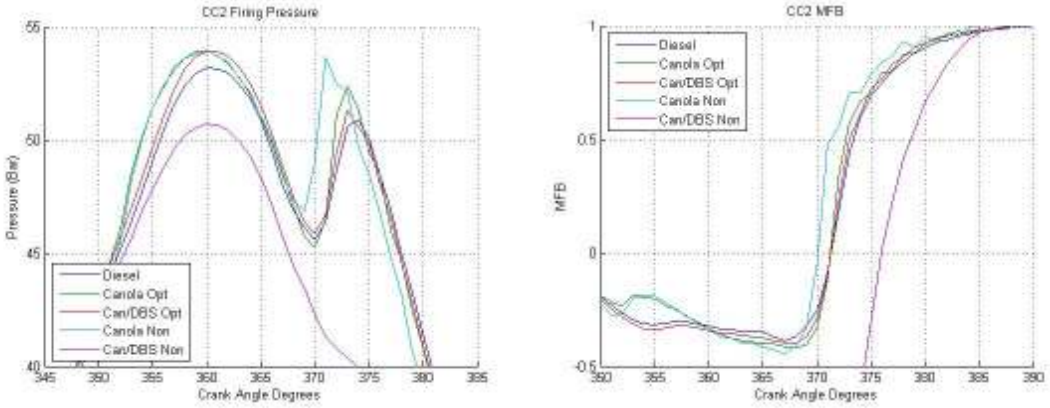

Figure V.15. Pressure data and MFB curves for the CC2 operating condition.

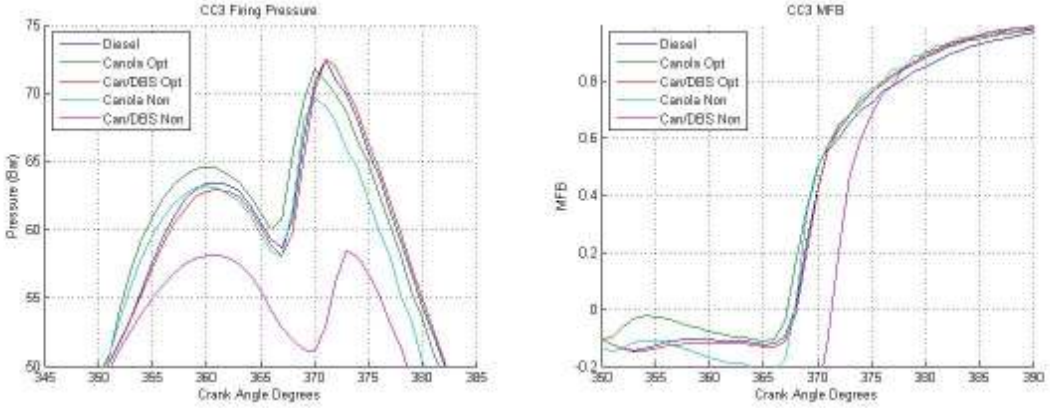

Figure V.16. Pressure data and MFB curves for the CC3 operating condition.

Vaporization Lengths: Vaporization lengths of the various fuels were calculated to determine the length needed for the liquid fuel jet to travel in order to vaporize the fuel. This study was accomplished by analyzing the visible high speed images using MATLAB for data processing. The images used were the non-optimized pulse widths, such that the same pulse

width and timing (and thus the in-cylinder conditions) of the fuel injection were similar between experiments. The backgrounds of the images were removed by subtracting the image directly before fuel spray was seen. The results to the three operating conditions are seen in Figure V.17. The liquid fuel for all cases exits the nozzle at similar speeds, as seen by comparing the initial slopes of the curves. The fuel plumes then develop and have a nearly constant length, which is taken as the vaporization length. A longer vaporization length could mean less air entrainment in the fuel vapors, which would lower the local air to fuel ratio. Longer vaporization lengths would also point to an increase in momentum of the jet, thereby causing more bowl impingement and leading to increased areas of soot production. From these results, it is clear that the biofuels have a longer vaporization length for the operating conditions studied here. All other things equal (no chemical composition differences), this result should show an increase in soot production for these fuels owing to the longer vaporization lengths.

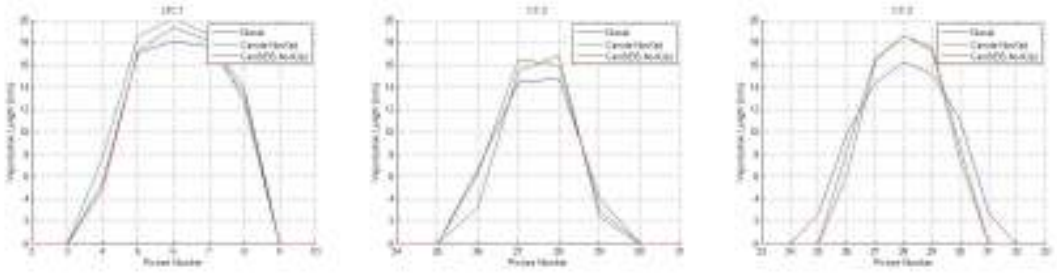

Figure V.17: Liquid fuel penetration curves for the three operating conditions.

Projected Combustion and Soot Areas: Another metric that was analyzed is the projected area of combustion recorded by the cameras. The projected area of combustion is the projected area of the combusting volume that is seen along the line-of-sight of the camera. The images used in these experiments were visible combustion without the use of the laser and the infrared combustion images, taken from separate experiments. The infrared images give all the areas of heat release and hot gases and are taken as the total area of combustion gases. The visible images will only show the regions of soot production. The images were analyzed using a MATLAB code that examined each pixel and determined if combustion (IR) or soot (visible) was present based on threshold values. The total number of pixels meeting the criteria were calculated and normalized to the view area. This analysis gives insight into the in-cylinder combustion development of the different fuels.

The combustion area curves of the LTC1 combustion condition (Figure V.18) show similar final behavior between the fuels, with the exception of the non-optimized Can/DBS case. However, the initial stages of combustion vary slightly. Cetane effects are seen through these plots, as the Can/DBS blend shows the longest ignition delay and expansion of combusting area than the other cases. Additionally, the B100 canola shows a faster initial spread of combustion than the others. It is seen that by around 10 CAD ATDC, the curves show similar areas of combustion. The curves of the visible combusting areas give additional insight into this operating condition. Under these conditions, it is seen that very little soot is formed with the canola /DBS blend, with only a small amount seen between 380-385 CAD for the optimized case. This operating condition also shows a higher maximum area of soot for the canola compared to that of the other fuels. However, even for the optimized case, these areas quickly reduce to values similar to diesel, suggesting possible earlier soot oxidation.

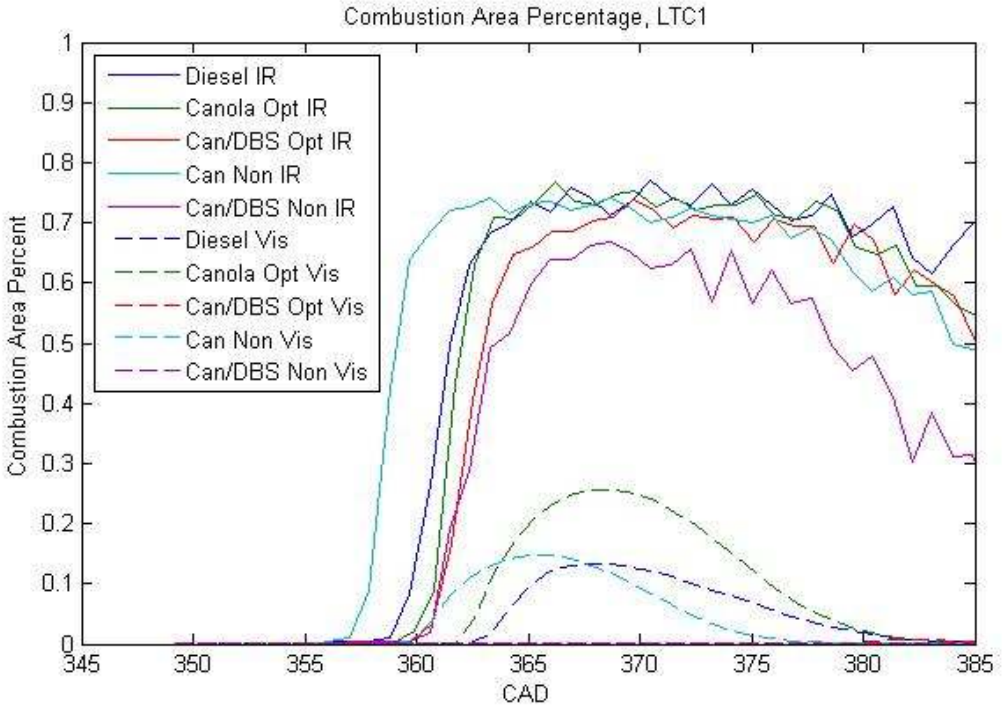

Figure V.18. Projected areas of combustion and soot for the LTC1 combustion condition.

The combustion area curves found from the CC2 operating point (Figure V.19) show differences between the fuels. The first noticeable difference is in the pilot injection combustion, where more area of combustion is seen for the canola B100 than the baseline diesel case. The least amount of combustion area seen during the pilot combustion is from both cases of the can/DBS mixture. This result is likely due to the increased cetane of the canola B100 allowing an earlier ignition of the fuel. At the beginning of the combustion of the main injection, the combustion area behavior is similar for the optimized conditions of biofuels and diesel. At the end of combustion, however, there are differences between the fuels. Diesel ends with almost a 15% higher total area of combustion. The optimized biofuels end with similar areas of combustion, although the area of combustion of both canola cases shows a rapid reduction of combusting area, indicating that the energy release of this fuel is faster than the others. The combustion area plot for the non-optimized Can/DBS operating condition illustrates the poor combustion seen in this fuel, with significantly less projected area of combustion in the cylinder. The areas of soot produced for these fuels under this operating condition show additional interesting trends. In this condition, the largest area of soot is seen for the Diesel case. A slight reduction in soot area is seen for canola compared to diesel, with the optimized case producing more soot than the non-optimized case, likely due to the increased fuel amount of the optimized case and, thus, more areas of increased fuel/air ratio throughout the cylinder for the optimized timing. Again, a large reduction in soot is seen for both Can/DBS cases, with only a small amount (~1% of view) seen between 370 and 380 CAD for the optimized case.

.

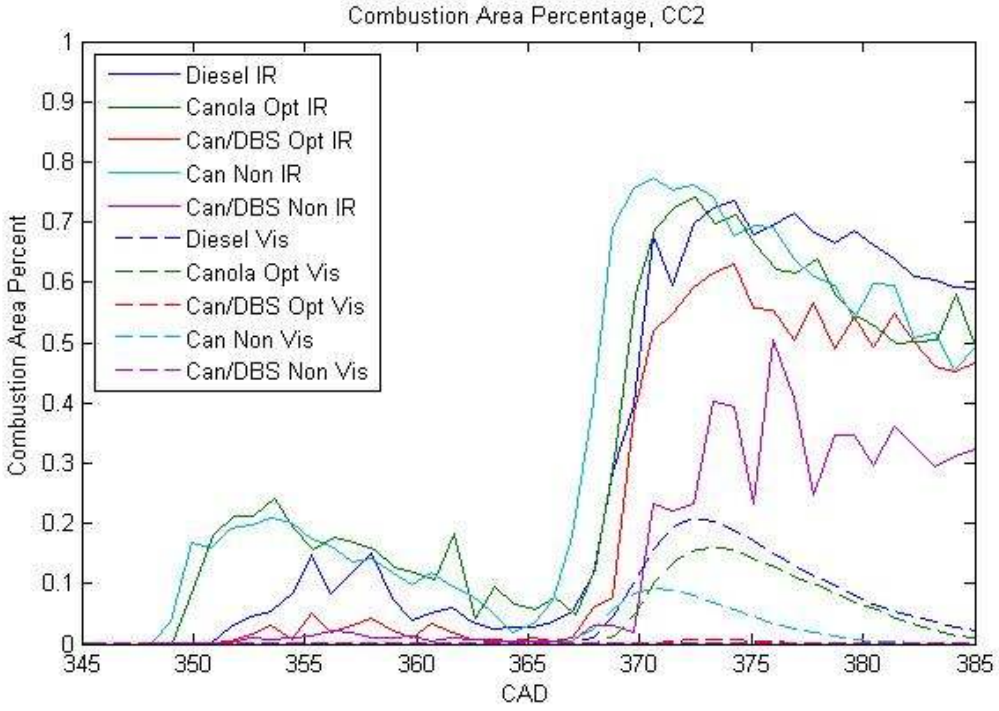

Figure V.19: Projected areas of combustion and soot for the CC2 combustion condition.

The CC3 condition shows very similar combustion area trends between the fuels in both pilot and main injection combustion between the fuels (Figure V.20). The main difference between the fuels is again seen in the onset of the pilot injection combustion. The canola is again seen to combust earlier than the other fuels. The canola /DBS non-optimized conditions show very little combusting area during the pilot combustion region. The lower energy release of the pilot injection for both cases of the fuel blend is likely the cause of the lower combustion areas later in the cycle, as the pilot energy release raises the temperature enough to allow the main injection to fully combust. The other note to make about these plots is the intial increase in soot area with the combustion area. It is seen that during the initial combustion of the main injection that the area of soot increases similarly with the total combusting area for the optimized canola and diesel cases. The total area of soot reaches the highest maximum, with the optimized Canola soot area reducing more quickly. The faster soot area reduction of the canola points to the possibility that this fuel might oxidize the soot more rapidly. The canola /DBS again shows lower soot amounts, with a maximum around 50% of the combustion bowl view. A necessary note to be made about the soot percentages under this condition is the reflection of the soot off of the cylinder head. This operating condition produced the most significant soot of the three conditions examined, and reflection was only significant under this operating condition. The reflection causes pixels outside of the actual sooting areas to be counted by the program, resulting in higher calculated areas of soot. However, the amount of reflection between fuels was seen to be similar enough to allow for an examination of trends. Some reflection is also seen in the infrared images, but to a lesser extent.

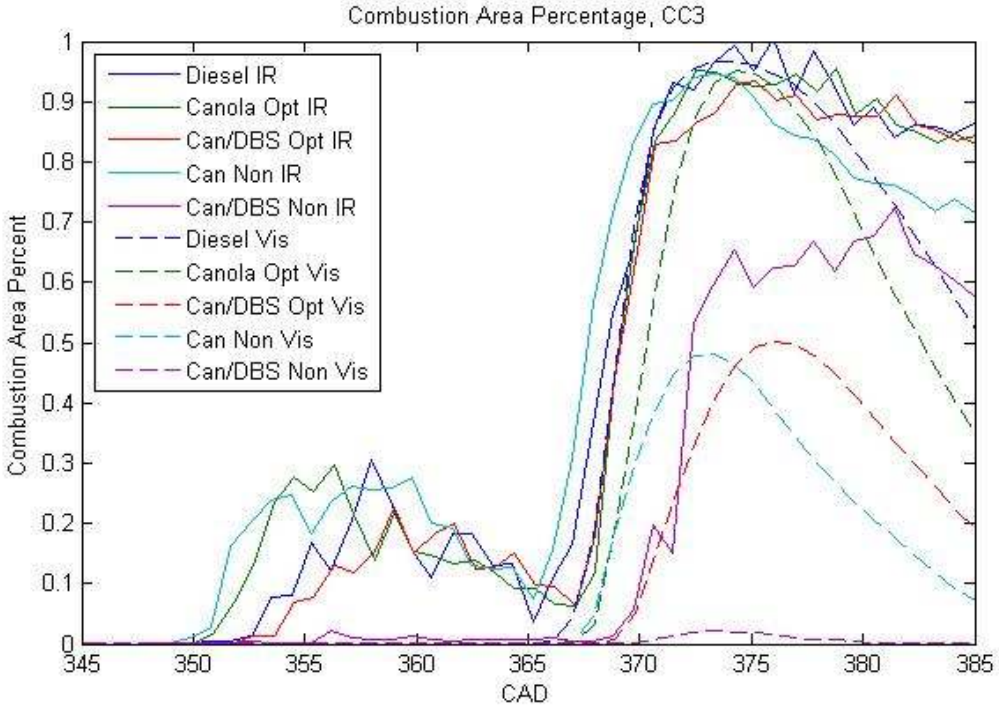

Figure V.20. Projected areas of combustion and soot for the LTC1 combustion condition.

The results from the analysis of the combustion areas led to interesting conclusions. It was seen that in the lower load cases (LTC1 and CC2) that a larger area of combusting gases was seen for diesel than the biofuels. For the higher load case, the combusting areas are similar for the optimized biofuel cases and diesel. The soot area results are extremely interesting, as these results show a significantly lower amount of soot area for the canola /DBS blend than the other two fuels. Canola and diesel are similar in maximum soot area for most cases, with a sharper decline in soot area for the canola B100 fuel. The soot area results are further examined in the following section.

Percent Projected Soot in Combustion: A furthered discussion of the percent area of soot in the total area of combustion is introduced by the previous section. The projected percentage of soot in combustion is taken as the projected area of soot (visible) and dividing by the projected area of combustion (IR) at each point in the cycle. This analysis yields a metric of the efficiency of a fuel to burn without producing soot that can easily be examined between the fuels. These values are not taken simultaneously, and care must be made of this note during discussion. However, trends can be seen through this analysis. The plots in this section are scaled from zero to unity, although some values are higher than 1 due to reflection and cycle-to-cycle inconsistencies.

The LTC1 condition showed the lowest percentages of soot production, especially for the canola /DBS blend (Figure V.21). At this operating condition, the canola optimized shows the highest percent of sooting areas in the piston bowl. However, the diesel percentage is greater when viewing through the valve view. For the canola /DBS blend, no substantial soot percentage is seen in either view. Through the analysis of this condition, it is clear that similar amounts of

combusting areas produce soot compared to the small amount of the canola /DBS blend in which soot is produced.

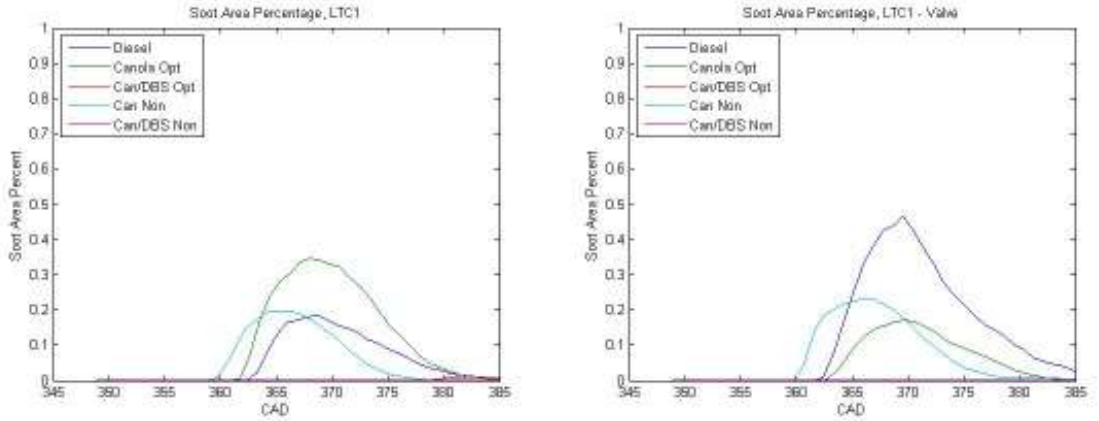

Figure V.21. Fraction of combusting area in which soot appears for the different fuels under the LTC1 condition.

The percent soot areas of the CC2 operating condition produced additional insight into the behavior of these fuels (Figure V.22). Under these conditions, it is clear that diesel causes the most percentage of sooting areas in combusting area. In both views it is clear that an increased area of soot production is evident for diesel fuel, with a slight reduction for the canola . Similar to the LTC condition, a low value of soot production percentage is seen for the canola /DBS blend. In this case, all fuels saw an increase of sooting area through the valve view, indicating that a greater percentage of combusting area produces soot in this area. Indeed, more soot area is seen than combusting area for a portion of combustion through the valve view for diesel. The values greater than unity can be attributed to the difference between experiments and reflection by the piston; the obvious trends are still valid.

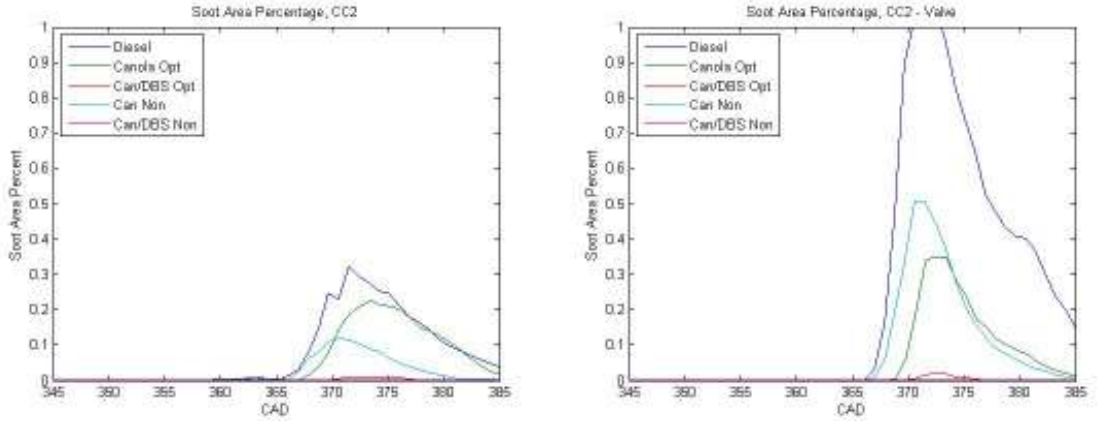

Figure V.22. Fraction of combusting area in which soot appears for the different fuels under the CC2 condition.

The soot area for the CC3 condition (Figure V.23) again showed the reduction in soot area when fueling with the canola /DBS blend. A similar percentage between both views was seen for the optimized condition of this fuel. Reflection is seen to be very prevalent in this condition, as much more area is of soot that is bright enough to cause significant reflection. This reflection causes some percentages to be greater than unity. However, from the previous section, it is clear that the soot and combusting areas increase at around the same rate, with diesel showing earlier soot production and an earlier reduction by the canola . It is also clear that a larger portion of the combusting area is of soot for this case compared to the lower load cases for all fuels. The increase in soot area for this condition is likely caused by the increase in local air to fuel ratio caused by an increased injection amount.

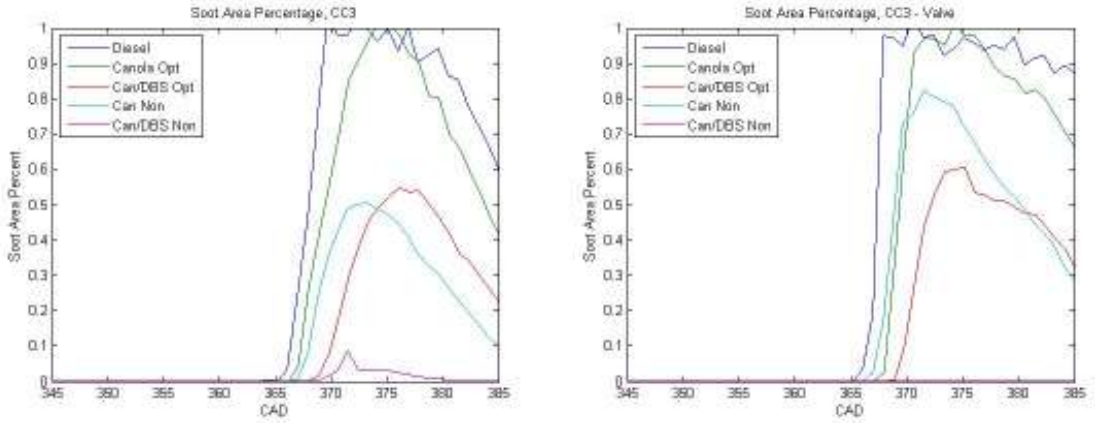

Figure V.23. Fraction of combusting area in which soot appears for the different fuels under the CC3 condition.

Average Image Intensity of Combustion: A beneficial analysis that was completed was examining the average pixel intensity of the infrared images in the areas of combustion. The average intensity is a scaled radiation amount captured by the infrared camera. These values were calculated for only the areas determined to show combustion energy by using a threshold value. The average intensity values produced from this examination can be affected by both emissivity (soot and/or combustion gas concentrations as well as optical path length) and temperature. Increases in both parameters would lead to higher intensity values. Trends can still be examined from these intensity values, despite these variances.

The LTC1 condition shown in Figure V.24 shows similar average pixel intensity behavior between the fuels. A small initial increase in intensity can be seen from all fuel cases except the non-optimized canola case. This initial increase could be seen as the premixed part of combustion. The average intensity increases at nearly the same rate, with similar values for the optimized biofuels and diesel fuel conditions at 5 CAD ATDC. It is also seen that the non-optimized canola /DBS case shows a lower maximum average intensity, likely due to the lower and later energy release of this fuel condition as well as a decreased sooting condition. The non-optimized canola condition shows earlier and higher combustion intensities, likely due to the earlier energy release causing higher temperatures in the cylinder. Overall, the conditions show very similar average intensity behavior, with the optimized biofuels showing slightly delayed and lower average combustion intensities than the baseline diesel conditions.

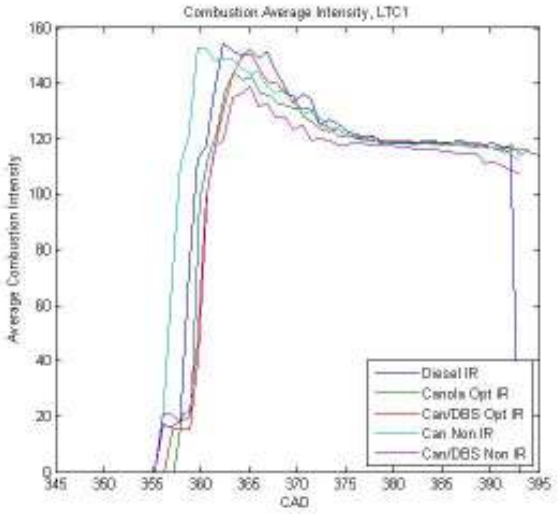

Figure V.24. Average intensity values of the infrared images in the areas where combustion occurs for the LTC1 combustion condition.

The CC2 operating condition (Figure V.25) shows some significant differences between the fuels in the average intensities in areas of combustion. The main difference in this operating condition and the previous condition is the addition of a pilot injection. The initial increase in energy seen by the infrared camera from around 10 CAD BTDC lasting to about 5 CAD ATDC is because of the combustion of this pilot injection. The non-optimized B100 canola shows an earlier and slightly higher increase in energy emission than the pump diesel. However, the non-optimized canola /DBS mixture shows a smaller energy release that is later in the cycle than the other fuels. The pilot injection for both cases of the canla/DBS is also more inconsistent, as seen by examining consecutive points in this pilot injection region. This result points to the lack of combustion of the pilot injection. When the main injection burns, this average intensity increases to similar values as the other fuels for the optimized cases. A lower intake charge temperature than specified was used for this operating point, and may have affected this fuel more than the others, because of the lower cetane of this blend. The other notable point of the main injection is that the pump diesel fuel causes higher average combustion intensities after around 370 CAD, which could be related to a higher soot value, but could also be caused by a higher temperature.

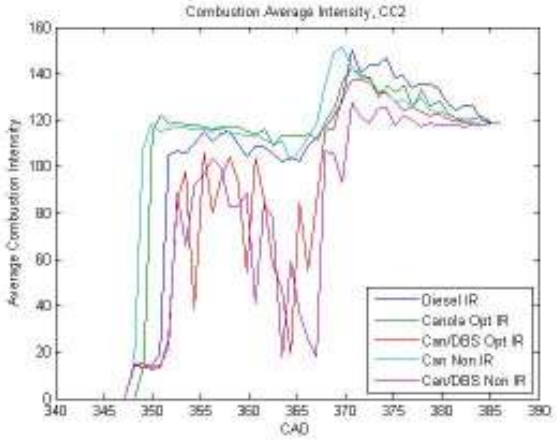

Figure V.25. Average intensity values of the infrared images in the areas where combustion occurs for the LTC1 combustion condition.

The CC3 operating condition (Figure V.26) showed similar behavior between the fuels for the average pixel intensity measurements. The main differences are seen in the earlier pilot ignition for the B100 canola and the higher later average intensities caused by diesel. For this operating condition, similar average intensities of pilot combustion are seen between the fuels. However, cetane effects are noticeable in the initial combustion of the pilot injection, as the canola ignites much faster than the other fuels. The non-optimized canola /DBS condition shows poor pilot combustion as well as lower final intensities, likely caused by the lower energy release of this fuel. Similar final intensities are seen for the optimized biofuels, indicating similar energy releases between the fuels. A higher final value of average intensity is seen for the diesel case, which could, again, be attributed to the increased soot production for this fuel.

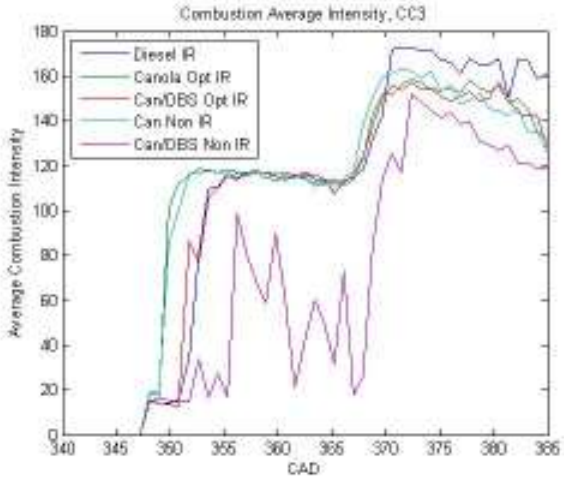

Figure V.26: Average intensity values of the infrared images in the areas where combustion occurs for the LTC1 combustion condition.

The average image intensity of combustion analysis showed several important trends. The LTC1 condition showed similar behavior between the fuels with an earlier increase in the

non-optimized canola case and slightly lower and later energy release for the optimized biofuels when compared with diesel. The CC2 condition shows the effect a pilot injection has on the different fuels. The pilot burn of the canola shows earlier energy release than diesel. When blending DBS, inconsistent and lower intensity values were observed during the pilot combustion stage, however. Higher final average pixel intensity values were seen for diesel, which could be attributed to either emissivity or temperature effects. The CC3 case showed similar behavior to the CC2 case. However, increasing the pilot injection for the Can/DBS case shows similar intensity values to the dDiesel case. An earlier energy release is seen, again, for the B100 canola under the CC3 operating condition. Higher final pixel intensities are also seen for diesel in this case. Overall, it is noted that the non-optimized conditions lead to unwanted combustion behavior for the fuels; Canola shows earlier energy release, with the canola /DBS mixture later. Similar results are seen between the optimized conditions to the baseline diesel, with diesel ending in slightly higher average pixel intensities for certain cases.

Combustion Distance: An analysis of the radial combustion and soot distance from the nozzle is also studied. This study was completed in order to give furthered insight into the combustion parameters of these fuels. The average analysis presented here was completed on the infrared images by taking an average of combustion or soot distances at 1 degree around the cylinder. If no combustion or soot was seen, the value was not used in the averaging. The maximum values shown in this section are the furthest distances away from the combustion bowl (nearest point to the injector) that combustion or soot is seen for each individual combusting plume. This was accomplished by dividing the image into six sections, one corresponding to each plume. A An image explaining this is seen in Figure 29. In the left side of this figure, the different divisions of the cylinder can be seen as well as the nearest points in that section, marked with green dots. The right image is a translation of that image into Cartesian coordinates to show the radii of combustion. By completing these analyses, it is possible to characterize the distances away from the injector in which combustion or soot is seen for the different fuels.

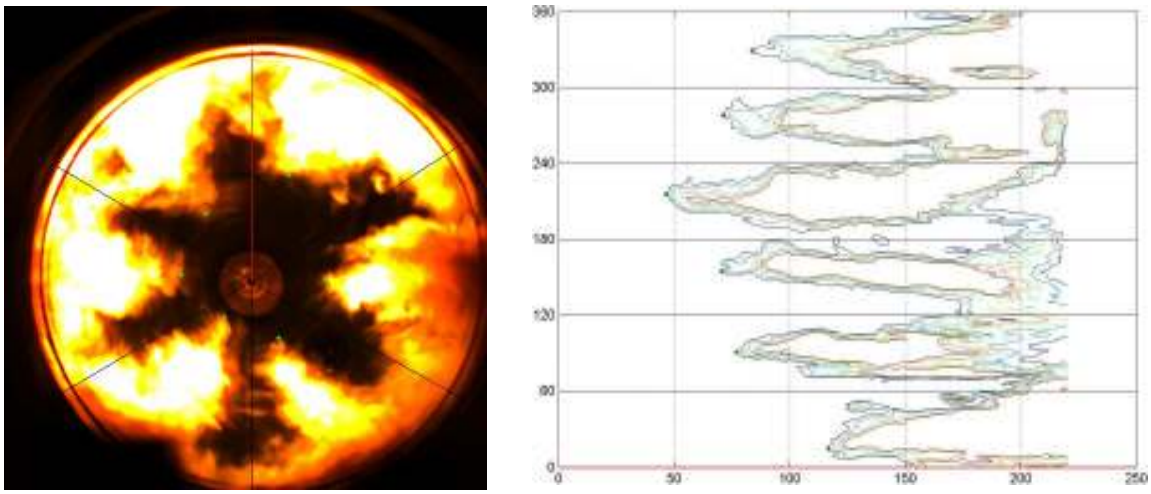

Figure V.27: Cartesian and normal soot images showing the nearest to the injector soot distances.

The curves produced in this analysis show similar results between the optimized fuels and the baseline diesel case (Figures V.28 – V.30). Of note are the distances of pilot combustion

between the fuels. For the cases including a pilot, CC2 and CC3, a closer distance of combustion of the pilot injection was seen for the canola, which could be related to the increase cetane of the canola derived fuel. Another interesting note is that, for the CC2 condition, the canola main injection of the canola burns farther back towards the injector sooner than the other fuels, which could lead to a richer combusting region, and thereby creating more soot for this condition. It is supposed that the higher cetane number of the pure canola causes earlier ignition in the fuel jet, likely aided by the increased energy release of in the pilot injection seen in previous sections. However, when blending the canola with DBS, the decrease in cetane causes longer lengths (or at least similar to the baseline diesel case), lending a possible explanation for the decrease in soot production. The soot distance trends mimic these results, as the furthest average soot distance is created by the canola/DBS blend, with the shortest lengths seen for the pure canola for the lower load condition. It can also be seen from these plots that the higher load case burns much closer to the injector than the lower load cases, with soot also occurring slightly closer to the injector.

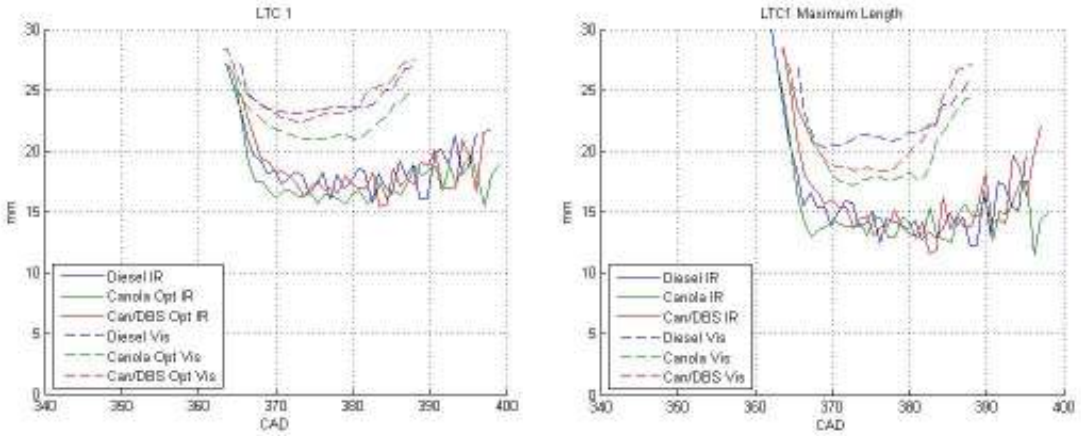

Figure V.28: Average and maximum combustion and soot lengths for the LTC1 condition.

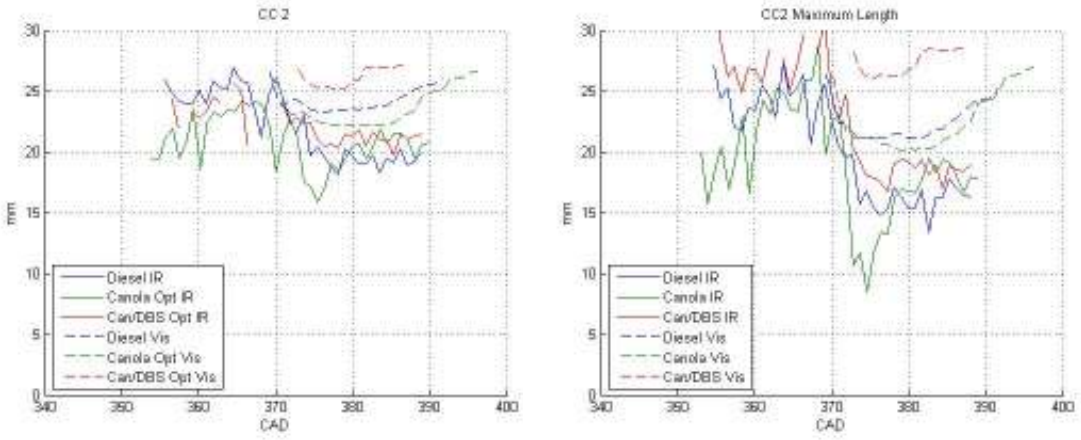

Figure V.29. Average and maximum combustion and soot lengths for the CC2 condition.

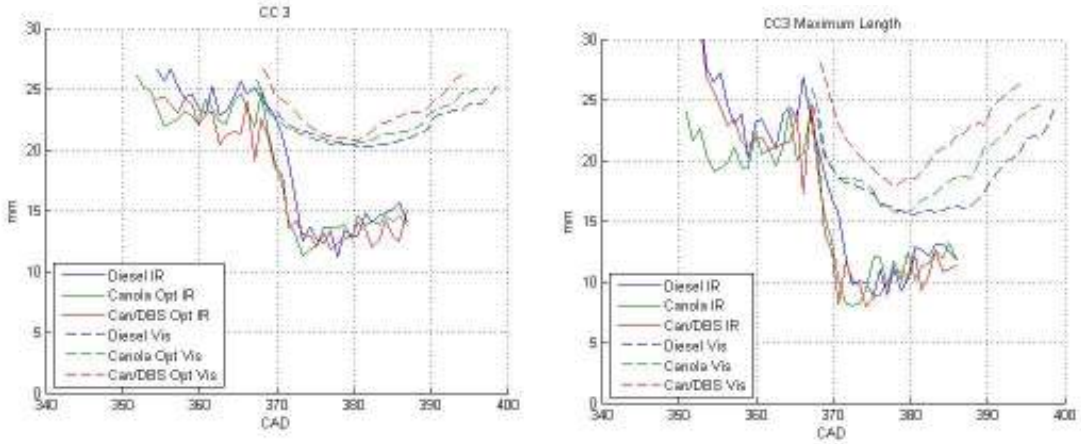

Figure V.30. Average and maximum combustion and soot lengths for the CC3 condition.

V.2.4 Enhanced imaging in optical engine combustion experiments

The major progress in this project from the previous update comes through the utilization of additional imaging techniques in viewing the in-cylinder combustion of the studied fuels. An intensifier was used with a 310 nm filter in order to view the luminosity produced from the hydroxyl radical. This radical is used as an indicator of lift-off length (LOL) in Diesel jet plumes. This technique, along with the previously completed techniques, gave insight into the combustion processes of the fuels.

As an example of the results found from these experiments, a sample composite cycle can be found in Figure V.31. These are in-cylinder images that show a sample of the results taken from the three imaging techniques used in the optical engine studies. For brevity, only the images from the CC3 operating condition are presented, and only for the fuel injection timings and fuel injection amounts that yield similar in-cylinder combustion behavior. The third cycle of the OH and the non-illuminated visible experiments are presented every 4.5 CAD in this figure. The IR images in Figure V.31 show every fifth image in the composite cycle, every 4.5 CAD. Through these sample images, it is clear that similar combustion events transpire inside the cylinder between the fueling cases. Fuel is injected and begins to react towards the outside of the combustion bowl in a similar manner, as seen in the IR images. Note, also, in the IR images, the similar combustion, in terms of area and energy scale between the fuels. The visible images show a reduced amount of natural luminosity of combustion for the 60/40 Can/DBS mixture, with only a small amount observed in the frames between 370 and 380 CAD. Canola and Diesel fuels show similar amounts of natural luminosity to each other, indicating similar areas of soot occurring in the cylinder. The OH images presented in this figure also show fairly comparable in-cylinder trends of this radical production between the fuels. The earliest OH is present near the bowl edge and then moves inward along the combusting plume. As the reaction depletes, the OH moves outward and disperses amongst the combustion products in distinct pockets. It must be remembered that the images presented in Figure V.31 are only sample images and the average behavior may be somewhat different to that seen in these images, but these images still allow for a general overview of the data.

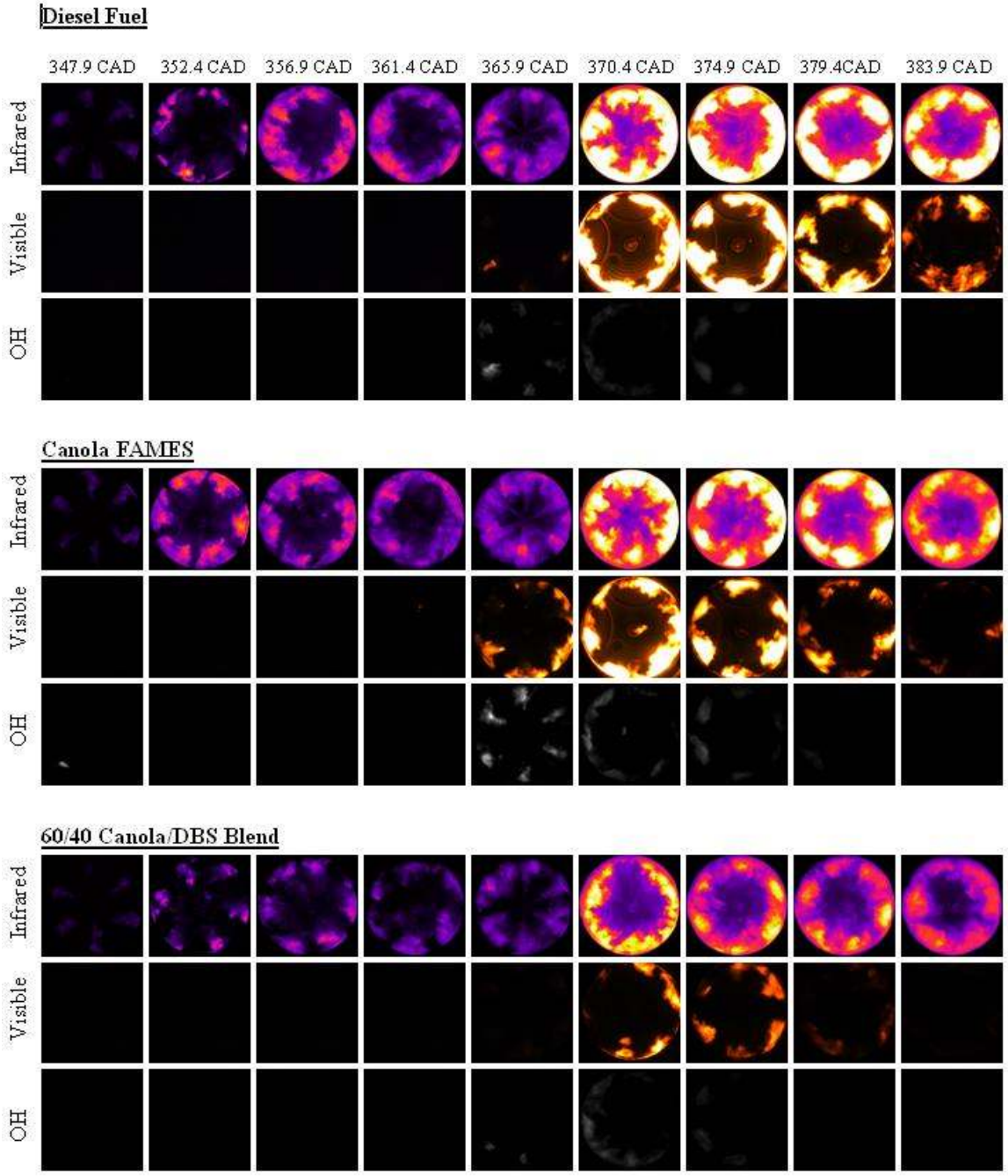

Figure V.31. Visible, infrared, and –OH analysis of combustion of biofuels in optical engine

V.3 Single Cylinder Engine Testing at Ford

V.3.1 Background on low-temperature combustion (LTC)

Since the use of biodiesel is likely to increase in the future, new combustion systems and combustion modes must be robust to its use. While the effect of biodiesel on combustion and

emissions has been studied, it is not well understood how possible next generation biodiesel fuels (such as blends of biodiesel and DBS) behave. In addition, not much is known about how new advanced modes of combustion such as LTC behave with oxygenated fuels, such as biodiesel. LTC is a combustion mode that has significant potential for reducing engine-out NOx and soot emissions[i,ii,iii,iv]. The formation of soot and NOx in a diesel engine can be visualized on the Φ-T diagram shown in Figure V.32. Conventional diesel combustion produces local equivalence ratios and temperatures giving rise to both soot and NOx. In LTC, the start of combustion is delayed until after the end of injection, thus providing time for fuel-air mixing prior to combustion, which reduces the hot-rich zones in the combustion chamber to avoid the soot formation area. Elevated levels of exhaust-gas recirculation (EGR) are also used both to suppress peak flame temperatures, thereby avoiding the NOx formation area, and to control the rate of combustion. Since fuel oxygenation is likely to alter in-cylinder equivalence ratios, it may impact the behavior of the engine in LTC and further study is warranted.

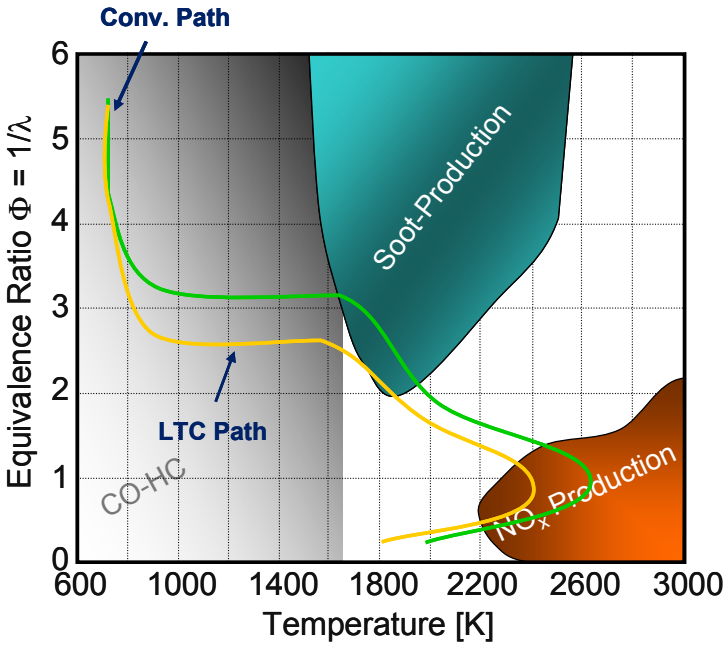

Figure V.32. Visualization of LTC and conventional combustion in φ-T space.

The intent of the current study was not only to develop next generation biofuels for a diesel engine with better cold flow properties, but also to understand the performance of those fuels in an engine relative to both diesel fuel and conventional biodiesel. In addition, the testing was aimed at understanding the effect of oxygenated fuels on combustion, emissions, and fuel consumption in LTC with particular emphasis on the robustness in that mode of combustion.

V.3.2 Biofuel properties

Both the 100% canola biodiesel (CME) and the 60%-40% CME-DBS blend (60-40) were evaluated on a single-cylinder engine to understand the impact of those fuels on combustion, emissions, NVH, fuel consumption and thermal efficiency. These two fuels were compared to a standard calibration fuel, XE-M4CX720-A (hereafter referred to as 720). A summary of the

properties of these fuels is shown in Table V.3.

Table V.3. Summary of fuel properties

	720	727	668	CME	60-40
Full Name/ Description	XE-M4CX720-A	XE-M4CX727-A	Ford REF 668	100% CME	60% CME 40% DBS
Cetane No.	45.6	41.8	56.5	50.8	40.8
Molar H:C	1.81	1.78	1.95	1.88	1.86
Molar O:C	0	0	0	0.106	0.191
NHV (MJ/kg)	42.9	42.4	43.2	37.4	33.2
Spec. Gravity*	0.8480	0.8534	0.8303	0.8825	0.9225

* at 15.56°C/15.56°C

As shown in Table V.3, the two biodiesel fuels studied have significantly different cetane numbers from 720 diesel fuel as well as each other. Consequently, a US cold operation diesel fuel, XE-M4CX727-A (727), was included to match the low cetane number of the 60-40 blend, while a high cetane fuel, Ford REF 668 (668), was added to match the cetane number of B100. The properties of the two additional fuels are also included in Table V.3.

Since the oxygen content of DBS is greater than that of the CME, the oxygen-carbon ratio of the 60-40 blend is higher than that of CME. Furthermore, the net heating value has a negative correlation with the oxygen content such that all three diesel fuels have similar energy content, while B100 is lower and 60-40 is the lowest.

V.3.3 Single cylinder engine description

The engine used for this study was a 0.83L single cylinder diesel engine. Details of the engine can be found in Table V.4. The engine was equipped with a piezo common rail fuel system capable of 2000 bar injection pressure.

Table V.4. Engine specifications

Bore	99 mm
Stroke	108 mm
Connecting Rod Length	176 mm
Number of Valves	4

The engine was lubricated by an externally driven oil pump that was set up to control oil pressure as a function of engine speed based on multi-cylinder engine data. Coolant was also externally supplied through a conditioned water system. Both oil temperature and coolant temperature were controlled to 90°C for all operating conditions.

A schematic of the single-cylinder engine test cell setup is shown in Figure V.33. Intake and exhaust pressure and temperature measurements were taken at various locations shown in the figure. The air path for the engine was set up to control the intake pressure, intake temperature and exhaust pressure to simulate turbocharging and to control the exhaust gas recirculation. Air was supplied from the critical air system, which provided dry air at up to 700

bar. Air pressure and critical flow orifice size were used to control the intake pressure measured in the intake manifold. A 15.5L intake surge tank was used to dampen out pressure pulses causes by the pulsed flow of single-cylinder operation. Intake temperature measured in the intake runner was controlled using a Chamalox heater as well as band heaters strapped to the intake surge tank. To facilitate rapid transition from high intake temperature to lower temperature, a heater bypass was also used and the heated and unheated streams were blended with a three-way valve. Air flow was measured both with a critical flow orifice and, when the flow across the critical flow orifice was subsonic, a Micromotion CMF050 flow meter. This was typically only necessary when high intake pressures were used, making it difficult to meet the sonic pressure ratio criteria across the critical flow orifice.

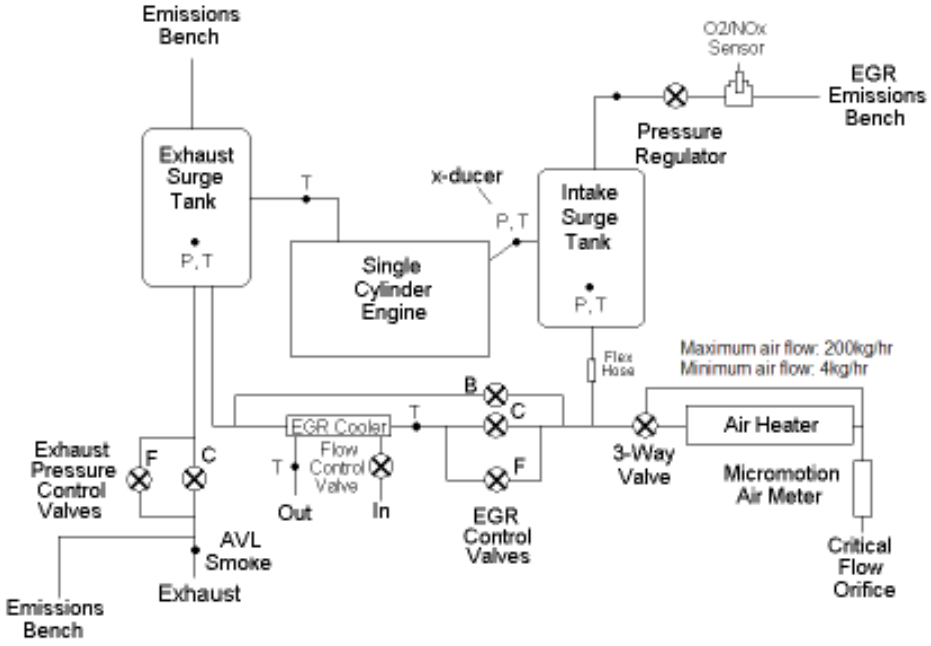

Figure V.33. Schematic of the single-cylinder engine test cell setup.

The exhaust system consisted of a specially designed exhaust runner that damped exhaust and a surge tank identical to the intake surge tank. Both of these combined provided for pumping loop that was reasonably close to that on a multi-cylinder engine. Exhaust pressure was controlled using two valves in parallel. The larger of those valves was controlled open loop, while the smaller was controlled closed loop based on exhaust surge tank pressure. EGR was extracted from the surge tank and was directed towards the engine through one of two paths, cooled or uncooled. The uncooled path had a single valve capable of being controlled closed loop based on EGR rate, while the cooled path had a two-valve control system similar to that used to control exhaust pressure. The uncooled path was used either to facilitate high intake temperature or to avoid overcooling and condensation in the cooled path at low load conditions. Additional temperature control was provided by an EGR cooler coolant flow control valve.

Exhaust NOx, CO, HC, CO_2 and O_2 concentrations were measured with separate emissions benches, one located in the exhaust surge tank (MEXA-7400DTRLE) and the second located in the exhaust line downstream of the exhaust pressure control valves (MEXA-

7100DEGR). Heated sample lines were used to maintain sample line temperature above the HC and water dew points and heated soot filters were used to protect the analyzers from contamination. The exhaust surge tank measurement was used whenever possible to minimize errors associated with water and hydrocarbons condensation, which could occur in the exhaust pipe as a result of heat transfer. A comparison of the result of the two analyzers showed that errors in HC and NOx emissions occurred primarily at the lowest speed and load conditions where the exhaust flow rate and temperature was very low. At high speed and load, the target exhaust surge tank pressure exceeded the analyzer limit of 150kPa. Consequently, the exhaust surge tank measurement was discontinued at those conditions to protect the analyzer and the downstream measurement was used as the primary measurement instead. Under those conditions, exhaust temperature and flow rate was sufficiently high and errors associated with condensation were negligible.

Intake CO_2 concentration was measured in the intake surge tank using the MEXA-7100DEGR analyzer to determine EGR rate when combined with the exhaust CO_2 measurement using Equation 3.1.

$$EGR = \frac{\dot{m}_{EGR}}{\dot{m}_{EGR} + \dot{m}_{air}} = \frac{CO_{2,\text{int}} - CO_{2,bg}}{CO_{2,exh} - CO_{2,bg}} \cdot 100 \qquad \text{Equation 3.1}$$

$CO_{2,\text{int}}$ and $CO_{2,\text{exh}}$ are the measured intake and exhaust CO_2 concentrations while $CO_{2,bg}$ is the atmospheric CO_2, which is assumed to be 0.03%. It is also useful to look at EGR in terms of intake oxygen concentration, a parameter that fundamentally controls NOx emissions. Consequently, an oxygen sensor was used in the intake sample line to measure intake oxygen concentration directly. Furthermore, the burnt mass fraction (FMAN), a control parameter that is directly related to intake oxygen proposed by Roettger *et al*[v] and calculated as shown in Equation 3.2, was used for analysis in this study.

$$FMAN = \left(\frac{EGR}{100}\right) \cdot \left(1 - \frac{O_{2,exh}}{21.95}\right) = 1 - \frac{O_{2,\text{int}}}{21.95} \qquad \text{Equation 3.2}$$

Smoke was measured using an AVL 415S smoke meter located after the exhaust backpressure control valves. Filter smoke number (FSN) was then correlated to soot concentration (K_C) in mg/Sm3 at 20°C and 101.3 kPa using the MIRA correlation (see equations 3.3).[vi]

$$Kc = 0.982e^{3} \cdot FSN \cdot 10^{(FSN \cdot 0.1272 - 1.66)} \qquad \text{Equation 3.3}$$

Soot concentration was then converted to mass flow rate (G_{soot}) in g/hr using equation 3.4.

$$G_{soot} = K_C \cdot (\dot{m}_{air} + \dot{m}_{fuel}) \cdot \frac{0.001}{1.2048} \qquad \text{Equation 3.4}$$

where air and fuel flow are in kg/hr.

Fuel flow rate was measured with a Pierburg low flow fuel cart. Results from the direct

measurement tended to be erratic. Consequently, fuel flow was verified using the critical flow orifice air flow measurement and the air fuel ratio determined by the emissions bench using the Spindt method[vii]. The result of this calculation tended to be more consistent than the low flow fuel cart measurement, so it was used in calculations of emissions or fuel consumption

Cylinder pressure was measured with an AVL GH12D flush mount pressure transducer. Data was recorded at a 0.05 CAD resolution. Analysis of the measured cylinder pressure trace was used both for heat release analysis, a first law analysis to determine the rate at which the fuel is burned in-cylinder, and Noise analysis, an analysis that determines the frequency content of the cylinder pressure trace, attenuates it appropriately and converts the result to an engine radiated noise level of dB attributable to combustion. The cylinder pressure measurement was also used to determine the projected multi-cylinder BMEP. This projected BMEP was based on the Net Mean Effective Pressure (NMEP) determined from the cylinder pressure trace and a projected multi-cylinder friction (FMEP) determined based on engine speed (or mean piston speed) and peak firing pressure. The transfer function for FMEP was generated based on 6.7L multi-cylinder data.

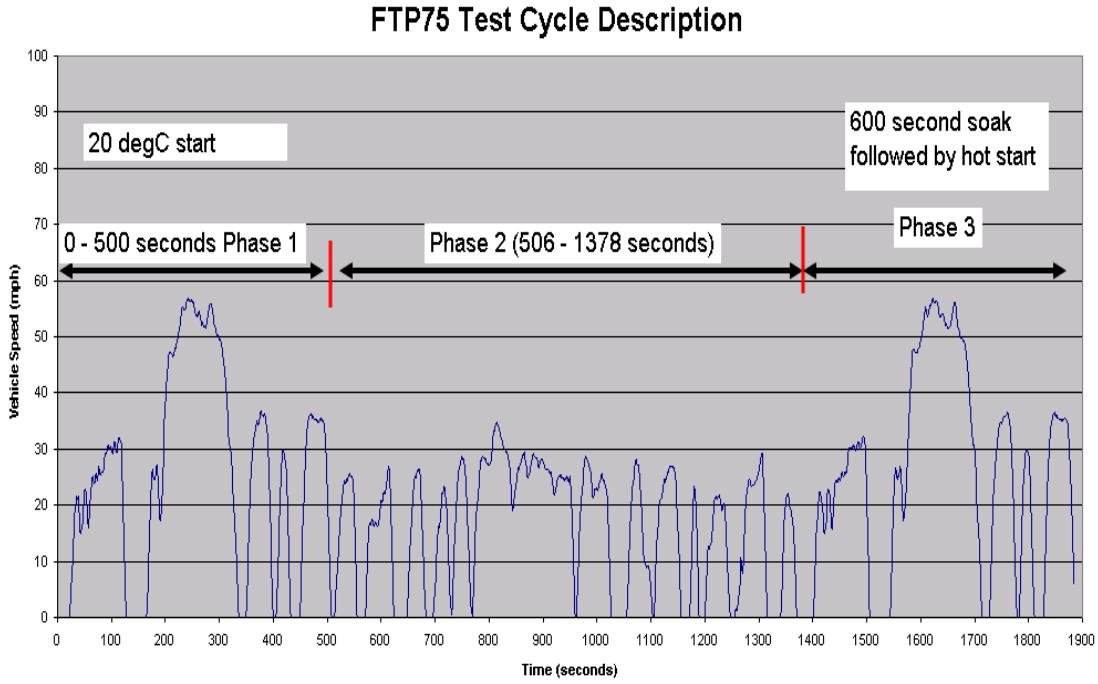

Figure V.34. FTP75 Test Cycle protocol for biofuel engine testing

V.3.4 Test conditions

Tests were conducted at the 11 engine speed and projected BMEP points shown in Figure V.35. Five of these conditions (CC1-CC5) were established to describe the FTP city cycle (Figure V.34). Three of these test points (CC1-CC3) and one additional condition (25-4), were tested in low temperature combustion mode. Two operating condition (A100, C100) were used

as an indicator of heavy-duty FTP performance. The remaining three test points (CF1, CF2, CF3) were used to assess potential light-duty full load performance.

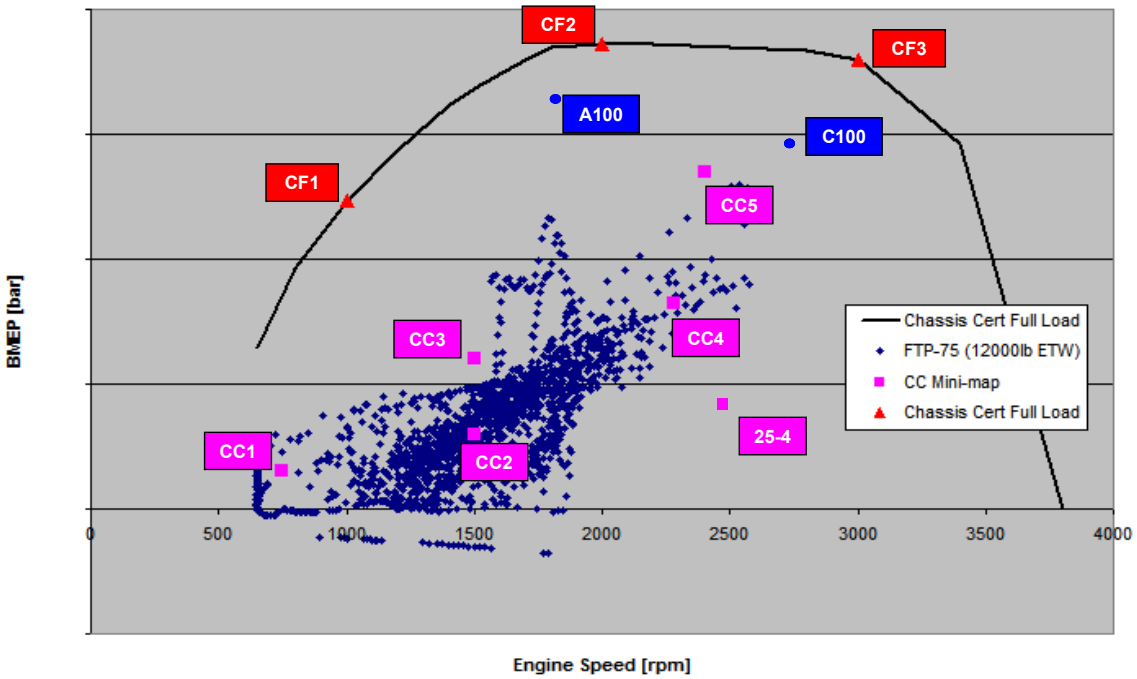

Figure V.35. Single-cylinder test conditions.

The intake pressure, intake temperature and exhaust pressure boundary conditions for each of these test points was established based on multi-cylinder data. At CC2, which had very high intake temperature on the multi-cylinder due to the use of the EGR cooler bypass, the intake temperature was lowered for LTC tests to increase ignition delay, thus enabling LTC. The calibration, while similar to the multi-cylinder, was optimized for the single-cylinder engine with the baseline fuel.

V.3.5 Test procedure

Conventional Combustion: A series of tests were established to evaluate the fuels as though tested at the same engine speed and pedal position on a multi-cylinder, which would yield the same calibration between fuels. To establish the main fuel quantity, tests were initially performed using the baseline fuel (720). The commanded main fuel quantity (or injector energizing time) was established based on the commanded fuel quantity required to reach the target projected BMEP at a nominal FMAN level with that baseline fuel. That same commanded main fuel quantity as well as the fuel rail pressure, main SOI, and pilot SOI and quantity (where applicable) were used in subsequent testing of the other four fuels. An FMAN sweep was used to generate a reliable data set for each fuel.

Low Temperature Combustion: A similar methodology was used to test fuel performance under the various LTC conditions; however, previous LTC testing results demonstrated that maintaining the 10% burn location (CA10) was beneficial for fuels of different cetane[viii].

Consequently, results at the nominal FMAN level with the 720 fuel were used to establish not only the commanded main injection quantity, but also the target CA10. While commanded main quantity was held constant for all fuels, along with rail pressure, the main injection timing was adjusted to maintain the CA10 at the target value throughout an EGR sweep for each test fuel at each speed-load point.

Chassis Certification Full Load: The goal of chassis certification full load testing was different from that of part load testing. Rather than minimizing emissions, NVH and fuel consumption, the primary goal was to determine the maximum torque at a given engine speed when operating within the physical limits of the engine (i.e. exhaust temperature, peak cylinder pressure). Consequently, the approach to testing was different. FMAN was set to zero percent and the injected fuel quantity was increased until a physical limit was reached, the smoke exceeded 2 FSN or lambda was at or below 1.0. Comparison of the various fuels at the same engine speed and pedal position was achieved in the analysis phase by comparing results from all fuels at the same commanded fuel quantity chosen based on 720 fuel results.

V.3.6 Results and discussion

*NOx emissions***:** The comparison of NOx emissions between diesel fuel (720) and CME as a function of intake oxygen shown in Figure V.36a indicates that NOx emissions are primarily a function of intake oxygen concentration, an effect which is well documented[ix,x,xi], and that both fuels behave similarly regardless of composition. This observation appears to be at odds with the results of vehicle testing, which showed an increase in NOx emissions with increasing biodiesel content[xii]. However, this result can be understood (in part) by graphing NOx emissions as a function of EGR rate as shown in Figure V.36b. This figure shows that NOx increased for a given EGR rate as the oxygen content of the fuel increased. Since the vehicle has closed loop EGR control based on measured air mass, which is inversely proportional to EGR rate when intake conditions are held constant (see equation 4.1.1.1), the vehicle behavior will more closely resemble Figure V.36b. This effect is a result of the fact that the biodiesel fuels have higher oxygen content, leading to an increase in exhaust oxygen concentration at a given EGR rate, air mass flow and fuel flow. In turn, this leads to an increase in intake oxygen concentration, which increases NOx.

$$EGR = \frac{m_{EGR}}{m_{total}} = 1 - \frac{m_{air} \cdot R \cdot T_{man} \cdot 2 \cdot 1000}{P_{man} \cdot N \cdot 60 \cdot V_{disp} \cdot \eta_{vol}} \qquad \text{Equation 4.1.1.1}$$

where T_{man} is the intake temperature in Kelvin, m_{air} is the intake air flow rate in kg/hr, P_{man} is the intake pressure in kPa, N is the engine speed in rpm, V_{disp} is the engine displacement in liters and η_{vol} is the volumetric efficiency.

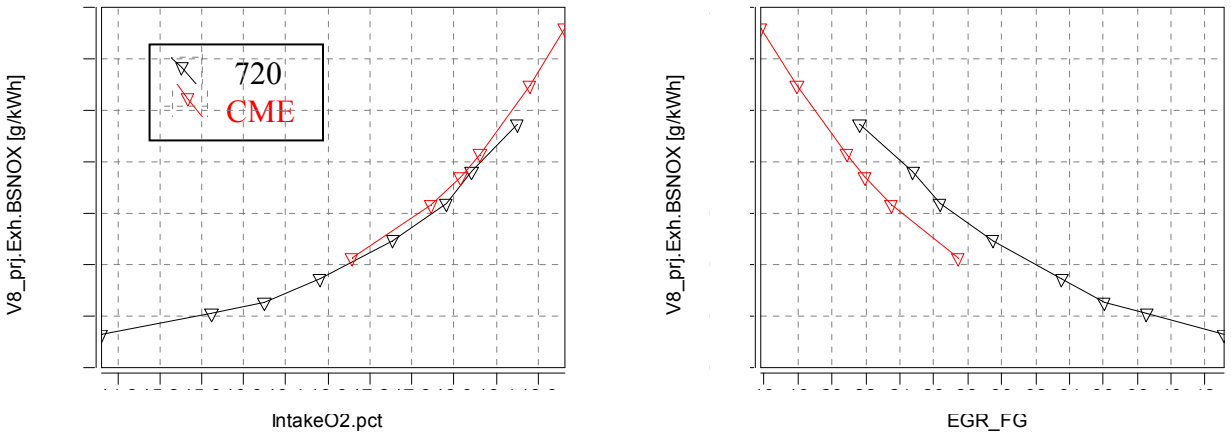

(a) (b)

Figure V.36. Engine-out NOx emissions for various fuels as a function of (a) intake oxygen concentration and (b) EGR rate.

This calibration effect is compounded by the fact that biodiesel fuels have lower energy content. As a result, in order to achieve the acceleration or vehicle speed the driver must increase the commanded fuel. This shifts the area of the engine map in which engine operates to a higher commanded fuel quantity. Such a shift will change the calibration settings, which will lead to a decrease in EGR rate and an increase in boost pressure. An example of this from an EU4 engine is shown in Figure V.37. Both of these changes in calibration will cause a further increase in intake oxygen concentration, and thus a further increase in NO_x emissions. Similar observations were made by Eckerle *et al*[xiii], who suggested that changes in engine control settings accounted for most of the NOx difference between a B20 (i.e.,20% biodiesel and 80% petroleum diesel) blend and an analogous petroleum diesel fuel.

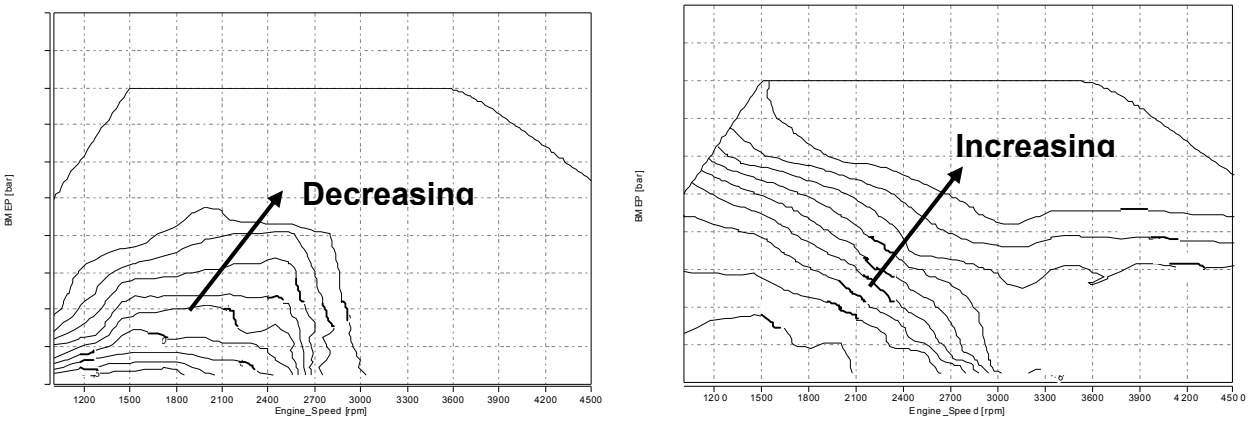

(a) EGR Rate (b) Intake Pressure

Figure V.37. (a) EGR rate and (b) Intake pressure maps on a typical diesel engine

This suggests that new control strategies may be employed to achieve equivalent emissions when using biodiesel fuels. One simple step would be to control EGR rate based on the intake oxygen concentration or an equivalent parameter to compensate for the increased oxygen in the fuel. Such a strategy has been proposed whereby either the intake oxygen concentration or the exhaust oxygen composition is taken into account when setting the EGR

flow using the burnt mass observer, FMAN.

Most of the remainder of this section presents the impact the fuels on various attributes at a fixed FMAN for each operating condition. This comparison is shown for NOx emissions at each of the various operating conditions Figure V.38. The figures show that the fuel had only a minor effect on NOx emissions.

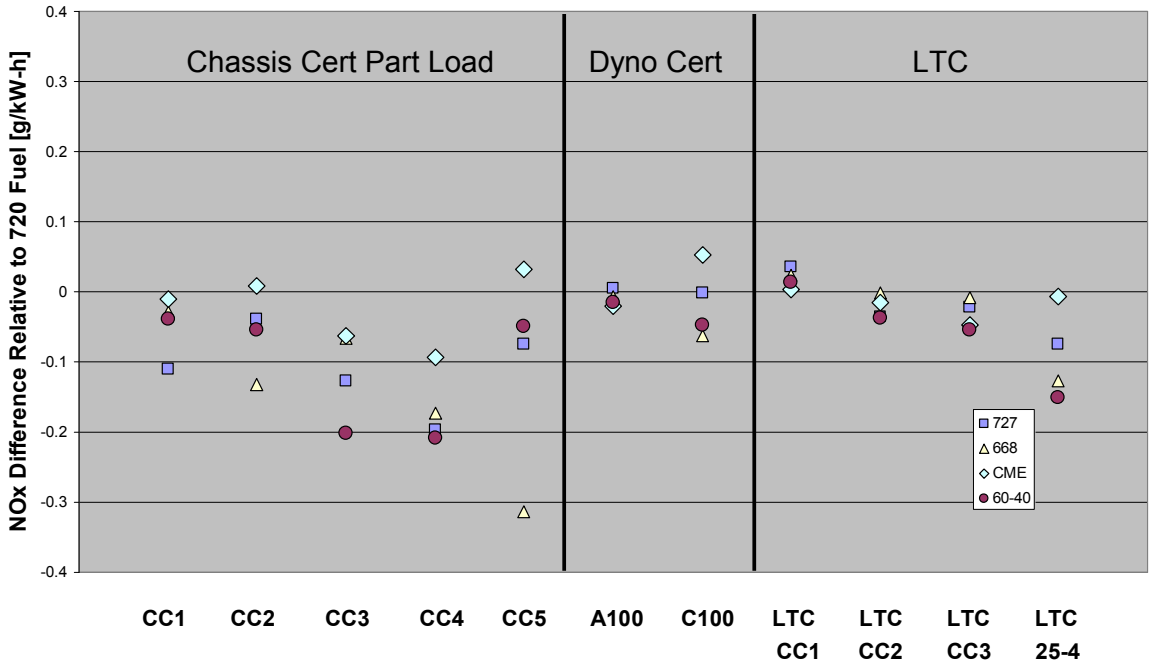

Figure V.38. Comparison of projected brake specific NOx emissions for four different fuels vs. 720 fuel at chassis cert part-load, dyno cert and LTC operating condition.

Paired t-tests between the average NOx value of the three petroleum-based diesel fuels and NOx with both CME and the 60-40 blend showed that the difference in NOx between the diesel fuels and the biodiesel fuels was statistically insignificant. However, when compared against 720 fuel alone rather than an average of the three diesel fuels, the 60-40 blend produced 10-15% lower NOx. There was no discernable difference between the 720 diesel fuel and CME.

Hydrocarbons: Figure V.39 shows a comparison of hydrocarbon (HC) emissions when comparing 4 fuels with 720 fuel at the various operating conditions tested. The results in conventional combustion (chassis cert part-load and dyno cert) indicate that the HC emissions with CME were comparable to those with petroleum-based diesel fuels, but that they were significantly increased with the 60-40 blend. Paired t-tests on the percent difference between each fuel from the average value at each operating condition confirm these conclusions to be statistically valid.

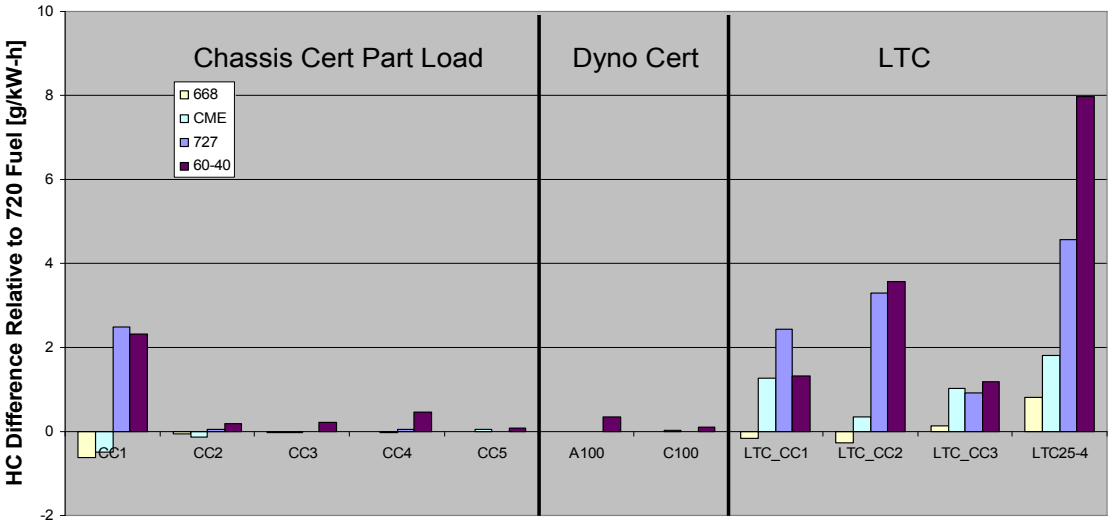

Figure V.39. Comparison of projected brake specific hydrocarbon emissions for various fuels.

The comparison of heat release at CC4 (2280 rpm, 8.2 bar projected BMEP), shown in Figure V.40, indicates the source of the higher HC emissions with the 60-40 blend. First, due to the lower cetane value of DBS, combustion of both the pilot injection and main injection were delayed with the 60-40 blend. In addition, the reduced energy content of the 60-40 blend combined with the later pilot heat release appears to have significantly reduced the pilot heat release, which further delayed main combustion phasing. Both the low heat pilot release and late combustion phasing lead to an increase in HC emissions with the 60-40 blend.

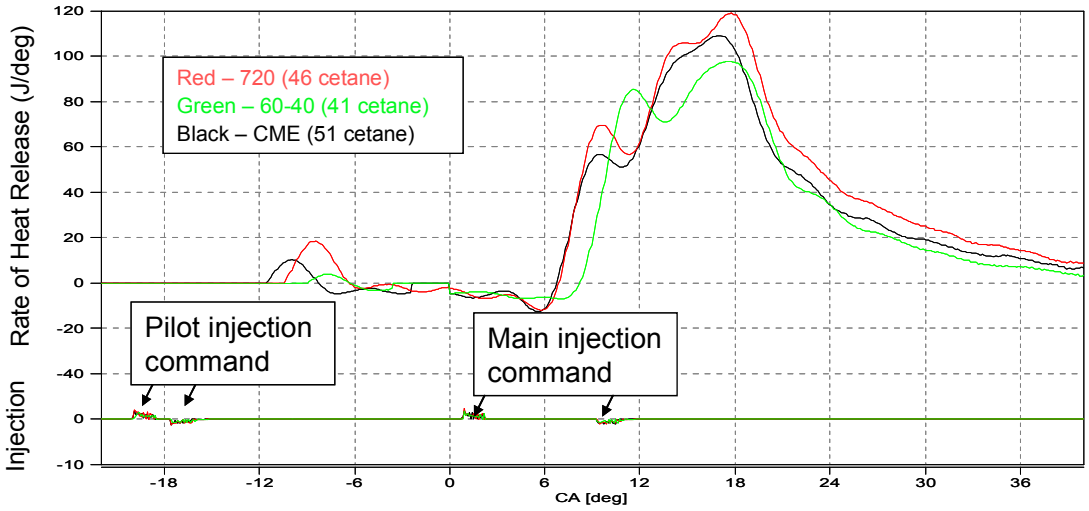

Figure V.40. Heat release and injector current trace at CC4 (2280rpm, 8.2 bar projected BMEP) for three different fuels: 720, CME and the 60-40 blend.

HC emissions in LTC shown in Figure V.39 did not appear to follow the same trend as seen in conventional combustion. Instead, HC emissions appeared to be more a function of the

fuel cetane, particularly with low cetane fuels, which had significantly higher HC than the other fuels. To understand this trend, it is important to remember that SOI was adjusted in LTC to maintain combustion phasing as measured by the 10% burn fraction (CA10). Consequently, injection timing was advanced with low cetane fuels and retarded with high cetane fuels. This caused ignition dwell, the time from end of injection to start of ignition, to increase for low cetane fuels and decreasing for high cetane fuels.

Musculus *et al*[xiv,xv] showed that there was a link between a positive ignition dwell and HC emissions due to the development of an entrainment wave, which causes rapid over-leaning of the fuel near the nozzle after the end of injection. Since the amount of over-leaning and over-lean mixture increases as ignition dwell increases due to the propagation of this entrainment wave, HC emissions increase with ignition dwell. Since injection timing was advanced to maintain combustion phasing with low cetane fuels, HC emissions were significantly higher when those low cetane fuels were used in LTC than the other fuels.

In the LTC results, compensation appeared to reduce HC emissions for both biodiesel fuels. This is believed to be attributed to the fact that the compensation effectively increased in duration of injection, thereby decreasing the ignition dwell. Since the fuel quantity adjust factor was greatest with the 60-40 blend due to its very low energy content, the HC reduction was most pronounced with that fuel.

Noise: A comparison of the noise for four fuels vs. 720 fuel is presented in Figure V.41. While differences in noise level could be observed between fuels, these differences did not appear to trend with biofuels or petroleum based fuels. Instead, the effect of noise appeared to be a function of cetane number, wherein fuels of similar cetane behaved similarly, but the noise was distinctly different when comparing the two high cetane fuels (668 and CME) against the two low cetane fuels (727 and the 60-40 blend). It is interesting to note that the effect of cetane on noise was different in conventional combustion and LTC. In conventional combustion, the high cetane fuels produced lower noise due to the shortened ignition delay and reduced pre-mixed burn fraction. However, in LTC, it is the low cetane fuels that produce less noise. Since LTC is a pre-mixed combustion mode, there should be no change in the pre-mixed burn fraction for different cetane fuels.

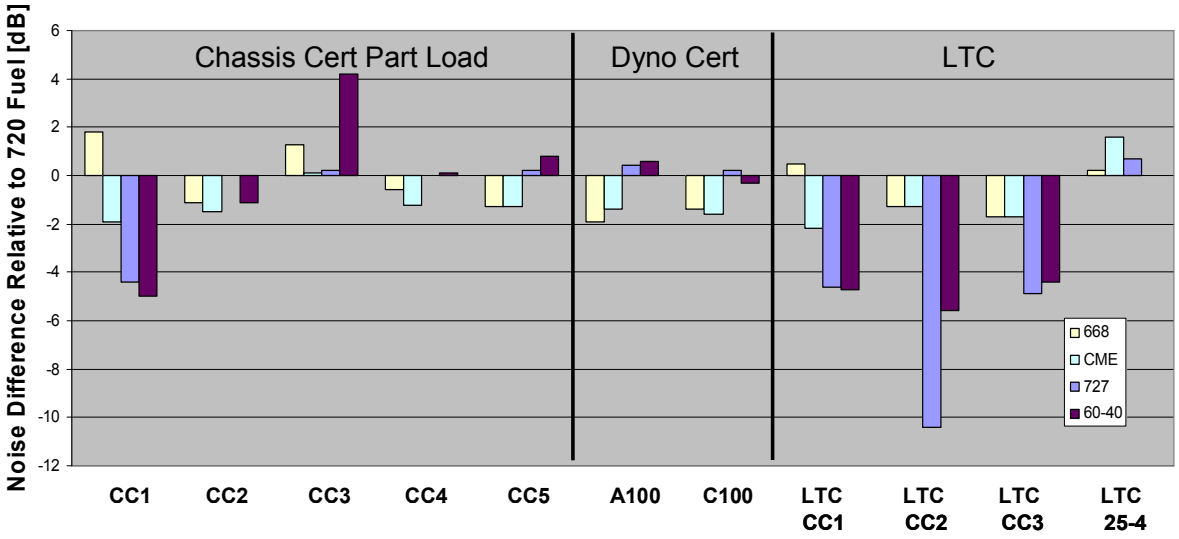

Figure V.41. Comparison of noise for various fuels.

The cause of the noise behavior in LTC seen in Figure V.41 is thought to be related to the over-leaning behavior explained above that was the source of differences in hydrocarbon emissions. It is believed that this over-leaning reduced the combustible mixture in the combustion chamber at the time of ignition, which reduced the strength of combustion in addition to increasing the unburned HC emissions. It is believed that this effect led to lower noise with low cetane fuels. This is supported by the fact that noise increased with the 60-40 blend once the compensation strategy was applied, thereby decreasing ignition dwell.

Although the results suggests a correlation between noise and fuel cetane number, paired t-tests showed that there was no statistical difference in noise between the various fuels in conventional combustion. However, in LTC, where trends were stronger, a statistical difference was found when comparing either 727 or the 60-40 blend to any of the other fuels.

Fuel consumption, projected BMEP and thermal efficiency: Figure V.42 shows that fuel consumption increased significantly with biodiesel fuels. The increase in fuel consumption was greater with the 60-40 blend than with CME. Since testing was conducted at constant commanded fuel quantity, this increased fuel consumption manifests itself in a decrease in projected BMEP. Analysis of the data shows that BMEP was an average of 12% lower with CME than with petroleum-based diesel fuels and 29% lower with the 60-40 blend. These differences are trend-wise well correlated with the fuel net heating value, which is highest for petroleum-based diesel fuels, lower for CME and lowest for the 60-40 blend. As a result of the heating value difference, vehicle fuel economy will be lower with biodiesel fuels, especially with the 60-40 blend.

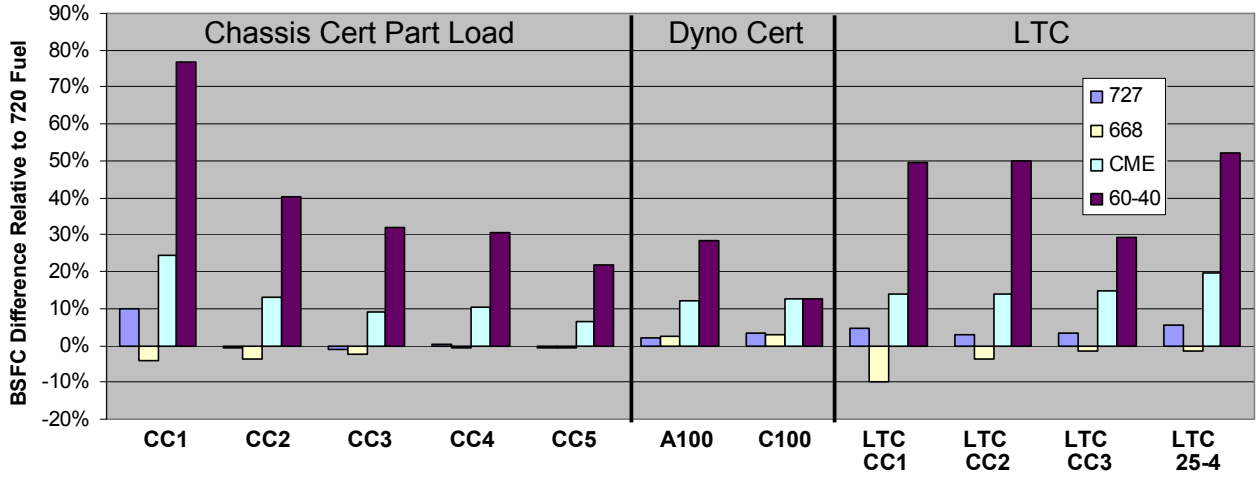

Figure V.42. Comparison of projected brake specific fuel consumption for various fuels.

To normalize the results for differences in net heating value, Figure V.43 shows a comparison of the projected brake thermal efficiency of the various fuels. A paired t-test comparing CME to both 720 and 668 fuels indicated that the thermal efficiency of those fuels were virtually identical and that there was no statistically significant difference between CME and the average of all three petroleum-based diesel fuels. The thermal efficiency with CME was

found to be statistically higher than that with 727 fuel (low cetane), a difference that was an average of 0.8%. The reason for this difference is not well understood, but it could be due to the effect of cetane, which would serve to advance combustion for the higher cetane fuels such as CME relative to the low cetane fuels such as 727.

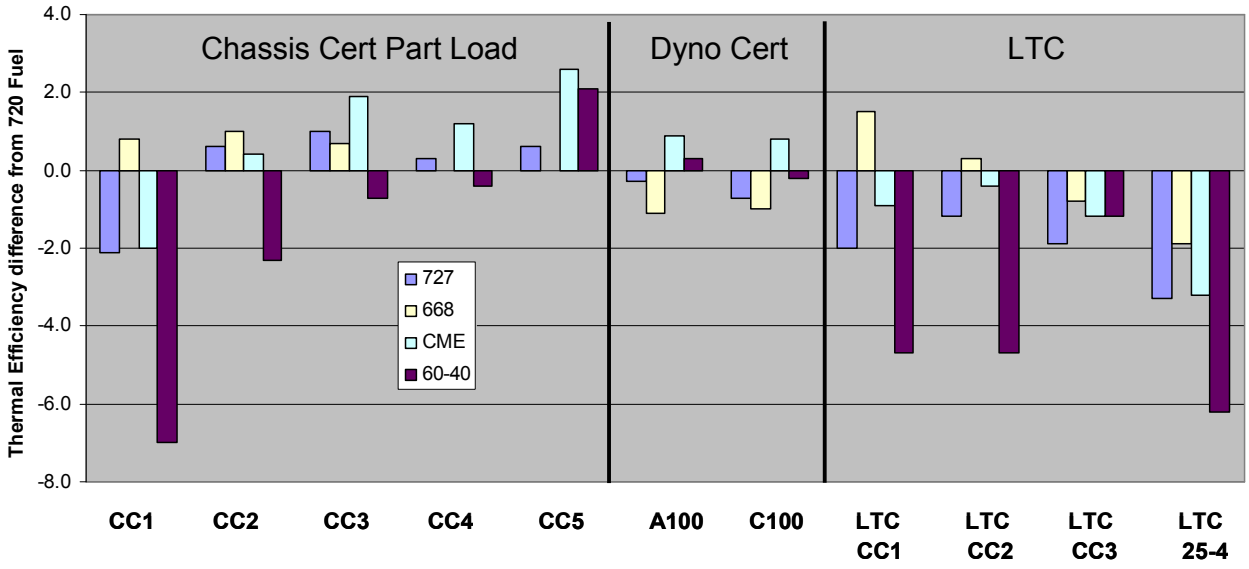

Figure V.43. Comparison of projected brake thermal efficiency with constant fuel quantity at each operating condition for four different fuels compared to 720 fuel.

Pair t-tests between the various diesel fuels and the 60-40 blend indicate that the thermal efficiency with the 60-40 blend was significantly lower than any of the other fuels tested and that the difference was an average of a little over 2% for all but 727, which had an average thermal efficiency that was 1.5% higher than the 60-40 blend. The source of the lower efficiency with the 60-40 blend is the result of much later combustion phasing and high hydrocarbon emissions, both thought to be caused by the low cetane and low pilot heat release as outlined above.

Particulate Matter (PM): Particulate reduction with biodiesel fuels is very well documented and is believed to be the result of the fact that the oxygen in the fuel lowers the equivalence ratio at the lift-off length, thus increasing the amount of oxygen that participates in the oxidation of soot and soot precursors in a diesel diffusion flame[xvi]. A comparison of particulate matter between the various fuels in the current study is shown in Figure V.44. It is apparent from the figure that PM emissions were significantly lower with both biodiesel fuels as compared to the three petroleum-based diesel fuels, regardless of combustion mode.

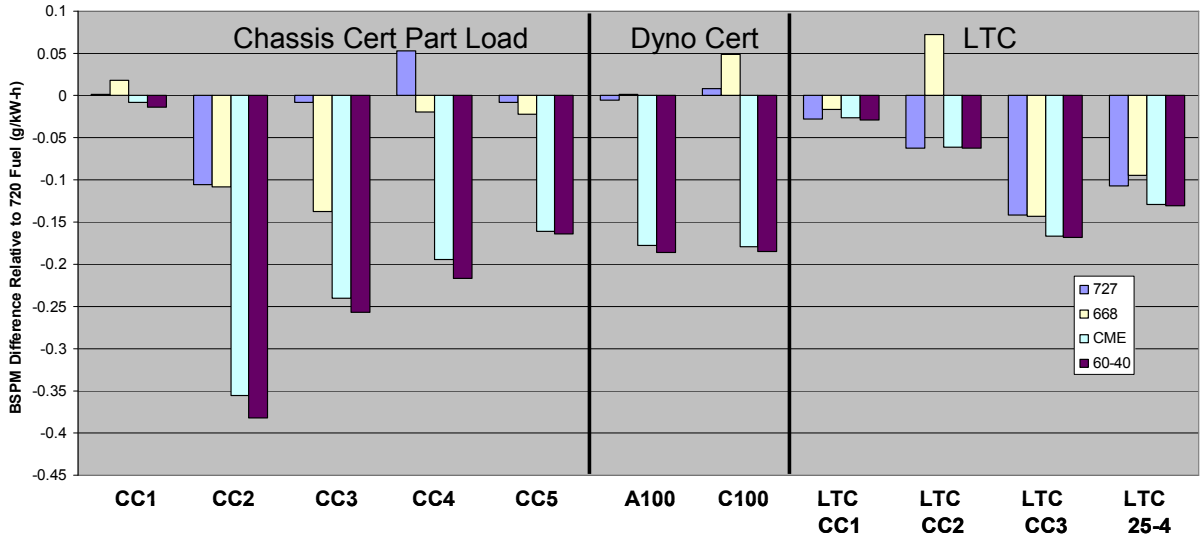

Figure V.44. Comparison of projected brake particulate matter with constant fuel quantity at each operating condition for various fuels.

Since the PM with both biodiesel fuels was very low compared to the diesel fuels, Figure V.45 shows the PM reduction relative to 720 fuel with only CME and the 60-40 blend for all operating conditions excluding the idle condition. The results show that PM was significantly lower with the 60-40 blend than with CME. Analysis of the data indicate that while CME reduced PM by an average of 89% over all operating conditions, the 60-40 blend reduced it by an average of 97%.

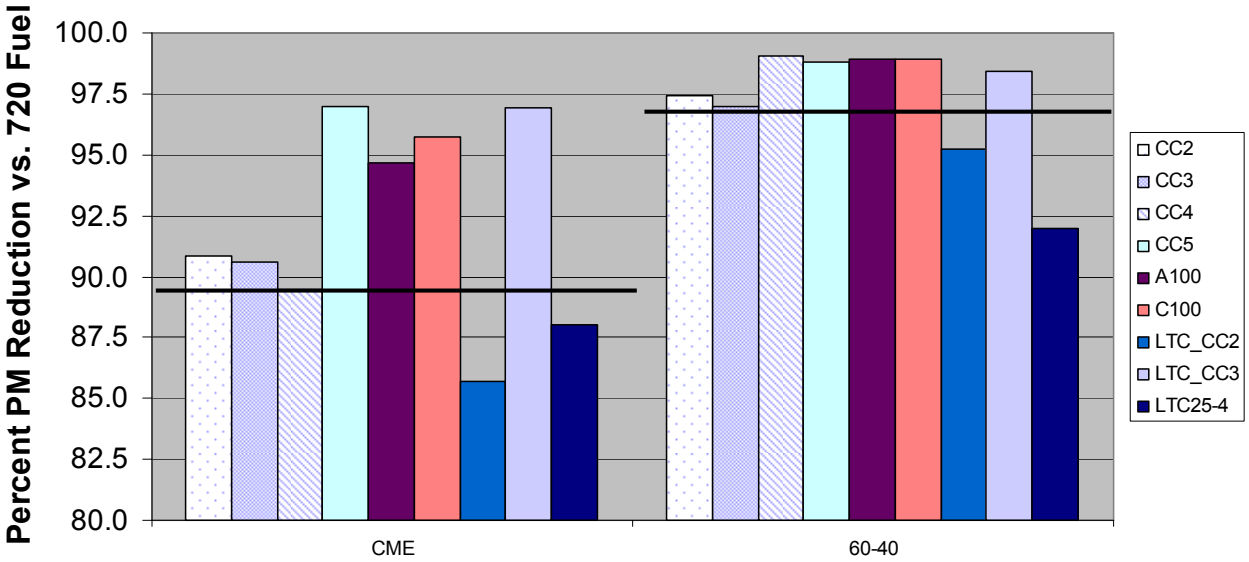

Figure V.45. Comparison of projected brake particulate matter with constant fuel quantity at each operating condition for CME and a 60-40 blend of CME and DBS.

It has been shown in the literature that soot formation is linked to the equivalence ratio at

the lift-off length (H)[xvi,xvii,xviii,xix]. Pickette *et al*[xix] has shown that fuel contributes to this effect. The oxygen ratio was proposed by Mueller *et al*[xx] to account for differences in mixture stoichiometry when oxygenated fuels are used. The method for estimating both the equivalence ratio at the lift-off length (φ) and the oxygen ratio (α) are outlined by Pickette *et al*[xix]. That methodology was used to generate Figure V.46, which shows the average oxygen ratio in the fuel spray as a function of axial location at one of the operating conditions tested, with points plotted showing the oxygen ratio at the lift-off length (H). The oxygen ratio is significantly lower for a given axial spray location with both biofuels. In addition, the oxygen ratio at the lift-off length trends with PM emissions where all three mineral diesel fuels had very similar oxygen ratios while a significant decrease was observed with CME and a further drop on oxygen ratio was observed with the 60-40 blend. This calculation was performed at several operating conditions. Since the trends were similar for all operating conditions, plots at additional operating conditions were not included for brevity.

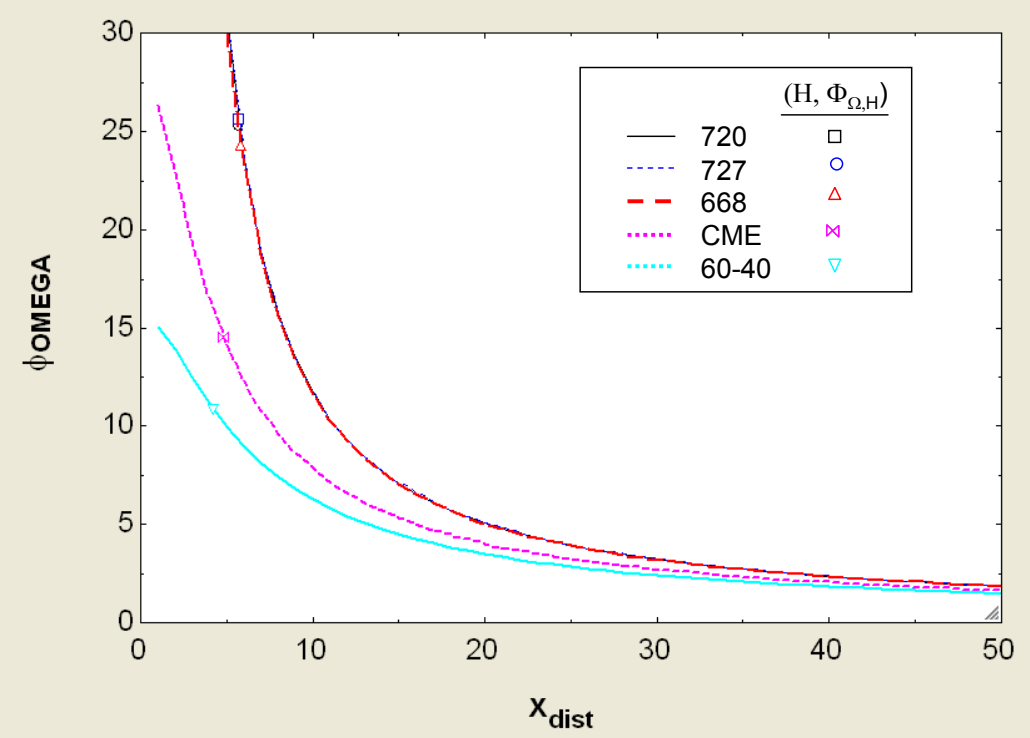

Figure V.46. A comparison of the average oxygen ratio across the spray cross section as a function of axial spray location for various fuels at 750rpm, 1.5 bar.

Genzale and Pickette[xxi] also found that soot inception times appeared to be longer for biodiesel fuels than petroleum diesel, suggesting that the effect of the biodiesel fuels on PM may also be chemical in nature. This may of particular importance in LTC where the added time to mix prior to soot formation may enable the fuel-air mixture to become leaner before forming soot, increasing the likelihood of avoiding the soot formation region shown in Figure V.32.

V.3.7 Conclusions

Neat canola biodiesel (CME) was evaluated using single-cylinder experiments. Results

showed that NOx has no discernable sensitivity to the fuel when compared at the same intake oxygen concentration. The results are counter to typical vehicle findings, which show increases in NOx emissions. That increase is believed to be the result of two factors related to calibration.

(1) Higher fuel oxygen content leads to increased exhaust oxygen. Since EGR is typically controlled by either maintaining a target air mass flow or an EGR rate, the higher exhaust oxygen concentration causes intake oxygen to increase relative to diesel fuel, leading to higher NOx.
(2) Lower fuel energy content leads to increased driver pedal demand to maintain vehicle speed, which shifts the calibration such that the commanded EGR rate decreases and boost pressure increase; further increasing intake oxygen concentration and, thus, NOx emissions.

A detailed single-cylinder study was conducted to assess the impact of two different biodiesel fuels. The second of these fuels, a mix of 60% neat canola methyl ester and 40% dibutyl succinate (60-40), was developed to improve the cold flow properties. Single-cylinder test assessed differences in emissions, noise, fuel consumption, thermal efficiency and torque at various operating conditions in both conventional combustion and low temperature combustion. Comparison at constant FMAN showed:

- Particulate emissions were 89% lower when CME was used as compared to diesel fuel. This particulate reduction grew to 97% with the 60-40 blend. The trend is consistent with the oxygen content of the two fuels.
- Except for a reduction in soot emissions, biodiesel fuels did not appear to have a significant impact on the emissions and noise behavior in low temperature combustion (LTC). Behavior in this mode appeared to track more closely with cetane number.
- Fuel consumption increased with the biodiesel fuels proportional to the differences in net heating value of the different fuels; however, the thermal efficiency was similar between diesel and biodiesel fuels.
- Higher hydrocarbons, higher noise and slightly lower thermal efficiency were observed with the 60-40 blend. This was attributed to poor pilot heat release resulting from a combination of the low cetane and low net heating value of that fuel, which retarded combustion phasing.
- No significant difference in NOx emissions could be identified between diesel fuels and CME. A slight reduction in NOx was observed with the 60-40 blend. This is believed to be related to the combustion phasing.

Summary: An assessment of basic fuel properties showed that canola biodiesel (canola methyl esters, CME) had better cold flow properties than soy biodiesel which is most commonly used in the United States. Further testing showed the addition of dibutyl succinate (DBS) to CME further improved cold flow properties, but reduced cetane number. A blend of 60% CME and 40% DBS provided cold flow benefits while staying within the US minimum cetane requirements. Single-cylinder testing of both CME and the newly proposed fuel blend showed no difference in NOx emissions between diesel fuel, CME, and the 60-40 CME-DBS blend, which does not appear to match data from vehicle testing. The result suggested that increases in vehicle NOx emissions may be largely due to two factors: the method for controlling Exhaust

Gas Recirculation (EGR), which is typically air mass-or EGR rate-based rather than intake oxygen-based, and a shift in the EGR and boost calibration set points with increasing pedal required to achieve the same load with the lower energy content biofuels. When compared at constant intake oxygen, NOx, combustion noise and thermal efficiency were similar between the diesel fuels and both biofuels. The oxygenation of the two biofuels lead to a substantial reduction in particulate matter, which amounted to an 89% reduction with CME and a 97% reduction with the 60-40 CME-DBS blend. Elevated hydrocarbon (HC) emissions were observed with the 60-40 CME-DBS blend, which were attributed to poor pilot burn caused by the low cetane number and low energy content of that fuel. Single-cylinder Low Temperature Combustion (LTC) testing with the two oxygenated fuels indicated that fuel related effects appear to track with the cetane number and are relatively insensitive to fuel oxygenation.

References

[i] Kimura, Shuji, Aoki, Osamu, Ogawa, Hiroshi, Muranaka, Shigeo and Enomoto, Yoshiteru, " New Combustion Concept for Ultra-Clean and High-Efficiency Small DI Diesel Engines," SAE Paper 1999-01-3681, 1999.

[ii] Akihama, Kazuhiro, Takatori, Yoshiki, Inagaki, Kazuhisa, Sasaki, Shizuo and Dean, Anthony M., " Mechanism of the Smokeless Rich Diesel Combustion by Reducing Temperature," SAE Paper 2001-01-0655, 2001.

[iii] Iwabuchi, Y., Kawai, K., Shoji, T., and Takeda, Y., "Trial of New Concept Diesel Combustion System – Premixed Compression-Ignition Combustion", SAE Paper 1999-01-0185, 1999.

[iv] Hasegawa, R. and Yanagihara, H., "HCCI combustion in DI diesel engine," SAE Paper 2003-01-0745, 2003.

[v] Röttger, Daniel, Vigild, Christian, Tumelaire, Charles, Karvounis, Evangelos and Calendini, Pierre Olivier, "A model based approach for diesel combustion control," Aachener Kolloquium Fahrzeug- und Motorentechnik 2006, 2006.

[vi] Dodd, A., Holubecki, Z., "The Measurement of Diesel Exhaust Smoke," MIRA Research Report 1965/10, 1965.

[vii] Spindt, R.S., "Air Fuel Ratios from Exhaust Gas Analysis," SAE Paper 650507, 1965.

[viii] Kurtz, Eric, and Kuhel, Douglas, "Cetane Effect and Compensation in Low Temperature Combustion", Ford Technical Report No. SRR-2010-0052, 2010.

[ix] Röpke, S., G.W. Schweimer, and T.S. Strauss, “NOx Formation in Diesel Engines for Various Fuels and Intake Gases,” SAE Paper 950213, 1995.

[x] Tsunemoto, H. and Ishitani, H. "The Role of Oxygen in Intake and Exhaust on NO Emission, Smoke and BMEP of a Diesel Engine with EGR System." SAE Paper 800030, 1980.

[xi] Mitchell, D. L., Pinson, J. A. and Litzinger, T. A. "The Effect of Simulated EGR via Intake Air Dilution on Combustion in an Optically Accessible DI Diesel Engine." SAE Paper 932798, 1993.

[xii] William Ruona, Ford Technical Leader, Personal Communication.

[xiii] Eckerle, W.A., Lyford-Pike, E.J., Stanton, D.W., LaPointe, L.A., Whitacre, S.D., and Wall, J.D., "Effects of Methyl Ester Biodiesel Blends on NOx Emissions," SAE Paper 2008-01-0078, SAE Trans. 117(4), 2008.

[xiv] Musculus, Mark P. B. , Lachaux, Thierry , Pickett, Lyle M. , Idicheria, Cherian A., " End-of-Injection Over-Mixing and Unburned Hydrocarbon Emissions in Low-Temperature-Combustion Diesel Engines," SAE Paper 2007-01-0907, 2007.

[xv] Musculus, Mark P. B. , Kattke, Kyle, " Entrainment Waves in Diesel Jets ," SAE Paper 2009-01-1354, 2009.

[xvi] Siebers, D.L. and Higgins, B.S., "Effects of Injector Conditions on the Flame Lift-Off Length of DI Diesel Sprays," Conference on Thermalfluidynamic Processes in Diesel Engines, Sept. 14-15, 2000.

[xvii] Higgins, B.S. and Siebers D.L., "Measurement of the Flame Lift-Off Location on DI Diesel Sprays Using OH Chemiluminescence," SAE2001-01-0918, 2001.

[xviii] Dec, J.E., "A Conceptual Model of DI Diesel Combustion Based on Laser-Sheet Imaging," Transactions of the SAE, Vol. 106, Sec. 3, pp. 1319-1348, 1997 (SAE970873).

[xix] Pickett, Lyle M. and Siebers, Dennis L., "Fuel Effects on Soot Processes of Fuel Jets at DI Diesel Conditions," SAE Paper 2003-01-3080, 2003.

[xx] Mueller, C.J., Pitz, W.J., Pickett, L.M, Martin, G.C., Siebers, D.L., and Westbrook, C.K., "Effects of Oxygenates on Soot Processes in DI Diesel Engines: Experiments and Numerical Simulations," SAE Paper 2003-01-1791, 2003.

[xxi] Genzale, Caroline and Pickette, Lyle, Sandia National Laboratory Combustion Research Facility, personal communication.

Definitions and acronyms

B20	blend of 20% biodiesel, 80% diesel fuel
B100	100% biodiesel
BMEP	brake mean effective pressure
BS	brake specific
BSFC	brake specific fuel consumption
CA10	crank angle location of 10% fuel mass burn fraction
CAD	crank angle degree

CME	canola methyl ester
CN	Cetane Number
CO	carbon monoxide
CO_2	carbon dioxide
CP	cloud point
CFPP	cold filter plugging point
DBS	dibutyl succinate
EGR	exhaust gas recirculation
FAME	fatty acid methyl ester
FMAN	burnt mass fraction in the intake manifold
FMEP	friction mean effective pressure
FSN	filter smoke number
FTP	federal test procedure
HC	hydrocarbon
LTC	low temperature combustion
MSU	Michigan State University
NHV	net heating value
NMEP	net indicated mean effective pressure (720 CAD)
NOx	oxides of nitrogen
NVH	noise, vibration and harshness
O_2	oxygen
PM	particulate matter
SOI	start of injection
URP	University Research Proposal

V.4 Ford Multicylinder Engine Testing

Background: Biodiesel has been pursued as an additional/alternative fuel for diesels for many years. The effects on biodiesel on combustion and emissions have been reported in a variety of forums throughout the world. Typical consensus (2012-01-1666, 2011-01-1939, many others) is that with biodiesel one typically sees a reduction in engine out particulates (PM), an increase in engine out NOx and similar levels of hydrocarbons (HC) and carbon monoxide. This has been attributed to the oxygenated content of the fuel and the typically lower energy content of the biofuel. The single cylinder research study done previously at Ford found that if the engine calibration was compensated/changed to maintain consistent intake oxygen levels with the different fuels tested, the emissions changes due to biodiesel were quite different from what has been typically reported. They found equivalent NOx, similar to reduced THC and a reduction in engine out PM.

Incremental vehicle testing was performed at Ford with three different fuels, two mineral diesel fuels and one B100 fuel from Michigan State University (MSU). The B100 is butyl nonanoate. Fuel properties for the three fuels are listed in Table V.5 below.

Table V.5. Properties of fuels used in multicylinder engine tests.

Fuel	Net Heat Value (BTU/lb)	Carbon weight fraction (CWF)	Hydrogen weight fraction (HWF)	Oxygen weight fraction (OWF)	Cetane number
MD1	18302	0.8707	0.1293	0	42.0
MD2	18440	0.8697	0.1303	0	44.0
MSU (But. Nonan.)	15120	0.7395	0.1243	0.1362	46.6

Test vehicle and conditions: A 2011 Ford F-350 with a 6.7L engine was tested on a chassis dynamometer using the 3 different fuels on several different emissions test cycles. The cycles run were a cold start FTP 75, a highway fuel economy test (HWFET) and the supplemental FTP test, US06. All were run at an emission test weight of 9500 lbs. Standard emissions measurements of total hydrocarbon (THC), CO, NOx, CO2, CH4 were taken as well as PM measurements with a Dekati Mass Monitor (DMM). Measurements were taken at the engine out location or feedgas (FG) location to quantify the difference in emissions due to the fuel type. For the two mineral diesel fuels the production engine calibration was used. For the B100 fuel, one set of tests was run utilizing the production calibration and two sets of tests were run with a modified calibration to compensate for the biofuel.

Results and discussion: The first set of Figures V.47-V.50 (1-4 below) shows the results from cold start FTP 75 testing. The results shown are for the weighted average over the entire 3-phase test. Figure 1 shows the results for engine out or feedgas (FG) total hydrocarbons (THC). As can be seen with no modifications to the calibration the biofuel had lower THC emissions, with the calibration changes the THC increased but still have an overall reduction compared to mineral diesel #1 and similar levels to MD2.

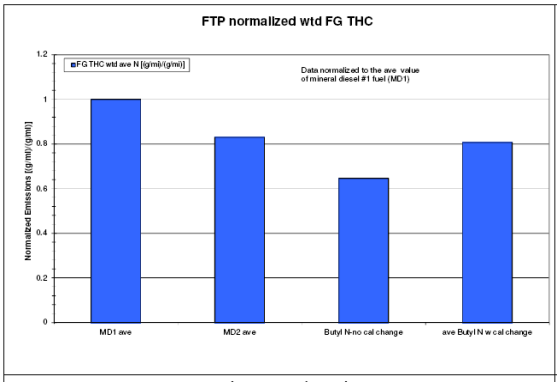

Fig 1.: FTP 75 wtd normalized THC emissions

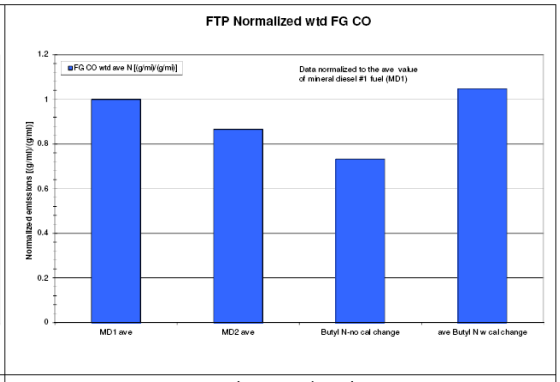

Fig 2.: FTP 75 wtd normalized CO emissions

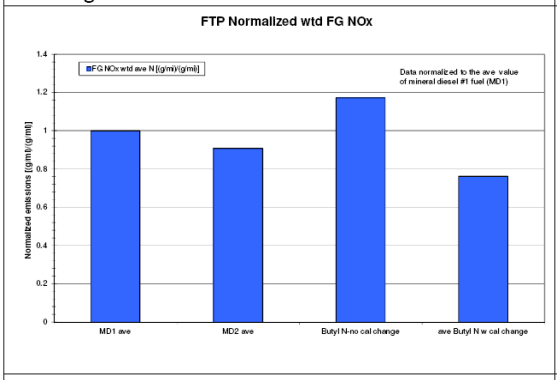

Fig 3.: FTP 75 wtd normalized NOx emissions

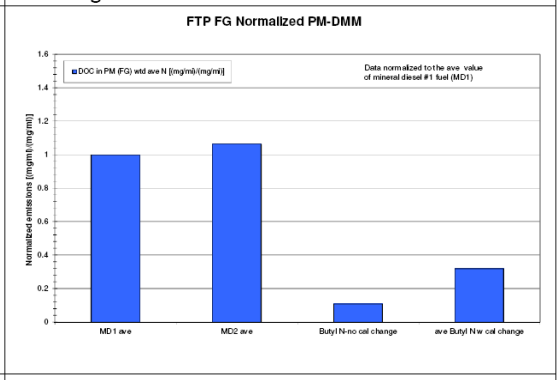

Fig 4.: FTP 75 normalized PM emissions

Similar results are seen for CO, Fig 2, with the no calibration change case having decreased CO and with the calibration changes the levels are approximately equivalent to both mineral diesel results. For NOx, Fig. 3, the trend is different, with no calibration change the NOx shows a clear increase while with the calibration change NOx has a clear reduction compared to both mineral diesel fuels. The PM benefits of the biofuel are clearly shown in Figure 4, with the no calibration change case for the biofuel having a dramatic decrease in PM. With the calibration changes, the PM increases slightly but still results in a significant decrease from the baseline mineral diesel fuels.

The next set of Figures V.51-V.54 (5-8 below) depicts the results from testing on the highway fuel economy test (HWFET). Overall the results from the HWFET are similar to the FTP results with some more significant differences in the emissions. As can be seen in Fig. 5, the biofuel cases with and without calibration changes both result in lower THC. Note the HWFET is a hot test compared to the cold start FTP 75. The engine strategy/calibration operates in a catalyst warm-up more which utilizes post injection and other actions to facilitate catalyst warm-up. These operating differences influence the results between a cold start and the hot test HWFET. Similar results are found for CO, shown in Fig. 6. NOx emissions shown in Figure 7 clearly show the dramatic effect the calibration changes can have in the engine emissions. With no calibration changes the NOx is 60% higher than the baseline case while with the calibration changes the NOx is 20% lower (an ~80% shift). The PM emissions, Fig. 8, show similar trends to the FTP results, significantly lower PM for the biodiesel with no calibration changes and a slight increase (but still much lower than the baseline) for biofuel run with calibration changes.

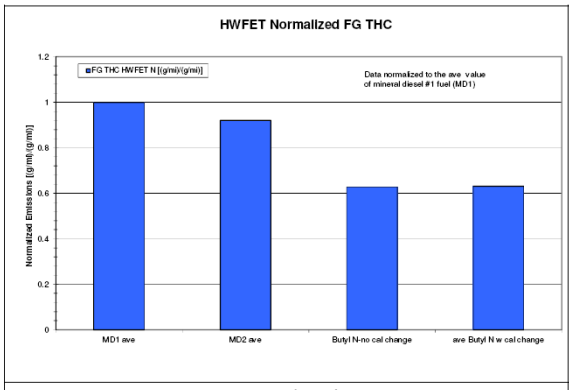

Fig 5.: HWFET normalized THC emissions

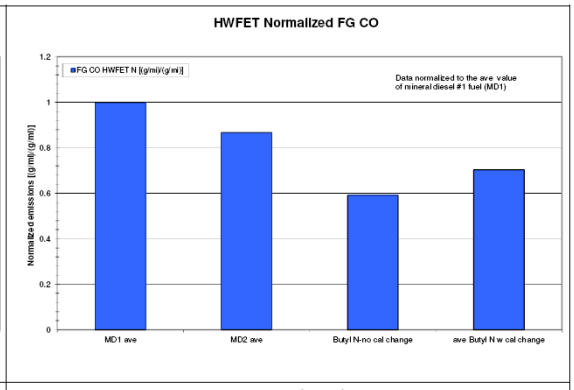

Fig 6.: HWFET normalized CO emissions

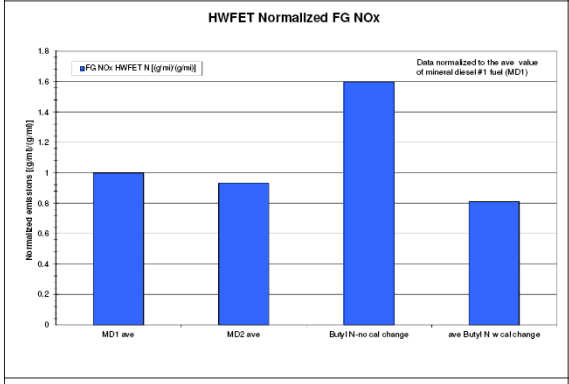

Fig 7.: HWFET normalized NOx emissions

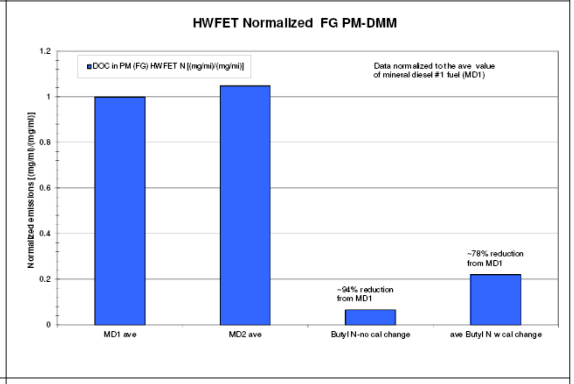

Fig 8.: HWFET normalized PM emissions

Results from the supplemental FTP test, US06, are shown in Figures V.55-V.58 (9-12 below). Overall the results follow the same trends seen in both the FTP75 testing and the HWFET testing. Again, note the US06 is a hot test as compared to the cold start FTP75. Overall the THC emissions, Fig. 9, show a decrease for the biofuel both with and without the calibration changes. Similar, though with a larger reduction, results are seen for CO in Fig. 10. The NOx emissions, Fig.11, again show an increase without the calibration change and a decrease back to similar mineral diesel levels with the calibration changes. Similar results are again seen for the PM emissions in Fig. 12.

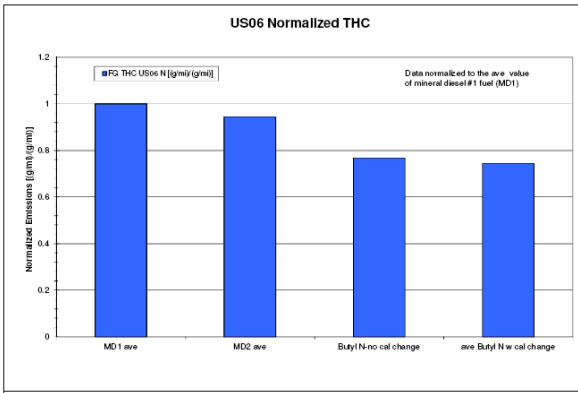

Fig 9.: US06 normalized THC emissions

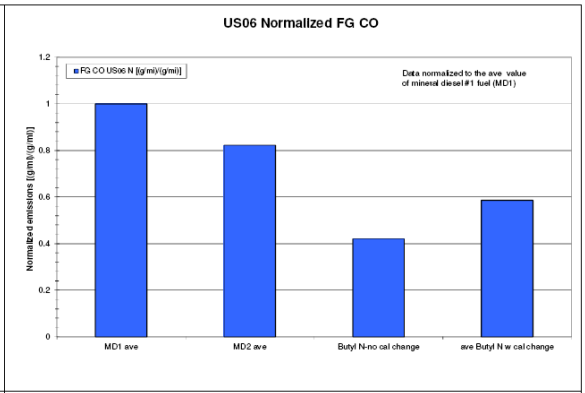

Fig 10.: US06 normalized CO emissions

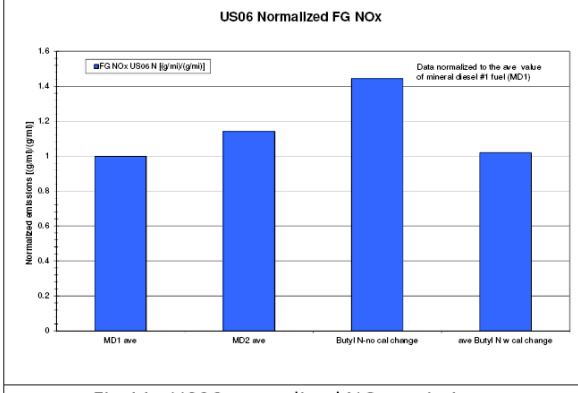

Fig 11.: US06 normalized NOx emissions

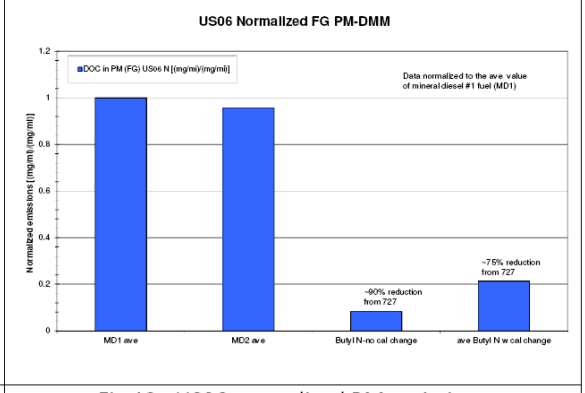

Fig 12.: US06 normalized PM emissions

Conclusions: Two different mineral diesel fuels and a B100 fuel (Butyl Nonanoate), with and without calibration changes to compensate for the fuel differences, were tested on a vehicle for engine out emissions. Results without any calibration changes confirmed the typical findings of higher NOx, lower PM and similar CO and THC as noted by many researchers. However, once the calibration was modified to compensate for the biofuel the emissions results changed dramatically. With the calibration changes the THC and CO emissions were similar for an FTP75 and reduced for both the HWFET and US06 tests. The calibration changes showed the most dramatic changes on the NO_x emissions, with no calibration changes the NO_x increased over the baseline mineral diesel on all three types of tests and with the calibration changes the NOx decreased for the FTP 75 and HWFET and was similar to mineral diesel results on the US06. The PM emissions showed a decrease with the biofuel, compared to the baseline mineral diesel fuels, both with and without the calibration changes (though not as large a decrease with the calibration changes).